Assessment and Mitigation of Wind Risk of Suspended-Span Bridges

Dissertation

submitted to and approved by the

Faculty of Architecture, Civil Engineering and Environmental Sciences
University of Braunschweig – Institute of Technology

and the

Faculty of Engineering
University of Florence

in candidacy for the degree of a
Doktor-Ingenieur (Dr.-Ing.) / Dottore di Ricerca
in Risk Management on the Built Environment *)

by
Luca Salvatori
born 16 February 1976
from Firenze, Italy

Submitted on	31 March 2007
Oral examination on	7 May 2007
Professoral advisor	Prof. Claudio Borri Prof. Udo Peil

2007

*) Either the German or the Italian form of the title may be used.

The dissertation is published in an electronic form by the Braunschweig university library at the address

http://www.biblio.tu-bs.de

Tutors

Prof. Dr.-Ing. Claudio Borri	*University of Florence*
Prof. Dr.-Ing. Udo Peil	*Technical University of Braunschweig*

Doctoral course coordinators

Prof. Dr.-Ing. Claudio Borri	*University of Florence*
Prof. Dr.-Ing. Udo Peil	*Technical University of Braunschweig*

Examining committee

Prof. Ing. Pierluigi Aminti	*University of Florence*
Prof. Dr. rer. nat. Heinz Antes	*Technical University of Braunschweig*
Prof. Dr.-Ing. Gianni Bartoli	*University of Florence*
Prof. Dr.-Ing. Claudio Borri	*University of Florence*
Prof. Ing. Teresa Crespellani	*University of Florence*
Prof. Dr.-Ing. Hocine Oumeraci	*Technical University of Braunschweig*
Prof. Dr.-Ing. Udo Peil	*Technical University of Braunschweig*
Prof. Dr.-Ing. Joachim Stahlmann	*Technical University of Braunschweig*

To my family and Germana

Abstract

Within the general framework of risk management, the vulnerability of flexible bridges under wind action is addressed. Particular attention is paid to the risk of aeroelastic instabilities and buffeting oscillations in presence of self-excited phenomena.

A computational framework based on semi-empirical cross-sectional models for the wind loading and on the three-dimensional finite-element discretization of the structure is developed. This represents a basic tool for assessing wind risk and it is used to obtain some results in the understanding of bridge behaviour under wind storms and in the comparison of different design solutions.

A time-domain model for unsteady wind loading is derived as a development of indicial function load models. Some inaccuracy issues of literature models are solved and the consistency with the quasi-steady limit is ensured. A numerical procedure for identifying the load model coefficients from wind tunnel experimental data in such a way that the reliability of the measured quantities is accounted for is proposed, implemented, and validated. Analyses including structural nonlinearities and damping devices are made possible by the developed time-domain methods.

The effects on aeroelastic stability and buffeting response of along-span wind coherence, mean deformations, and load and structural nonlinearities are quantified.

Finally, mitigation strategies against aeroelastic instability and excessive buffeting oscillations are discussed. A risk-based comparison of some possible solutions is performed in the special case of a suspension bridge. Crossed hangers, secondary cables with opposed curvature, and tuned mass control devices are considered. The results, rendered in terms of yearly probability of collapse and expected number of days of closure to traffic, easily allow a cost-benefit analysis for deciding among different designs. Interesting results are obtained from the simulation of bridges controlled by tuned mass devices.

Sommario

Nel quadro generale della gestione del rischio, questa tesi si occupa della vulnerabilità dei ponti flessibili soggetti all'azione del vento. In particolare vengono analizzati i rischi di instabilità aeroelastiche e di eccessive oscillazioni di buffeting in presenza di fenomeni auto-eccitati.

Viene sviluppato un approccio computazionale basato su modelli sezione semi-empirici per il carico eolico e sulla discretizzazione tridimensionale della struttura in elementi finiti. Tramite tale strumento si ottengono risultati utili nella comprensione del comportamento dei ponti sotto l'azione del vento e si effettuano confronti fra differenti soluzioni progettuali.

Un modello di carico non-stazionario nel dominio del tempo viene sviluppato partendo da modelli basati sulle funzioni indiciali. Alcuni problemi di inaccuratezza dei modelli di letteratura vengono risolti e viene inoltre introdotta la compatibilità con il limite quasi-stazionario. Una procedura numerica per l'identificazione dei coefficienti del modello a partire da dati sperimentali viene proposta, sviluppata e validata. L'approccio nel dominio del tempo rende possibile la simulazione di nonlinearità strutturali e di dispositivi di smorzamento.

Vengono valutati gli effetti della coerenza del vento lungo l'impalcato, delle deformazioni medie e delle non linearità strutturali e di carico sulla stabilità aeroelastica e sulla risposta di buffeting.

Infine differenti strategie progettuali per la riduzione del rischio vengono messe a confronto. In particolare, nel caso di un ponte sospeso, viene valutata la possibilità di usare pendini incrociati, cavi secondari con curvatura contrapposta e dispositivi a massa accordata. I risultati, in termini di probabilità annuale di collasso e numero previsto di giorni di chiusura al traffico, consentono un'analisi costi-benefici ed il confronto quantitativo fra le differenti soluzioni progettuali. Risultati di particolare interesse vengono ottenuti dalle simulazioni con dispositivi a massa accordata.

Zusammenfassung

Im Rahmen des Risikomanagements befasst sich diese Arbeit mit der Vulnerabilität flexibler Brücken unter auftretender Windbelastung. Im Besonderen werden die Risiken der aeroelastischen Instabilitäten und der „Buffeting"-Schwingungen in Gegenwart selbsterregender Phänomene analysiert.

Es wird ein Berechnungsansatz entwickelt, der auf halb-empirischen Querschnittsmodellen für die Windlasten und auf einer 3D-FE-Diskretisierung der Struktur basiert. Der Berechnungsansatz bietet ein grundlegendes Werkzeug zur Bewertung der Windgefahr und wird verwendet, um das Verhalten einer Brücke unter starken Windbelastungen besser zu verstehen und um Ausführungslösungen zu vergleichen.

Ein Modell für instationäre Windlasten im Zeitbereich wird aus den Grundmodellen der Indizialfunktionen abgeleitet. Einige Ungenauigkeitsprobleme der Literaturmodelle werden gelöst und die Kompatibilität mit dem quasistationären Grenzwert wird sichergestellt. Es wird eine numerische Berechnung zur Bestimmung der Lastmodellkoeffizienten aufgrund experimenteller Windkanaldaten vorgeschlagen, ausgeführt und validiert. Analysen mit strukturellen Nichtlinearitäten und Dämpfungsvorrichtungen werden durch die entwickelte Methode ermöglicht.

Die Auswirkungen der Windkohärenz, der Durchschnittsverformungen und der strukturellen Nichtlinearitäten der Belastung und der Struktur auf die aeroelastiche Stabilität und auf die „Buffeting"-Antwort werden quantifiziert.

Abschließend werden Vorschläge zur Abminderung des Windrisikos diskutiert. Ein risikobasierter Vergleich möglicher Lösungen, wie gekreuzte Aufhänger, sekundäre Kabel mit gegensätzlicher Krümmung und Schwingungsdämpfer, wird am Beispiel einer Hängebrücke durchgeführt. Die Ergebnisse, in Abhängigkeit der jährlichen Wahrscheinlichkeit eines Einsturzes und der erwarteten Anzahl von Tagen der Verkehrschließung, erlauben, sich fuer ein Design zu entscheiden. Erfolgversprechende Ergebnisse werden bei der Simulation der Brücken mit Schwingungsdämpfern erhalten.

Acknowledgements

I wish to thank Prof. Claudio Borri and Prof. Udo Peil for their advice and tutoring activity. My gratitude goes to Prof. Paolo Spinelli for his suggestions and support, and to Prof. Paolo Maria Mariano for his encouragement and for being a constant example of dedication to research and teaching. Special thanks to Prof. Wolfhard Zahlten, who co-tutored this work, Dr. Renato Eusani, and Dr.-cand. Christian Neuhaus for the scientific discussions, the exchange of ideas and data, and their warm welcome to the University of Wuppertal at the beginning of my doctoral experience. The discussions with Prof. Gianni Bartoli, Dr. Carlotta Costa, Dr. Claudio Mannini, and Dr. Stefano Pastò are gratefully acknowledged. I am thankful to Prof. Luca Facchini for sharing his competence on wind-field generations, Prof. Herman G. Matthies for welcoming me at the Course on Nonlinear Computational Mechanics in Braunschweig, and Prof. Masaru Matsumoto for the experimental data he kindly sent me. Finally, thanks to my friend Carlo Salinari for proofreading part of this work, to Dr.-cand. Nadine Kimme for helping me with the German translation of the abstract, and to Dr.-cand. Anna Bosi and Dr.-cand. Emanuele Marfisi for their encouragement and counsel.

Contents

List of Symbols

a_h^{Rr}	Indicial function coefficient [-]
b	Half-width of cross-section [m]
b_h^{Rr}	Indicial function coefficient [-]
d_{Rr}	Quasi-steady coefficient, real part [-]
e_{Rr}	Quasi-steady coefficient, imaginary part [-]
f	Frequency [Hz]
$k = K/2$	Reduced frequency (aerospace engineering) [-]
$s = tU/b$	Non-dimensional time [-]
t	Time [s]
u	Along-wind turbulence component [m/s]
u_*	Friction velocity [m/s]
v	Lateral turbulence component [m/s]
w	Vertical turbulence component [m/s]
x	Horizontal displacement [m]
z	Vertical displacement [m]
$\mathbf{A}$	Characteristic matrix
A_h	Moment aeroelastic derivatives [-]
B	Cross-section width [-]
C	Theodorsen function [-]
$\mathbf{C}$	Damping matrix
$\mathbf{C}_a$	Aerodynamic damping matrix
C_D	Drag aerodynamic coefficient [-]
C_L	Lift aerodynamic coefficient [-]
C_M	Moment aerodynamic coefficient [-]
D	Cross-section height [m]
D_{Rr}	Unsteady coefficients (real part) [-]
E_{Rr}	Unsteady coefficients (imaginary part) [-]
$\mathbf{F}_K$	Vector of internal force
F_x	Along wind force [N/m]
F_z	Vertical force [N/m]
H_h	Lift aeroelastic derivatives [-]
$K = \omega B/U$	Reduced frequency (wind engineering) [-]
$\mathbf{K}$	Tangent stiffness matrix
$\mathbf{K}_a$	Aerodynamic stiffness matrix
$\mathbf{M}$	Mass matrix
M_y	Pitching moment [Nm/m]
P_h	Drag aeroelastic derivative [-]

Re	Reynolds number [-]
$\mathbf{S}$	Matrix of turbulence power spectra
Sc	Scruton number [-]
St	Strouhal number [-]
T	Period [s]
U	Mean wind velocity [m/s]
$U_* = U/(fB)$	Reduced velocity [-]
X	Along-wind coordinate [m]
Y	Along-span coordinate [m]
Z	Vertical coordinate [m]
Z_0	Terrein roughness [m]
α_y	Rotation [rad]
ε_{Rr}	Error function in the indicial function identification [-]
κ	Von Kármán constant [-]
ν	Damping ratio to critical [-]
ρ	Air density [kg/m^3]
ϕ	Wagner function [-]
χ	Sears function [-]
χ_{Rr}	Admittance function [-]
ψ	Küssner function [-]
ω	Circular frequency [-]
Φ_{Rr}	Indicial function [-]
ℓ	Element length [m]

List of Figures

List of Tables

Chapter 1

Introduction

In this Chapter the general framework of risk management is briefly recalled. Then the special case of wind risk and its management in suspended-span bridges is considered. In particular, the major wind-related issues, their effects on bridge performances, and the possible strategies to manage them are introduced. Finally the organization of the Thesis and its original contributions are illustrated.

1.1 Risk-management framework

The risk-management framework includes the processes of identifying and measuring risk and developing strategies to manage it (Figure 1.1).

Risk identification consists in recognizing potential sources of harm (natural phenomena, human activities, etc.) and the negative effects they can possibly produce. The analysis may start from either sources or targets. One can start considering an issue (e.g. fatigue in bridge decks) and then look for the possible causes (e.g. traffic, vortex shedding, buffeting); or, vice versa, one can start considering a phenomenon (e.g. buffeting excitation) and then identify the issues it may produce (e.g. reduction of serviceability, fatigue, collapse). The result of the risk identification phase is a graph of problems and potential sources.

Once a risk has been identified, it must be somehow measured, i.e. the probability of a problem to occur and the consequent losses must be estimated. *Risk assessment* includes the collection of data, the development of suitable mathematical models, the definition of possible scenarios, and finally the quantification of risk.

Measuring risk is often difficult. On one hand, rare events are very complicated to estimate, since the tails of the distributions are not accurately obtained from statistics. On the other hand, some consequences are arduous to quantify and compare (e.g. it is very difficult to homogenize human and economical losses).

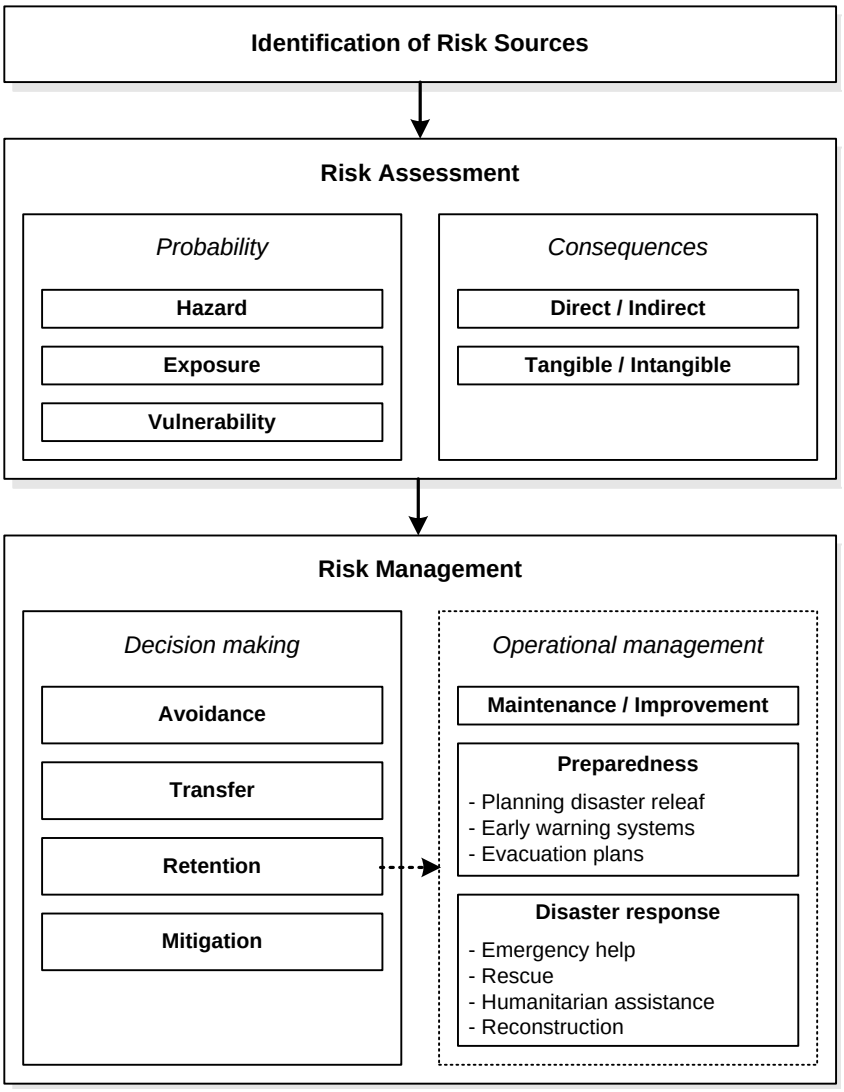

Figure 1.1 Risk management framework

In civil engineering, risk management applies to risk induced by natural disasters (earthquakes, wind storms, fire, etc.). Risk concepts are in general applied also to financial and legal issues.

As a first step an objective definition of risk is required.

Risk is a very general concept that denotes a potential negative impact on an asset. The term 'risk' can be quite equivocal since it may take several meanings. In everyday usage, *risk* is the presence of a danger, its counterpart being absence of danger, i.e. *safety* (Augusti et al., 2001). This yes-or-no definition seldom applies to real life, and never to engineering. The possibility of unwanted events and the consequent losses can never be excluded altogether; therefore, the 'Boolean' definition of risk must be

substituted with a probabilistic one. Numerous definitions of risk are available in the literature, depending on the specific field or situational context of application. Generally speaking, risk is related to the probability of a dangerous event and to the expected losses that may be caused by the same event. The most widely accepted formula for risk quantification is (e.g. Peil, 2006)

$$Risk = Probability * Consequences, \tag{1.1}$$

where, in the general case, the symbol $*$ denotes the convolution operator.

The *probability* of the unwanted consequences to occur is usually decomposed as (e.g. Augusti, 2006)

$$Probability = Hazard * Exposure * Vulnerability. \tag{1.2}$$

The complement of the probability of the harmful event is often referred to as *reliability*, i.e. we have that $Reliability = 1 - Probability$.

The *hazard* is the probability of occurrence of a potentially harmful event (e.g. earthquake, flood, wind storm, fire, terrorist attack). If a hazardous event is characterized by an intensity (peak ground acceleration, mean wind velocity, water level, etc.), then the hazard is a map that relates a given level of intensity to its probability of occurrence in a given time span.

The *exposure* is the probability that the hazardous event meet something vulnerable (urban areas, facilities, lifelines, historical heritage, etc.). As to natural phenomena such as earthquakes, wind storms, floods, fires, avalanches, the exposure is what distinguishes a *natural event*, which does not impact the human sphere, from a *natural catastrophe*, which does impact the human sphere and exceeds man's capacity of overcoming the consequences of the event. When the risk of a particular structure or area is considered, the concept of exposure is often included in the hazard, since the probability of the event will be referred to the specific location.

The *vulnerability* is the conditional probability of obtaining a certain level of damage, given an intensity of the hazardous event. This requires the definition of a quantitative measure of the degree of damage.

Finally, the *consequences* represent the costs of the damage. These can be human, economical, ecological, cultural, or social losses. Losses are usually divided in *tangible*, i.e. consequences that are monetarily quantifiable, and *intangible*, i.e. consequences that are considered beyond estimation, such as human losses or damages to the cultural heritage. Tangible losses are measured in monetary units, whereas several indexes have been proposed for intangible losses (e.g. casualties can be just numbered or measured in years of life lost, social losses are measured through the life quality index). A further classification of the consequences

distinguishes *direct*, i.e. originating immediately from the event (including the costs of reparation or rebuilding, the loss of profit, etc.), and *indirect*, i.e. long-term effects[1] such as the reduction of the durability of facilities, the increased maintenance costs, the modification of economic or social equilibriums, etc. If indirect losses are included in the calculation of risk, as they should, they might be suitably discounted with estimated inflation and interest rates.

It is worth noting that in the literature different definitions of *risk*, *hazard*, *exposure*, *vulnerability*, and *consequences* are present. Sometimes two or more of the concepts described above are incorporated in a single definition. In any case, the final result is a quantity that measures the expected losses in a given time-span, and it is therefore expressed in *losses/time* (e.g. Euros per year, or casualties per year).

Risk assessment allows its comparison of different risks and produces information that is used for decision making, i.e. choosing the most suitable way to manage a given risk. If several problems have been assessed, the quantitative estimates of risk make *prioritization* ideally possible, allowing the risks with greater probable losses to be handled before those with lower risks. Risk assessment also provides a criterion to guide the decision maker in allocating resources, which are available in finite amount. If a purely economic evaluation is performed, the costs of risk management itself should be included in the resource allocation process, since the resources spent in performing risk management could be spent in more profitable activities.

According to (Dorfman, 1997), all techniques of *risk management* fall into one or more of the following four categories:

- Avoidance;
- Transfer;
- Mitigation;
- Retention.

Risk avoidance is the most radical strategy and includes not performing the activity at risk (e.g. not building a structure). Of course, this strategy also implies forgoing the potential benefits and gains that accepting the risk may have allowed.

Risk transfer means causing another party to accept the risk, being insurance the most typical example.

[1] Sometimes the term 'indirect' is used with a 'spatial' meaning instead of a 'temporal' one. For example, if the risks induced by the closure of a long-span bridge are considered, the direct losses with respect to the company that manages the bridge are the tolls not received, the indirect losses are caused to other companies and to society in general, such as the work hours lost by people who are prevented to reach their work places.

Risk mitigation consists in reducing the risk. It involves methods that reduce the probability or the severity of the loss. If it is possible to mitigate risk by reducing the hazard for some man-induced risks (e.g. it is possible to reduce the probability of a terrorist attack by improving social or political conditions), the same is not possible for natural events. Nevertheless, it is often possible to reduce the exposure, e.g. not building houses in a flood prone area. The reduction of the vulnerability by technical solutions and enforced codes is the mitigation strategy where the contribution of engineers plays the most important role; it is worth to stress that the reduction of vulnerability is achieved not only by increasing the resistance of a structure but also by improving the understanding of a phenomenon so that a more efficient design can be performed (Peil, 2006). Finally, it is possible to mitigate risk by reducing its consequences: early warning systems are a typical example of this.

Risk retention means accepting some of, or all, the consequences of a risk. It must be clear that each risk which is not avoided or transferred is, at least partially, retained by default. In civil engineering, in particular, it is not possible to reduce a risk to zero; therefore, risk retention is unavoidable. The amount of risk that is not mitigated is called *residual risk* and must be compared with the *acceptable risk*, i.e. the one that the decision maker is willing to retain. In most cases, the acceptable risk is affected by unobjective factors, such as the *perception* of the risk by individuals and society that acts as a 'cultural filter' (Alexander, 2004). How a risk is perceived is in turn affected by communication (e.g. Starr et al., 1976) and by the nature of the risk (e.g. voluntary risks, such as those associated to car transportation, are accepted more willingly than involuntary risk such as terrorist attacks).

Operational risk management is often treated as a concept distinct from decision making (e.g. Plate, 2000); nevertheless, it is clear that this process easily fits into the category of risk retention. Maintenance and improvement of a system are part of operational risk management, as well as the concepts of preparedness and disaster response. *Maintenance* of an existing protection system is a necessary process in order for it to function as planned, and *improvement* is a special case of maintenance aimed to update a system to new issues that were not present or known before. *Preparedness* to catastrophic events is a necessary response to the fact that a residual risk is unavoidable. Planning disaster relief, early warning systems, and emergency plans are part of the preparedness concept. Finally, *disaster response* includes emergency help, rescue, humanitarian assistance to victims, lifeline restoring, and reconstruction.

1.2 Aeolian risk

Wind storms are one of the natural events with the most catastrophic impact on human life. According to the data collected by the Munich Reinsurance Group (Berz and Rauch, 1997) wind storms caused in the last 30 years 45% of the total fatalities due to natural hazards (second cause after earthquakes causing 47%) and 28% of the total economic losses (third cause after earthquakes with 35% and floods with 30%). If only insured losses are considered, then the percentage of losses due to wind increases up to 70%. It is therefore clear that wind risk cannot be neglected in comparison with other environmental risks. Moreover, the data show a dramatic increase of wind risk in the last decades. This trend seems destinated to continue in future. Causes of the increasing wind risk can be found in all risk components in Eqs (1.1) and (1.2): hazard, exposure, vulnerability, and consequences.

It is now almost universally accepted that climate changes are in act, and that their natural evolution has been dramatically accelerated in the last decades by human activities. The increasing combustion of fossil fuels releases a large amount of carbon dioxide in the atmosphere which is the main responsible for the infamous greenhouse effect. The consequent global warming is causing faster ocean evaporation and a redistribution of precipitations and temperature gradients. There is therefore more energy available for atmospheric processes in the tropical and extra-tropical regions, which explains the increase in frequency and strength of wind storms, i.e. in wind *hazard*, that is being registered since the 1930s (e.g. Kasperski, 1998).

The *exposure* to wind hazard is also increasing due to the growth of Earth's population and the migration of people and goods into wind-hazardous areas.

Structures are becoming more vulnerable to wind action due to the trend toward lightweight design, encouraged by new materials and computational techniques. For structures with challenging design, wind action becomes a dominant effect. Although great advances in the comprehension of wind-structure interaction have been made in the last decades, this process is still in action. Moreover, very innovative designs may suffer from effects of which designers are not aware. These are the reasons of the general increase in the *vulnerability* to wind action.

Finally, the number of people and goods exposed to risk increases, i.e. also the *consequences* of wind damage increase.

The main parameter for determining wind hazard and the consequent damage is maximum wind velocity expected in a given time span. Typically the 10-min-average velocity with a return period of 50 years is considered by codes and standards that are enforced in 'well-behaved' wind climates (i.e. where cyclones and tornadoes can be excluded).

However, in case of wind hazard, also non extreme events must be considered in evaluating the total risk. Moderate, and therefore relatively frequent, wind velocities may produce serviceability issues with a possibly great economic impact. Let us think to the economical and social losses produced by the closure to traffic for several hours, several times a year, of a crucial bridge linking two parts of a town or country. Furthermore small storms, even if not causing significant structural damage, may affect non-structural components and give rise to costly maintenance.

Moderate winds can be the source of the so-called *dissatisfaction risk*. They can be of great discomfort both outdoors (pedestrian discomfort, canyoning between buildings may cause some social-economic negative effects on the use of commercial areas) and indoors (e.g. window shatters slamming), may produce noise, and affect the dispersion of gas and pollutants in the air (often this is a positive effect, but can sometimes produce unwanted pollutant concentrations, or bring pollutants from industrial areas to urban ones). In the long run these can produce concrete negative effects (e.g. reduction of productivity of employees, and consequent value of buildings)

For these reasons wind design should account also for the whole wind climate and not only for extreme winds and for structural resistance.

1.3 Wind-risk management in suspended-span bridges

The flexibility of suspended-span bridges (i.e. cable stayed and suspension bridges) makes their design particularly sensitive to wind action, to such an extent that wind is the principal issue for the designers of such structures. Already in the XIX century, wind action was recognized as the cause of some collapses and severe damaging of bridges. An example is the Brighton Chain Pier (Figure 1.2a), a suspension bridge that was severely damaged by wind storms in 1833 and 1836 and then finally destroyed on Dec. 4, 1896. However, fluid-structure interaction phenomena, previously prerogative of aeronautic field, have been brought to the attention of structural designers only after the infamous collapse of the original Tacoma Narrows Bridge on Nov. 10, 1940 (Figure 1.2b).

Nowadays, wind effects are more and more a concern for bridge designers due to the increasing flexibility of these structures, which is encouraged by the use of new materials and by the advances in the computational techniques. On the one hand, crucial links overcome increasingly long spans. On the other hand, smaller bridges and footbridges are becoming more and more transparent and architectonically appealing; however, these aesthetic needs penalize sometimes the structural stiffness and dynamic behaviour.

In the last decade suspension bridges with challenging span lengths have been realized; examples are the Storebælt Bridge in Denmark (1998), with a

main span of 1624 m, and the Akashi-Kaikyo Bridge in Japan (1998), with a main span of 1991 m. Also cable-stayed bridges are increasing in length and approaching 1-km spans; examples are the Pont de Normandie in France (1995, 856 m) and the Tatara Bridge in Japan (1999, 890 m). There also exist proposal designs for extreme bridges as the suspension one crossing the Messina Strait (Italy), for which a 3300-m main span carrying both highway and railway has been conceived, and even a Gibraltar Strait crossing has been imagined with an overall length which exceeds 5 km.

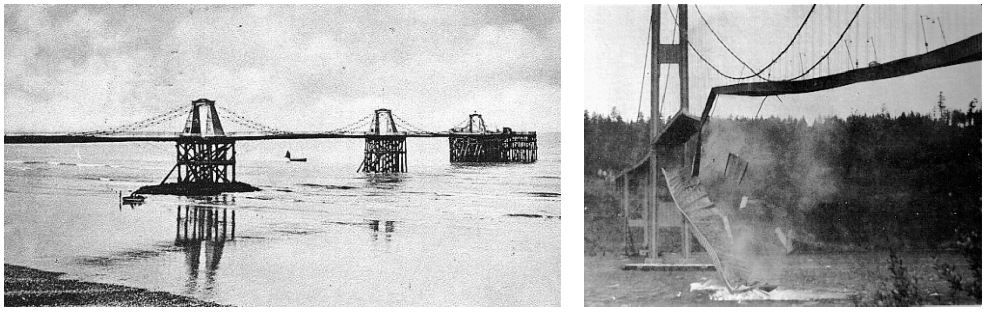

(a) (b)

Figure 1.2 Brighton Chain Pier (a); collapse of the original Tacoma Narrows Bridge (b)

For bridges with very long spans, seismic risk is relatively small because of the very low eigenfrequencies. Also the risk induced by geotectonic motions or geological settlement is a secondary one, due to the high flexibility of the long suspended spans, for which large settlements result in relatively small adjustments of the geometry, comparable to those due to thermal dilatation. During the erection of Akashi-Kaikyo Bridge a 7.2-magnitude earthquake with the epicentre only a few kilometres away from the bridge location produced over 6000 fatalities in Kyoto, but caused almost no damage to the bridge (Nasu and Tatsumi, 1995; Yamagata et al., 1996), whose main span was reportedly lengthened by a full meter due to horizontal displacement along the activated tectonic fault. Also for suspended-span footbridges, the seismic risk is a secondary one due to their small mass.

Below, the framework presented in Section 1.1 is specialized to the case of wind risk and suspended-span bridges. The main aerodynamic phenomena and their possible effects on these structures will be identified; some common aspects on the assessment of the consequent risk will be examined, and general concepts of bridge management will be discussed.

Under the action of the wind a bridge must withstand the static forces induced by the mean wind (mainly the drag force acting in the lateral direction). In addition, it is susceptible to aeroelastic effects. These include static instability (torsional divergence, lateral buckling, etc.), vortex induced oscillations, dynamic instabilities (e.g. galloping, torsional flutter,

coupled flutter), and buffeting in presence of self-excited forces. These aeroelastic phenomena are more thoroughly described in Section 2.2.

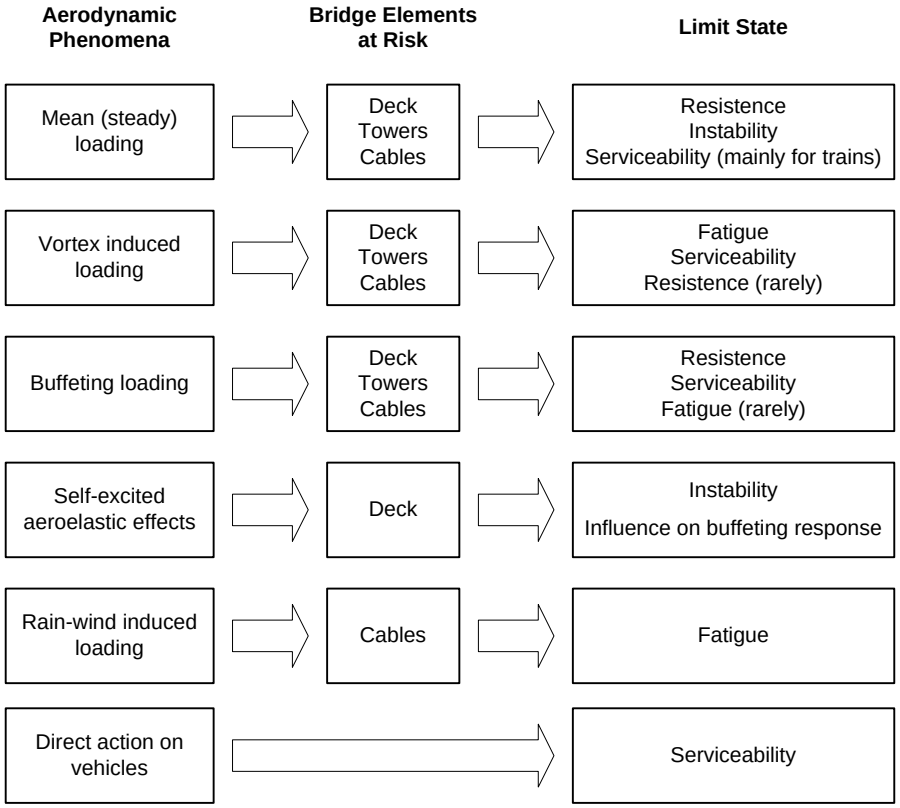

Figure 1.3 Summary of aerodynamic phenomena and their effects on bridges

The aerodynamic effects on bridges can be summarized as follows (see also Figure 1.3):

- Mean steady loading;
- Oscillations of the deck due to vortex shedding;
- Buffeting loading due to oncoming wind gusts;
- Aeroelastic phenomena affecting buffeting response and resulting in possible instabilities;
- Vibration of cables due to wind-rain interaction phenomena;
- Direct effect of wind on the safety and comfort of the traffic.

The mean wind is responsible for static forces acting on the main structural elements. The most important component of this loading is the drag force acting on bridge deck, towers, and main cables. Mean loading may produce large stresses in all the structural elements and is one of the most important parameters for the design of very long-span bridges. For this reason it is particularly important to achieve low drag forces in bridge

decks: a requirement that encouraged the development of streamlined box girders.

Vortices are shed periodically from the sides of bluff obstacles and produce alternating aerodynamic forces (see Section 2.2.1) and consequent oscillations. These do not usually cause very large level of stresses, but if the wind speed for their onset is sufficiently low, they may occur frequently and result in a fatigue damage (e.g. Pastò, 2005). In addition, vertical and torsional oscillations of the deck can cause problems to bridge users, by alarming and unpleasing pedestrians and causing problems to vehicle traffic. A paradigmatic case is the one of the Storebælt Bridge (Larsen et al., 2000): during the final phases of girder erection and road surfacing works the suspended spans of the bridge displayed unacceptable vortex-induced oscillations (Figure 1.4), which have been mitigated by devising a guide vane (Figure 1.5). The improvement of the aerodynamic shape is indeed an effective countermeasure against vortex-induced vibrations. A further possibility is the increase of the structural damping; this solution is often mandatory for the towers, where tuned mass control devices are often installed. Also hangers and stays are sensitive to vortex induced vibrations since their lengths, and consequently their frequencies, vary within a given structure so that a wide range of natural frequencies are likely to be excited by vortex-shedding. Typical countermeasures to this effect are the use of cables constituted by wire strands which posses an internal damping, the installation of local viscous dampers, the introduction of secondary cables linking the principal ones together or the introduction of helical strakes breaking the coherence of the shed vortices.

Wind gustiness results in a random loading on the structure, which is referred to as *buffeting* (see Section 2.2.5). Although also towers and cables are subjected to this excitation mechanism, the bridge deck is the most exposed and is subjected to lateral, vertical, and torsional oscillations. Buffeting oscillations may rise strength, serviceability, and, more rarely, fatigue issues. Loading mechanism, simulations, assessment, and mitigation of buffeting effects will be discussed throughout all the next Chapters.

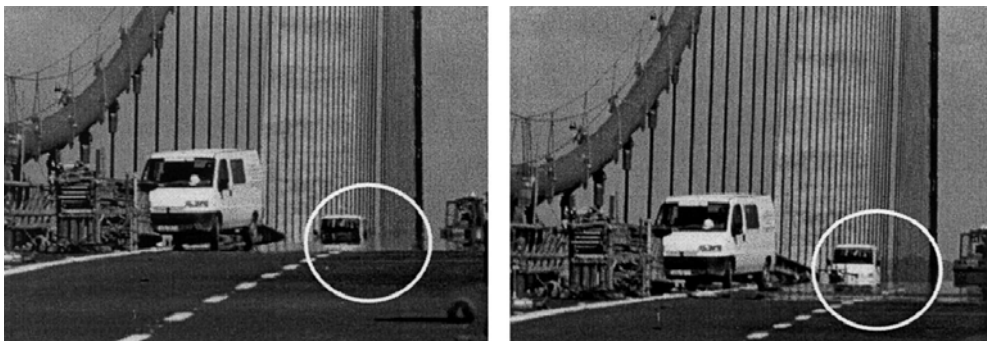

(a) (b)

Figure 1.4 Crest (a) and trough (b) of a large amplitude vertical oscillation in the Storebælt Bridge (Larsen et al., 2000)

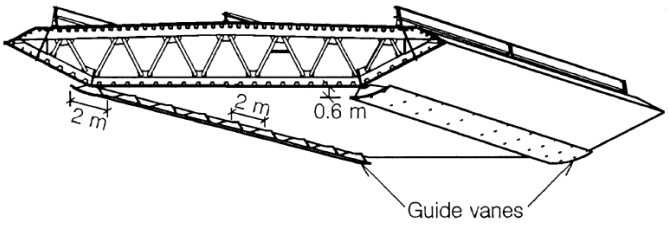

Figure 1.5 Arrangement of the guide vanes along the bottom/lower side panel joint of the Storebælt Bridge girder cross section (Larsen et al., 2000)

Aeroelastic instabilities develop when the mean wind velocity reaches a critical value. They are produced by steady forces, which may lead to the loss of stiffness of the structure-flow system (divergence in torsion or bending, see Section 2.2.2), or by self-excited aeroelastic effects, which may lead to modes where the structural damping is cancelled by the aeroelastic one (Hopf bifurcations such as galloping, see Section 2.2.3, and torsional and coupled flutter, see Section 2.2.4). Since the collapse of the original Tacoma Narrows Bridge, the evaluation of the aeroelastic stability of the deck has become an essential part of the design process. Aeroelastic stability will be also addressed throughout the rest of this Thesis.

Wind-rain interaction (see Section 2.2.6) is a complex multi-meteorological effect due to the interaction between rain rivulets along the cables, the cables motion, and the wind flow. It may produce large oscillations also for relatively low, and therefore frequent, wind velocities, with consequent fatigue risk.

Besides acting on the bridge, wind also has direct effects on traffic. The difficulty of driving in windy conditions is a source of discomfort and may cause accidents due to the impaired directional control or to the overturning of high-sided, light vehicles. Long span bridges constitute crucial links; therefore, their closure due to excessive discomfort for the

users or to blockage by an accident must be avoided as far as possible. A protection that would enable the bridge to be usable in all but the most extreme condition would require continuous edge barriers of sufficient height to produce adequately sheltered conditions on the roadway deck. However there are considerable difficulties in providing such barriers, since the drag would be significantly increased and the aeroelastic stability unacceptably reduced. Protecting the driving lanes is particularly important next to the towers, since their sheltering effect may produce rapid changes in the wind load on vehicles.

So far, wind risk and technical solution for its mitigation have been discussed, by keeping in mind the design phase of a structure or the evaluation a possible improvement. For example, the feasibility of installing a vibration control system for reducing the probability of closure to traffic shall consider the costs of design and installation against the potential economical losses due to the closure to traffic. A further aspect of (operational) risk management is bridge maintenance.

Preventive *maintenance* (e.g. Vassie, 2000) has the objectives of ensuring that a bridge achieves its design life, that its risk of failure keeps below acceptable values, and that it remains open to traffic continuously throughout its life. Bridge maintenance encompasses *inspection*, *monitoring*, and various types of testing of the structure during its whole life. This information is needed for deciding the most appropriate type and timing of maintenance works (e.g. Neves and Frangopol, 2005). The idea is that expenditures which are deferred to later date 'saves' money, since that money could be invested during the period of deferral and therefore have an increased value when the expenditure is eventually made. On the other hand, during the deferral period the cost of maintenance tends to increase due to the progressive deterioration of the structure and to inflation. The planning of maintenance consists in finding the optimum timing for the maintenance that minimizes the total costs.

The prioritization of maintenance requirements is usually done by means of a *cost-benefit* analysis, where the *whole-life costing* is optimized by using economic and probabilistic models. All the costs of engineering, traffic management, and traffic delays should be included. A typical framework for this analysis is the so-called *performance based design* (e.g. Hamburger et al., 1995), originally developed by the Pacific Earthquake Engineering Research (PEER) Centre for seismic design and later tentatively applied to wind engineering (Paulotto et al., 2004). The concept of whole-life costing is apparently obvious but changed the approach to the design of large structures since the last decade. The process consists in estimating the costs of general management, planned and extraordinary maintenance, and (possibly) dismantlement, and in adding them (suitably discounted) to the costs of the design and construction.

1.4 Contribution of the present work

As it has been shown in the previous Sections, risk management of bridges includes a large variety of physical, technical, operational and economical aspects. Within the general risk-management framework, the task of structural engineers is focused on the evaluation of vulnerability and on its reduction.

In this research work a framework for the analysis of flexible bridges under wind action is developed, validated, and applied to some specific calculations.

Among the wind-related risk sources presented in the previous Section, the aeroelastic instabilities (either static or dynamic) and the buffeting vibrations in presence of aeroelastic effects are considered.

As it has been already discussed, aeroelastic instabilities may lead to the total or partial collapse of a bridge. The consequent losses are not only those due to the intrinsic value of the structure but also those related to the strategic role usually played by bridges, especially those with long spans, that are also those more sensitive to wind action. In fact, bridges may have a crucial value for evacuating an area hit by a catastrophic event and for allowing humanitarian assistance. It is therefore decisive that they remain serviceable in those critical circumstances.

Hence, the (at least partial) serviceability of such structures should be preserved even in extreme conditions. Among the problems that may be induced by buffeting vibrations, I will focus on the risk of temporary interruption of serviceability. Further possible problems induced by buffeting oscillations are strength failure and fatigue failure. Although these aspects can be easily studied with the computational framework developed in this research work, they will not be examined, since they depend strongly on constructive details, so that very specific considerations should be done for each bridge.

1.4.1 Outline of the work

In this Chapter a general framework for risk management has been presented, and the specific importance of aeolian risk has been highlighted. Then, wind-risk management on suspended-span bridges is discussed.

In Chapter 2, some preliminary aspects of wind engineering are reviewed. The mathematical modelling of the turbulent velocity field of natural wind is recalled, and it will be used later on for the buffeting analyses. Also, the principal aeroelastic phenomena that can be a concern for suspended-span bridges are examined.

In Chapter 3, wind load models for bridge decks are dealt with. In particular, steady, quasi-steady, and unsteady models for self-excited and buffeting forces are presented, both in the frequency and the time domain.

All load models are placed in a common framework, where a specific notation is introduced which simplifies the understanding of some physical aspects and allows an easier mutual comparison. Besides the critical review of literature models, a new formulation for self-excited loads in the time domain is proposed as a development of existing load models based on indicial functions. In particular, the extended model includes the consistency with the quasi-steady limit and corrects some aspects that used to lead to an inaccurate identification of the same indicial functions. A specific numerical procedure for the identification of indicial functions from measured aeroelastic derivatives is developed, in such a way that the reliability of the experimental data is taken into account. Some examples of identification are provided and discussed. The developed time-domain unsteady formulations will be particularly important for the following parts of this work, since it will allow simulating nonlinear structures and localized damping devices for mitigating bridge oscillations.

In Chapter 4, a numerical framework for the numerical analysis of bridges under wind action is developed. It is based on a finite element discretization of the structure and on the semi-empirical load models presented in Chapter 3. A specific computer program and original numerical procedures are developed for evaluating aeroelastic stability and buffeting response in presence of self-excited forces, both in the frequency and time domain. The program includes the generation of the wind velocity field, nonlinear structural finite elements formulated according to the co-rotational approach, several types of analysis, and macros for the parametric generation of the structural models and for Monte Carlo simulations.

In Chapter 5, numerous computational results are presented. First of all, the proposed load model based on indicial functions is validated by means of a full-bridge analysis, in which time-domain simulation results are compared with multi-modal frequency-domain ones. Then, the reliability of the indicial function approach is discussed. Furthermore, by means of a simplified structural model, it is shown how secondary critical modes can be simulated and visualized. Finally, several comparisons helpful in the prediction of structural vulnerability are presented; in particular, the effects on flutter and buffeting response of the along-span wind coherence, of the mean steady deformations, and of the load and structural nonlinearities are evaluated.

In Chapter 6, some design strategies for the mitigation of vulnerability are presented and compared by means of a risk-based analysis. In fact, a methodology for choosing a design solution rather than another one is easily offered if a comparison of probable-losses, i.e. of risk, can be performed. In particular, the collapse risk due to aeroelastic instabilities and the risk of closure to traffic due to excessive oscillations are considered. Among the structural solutions for suspension bridges: counter-opposed curvature cables, crossed hangers, and tuned mass control devices are evaluated.

Finally, some general conclusions are drawn in Chapter 7.

1.4.2 Original achievements

The original scientific results and contributions of this dissertation are roughly summarized below:

- Further development and validation of time-domain load models for unsteady wind loading:
  - Development of a common framework for cross-sectional wind load models and introduction of a simplified notation clarifying physical aspects;
  - Introduction of the consistency of the indicial function load model for self-excited forces with the quasi-steady limit behaviour;
  - Development of a numerical procedure for the identification of indicial functions from measured aeroelastic derivatives by taking into account the reliability of experimental data and preserving the load accuracy also at the low reduced velocities;
  - Evaluation of the reliability of the indicial function approach.
- Development of a computational framework for the analysis of suspended-span bridges under wind action, based on finite element discretization, and including original procedures for the aeroelastic stability analysis and the buffeting simulation.
- Results on the assessment of bridge vulnerability, including the investigation of the following effects on stability and buffeting response:
  - Effects of load nonlinearities;
  - Effects of structural nonlinearities;
  - Effects of along-span correlation of wind;
  - Effects of mean steady deformations.
- Risk-based comparison of the following design strategies for the mitigation of aeroelastic instability and buffeting risks on suspension bridges:
  - Secondary cables with opposed curvature;
  - Crossed hangers;
  - Tuned mass control systems.

Chapter 2

Preliminary Notions on Wind Engineering

In this Chapter the fundamentals of wind engineering that will be useful in the following of this Thesis are briefly reviewed. In the first Section, the properties of the flow in the atmospheric boundary layer are recalled, with particular consideration for the mathematical description of the velocity field and on its numerical simulation. The second Section deals with the aeroelastic phenomena according to a classification that is consolidated in the literature. Special attention is paid to those phenomena that may occur in suspended-span bridges, either to the whole structure or to its individual parts (e.g. cables, towers).

2.1 Wind modelling

Wind is the moving of air masses basically caused by the uneven heating of Earth's surface. From the meteorological point of view the phenomenon is, of course, very complex and is affected by a large variety of factors (for an overview on them, see e.g. Simiu and Scanlan, 1996, and references therein). From the engineering point of view, on the other hand, only the principal features of the phenomenon need to be modelled.

At sufficiently great heights, the motion of air relative to the Earth's surface is independent on the friction with the ground and is determined only by the pressure gradient and by the inertial effects due to Earth's rotation ('centrifugal' and Coriolis forces). At these heights, the wind velocity may be assumed as horizontally homogeneous and stationary, and it is referred to as *gradient velocity*.

Earth's surface exerts upon the moving air a horizontal drag force, which retards the flow and produces a turbulent mixing throughout a region of the atmosphere called *atmospheric boundary layer*, whose depth

ranges from a few hundred meters to some kilometres, depending on the gradient velocity and on the roughness of the terrain.

In wind engineering, we are interested in the effects of wind on civil structures; therefore, a mathematical description of the flow within the boundary layer is required. Since wind velocity varies both in space and time in a complex, random way, it is described in statistical terms.

Long-period field observations (van der Hoven, 1957) showed that the power spectral density function of the modulus of wind velocity exhibits two main peaks (see Figure 2.1): a mesometeorological one centred around a period of about four days, associated with the passage of a typical weather system past a fixed point; and a micrometeorological one centred around a period of about one minute, associated with local gusts. The two peaks are separated by the so-called *spectral gap*, i.e. a range of frequencies with very small power content. The spectral gap allows the decomposition of the instantaneous velocity as the sum of a *mean velocity* and of a *turbulence velocity*.

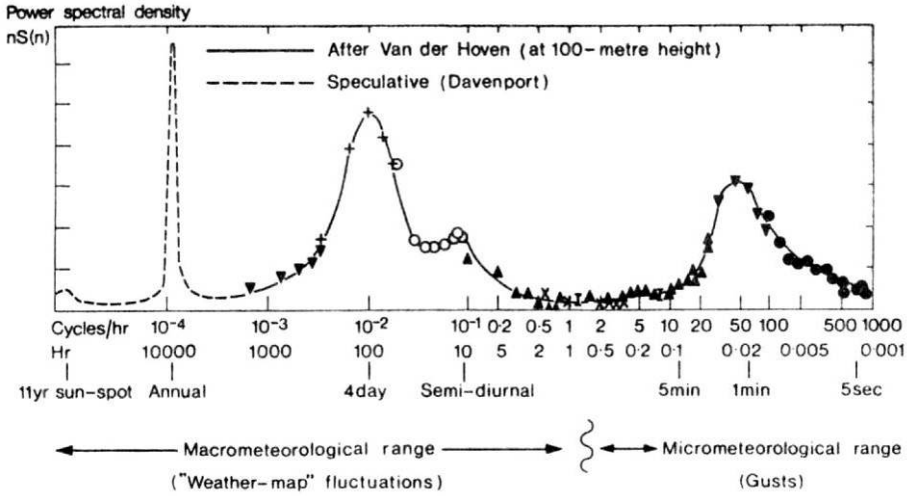

Figure 2.1 Van der Hoven spectrum (van der Hoven, 1957)

The mean velocity varies very slowly with respect to the typical periods of a structure; for this reason, it may be considered as constant in time during a structural analysis, and we are only interested in the probability of exceeding a certain value. On the other hand, the frequencies contained in the turbulence components are likely to interact dynamically with the structures; therefore, a detailed description in time and space is required.

Of course, the velocity also varies in direction. In a given location, for topographic and orographic reasons (vicinity of the sea, presence of mountain ranges, etc.), the probability of occurrence of a given mean wind velocity is not the same in all directions. Detailed information can be obtained only through on-site measurements and is usually presented through directional probability diagrams (the so-called wind speed

rosettes). For bridges the direction of main concern is usually the one orthogonal to the bridge span.

A right-handed Cartesian coordinate system $\{X, Y, Z\}$ is introduced, with the X-axis in the direction of the mean wind velocity, positive along wind; and the Z-axis vertical, positive upwards. The velocity at the time t is decomposed as (Figure 2.2)

$$\begin{aligned} U(Z) + u(X,Y,Z,t) &\quad \text{in the } X\text{-direction,} \\ v(X,Y,Z,t) &\quad \text{in the } Y\text{-direction,} \\ w(X,Y,Z,t) &\quad \text{in the } Z\text{-direction,} \end{aligned} \tag{2.1}$$

where U is the mean velocity, which depends only on the height Z above the ground; u, v, and w are the (zero mean) fluctuating components of the wind velocity field and are treated as stationary stochastic processes.

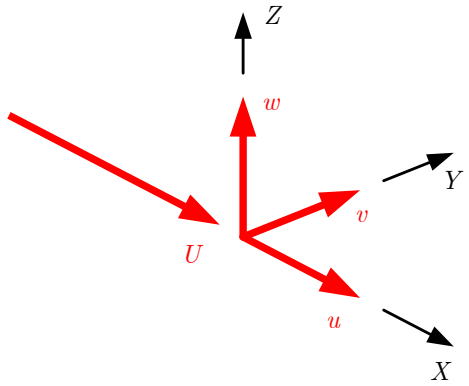

Figure 2.2 Wind velocity components

2.1.1 Mean velocity

Within the boundary layer, the mean wind velocity increases with elevation and is assumed as horizontally homogeneous. In the case of field measurements, the mean velocity is calculated by convention over a time interval of 10 minutes.

By dividing the boundary layer into two regions and by using a dimensional analysis, a simple expression for the mean wind velocity in the lower region of the boundary layer (surface layer) can be obtained:

$$U(Z) = \frac{u_*}{\kappa} \ln \frac{Z}{Z_0}, \tag{2.2}$$

in which u_* is the friction velocity, defined by $u_* = \sqrt{\tau_0/\rho}$, being τ_0 the shear stress at the ground surface; $\kappa \simeq 0.4$ is von Kármán's constant; and Z_0 is the roughness length of the terrain. Figure 2.3 shows a sample mean wind velocity profile.

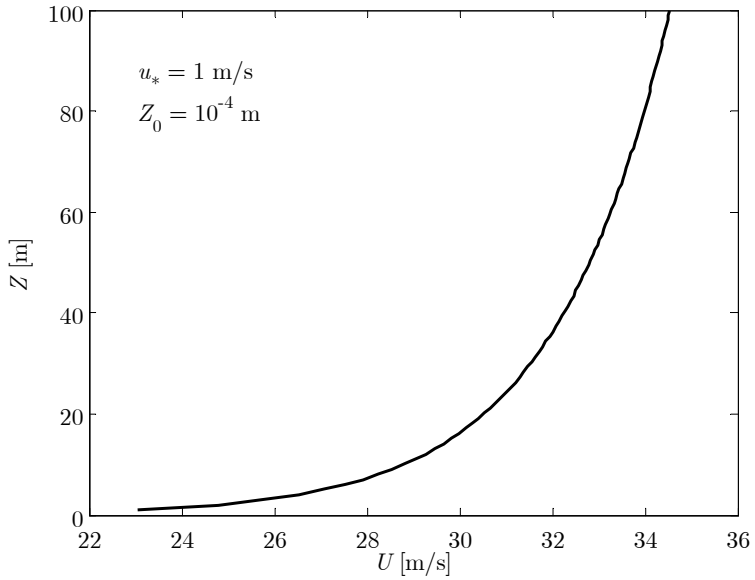

Figure 2.3 Example of mean wind velocity profile

Eq (2.2) is valid up to a certain height above ground level that can be approximated by the relation $Z_L = b_L u_* \big/ \left(2\omega_{Earth} \sin \phi_{lat}\right)$, in which $b_L = 0.015 \div 0.030$ is an experimental constant, ω_{Earth} the circular frequency of Earth's rotation, and ϕ_{lat} the latitude angle.

The friction velocity can be obtained from field measurements or is provided by codes as a function of the location, i.e. of region, height above sea level, distance from the sea, orography, topography, and roughness category of terrain. In codes and standards (e.g. Eurocode 1, 1997; Istruzioni CNR, 2006) a reference (or base) velocity is usually provided, which is a characteristic of the location site and is defined as the maximum mean wind velocity in an interval of 10 minutes, at $Z = 10\,\text{m}$, on a flat and homogeneous terrain with roughness length $Z_0 = 0.05\,\text{m}$, with a return period of 50 years.

The roughness length Z_0 can be interpreted as the average size of vortexes produced by the friction between air and Earth's surface at ground level. According to Eq (2.2), Z_0 is the height above the ground at which the mean wind velocity is zero. The roughness length can be estimated from on site measurements. Codes and standards report tables which associate roughness length values to terrain categories. The values of Z_0 range from few microns (~10^{-5} m for plane ice) up to some meters (~10 m for urban

areas). Over water, as it is the case of most suspended-span bridges crossing straits and estuaries, the roughness length depends on the wind velocity since the wind interacts with the water surface by inducing waves, which in turn represent an increased roughness. In case of strong winds ($U > 25\,\mathrm{m/s}$), as are those that are considered in next Chapters for the limit states of bridges, the roughness length can be assumed as constant and estimated as $Z_0 \simeq 0.0035\,\mathrm{m}$ (Simiu and Scanlan, 1996).

Field measurements and codes usually provide a characteristic value of the mean wind velocity in a given location that represents the velocity with return period $T_R = 50\,\mathrm{years}$, i.e. the one with a yearly probability of exceedance $p_R = 1/T_R$ of $0.02\,\mathrm{year}^{-1}$. In order to relate mean wind velocities and return periods, a *Type I* extreme value distribution (Gumbel distribution) can be assumed; in Eurocode 1, 1997, the relation

$$\frac{U_{T_R}}{U_{50}} = \left(\frac{1 - K_1 \ln\left(-\ln\left(1 - 1/T_R\right)\right)}{1 - K_1 \ln\left(-\ln\left(0.98\right)\right)} \right)^{n_R} \tag{2.3}$$

is suggested, with the coefficients $n_R = 0.50$ and $K_1 = 0.2$ and T_R expressed in years; whereas in the Italian CNR Guidelines (Istruzioni CNR, 2006)

$$\frac{U_{T_R}}{U_{50}} = 0.65 \left(1 - 0.14 \ln\left(-\ln\left(1 - \frac{1}{T_R}\right)\right)\right) \tag{2.4}$$

is used (Figure 2.4).

Finally, it is worth noticing that field observations suggest that climate changes are leading to a progressive increase in the frequency of extreme events (e.g. Kasperski, 1998), in such a way that wind storm occurrence can no longer be considered as a stationary process. In this case the design velocity for civil buildings should depend not only on the expected life of a structure but also on the year of construction.

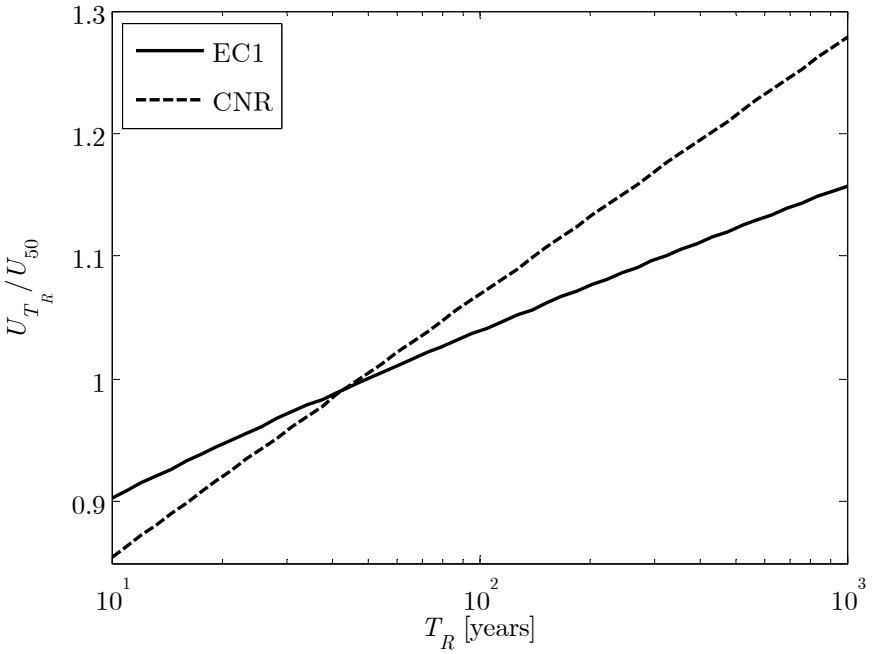

Figure 2.4 Relation between mean wind velocity and return period

2.1.2 Fluctuating velocity

The turbulence components u, v, and w are usually modelled as stationary Gaussian processes.

Since the flow is assumed as horizontally homogeneous, the statistical characteristics depend, in general, only on the height above the ground Z. The *standard deviations* σ_u, σ_v, and σ_w are close to zero at the top of the boundary layer, where the flow is not disturbed by the interaction with terrain roughness, and they increase toward the ground. Experimental observations show that at the typical heights of civil structures, standard deviations can be assumed as independent on the height and they can be approximated as

$$\sigma_u = \frac{u_*}{\kappa}, \qquad \sigma_v = 0.75\sigma_u, \qquad \sigma_w = 0.50\sigma_u. \tag{2.5}$$

The *turbulence intensities* are defined as the ratios of the standards deviations with the mean velocity:

$$I_u = \sigma_u/U\,, \qquad I_v = \sigma_v/U\,, \qquad I_w = \sigma_w/U\,. \tag{2.6}$$

From Eqs (2.2), (2.5) and (2.6), it follows that

$$I_u(Z) = 1\Big/\ln\Big(Z\Big/Z_0\Big), \qquad I_v = 0.75 I_u, \qquad I_w = 0.50 I_u. \tag{2.7}$$

The *integral length scales* of turbulence are measures of the average sizes of vortices in every direction. For instance, the integral length scale L_u^X describe the average turbulence component u measured in the direction X, and it is formally defined as

$$L_u^X(Z) = \int_0^\infty \rho_u\big(Z, r_X\big)\,\mathrm{d}r_X, \tag{2.8}$$

where

$$\rho_u\big(Z, r_X\big) = \frac{1}{\sigma_u^2}\lim_{T\to\infty}\frac{1}{T}\int_0^T u(X,Y,Z,t)\cdot u\big(X + r_X, Y, Z, t\big) \tag{2.9}$$

is the cross-correlation function between the turbulence component u in two points separated by a distance r_X in the X-direction. In the same way, a total of 9 length scales are defined, namely

$$\begin{array}{lll} L_u^X & L_u^Y & L_u^Z \quad \text{for the longitudinal component,} \\ L_v^X & L_v^Y & L_v^Z \quad \text{for the lateral component,} \\ L_w^X & L_w^Y & L_w^Z \quad \text{for the vertical component,} \end{array} \tag{2.10}$$

which are generally modelled by using purely empirical expressions.

The frequency distribution of the turbulent velocity component is described by *power spectral density functions*. Many empirical expressions are available[1]. Two classical expressions for the along wind turbulence spectrum deserve a mention: the one proposed by von Kármán, 1948,

[1] Theoretical indications are only available in the *inertial subrange*, i.e. the range of frequencies where the motion can be considered as independent of the viscosity. The energy in the flow is transferred from larger eddies to smaller ones through an inertial mechanism (Kolmogorov's chain). Dissipation of energy occurs in smaller eddies where the shear deformations (and therefore the viscous stresses) are larger. According to Kolmogorov's hypotheses the motion of smaller eddies is determined only by the rate of energy transferred from larger eddies (which is equal to energy dissipated, in the hypothesis of stationarity); moreover, it is assumed that the energy is dissipated only by the very smallest eddies, in such a way as the motion of larger ones is independent of the viscosity. This defines the inertial subrange. There, by means of dimensional analysis, it is possible to obtain a theoretical expression for the power spectral density of the turbulence.

$$S_u = \frac{\sigma_u^2}{f} \frac{4f_L}{\left(1+70.8f_L^2\right)^{5/6}}, \tag{2.11}$$

in which $f_L = fL_u^X/U$; and the one proposed by Davenport, 1967,

$$S_u = \frac{\sigma_u^2}{f} \frac{2f_{\bar{L}}^2}{3\left(1+f_{\bar{L}}^2\right)^{4/3}}, \tag{2.12}$$

in which $f_{\bar{L}} = f\bar{L}/U$ with $\bar{L} = 1200\text{m}$.

More modern expressions of the spectra of the three turbulence components are

$$S_u = \frac{u_*^2}{f} \frac{200f_*}{\left(1+50f_*\right)^{5/3}}, \tag{2.13}$$

$$S_v = \frac{u_*^2}{f} \frac{15f_*}{\left(1+9.5f_*\right)^{5/3}}, \tag{2.14}$$

$$S_w = \frac{u_*^2}{f} \frac{3.36f_*}{1+10f_*^{5/3}}, \tag{2.15}$$

where $f_* = fZ/U$ is a non-dimensional frequency, also known as Monin coordinate. Eqs (2.13) and (2.14) are proposed by Kaimal, 1972, and Eq (2.15) by Lumley and Panofsky, 1964 (see also Simiu and Scanlan, 1996).

Alternative expressions are proposed in codes and standards; for instance the Italian CNR Guidelines (Istruzioni CNR, 2006) suggest

$$S_u = \frac{\sigma_u^2}{f} \frac{6.868f_u}{\left(1+10.302f_u\right)^{5/3}}, \tag{2.16}$$

$$S_v = \frac{\sigma_v^2}{f} \frac{9.434f_v}{\left(1+14.151f_v\right)^{5/3}}, \tag{2.17}$$

$$S_w = \frac{\sigma_w^2}{f} \frac{6.103f_w}{1+63.181f_w^{5/3}}, \tag{2.18}$$

where the standard deviations of the turbulence components are assumed as in Eq (2.5), the non-dimensional frequencies are defined as $f_u = fL_u/U$, $f_v = fL_v/U$, and $f_w = fL_w/U$, and the integral length scales of turbulence are assumed as

$$L_u = \bar{L}\left(Z/\bar{Z}\right)^{\nu}, \qquad L_v = 0.25L_u, \qquad L_w = 0.10L_u, \tag{2.19}$$

with $\overline{L} = 300\text{m}$, $\overline{Z} = 200\text{m}$, and $\nu = 0.67 + 0.05\ln(Z_0)$ with Z_0 in meters. Eurocode 1, 1997, only provides an expression for the along wind turbulence spectrum, identical to Eq (2.16). For further experimental spectra see e.g. Jain et al., 1996a; Jain et al., 1996b; Katsuchi et al., 1999.

The nondimensional form of the longitudinal turbulence spectra in Eqs (2.11), (2.12), (2.13), and (2.16) are compared in Figure 2.5; lateral turbulence spectra in Eqs (2.14) and (2.17) are compared in Figure 2.6; and vertical turbulence spectra in Eqs (2.15) and (2.18), in Figure 2.7. In all cases $Z_0 = 0.0035\,\text{m}$, $Z = 60\,\text{m}$, and $U(Z) = 30\,\text{m/s}$ have been considered. It is observed that the longitudinal turbulence spectra that have been considered are quite similar, except for Davenport's whose energy content is shifted at higher frequencies with respect to the other spectra.

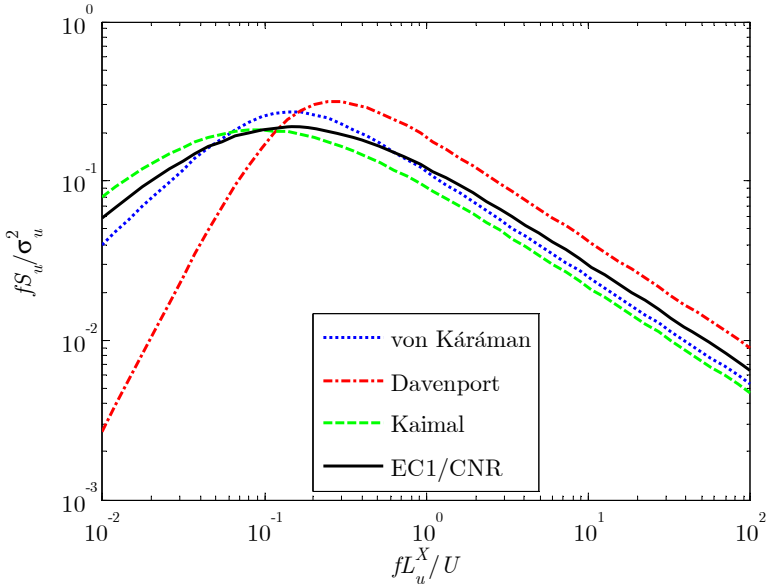

Figure 2.5 Spectra of the longitudinal component of turbulence

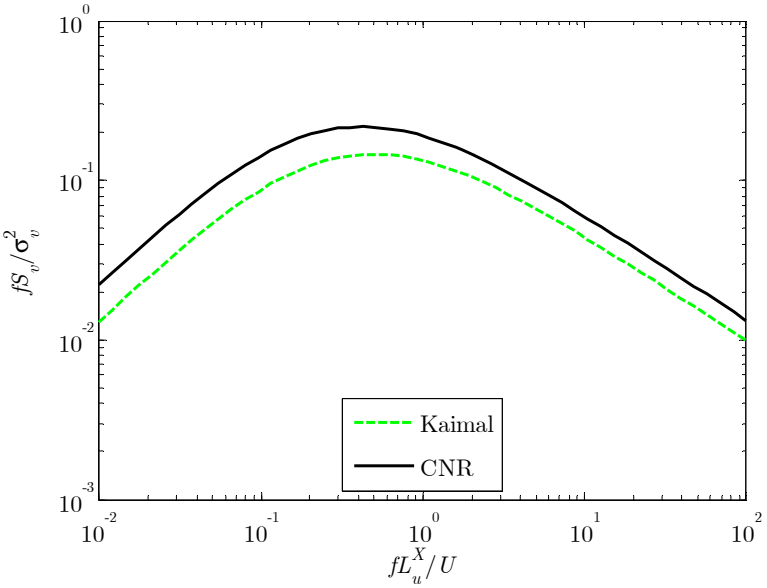

Figure 2.6 Spectra of the lateral component of turbulence

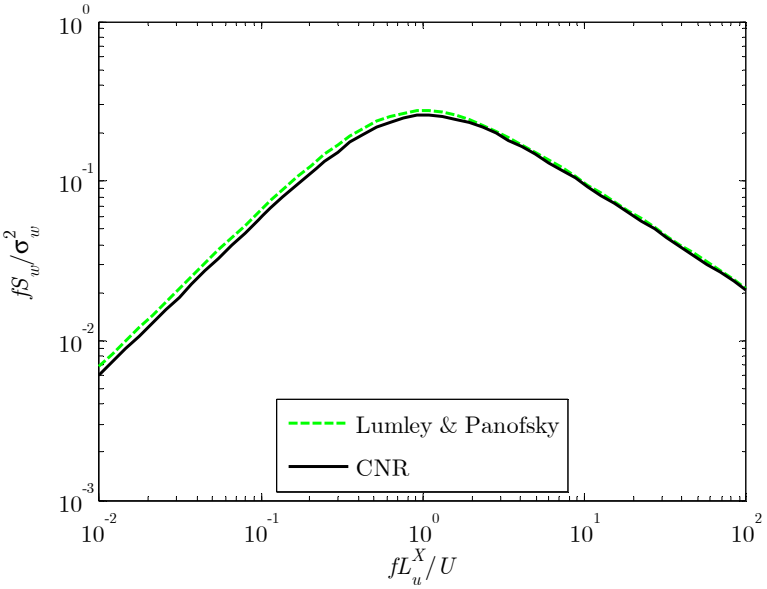

Figure 2.7 Spectra of the vertical component of turbulence

The longitudinal and the vertical components of turbulence have a negative cross-correlation. In fact the mean velocity increases with the height; therefore, a positive vertical gust transports an air particle in a position with an increased average longitudinal velocity; this results in a

negative longitudinal velocity fluctuation. In Minh et al., 2000 a possible co-spectrum of vertical and longitudinal turbulence is proposed:

$$S_{uw} = -\frac{u_*^2}{f}\frac{1.5 f_*}{\left(1+2.94 f_*\right)^{2.4}}. \tag{2.20}$$

The lateral component of turbulence can be considered as uncorrelated with the longitudinal and vertical ones (Solari and Piccardo, 2001).

Let us now consider the turbulence in two spatial points $M_i = \{X_i, Y_i, Z_i\}$ and $M_j = \{X_j, Y_j, Z_j\}$ (Figure 2.8). The cross-spectra of the components of the velocity fluctuations (e.g. Vickery, 1970) are given by

$$\begin{aligned} S_{u_i u_j} &= \mathrm{Coh}_u \sqrt{S_{u_i} S_{u_j}}, \\ S_{v_i v_j} &= \mathrm{Coh}_v \sqrt{S_{v_i} S_{v_j}}, \\ S_{w_i w_j} &= \mathrm{Coh}_w \sqrt{S_{w_i} S_{w_j}}, \end{aligned} \tag{2.21}$$

where the coherence functions (e.g. Panofsky and Singer, 1965) are

$$\begin{aligned} \mathrm{Coh}_{u_i u_j} &= \exp\left(-\frac{f}{U_{ij}}\sqrt{\left(C_{uX}\left|X_i - X_j\right|\right)^2 + \left(C_{uY}\left|Y_i - Y_j\right|\right)^2 + \left(C_{uZ}\left|Z_i - Z_j\right|\right)^2}\right), \\ \mathrm{Coh}_{v_i v_j} &= \exp\left(-\frac{f}{U_{ij}}\sqrt{\left(C_{vX}\left|X_i - X_j\right|\right)^2 + \left(C_{vY}\left|Y_i - Y_j\right|\right)^2 + \left(C_{vZ}\left|Z_i - Z_j\right|\right)^2}\right), \\ \mathrm{Coh}_{w_i w_j} &= \exp\left(-\frac{f}{U_{ij}}\sqrt{\left(C_{wX}\left|X_i - X_j\right|\right)^2 + \left(C_{wY}\left|Y_i - Y_j\right|\right)^2 + \left(C_{wZ}\left|Z_i - Z_j\right|\right)^2}\right). \end{aligned} \tag{2.22}$$

In Eqs (2.22) $U_{ij} = \left(U_i + U_j\right)/2$ is the average mean wind velocity of the two points, and C_{rR} ($r = u, v, w$; $R = X, Y, Z$) are coefficients determined experimentally and controlling the decay of the correlation of the turbulence components with the distance between the two points. Possible values of the coherence decay coefficients are collected below from various references in Simiu and Scanlan, 1996. According to Vickery, 1970, one can assume $C_{uZ} = 10$ and $C_{uY} = 10$. The coefficient C_{uX} has been found to depend on the terrain, $C_{uX} = 3$ can be assumed over sea and $C_{uX} = 6$, over land (Panofsky and al., 1974). In Kristensen and Jensen, 1979, $C_{wY} = 8$, $C_{vY} = 0.66 C_{uY}$, and $C_{vZ} = 0.66 C_{uZ}$ are suggested. It can be further assumed that also the coefficient for along-wind decay of the lateral turbulence coherence is in the ratio 0.66 with the relevant one for the

longitudinal turbulence, i.e. $C_{vX} = 0.66C_{uX}$. Also, $C_{wX} = C_{uX}\,C_{wY}/C_{uY}$ and $C_{wZ} = C_{uZ}\,C_{wY}/C_{uY}$ can be assumed. In CNR Guidelines (Istruzioni CNR, 2006), values for the coherence decay coefficients are provided. They are reported in Table 2.1, where they are compared to those in the references in Simiu and Scanlan, 1996.

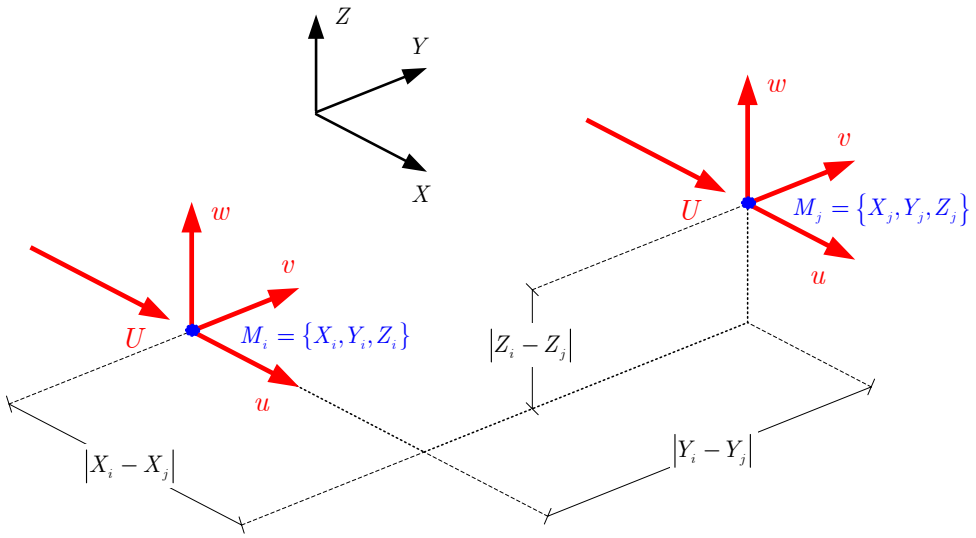

Figure 2.8 Wind velocity in two points

The cross-spectrum of the longitudinal component u in the point M_i and the vertical component w in the point M_j can be expressed as

$$S_{u_i w_j} = S_{uw}\sqrt{\frac{\mathrm{Coh}_u^2 + \mathrm{Coh}_w^2}{2}}, \tag{2.23}$$

where the co-spectrum S_{uw} and the coherence functions Coh_u and Coh_w are evaluated by considering the average velocity U_{ij} and the average height of M_i and M_j.

Table 2.1 Coefficients of exponential decay of turbulence coherence according to Italian CNR Guidelines and various references in Simiu and Scanlan, 1996

	C_{uX}	C_{uY}	C_{uZ}	C_{vX}	C_{vY}	C_{vZ}	C_{wX}	C_{wY}	C_{wZ}
CNR Guidelines	3	10	10	3	6.5	6.5	0.5	6.5	3
Various Refs(*)	3	16	10	(2)	10.66	6.66	(1.5)	8	(5)

(*) values in parentheses are further assumptions

2.1.3 Numerical generation of multi-correlated random processes

Here, some methods for the generation of a discrete set of multi-correlated random processes (e.g. Borri, 1988; Borri and Pastò, 2006; Facchini, 1996; Iannuzzi and Spinelli, 1986) are described in brief.

The *Weighted Amplitude Wave Superposition (WAWS) method* (Shinozuka and Jan, 1972) is probably the simplest method for the generation of multi-correlated processes. It consists in subdividing the frequency domain into M intervals, centred at the frequency f_h and with amplitude Δf_h ($h = 1,\ldots,M$). The time histories of the processes are obtained as a superposition of harmonics:

$$\mathbf{x}(t) = \sum_{h=1}^{M} \mathbf{H}_{(h)} \cos\left(2\pi \tilde{\mathbf{f}}_{(h)} t + \phi_{(h)}\right), \tag{2.24}$$

in which $\mathbf{x} = \left[x_1,\ldots,x_N\right]^T$ is a vector collecting the N processes (the components x_i are the turbulence components u, v or w in distinct spatial points), $\tilde{\mathbf{f}}_{(h)} = \left[f_h + \delta f_h^1,\ldots,f_h + \delta f_h^N\right]^T$ is a set of N frequencies obtained by the perturbation of f_h through random shifts $\delta f_h^n \ll \Delta f_h/2$, $\phi_{(h)}$ is a set of N random phases uniformly distributed from 0 to 2π, and $\mathbf{H}_{(h)}$ are lower triangular $N \times N$ matrixes. It can be demonstrated that $\mathbf{H}_{(h)}$ is proportional to the Cholesky factor of the power spectral density matrix evaluated at the frequency f_h; more precisely one has that

$$\mathbf{H}_{(h)}\mathbf{H}_{(h)}^T = 2\Delta f_h \mathbf{S}_{\mathbf{x}}\left(f_h\right). \tag{2.25}$$

WAWS method is simple to implement but it requires a very fine discretization of the frequencies in order to accurately match the target spectra.

The *common spectrum method* (e.g. Borri and Marradi, 1986) is based on the superposition of a signal generated for a spectrum that is common to all processes which include cross-correlations and of uncorrelated processes whose spectra are the differences between the common spectrum and the spectra of the target processes:

$$\mathbf{x}(t) = \mathbf{C}\boldsymbol{\xi}(t) + \mathbf{y}(t) \tag{2.26}$$

where $\boldsymbol{\xi}$ is a vector collecting independent random processes with a common spectrum S_{comm}, $\mathbf{C}$ is a matrix that is obtained from the equation $\mathbf{R}_{\mathbf{y}}(0) = \sigma_{\text{comm}}^2 \mathbf{C}\mathbf{C}^T$, and $\mathbf{y}$ is a vector collecting independent processes whose spectra are the differences between the target auto-spectra and the common spectrum $S_{y_i}(f) = S_{x_i}(f) - S_{\text{comm}}(f)$, $i = 1,\ldots,N$. Of course a method for the generation of the single process is required (e.g. WAWS

method). The method is numerically very efficient but approximated since the target correlation is obtained only at zero time lag.

Auto-regressive filters (e.g. Saul et al., 1976) can be used for generating discrete time histories of the turbulent velocity field too. In this case the processes are generated as

$$\mathbf{x}(t) = \sum_{h=1}^{P} \mathbf{\Psi}_{(h)} \mathbf{x}\left(t - h\Delta t\right) + \mathbf{n}(t), \tag{2.27}$$

where P is the order of the filter, $\mathbf{\Psi}^{(h)}$ are the matrixes of the coefficients of the filter, and $\mathbf{n}$ is a vector of noise. The coefficients can be determined from the matrix of the correlation functions of the process $\mathbf{R}_{\mathbf{x}}$, by solving the linear system

$$\mathbf{R}_{\mathbf{x}}\left(k\Delta t\right) = \frac{1}{T}\sum_{h=1}^{P} \mathbf{\Psi}^{(h)} \mathbf{R}_{\mathbf{x}}\left(\left(h-k\right)\Delta t\right), \quad k = 1,\ldots,P; \tag{2.28}$$

where T is the duration of the sample. After evaluating matrixes of the filter coefficients, the correlation function of the noise can be obtained from the relation

$$\mathbf{R}_{\mathbf{x}}(0) = \frac{1}{T}\sum_{h=1}^{P} \mathbf{\Psi}^{(h)} \mathbf{R}_{\mathbf{x}}\left(h\Delta t\right) + \mathbf{R}_{\mathbf{n}}(0). \tag{2.29}$$

Then, the vector of the noises is obtained as

$$\mathbf{n}(t) = \mathbf{L}\boldsymbol{\epsilon}(t) \tag{2.30}$$

where $\boldsymbol{\epsilon}$ is a vector of uncorrelated white noises with zero mean and unit variance, and $\mathbf{L}$ is the Cholesky factor of $\mathbf{R}_{\mathbf{n}}(0)$.

2.2 Wind loading and fluid-structure interaction

A body immersed in a flow is subjected to surface pressures induced by that flow. These pressures are, in general, time-dependent since they are affected by the fluctuations of the fluid velocity due to both the turbulence in the incident flow and the one initiated by the body itself.

If the body deforms or moves significantly under the fluid pressures, the changes of configuration of the body will affect the flow by modifying its boundary conditions. This will influence the aerodynamic loads which in turn will affect the deformations. In these cases where aerodynamic forces and structural motion interact, one speaks of *aeroelastic phenomena.*

These phenomena have been thoroughly studied in the aeronautic field since the beginning of the XX century. In civil engineering, although wind action was recognized as the cause of some collapses and severe damaging of bridges already in the XIX century, aeroelastic effects have been brought to designers' attention only after the collapse of the original Tacoma Narrows Bridge in 1940. Nowadays, aeroelastic effects are more and more a concern for designers of bridges due to the increasing flexibility of these structures.

Let us first analyze the non aeroelastic loading mechanisms, i.e. those affecting a non-deformable, fixed structure. It is classical to identify a *steady* or *mean load*[2], which is the time-average of the fluid pressures. The time-dependent load due to the oncoming turbulence, is classically referred to as *buffeting load*, whereas the time-dependent load due to the turbulence initiated by the body – even in case of laminar incident flow – is referred to as *vortex-shedding load.*

If the body is left free to deform or move, it starts interacting with the flow and aeroelastic effects may occur. The possible situations are extremely various and complicated. Here, however, the analysis is restricted to those phenomena that may affect suspended-span bridges or parts of them (cables, towers, etc.). These aeroelastic phenomena may be categorized as:

- Synchronization mechanisms of the vortex shedding with the structural vibrations (lock-in);
- Static instabilities (torsional divergence, lateral-buckling);
- Dynamic instabilities (galloping, torsional flutter, coupled flutter, along-wind instability near critical Reynolds number);
- Modal coupling affecting buffeting response (coupled buffeting);
- Multi-meteorological effects (rain-wind interaction on cables).

Below, some of these aeroelastic phenomena will be briefly presented, according to a consolidated classification (e.g. Simiu and Scanlan, 1996).

In Chapter 3 and Chapter 4, load models and a computational framework for aerodynamic and aeroelastic bridge analysis will be presented. Only the wind effects on the bridge deck will be considered. The model covers the effects of the mean actions, static and dynamic stability analysis, and coupled buffeting response prediction.

[2] Actually, a steady state for the fluid-structure system is only possible if (i) the incident flow is laminar, (ii) the body is rigid and fixed, and (iii) the Reynolds numbers are very small. In case of civil structures the hypothesis (i) and (iii) are never satisfied; therefore, it is more appropriate to speak of mean loading, i.e. the time-average of the wind pressure on the body surface.

2.2.1 Vortex shedding and lock-in

Experimental observations show that, within a certain range of Reynolds numbers, a fixed line-like structure sheds alternating vortices whose principal frequency f_S satisfies the relation

$$\frac{f_S D}{U} = St, \tag{2.31}$$

in which D is the across-wind dimension of the body, and St, is the *Strouhal number*, a nondimensional coefficient which depends on the geometry of the body and on Reynolds number. The relevant surface pressures result in along- and across-flow forces whose principal harmonics have a frequency $2f_S$ and f_S respectively; and, in general, in a pitching moment with main frequency f_S.

Let us recall the definition of the Reynolds number Re representing the ratio between inertial and viscous forces,

$$Re = \frac{\rho U D}{\mu}, \tag{2.32}$$

where μ is the dynamic viscosity of the fluid ($\mu = 1.78 \times 10^{-5}$ kg m^{-1}s^{-1} for air at 15°C).

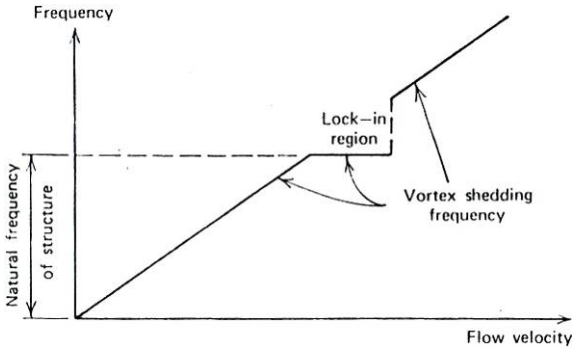

Figure 2.9 Schematic representation of lock-in phenomenon Simiu and Scanlan, 1996

Now, let us consider the body as elastically supported. The response is usually small, unless the Strouhal frequency approaches the natural frequency of the structure f_0; in this case the oscillation amplitude starts increasing and the structure motion strongly interacts with the flow, so that the phenomenon becomes aeroelastic. It is experimental evidence that at this point, the structural frequency controls the vortex shedding frequency even if the flow velocity, and consequently the nominal Strouhal frequency,

is varied within a certain range (Figure 2.9). This effect is known as *lock-in* or *synchronization*.

It has also been observed that during synchronization the across-wind force increases with oscillation amplitude until a limit cycle is reached. Moreover, the along-structure correlation of the force increases with oscillation amplitude too.

The most successful semi-qualitative models for the mathematical modelling of the lock-in response are based on coupled oscillators representing the structure and its wake (e.g. Diana et al., 2006). In practice, however, single-degree-of-freedom models are usually considered for the structural analyses; a classical one is proposed in Simiu and Scanlan, 1996, where the across-wind force is expressed as

$$L_S = q\left[C_{LS}(K)\sin(\omega t+\phi)+Y_1(K)\left(1-\varepsilon(K)\frac{y^2}{D^2}\right)\frac{\dot{y}}{U}+Y_2(K)\frac{y}{D}\right], \tag{2.33}$$

where C_{LS}, Y_1, Y_2, and ε are experimental parameters, functions of the Strouhal reduced frequency $K_S = f_S D/U$. In Eq (2.33), three terms are distinguished: (i) a harmonic forcing term, (ii) a non-linear aerodynamic damping term, and (iii) an aerodynamic stiffness term. The harmonic term models the alternating lift due to vortex-shedding in the velocity ranges where lock-in does not occur. Close to lock-in, the forcing term becomes negligible ($C_{LS} \simeq 0$) and the synchronized oscillations are controlled by the other terms. The idea is to use a Van der Pol oscillator, where the nonlinear damping term models the self-limiting oscillations and the stiffness term keeps the frequencies synchronized in the lock-in region. An extensive, interesting discussion on load models for vortex-shedding and lock-in is available in Pastò, 2005, which is also a valuable source for further references.

A fundamental parameter for the design is the amplitude of limit cycle oscillations. This is usually expressed as a function of the *Scruton number* Sc, a nondimensional parameter defined as

$$Sc = \frac{\xi m}{\rho D^2}, \tag{2.34}$$

where ξ is the damping ratio to critical of the structural mode considered, and m its mass.

Actually, it has been experimentally observed (e.g. Pastò, 2005) that the resonant response is significantly different, in the case that the lock-in region is reached by increasing or decreasing the mean wind velocities (Figure 2.10).

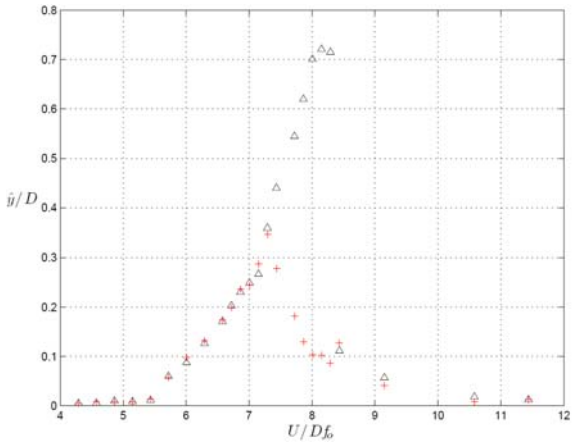

Figure 2.10 Across-wind oscillation amplitude of a circular cylinder for increasing (black triangles) and decreasing (red crosses) mean wind velocity (Pastò, 2005)

Vortex induced vibrations can be a risk source for suspended-span bridges due to the flexibility of these structures and the presence of line-like elements that are likely to shed organized vortices; in particular the bridge deck, the towers, and the cables may exhibit vulnerability to vortex induced vibrations, which may produce fatigue or serviceability issues. Moreover, the vortex induced vibrations may produce the initial disturbance that triggers self-excited instability phenomena such as flutter, as it was probably the case of the failure of Tacoma Narrows Bridge in 1940 (Billah and Scanlan, 1991).

Closed box girders are particularly vulnerable since they are able to shed large vortices. For typical structures, synchronization phenomena may occur at relatively low mean wind velocity (Ricciardelli et al., 2002), so that they may affect the bridge serviceability. A paradigmatic example is provided by the Storebælt Bridge in Denmark, where guide vanes (Figure 1.5) had to be added to the deck in order to mitigate the oscillations (Figure 1.4). On the other hand, latticed girders 'shred' the oncoming flow to such an extent that large, synchronized vortices, capable of exciting the bridge, are not likely to be shed.

The introduction of fairings or other aerodynamic appendages may be in fact effective for mitigating the vortex induced vibrations in deck girders. On the other hand, the presence of guardrail and barriers must be considered already in the design and in the wind tunnel tests, since these non-structural details may have a strong influence on the vortex shedding phenomenon.

Further useful countermeasures are the increase of structural damping, and the introduction of devices that break the along-structure coherence of the detached vortexes. Note that the turbulence in the oncoming flow is sometimes sufficient to break this coherence.

Vortex shedding is often a concern for bridge towers too. A possible solution is to increase tower stiffness in such a way as to increase the critical velocity for synchronization $U_{cr}^{S} = f_0 D / St$, where f_0 is the main frequency of the tower. A second strategy consists in providing devices (e.g. spoilers, helical strakes) that spoil the coherence of the shred vortices. Furthermore, it is possible to install damping devices (e.g. tuned mass control systems shaped as vertical pendulums weighted at the lower end).

Fatigue risk is a main concern for cables. In order to reduce vortex-induced oscillations of stays or hangers, cable-to-cable ties reducing the free-vibration length are often installed. Friction or hydraulic dampers, and tuned mass control systems are also frequently adopted solutions (e.g. Modi et al., 1995).

2.2.2 Torsional divergence

Torsional divergence is an instability phenomenon produced by the loss of torsional stiffness due to the increase of the mean aerodynamic moment. The phenomenon is typical of aircraft wings and is not usually a main concern for suspended-span bridges, unless the bridge deck is torsionally weak.

Since the phenomenon has a static nature (from the structural point of view), it can be approached by using the steady load model. A simplified analytical description can be obtained by considering only the torsional degree of freedom of the bridge deck and by linearizing the static equilibrium equation under steady aerodynamic forces. The critical condition is obtained when the total (structural and aerodynamic) stiffness of the system vanishes, i.e. for

$$U_{cr}^{divergence} = \sqrt{\frac{2\overline{k}_{\theta_y}}{\rho B^2 \overline{C}'_M}} \tag{2.35}$$

where $\overline{k}_{\theta_y}$ is the torsional stiffness of the bridge deck per unit length evaluated for the mean steady rotation $\overline{\theta}_y$, and $\overline{C}'_M$ is the derivative of the moment aerodynamic coefficient evaluated at $\overline{\theta}_y$.

In principle, static instabilities may occur also for the vertical and lateral displacement of the bridge (vertical and lateral buckling). Although they never realize for actual structures, they may be approached in the same way torsional divergence is.

Eq (2.35), where $\overline{\theta}_y = 0$ is often assumed, can be used to obtain a first estimate of the critical velocity for torsional divergence, which suggests whether the risk for this instability can be excluded without further analyses.

The stability analysis procedure proposed in Chapter 4 provides a more sophisticated tool which cover static and dynamic instabilities. In particular, the along-span variation of the angle of attack due to the steady loading and the correct changes in the geometrical stiffness of the structure are accounted for. Moreover, lateral and vertical buckling and further possible static instabilities can also be detected.

2.2.3 Galloping

Slender structures with special cross-section shapes may exhibit large oscillations in the across-wind direction. This phenomenon is called *galloping* and it is typical of rectangular or D-shaped cross-sections or the effective sections of power line cables that received an ice coat under freezing rain conditions.

Analytically, this aeroelastic phenomenon represents a single-degree-of-freedom dynamic instability (Hopf bifurcation), in which a negative aerodynamic damping cancels the structural damping. Experience has shown that the quasi-steady approach (see Chapter 3) is sufficient for describing the phenomenon.

A first estimate of the critical wind velocity for galloping instability can be obtained by considering the across-wind degree of freedom of the structure and a linearized quasi-steady loading (den Hartog, 1932; Glauert, 1919). The equation of motion reads:

$$m_z\left(\ddot{z}+2\xi_z\omega_z\dot{z}+\omega_z^2 z\right)=-\frac{1}{2}\rho U^2 B\left(\overline{C}_L'+\overline{C}_D\right)\frac{\dot{z}}{U}, \tag{2.36}$$

where m_z is the mass per unit length, ω_z is the circular frequency of the across-wind structural mode, ξ_z the relevant damping ratio, $\overline{C}_L'$ and $\overline{C}_D$ are the derivative of the lift aerodynamic coefficient and the drag coefficient evaluated at the mean configuration. The instability is reached when the total damping of the system (including structural and aerodynamic damping) $c_{tot}=2\xi\omega+1/2\,\rho U\left(C_L'+C_D\right)$ becomes negative. Since the structural damping is positive, galloping instability may occur only if $C_L'<-C_D$ (Glauert–Den-Hartog criterion). Since drag coefficient is positive[3], the lift coefficient must have a strong negative slope for the galloping instability can occur. Also note that symmetric cross-sections have $\overline{C}_L'=0$; therefore, galloping only occur in non-symmetric sections.

The critical condition for galloping is reached for a mean wind velocity

[3] A negative drag coefficient would allow a paradoxal average motion in opposite direction with respect to the mean flow one.

$$U_{cr}^{galloping} = -\frac{4m_z\xi_z\omega_z}{\rho B\left(\overline{C}_L' + \overline{C}_D\right)}. \tag{2.37}$$

From Eq (2.37), it is clear that a possible strategy for mitigating galloping risk is to increase the structural damping, since the critical velocity is proportional to it.

A more accurate prediction of galloping critical velocity can be obtained by using unsteady coefficients (see Chapter 3), of which the term $\left(\overline{C}_L' + \overline{C}_D\right)$ represent the asymptotic value for oscillation frequency that goes to zero (quasi-steady limit).

The stability analysis procedure presented in Chapter 4 is able to capture galloping instability as well as torsional flutter and coupled flutter, which are further possible dynamic instability phenomena which, contrary to galloping, can only be studied by including unsteadiness in the load models.

Nonlinear quasi-steady load models are available for the description of post-critical galloping conditions, in which limit cycle oscillations appear (Dyrbye and Hansen, 1996; Simiu and Scanlan, 1996). Alternatively, time-domain simulations using the quasi-steady load model are able to model the phenomenon (Salvatori and Spinelli, 2006b).

Take notice that single-degree-of-freedom dynamic instabilities may occur also for torsion or along-wind bending.

Torsional dynamic instability may occur in some bridge sections and is usually referred to as torsional flutter. As a quasi-steady treatment is not possible for the torsional degree of freedom (see discussion in Section 3.2.4), unsteady coefficients must be measured for studying the phenomenon.

A possible along wind dynamic instability could be modelled through the quasi-steady approach, as the quasi-steady aerodynamic damping is well defined and is equal to $2\overline{C}_D$. Since its value is always positive, it may seem that single-degree-of-freedom instability cannot occur. Nevertheless along-wind instabilities have been hypothesized (Macdonald, 2002) – but not observed – in the vicinity of drag crisis Schewe, 1983. In this case the dependence of drag coefficient on Reynolds number (evaluated considering the flow velocity relative to the body) must be included in an analytical model.

It is just worth to mention that the name 'galloping' is also used to indicate a different aeroelastic phenomenon that is also characterized by large oscillations and that also typically occurs in power line cables. In this case two (or more) cylinders are considered, one of which is located upstream of the other(s). Typical examples are power line cables grouped in bundles or group of chimneys. Under certain conditions the downstream cylinder may exhibit large oscillations induced by the wake generated by the upstream cylinder; hence, this phenomenon is named *wake galloping*. It is characterized by large oscillations that reach a limit cycle and describe an

elliptical orbit with the longer ellipse axis in the along-wind direction. The phenomenon can be modelled by considering a two-degree-of-freedom system and adopting a quasi-steady approach. The lift and drag coefficients must be experimentally determined as a function of the relative position of the two cylinders (Simpson, 1971). Post-critical limit-cycle oscillation can also be described by using a quasi-steady nonlinear model (e.g. Kern and Matiz, 1998).

2.2.4 Flutter

The theory of flutter was originally applied to airfoils but after the collapse of Tacoma Narrows Bridge in 1940, flutter has become a main concern also in the design of flexible bridges. In some special cases, besides the deck, further bridge elements may need to be checked for flutter stability; an example are the slender, 340-m-high piers of the Millau Viaduct in France that have also been verified against this instability phenomenon.

Coupled flutter (or *binary flutter*, or *classical flutter*) is a two-degree-of-freedom instability phenomenon in which the vertical and the torsional degrees of freedom of a structure couple together in diverging oscillations driven by the flow. Typical cross-sections prone to this instability are those of airfoils and streamlined bridge decks.

The coupled flutter mechanism is mainly driven by the phase shift between the vertical and the torsional oscillations (e.g. Bisplinghoff et al., 1955; Fung, 1968; Scanlan and Sabzevari, 1969) that, at a critical mean wind velocity, occur with the same frequency (critical frequency), coupled together into a zero-damping mode. At super-critical velocities, the total damping of the system becomes negative and diverging oscillations are initiated (e.g. Righi, 2003). These are eventually limited by structural (e.g. Salvatori and Spinelli, 2006b) or aerodynamic (e.g. Chen and Kareem, 2001) nonlinearities.

The critical velocity for flutter instability is a crucial design parameter for bridges and depends on the cross-section shape of the deck (more precisely on the unsteady aeroelastic characteristics, see below), and on the dynamic properties of the structure; in particular, on the masses and damping of the vertical and torsional modes, and, prominently, on their frequency ratio.

Torsional flutter is a single-degree-of-freedom instability, which typically occurs in relatively bluff cross-sections undergoing strongly separated flow. In these cases, the diverging torsional oscillations are driven by the relevant aerodynamic damping (e.g. Matsumoto et al., 1997).

Nakamura (Nakamura, 1978; Nakamura, 1996) observed that, between the coupled and the torsional flutter, intermediate excitation mechanism are also possible.

More in general, more than two modes can participate to the flutter mechanism of a true bridge (see Chapter 4).

Matsumoto and co-workers (e.g. Matsumoto, 2005; Matsumoto et al., 1993; Matsumoto et al., 1999) extensively studied the mechanism of flutter, either mono-, bi-, or multi-modal, and highlighted 'flutter branches', i.e. the structural modes, modified by aeroelastic effects, that eventually reach negative damping and initiate the instability.

In any case, the study of flutter requires an unsteady approach, since the so-called *fluid memory*, i.e. the unsteady structure of the wake, plays a crucial role in this phenomenon.

The unsteady load models for self-excited forces that are used for predicting flutter instability are discussed and further developed in Chapter 3, whereas a numerical procedure for the aeroelastic stability analysis of a true bridge is developed in Chapter 4.

It is just worth to point out that the term 'flutter' is used also to indicate further aeroelastic phenomena studied in the aeronautic and aerospace field. For example, *stall flutter* is a single-degree-of-freedom torsional oscillation of airfoils due to nonlinear characteristics of the aerodynamic forces in the vicinity of the stall, and *panel flutter* is the oscillation of panels in special condition of super-sonic flow.

2.2.5 Buffeting and coupled buffeting

Buffeting is the loading of a structure due to the turbulence in the oncoming flow. For most structures, buffeting does not need to be treated as an aeroelastic phenomenon since the effects of the wind gusts are prominent with respect to those of the structure motion.

However, flexible line-like elements as slender towers or the decks of suspended-span bridges, once excited by buffeting, undergo significant oscillations which interact with the flow and may appreciably affect the response (e.g. Chen et al., 2004). In these cases the modal coupling due to self-excited forces must be considered for an adequate evaluation of the phenomenon, which is then indicated as *coupled buffeting*.

Load models for bridge deck buffeting are described in Chapter 3. The simpler approach is based on the hypothesis of quasi-steadiness, i.e. it is assumed that the gusts are larger than the width of the bridge deck. The quasi-steady approach results in an overestimation of the contribution of the smaller gusts to the structural response. In order to account for unsteady effects, admittance functions are introduced in the load model. Aeroelastic effects are usually superposed to those of buffeting by simply adding buffeting and self-excited forces. The hypothesis of superposition of these effects is questionable but unavoidable for practical calculations. Nonlinear effects in buffeting may also be relevant (e.g. Peil and Behrens, 2007).

Frequency- and time-domain numerical procedures for the buffeting analysis of bridges are developed in Chapter 4.

Buffeting oscillations of the deck may affect the serviceability by preventing regular traffic on the bridge. Ultimate limit state can be reached too, by the exceedance of the maximum stresses in structural members or by producing fatigue issues.

Besides decks, further bridge elements such as towers (e.g. Ricciardelli, 1996) and cables (e.g. Peil et al., 1996) may undergo buffeting oscillations.

2.2.6 Rain-wind-cable interaction

Under the combined action of rain and wind, inclined cables and stays may exhibit large amplitude vibrations. The rain water flows along the cables by forming one or two rivulets, whose positions are determined by the action of gravity and wind. The presence of rivulets may strongly affect the pressure distribution around the circular surface of the cables, since the rivulets fix the separation points for the flow. The phenomenon is then characteristically aeroelastic, since the rivulets motion in turn is affect by both the flow and the cable motion.

Wind-rain interaction is a very complex phenomenon and, despites the numerous studies (e.g. Flamand, 1995; Hikami and Shiraishi, 1988; Matsumoto, Saitoh et al., 1995; Verwiebe and Ruscheweyh, 1998), it is not yet fully understood.

The most successful models consider a cable section with its across-wind (and sometimes also along-wind) motion and schematize each rivulet as a rigid body moving around the cable surface, so that the rivulet configuration is described by a single degree of freedom (e.g. Geurts et al., 1998; Wilde and Witkowski, 2003). Of course, special constitutive equations must be provided for describing the motion of the rivulet. In (Peil and Nahrath, 2003), four degrees of freedom are used, namely the along- and across-wind translations of the cable section and the positions of two rivulets around it; the same model has then been extended to the time-domain simulation of spatial cables (Peil and Dreyer, 2007).

Rain-wind vibrations may produce fatigue issues. The use of ribs, either parallel or helicoidal, in the outer surface of the stay prevents the rivulets from forming long, continuous lengths, and thus reduces the correlation of the wind-induced forces, suppressing the vibrations.

Chapter 3

Wind Load Models

In this Chapter steady, quasi-steady, and unsteady wind-load models for self-excited and buffeting forces are presented, both in the frequency and the time domain. All load models are placed in a common framework, where a specific notation is introduced which simplifies the understanding of some physical aspects and allows an easier mutual comparison of the models. Besides the critical review of literature models, a new formulation for self-excited loads in the time domain is proposed as a development of existing load models based on indicial functions. In particular, the extended model includes the consistency with the quasi-steady limit and corrects some aspects that used to lead to an inaccurate identification of the indicial functions. A specific numerical procedure for the identification of indicial functions from measured aeroelastic derivatives is developed, in such a way that the reliability of the experimental data is taken into account. Some examples of identification are provided and discussed.

3.1 Semi-empirical cross-sectional load models

Due to the complexity of the wind-structure interaction, the problem of the aeroelastic and aerodynamic response of bluff bodies is practically approached by adopting semi-empirical load models based on experimental coefficients obtained in the wind tunnel.

For line-like structures like bridge decks, the semi-empirical models are based on assumptions guided by the theoretical solution for the thin airfoil and on experimental evidences obtained from wind tunnel tests on scaled down cross-sectional models.

Three basic kinds of experiments are performed: (i) static[1] tests in laminar oncoming flow to obtain aerodynamic coefficients and Strouhal

[1] The term static is often used, in the literature as well in the practice, to refer to the cases where the structure is fixed and the flow reaches a steady state (or average considerations are possible). The term, acceptable from the structural point of view, is indeed inappropriate if the fluid-structure system is considered.

numbers, (ii) dynamic tests in laminar oncoming flow to obtain unsteady information such as the aeroelastic derivatives, and (iii) tests in turbulent oncoming flow to estimate aerodynamic admittances.

In this Chapter the attention focuses on the decks of suspended span bridges (cable stayed and suspension bridges, e.g. Ryall et al., 2000). However, cross-sectional load models are used for many line-like structures such as slender piers (e.g. Milleau Viaduct, France Figure 3.1a), or light cable roofs (e.g. Figure 3.1b).

(a) (b)

Figure 3.1 Millau Viaduct, France (a); design for a new tollgate of A1 motorway at Reggio Emilia, tested in the CRIACIV wind tunnel in Prato (b)

A bridge with straight span subjected to a wind flow, the mean velocity of which is horizontal and orthogonal to the bridge span is considered.

Let us introduce a right-handed reference frame $\{X,Y,Z\}$ (X along-wind, Y along-span, Z upwards). The bridge deck cross-section, lying in the $\{X,Z\}$ plane, is treated as a rigid body. Hence, the motion of the cross-section is described by three degrees of freedom, namely the horizontal displacement x (positive along-wind), the vertical displacement z (positive upwards), and the rotation θ_y (positive nose-up), see Figure 3.2. Translations are referred to an arbitrary point of the cross-section; here the centre of mass is used and it is assumed as coincident with the shear centre.

The wind velocity field is assumed as stationary with the mean component U in the X direction. In general, also zero-mean fluctuating components u (X direction) and w (Z direction) are present and they are responsible for the buffeting excitation. The lateral wind velocity fluctuations of component v (Y direction) are not considered because they have no influence on the cross-sectional behaviour.

The pressure field around the cross-section (e.g. Ricciardelli, 2003) results in a horizontal force F_x, a vertical force F_z, and a pitching moment M_y, power-conjugated with the rates of x, z, and θ_y, respectively. Take note that all the expressions of the forces given in this Chapter refer to a unit span length.

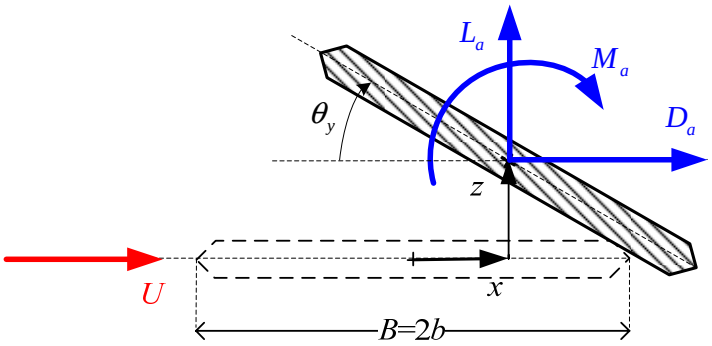

Figure 3.2 Adopted convention for cross-sectional displacements and wind forces

Wind actions on each elementary strip of bridge deck are considered as functions of the motion of its cross-section and of the local wind velocity.

The three-dimensional behaviour of the whole bridge will then be taken into account by means of spatial correlation functions of the wind field and by connecting neighbouring cross-sections with structural (finite) elements (see Chapter 4).

From the linearization of the quasi-steady load model, three independent load contributions are highlighted: a constant steady contribution, a buffeting contribution depending only on the oncoming wind velocity fluctuations, and a self-excited contribution depending on the cross-sectional motion. In order to account for unsteadiness, the buffeting contribution may be corrected by means of admittance functions, whereas the self-excited forces can be modelled by means of aeroelastic derivatives. Admittance functions and aeroelastic derivatives, as parts of linearized models, are measured considering a single mean angle of attack (usually zero). Only recently aeroelastic derivatives at different angles of attack have been measured, but only a few values of the angle have been considered in experiments. Frequency dependent load models can be extended to the time domain through the approach based on indicial functions (e.g. Scanlan et al., 1974) in order to consider structural nonlinearities (e.g. Salvatori and Spinelli, 2006b) but cannot account for load nonlinearities, as a linearized theory is assumed already for the experimental measurements. Nonlinear extension of unsteady models are possible by using hybrid approaches, for instance through the subdivision of the response into frequency bands, where high frequencies are treated with unsteady linear models considering instantaneous angles provided by the low frequency quasi-steady response). An interesting proposal of nonlinear unsteady model is given by Chen and Kareem, 2001.

A more thorough discussion is developed in Salvatori, 2007, where the notation and the framework adopted here are extended and presented in detail.

3.2 Load models based on steady aerodynamic coefficients

In the next Sections the load models based on steady aerodynamic coefficients are presented. The steady coefficients are obtained in the wind tunnel through experimental tests in which the average forces on the bridge deck are measured under the conditions of laminar oncoming flow and fixed cross-section. The steady load model is therefore appropriate for describing steady-state problems, i.e. for obtaining static forces on the bridge deck. The quasi-steady load model is a tentative extension of the steady approach to turbulent flow and bridge dynamics (e.g. Stoyanoff, 2001).

3.2.1 Steady load model

A rigidly supported cross-section under constant wind is subjected to a mean surface pressure that results in an along-wind drag force D_s, an across-wind (upward) lift force L_s, and a pitching moment M_s (Figure 3.3). They are expressed per unit span-length as

$$\begin{aligned} F_x^{\mathrm{s}} &= D_s = q_0 B C_D(\alpha), \\ F_z^{\mathrm{s}} &= L_s = q_0 B C_L(\alpha), \\ M_y^{\mathrm{s}} &= M_s = q_0 B^2 C_M(\alpha), \end{aligned} \tag{3.1}$$

where $q_0 = \rho U^2/2$ is the mean kinetic pressure, ρ the air density, U the mean wind velocity, $B = 2b$ the bridge deck width, and C_R ($R = D, L, M$) the drag, lift and moment aerodynamic coefficients respectively. These coefficients depend on the geometrical shape of the cross-section and are obtained experimentally from standard wind tunnel tests as a function of the angle α between the cross-section chord and the mean flow direction (angle of attack). In Eq (3.1), F_x, F_z, and M_y are the components of the action with respect to the reference frame $\{X, Y, Z\}$, whereas the notation 's' reminds that we are considering a steady-load regime.

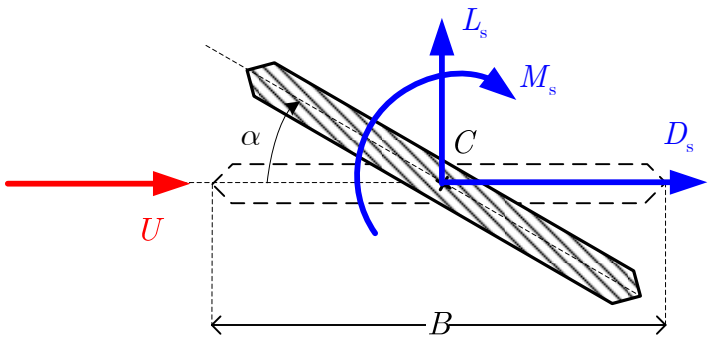

Figure 3.3 Steady load model

3.2.2 Quasi-steady load model

If the motion of the cross-section is allowed and the fluctuations of wind velocity are included, it is possible to extend the steady load model to the dynamics by imagining that at each instant the wind action can be modelled by using the steady state expressions holding for the configuration of the cross-section at that instant. This hypothesis is of course acceptable only in the case in which motion of the cross-section is 'slow enough' with respect to the flow; in this case, the fluid can reach a steady state as the cross-section undergoes only 'small' displacements.

Let us consider the point P of the cross-section chord at distance βB (positive in the flow direction) from C (Figure 3.4). At a given time instant, the relative velocity components of the undisturbed flow in P would be

$$U_x^{\mathrm{rel}} = U + u - \dot{x} + \beta B \dot{\theta}_y \sin\theta_y, \quad U_z^{\mathrm{rel}} = w - \dot{z} + \beta B \dot{\theta}_y \cos\theta_y, \tag{3.2}$$

where the dot is used to denote the derivative with respect to time t, as usual. The meaning and role of the dimensionless parameter β will be discussed in Section 3.2.3.

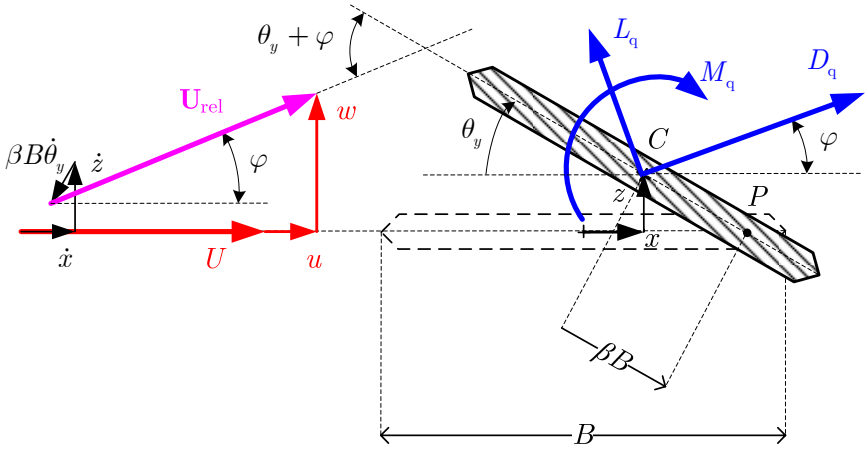

Figure 3.4 Quasi-steady load model

Wind actions are then evaluated through the steady model, taking into account the instantaneous kinetic pressure

$$q = \frac{1}{2}\rho\left(U_x^2 + U_z^2\right) \tag{3.3}$$

and the instantaneous angle of attack that, in turn, is given by the sum of θ_y and the angle

$$\varphi = \arctan\frac{U_z}{U_x} \tag{3.4}$$

between the X axis and the relative wind velocity direction. The aerodynamic forces are then

$$\begin{aligned} D_{\text{qs}} &= qBC_D\left(\theta_y + \varphi\right), \\ L_{\text{qs}} &= qBC_L\left(\theta_y + \varphi\right), \\ M_{\text{qs}} &= qB^2C_M\left(\theta_y + \varphi\right), \end{aligned} \tag{3.5}$$

with drag force parallel to the relative wind velocity and lift force orthogonal to it. In the $\{X, Y, Z\}$ reference system one obtains

$$\begin{aligned} F_x^{\text{qs,nl}} &= D_{\text{qs}}\cos\varphi - L_{\text{qs}}\sin\varphi, \\ F_z^{\text{qs,nl}} &= D_{\text{qs}}\sin\varphi + L_{\text{qs}}\cos\varphi, \\ M_y^{\text{qs,nl}} &= M_{\text{qs}}, \end{aligned} \tag{3.6}$$

in which the notations 'qs' and 'nl' underline the quasi-steady nature of the forces and their nonlinear dependence on the motion and on the oncoming turbulence.

3.2.3 Linearization of quasi-steady load model

In order to allow standard frequency domain analyses, the quasi-steady load model is often linearized. It is assumed that the fluctuations of the wind turbulence and the speed of the cross-section motion are 'much smaller' than the mean wind and that the motion develops with small oscillations around the mean angle corresponding to the steady configuration $\overline{\theta}_y$; that is

$$\left|u/U\right|, \left|w/U\right|, \left|\dot{x}/U\right|, \left|\dot{z}/U\right|, \left|B\dot{\theta}_y/U\right|, \left|\theta_y - \overline{\theta}_y\right| \ll 1. \tag{3.7}$$

Eqs (3.6) are then approximated to the first order as

$$\begin{aligned} F_x^{\mathrm{qs,nl}} &\simeq \overline{F}_x^{\mathrm{qs,l}} = \overline{F}_x^{\mathrm{s}} + \overline{F}_x^{\mathrm{qs,b}} + \overline{F}_x^{\mathrm{qs,a}}, \\ F_z^{\mathrm{qs,nl}} &\simeq \overline{F}_z^{\mathrm{qs,l}} = \overline{F}_z^{\mathrm{s}} + \overline{F}_z^{\mathrm{qs,b}} + F_z^{\mathrm{qs,a}}, \\ M_y^{\mathrm{qs,nl}} &\simeq \overline{M}_y^{\mathrm{qs,l}} = \overline{M}_y^{\mathrm{s}} + \overline{M}_y^{\mathrm{qs,b}} + \overline{M}_y^{\mathrm{qs,a}}, \end{aligned} \tag{3.8}$$

where one can recognize the following three contributions:

1) A constant term, equal to the *steady* mean load:

$$\begin{aligned} \overline{F}_x^s &= F_x^s\left(\overline{\theta}_y\right), \\ \overline{F}_z^s &= F_z^s\left(\overline{\theta}_y\right), \\ \overline{M}_y^s &= M_y^s\left(\overline{\theta}_y\right); \end{aligned} \tag{3.9}$$

2) A term depending on wind velocity fluctuations, which is referred to as *buffeting* contribution, and denoted by 'b':

$$\begin{aligned} \overline{F}_x^{\mathrm{qs,b}} &= q_0 B\left[2\overline{C}_D\,\frac{u}{U} + \left(\overline{C}'_D - \overline{C}_L\right)\frac{w}{U}\right], \\ \overline{F}_z^{\mathrm{qs,b}} &= q_0 B\left[2\overline{C}_L\,\frac{u}{U} + \left(\overline{C}'_L + \overline{C}_D\right)\frac{w}{U}\right], \\ \overline{M}_y^{\mathrm{qs,b}} &= q_0 B^2\left[2\overline{C}_M\,\frac{u}{U} + \overline{C}'_M\,\frac{w}{U}\right]; \end{aligned} \tag{3.10}$$

3) A term depending on the motion of the cross-section, which is referred to as self-excited or *aeroelastic* contribution, and denoted by 'a':

$$\begin{aligned}
\overline{F}_x^{\mathrm{qs,a}} &= q_0 B\left[-2\overline{C}_D\,\frac{\dot{x}}{U}-\left(\overline{C}'_D-\overline{C}_L\right)\frac{\dot{z}}{U}+\overline{C}'_D\alpha_y+\left(2\overline{C}_D\overline{s}+\left(\overline{C}'_D-\overline{C}_L\right)\overline{c}\right)\beta\,\frac{B\dot{\alpha}_y}{U}\right],\\
\overline{F}_z^{\mathrm{qs,a}} &= q_0 B\left[-2\overline{C}_L\,\frac{\dot{x}}{U}-\left(\overline{C}'_L+\overline{C}_D\right)\frac{\dot{z}}{U}+\overline{C}'_L\alpha_y+\left(2\overline{C}_L\overline{s}+\left(\overline{C}'_L+\overline{C}_D\right)\overline{c}\right)\beta\,\frac{B\dot{\alpha}_y}{U}\right],\\
\overline{M}_y^{\mathrm{qs,a}} &= q_0 B^2\left[-2\overline{C}_M\,\frac{\dot{x}}{U}-\overline{C}'_M\,\frac{\dot{z}}{U}+\overline{C}'_M\alpha_y+\left(2\overline{C}_M\overline{s}+\overline{C}'_M\overline{c}\right)\beta\,\frac{B\dot{\alpha}_y}{U}\right],
\end{aligned} \tag{3.11}$$

where $\alpha_y=\theta_y-\overline{\theta}_y$, $\overline{c}=\cos\overline{\theta}_y$, $\overline{s}=\sin\overline{\theta}_y$, $\overline{C}_R=C_R\left(\overline{\theta}_y\right)$, $\overline{C}'_R=\left[\partial C_R/\partial\alpha\right]_{\alpha=\overline{\theta}_y}$, $R=D,L,M$. From now on, the overdash denotes that a quantity is evaluated at the mean steady configuration.

Linearized load models are usually considered for practical calculations, because they allow the introduction of frequency-dependent 'corrections' accounting for the unsteadiness of the fluid-structure interactions, i.e. the admittance functions for the buffeting actions (see Section 3.4.3) and the aeroelastic derivatives for the self-excited actions (see Section 3.4.1). The linearized quasi-steady model represents in fact the asymptotic aerodynamic behaviour for the non-dimensional frequency $K=B\omega/U$ (the so-called reduced frequency) that tends to zero, where ω is the circular frequency.

3.2.4 Further considerations on quasi-steady aeroelastic forces

The choice of the value of the dimensionless parameter β should follow from dynamic experimental tests. It is in general not correct to use the same value of the parameter β for all the components of the wind force. Instead, three different values of β, for the horizontal and the vertical force and for the moment, should be determined by considering the asymptotic behaviour for vanishing oscillation frequency of the aeroelastic derivatives P_2^*, H_2^*, and A_2^*, respectively (see Section 3.4). Eqs (3.11) become then

$$\begin{aligned}
\overline{F}_x^{aq} &= q_0 B\left[-2\overline{C}_D\frac{\dot{x}}{U}-\left(\overline{C}'_D-\overline{C}_L\right)\frac{\dot{z}}{U}+\overline{C}'_D\alpha_y+\left(\overline{C}'_D-\overline{C}_L\right)\overline{\beta}_{F_x}\frac{B\dot{\alpha}_y}{U}\right],\\
\overline{F}_z^{aq} &= q_0 B\left[-2\overline{C}_L\frac{\dot{x}}{U}-\left(\overline{C}'_L+\overline{C}_D\right)\frac{\dot{z}}{U}+\overline{C}'_L\alpha_y+\left(\overline{C}'_L+\overline{C}_D\right)\overline{\beta}_{F_z}\frac{B\dot{\alpha}_y}{U}\right],\\
\overline{M}_y^{aq} &= q_0 B^2\left[-2\overline{C}_M\frac{\dot{x}}{U}-\overline{C}'_M\frac{\dot{z}}{U}+\overline{C}'_M\alpha_y+\overline{C}'_M\overline{\beta}_{M_y}\frac{B\dot{\alpha}_y}{U}\right].
\end{aligned} \tag{3.12}$$

where also the dependence on the angle of attack has been included in the coefficients $\overline{\beta}_R$ ($R=F_x,F_z,M_y$).

Different authors report different interpretations for obtaining the coefficients $\overline{\beta}_R$. In Diana et al., 1993, where only two degrees of freedom are considered, the relative velocity for the quasi-steady approach is evaluated at two different points for lift and moment forces, and the parameters $\overline{\beta}_R$ are obtained from dynamic experimental tests. Another possibility is to consider the analogy with the theoretical solution for the thin airfoil and use $\overline{\beta}_{F_z}=1/2$ and $\overline{\beta}_{M_y}=0$ (the along wind component is identically zero for the thin airfoil; therefore, no analogy with this theory can be established). Other authors uses the same value of $\overline{\beta}_R$ for all three force components: Stoyanoff, 2001, evaluates the mean wind velocity with respect to the cross-section centroid, i.e. $\overline{\beta}_{F_x}=\overline{\beta}_{F_z}=\overline{\beta}_{M_y}=0$; Borri and Costa, 2004, consider the leading edge of the cross-section, i.e. $\overline{\beta}_{F_x}=\overline{\beta}_{F_z}=\overline{\beta}_{M_y}=-1/4$. Also, there are proposals for specific experimental procedure for determining $\overline{\beta}_R$ (e.g. Falco et al., 1978). As a matter of fact, a consistent extension to the dynamics of the steady model is simply not possible, and the model remains valid only as limit behaviour.

Let us now introduce a compact notation that will also be adopted for the load models presented in the following Sections. Eqs (3.11) are rewritten as

$$\boxed{\overline{R}^{aq}=q_0 B^{\gamma_R}\sum_{r=\dot{x}/U,\dot{z}/U,\alpha_y}\left(\overline{d}_{Rr}r+\overline{e}_{Rr}\frac{B}{U}\dot{r}\right);\qquad R=F_x,F_z,M_y;} \tag{3.13}$$

where the symbol

$$\boxed{\gamma_R=\begin{cases}1, & \text{if } R=F_x,F_z,\\ 2, & \text{if } R=M_y,\end{cases}} \tag{3.14}$$

is introduced. From Eq (3.13) on, the equations enclosed in boxes are those using the new compact notation or those for which some enhancement are made here.

This notation, by choosing $\dot{x}/U$, $\dot{z}/U$, and α_y as fundamental parameters r for describing the motion, underlines that a constant value of the angle of attack can only be produced by a constant translational velocity or by a constant rotation. In other words, if a constant value of $\dot{x}/U$, $\dot{z}/U$, or α_y is imposed, it is theoretically possible for the flow to reach a steady state with respect to the cross-section. Further advantages of this notation will be clarified in the following Sections.

Now, it is clear that the coefficients $\overline{d}_{Rr}$ can be univocally determined by using information obtained in steady experimental tests. By considering a steady state ($r = \text{const}$) and comparing Eqs (3.12) and (3.13), one obtains that

$$\boxed{\begin{array}{lll} \overline{d}_{F_x\dot{x}} = -2\overline{C}_D, & \overline{d}_{F_x\dot{z}} = -\left(\overline{C}'_D - \overline{C}_L\right), & \overline{d}_{F_x\alpha_y} = \overline{C}'_D, \\ \overline{d}_{F_z\dot{x}} = -2\overline{C}_L, & \overline{d}_{F_z\dot{z}} = -\left(\overline{C}'_L + \overline{C}_D\right), & \overline{d}_{F_z\alpha_y} = \overline{C}'_L, \\ \overline{d}_{M_y\dot{x}} = -2\overline{C}_M, & \overline{d}_{M_y\dot{z}} = -\overline{C}'_M, & \overline{d}_{M_y\alpha_y} = \overline{C}'_M. \end{array}} \tag{3.15}$$

On the other hand, the coefficients $\overline{e}_{Rr}$ cannot be directly obtained by steady experimental tests as no steady state can be reached if the angle of attack changes in time ($\dot{r} \neq 0$). The equivalences obtained by the comparison of Eqs (3.12) and (3.13)

$$\begin{array}{lll} \overline{e}_{F_x\dot{x}} = 0, & \overline{e}_{F_x\dot{z}} = 0, & \overline{e}_{F_x\alpha_y} = \left(\overline{C}'_D - \overline{C}_L\right)\overline{\beta}_{F_x}, \\ \overline{e}_{F_z\dot{x}} = 0, & \overline{e}_{F_z\dot{z}} = 0, & \overline{e}_{F_z\alpha_y} = \left(\overline{C}'_L + \overline{C}_D\right)\overline{\beta}_{F_z}, \\ \overline{e}_{M_y\dot{x}} = 0, & \overline{e}_{M_y\dot{z}} = 0, & \overline{e}_{M_y\alpha_y} = \overline{C}'_M\overline{\beta}_{M_y}, \end{array} \tag{3.16}$$

have no physical meaning. An estimate of $\overline{e}_{Rr}$ may be useful for performing simplified quasi-steady analyses. Reasonable values can be obtained by considering the asymptotic behaviour of the unsteady coefficients, as it will be described in Section 3.4.

3.3 Unsteady forces: Theoretical approach to thin airfoil

The theory of thin airfoil is briefly recalled below. This theoretical approach, although it is not a wholly appropriate for the detailed appreciation of unsteady forces in bluff cross-sections, has historically provided a guide to the study of the motional aerodynamics of bridge decks.

The airfoil is idealized as a flat plate with vanishing thickness-to-width ratio immersed into a two-dimensional flow. The motion in the along-wind direction is restrained, so that only two degrees of freedom are used, namely the heaving and the pitching motion. The flow is assumed as inviscid, and incompressible (Fung, 1968). The standard convention for cross-sectional degrees of freedom and aerodynamic forces in the theory of thin airfoil is depicted in Figure 3.5.

As to the steady behaviour, all the forces vanish at zero angle of attack, i.e. $C_D(0) = C_L(0) = C_M(0) = 0$. Moreover, theoretical calculations (e.g. Bisplinghoff et al., 1955) show that $C'_L(0) = 2\pi$ and $C'_M(0) = \pi/2$.

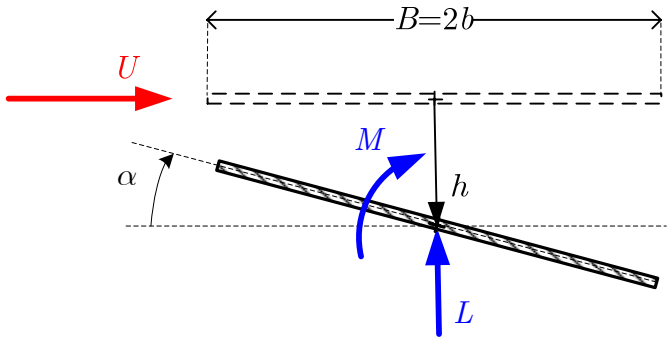

Figure 3.5 Thin airfoil convention

3.3.1 Self-excited forces in frequency domain

For a harmonic motion with circular frequency ω, lift force and pitching moment reads

$$\begin{aligned} L &= L_{NC} + L_{QS} + L_C, \\ M &= M_{NC} - L_{QS}\, b/2 + L_C\, b/2, \end{aligned} \tag{3.17}$$

in the special case in which the mid-chord coincides with the shear centre (for the general case see Bisplinghoff et al., 1955). In this formulation three contributions can be distinguished: (i) non-circulatory terms $L_{NC} = \pi\rho b^2 \ddot{h}$ and $M_{NC} = -\pi\rho\, b^4/8\, \ddot{\alpha}$ that can be interpreted as the inertial forces of a portion of air which moves with the cylinder[2] and can often be neglected; (ii) non-circulatory quasi-steady terms with resultant force $L_{QS} = \pi\rho b^2 U\dot{\alpha}$ that are independent of the frequency of oscillations; and (iii) circulatory terms with resultant

[2] Note that the signs of the inertial terms are correct; in fact, the lift force is directed in opposite direction with respect to the heaving degree of freedom etc.

$$L_C = 2\pi \frac{1}{2} \rho U^2 (2b) C(k) \left(\frac{\dot{h}}{U} + \alpha + \frac{b\dot{\alpha}}{2U} \right) = \bar{C}'_L q_0 B C(k) w_{(3/4)} \tag{3.18}$$

that represents the non-stationary effects due to the vortex sheets around the airfoil and in the wake. In Eq (3.18)

$$w_{(3/4)} = -\left(\dot{h} + U\alpha + b\dot{\alpha}/2 \right) \tag{3.19}$$

is the instantaneous vertical velocity of the air particle in contact with the tree-quarter chord point of the airfoil,

$$C(k) = F(k) + iG(k) = \frac{H_1^{(2)}(k)}{H_1^{(2)}(k) + iH_0^{(2)}(k)} \tag{3.20}$$

is Theodorsen's circulatory function (Theodorsen, 1935), see Figure 3.7, $H_\nu^{(2)}$ $(\nu = 0,1)$ are Bessel functions of third kind (Hankel functions), and $k = K/2$ is a different definition for the reduced frequency that is used in the aeronautic field. Also, the reduced velocity is defined as $U_* = U/(Bf)$.

3.3.2 Self-excited forces in time domain

The equivalent problem in time domain was solved by Wagner (Wagner, 1925):

$$L_C = -2\pi q B \int_{-\infty}^{s} \frac{1}{U} \phi(s-\sigma) w'_{(3/4)}(\sigma) \, d\sigma \,, \tag{3.21}$$

where ϕ is Wagner's function, and the prime denotes the derivative with respect to the non-dimensional time $s = tU/b$.

Garrick, 1938, pointed out that Wagner's and Theodorsen's functions are in a Fourier transform relationship,

$$\phi(s) = \frac{1}{2\pi} \int_{-\infty}^{\infty} \frac{C(k)}{ik} e^{iks} \mathrm{d}k \,, \tag{3.22}$$

and gave a rational approximation of Wagner's function as

$$\phi(s) \simeq \frac{2+s}{4+s} \,, \tag{3.23}$$

which is correct in its limits, since $\Phi(0) = \frac{1}{2}$ and $\lim_{s \to \infty} \Phi(s) = 1$, see Figure 3.6. Jones, 1945, proposed the approximation in the form

$$\phi(s) \simeq 1 - \sum_{n=1}^{N} a_n \exp(-b_n s) \tag{3.24}$$

with $N = 2$, $a_1 = 0.165$, $b_1 = 0.041$, $a_2 = 0.335$, $b_2 = 0.320$.

According to Jones' approximation the real and imaginary part of Theodorsen's function are given by

$$F(k) = 1 - k^2 \sum_{n=1}^{N} \frac{a_n}{b_n^2 + k^2}, \quad G(k) = -k \sum_{n=1}^{N} \frac{a_n b_n}{b_n^2 + k^2}. \tag{3.25}$$

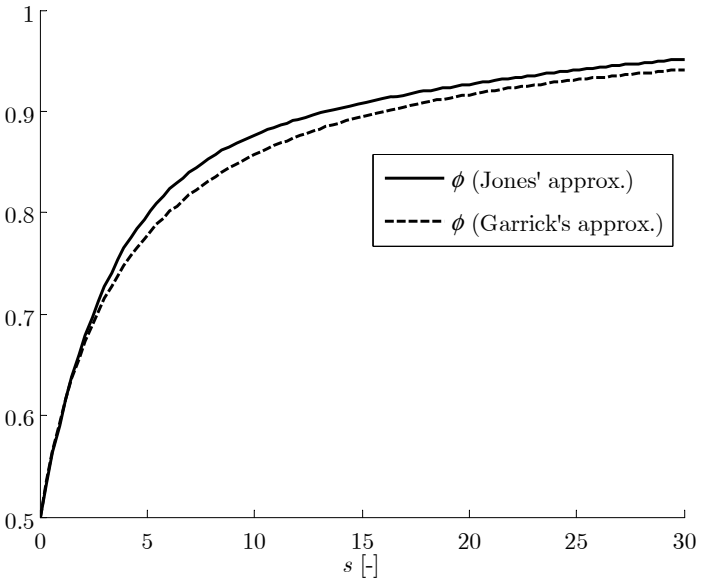

Figure 3.6 Wagner function after Jones' and Garrick's approximations

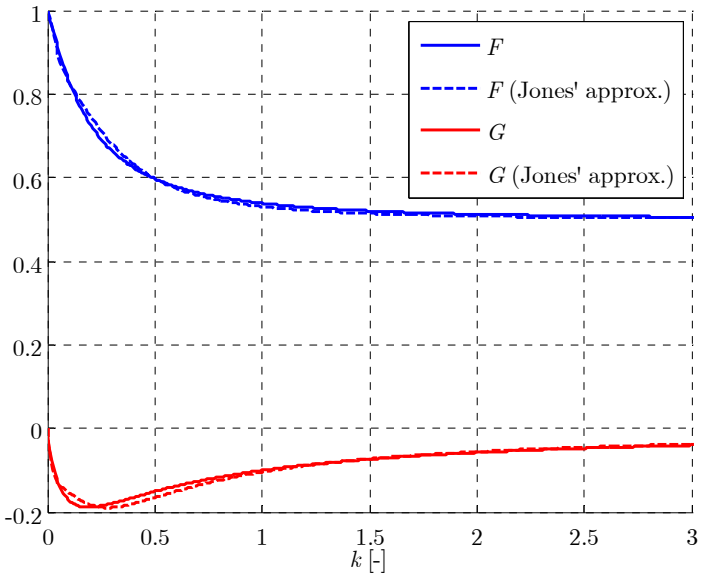

(a)

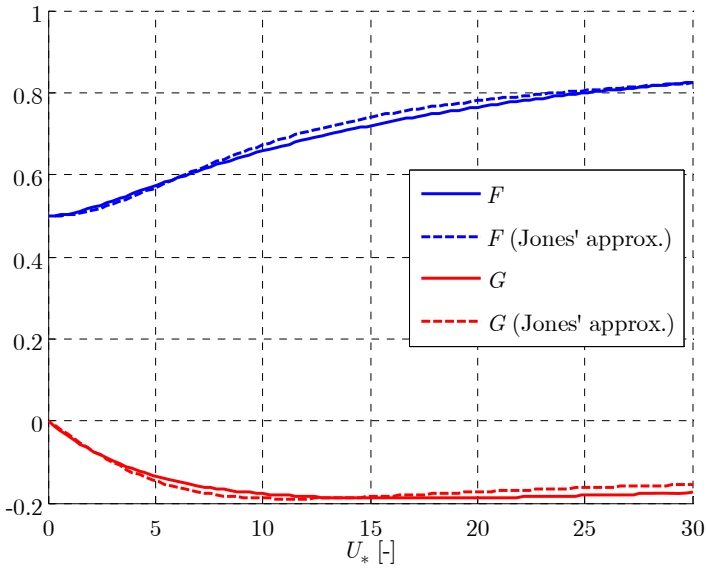

(b)

Figure 3.7 Real and imaginary parts of Theodorsen's circulatory function, plotted as a function of the reduced frequency (a) and of the reduced velocity (b)

3.3.3 Gust response in frequency domain

After Fung, 1968, we consider an airfoil flying at a uniform speed U that is invested by a vertical sinusoidal gust $w(x,t) = W \exp\left(i\omega\left(t - x/U\right)\right)$ of constant amplitude W. The lift force reads

$$L_W = \pi\rho c U W \exp(i\omega t)\,\phi(k)\,, \tag{3.26}$$

where

$$\chi(k) = \left(J_0(k) - iJ_1(k)\right)C(k) + iJ_1(k) = F_G(k) + iG_G(k) \tag{3.27}$$

is Sears' function (Sears, 1941) and $J_\nu(k)$ are Bessel function of the first kind, see Figure 3.9.

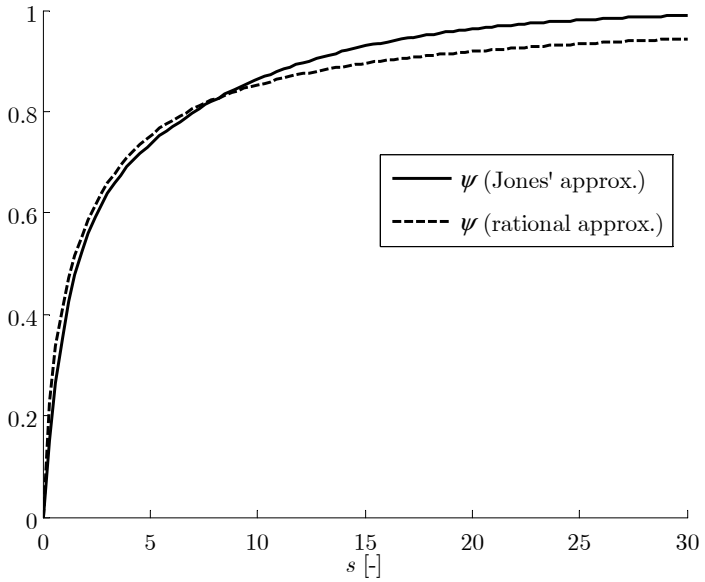

Figure 3.8 Küssner's function after Jones' and rational approximations

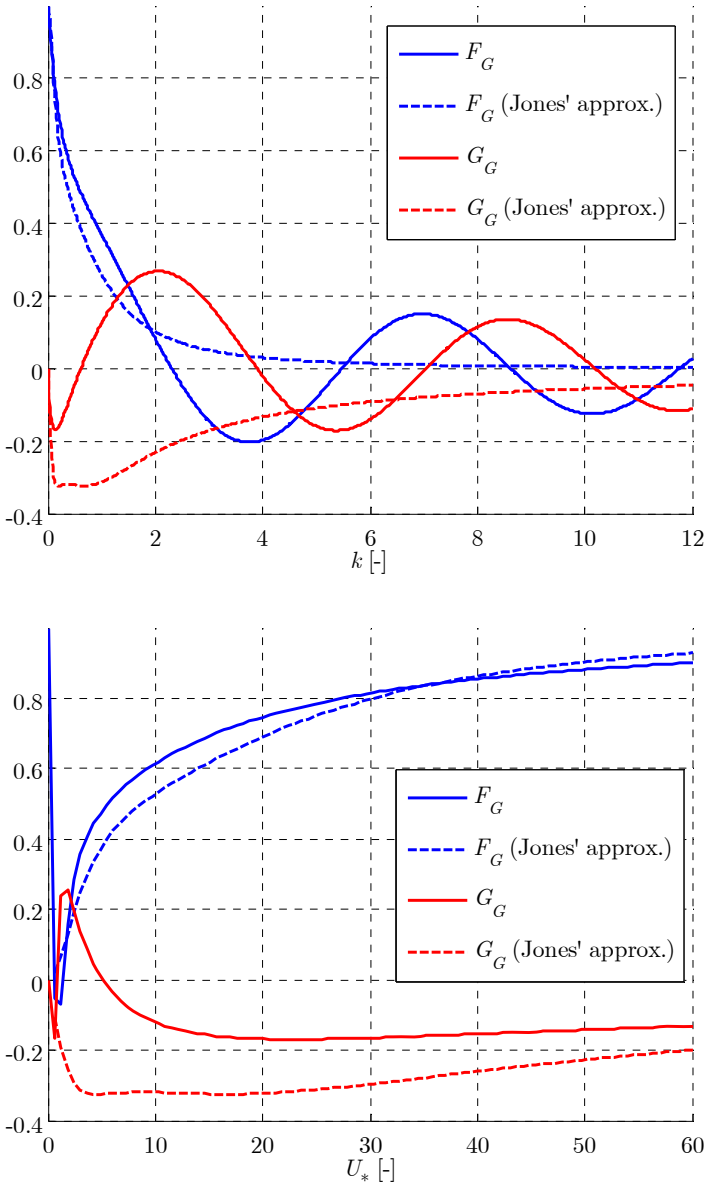

Figure 3.9 Sears function, plotted as a function of the reduced frequency (a) and of the reduced velocity (b)

3.3.4 Gust response in time domain

The gust loading problem can be treated also in the time domain. In this case a sharp-edged gust is considered:

$$w(x,t) = WH(t - x/U)\,, \tag{3.28}$$

where $H(.)$ is Heavyside's function. The resulting lift force is

$$L_W = 2\pi \frac{1}{2}\rho U^2 (2b)\frac{W}{U}\psi(s)\,, \tag{3.29}$$

where ψ is Küssner's function (Küssner, 1936).

A rational approximation of Küssner's function is available (Bisplinghoff et al., 1955)

$$\psi(s) \simeq \frac{s^2 + s}{s^2 + 2.82s + 0.80}\,, \tag{3.30}$$

see Figure 3.8. Alternatively, it is possible to use exponential filters as already made for Wagner's function:

$$\psi(s) \simeq 1 - \sum_{n=1}^{N} a_n \exp\left(-b_n s\right). \tag{3.31}$$

According to Jones, 1945, a suitable approximation is given by $N = 2$, $a_1 = 0.500$, $b_1 = 1.000$, $a_2 = 0.500$, $b_2 = 0.130$. Take notice that $\psi(0) = 0$ and $\lim_{s\to\infty} \psi(s) = 1$.

The transform between Sears' and Küssner's functions is analogous the one between Theodorsen's and Wagner's functions:

$$\psi(s) = \frac{1}{2\pi}\int_{-\infty}^{\infty} \frac{\chi(k)}{ik} e^{iks}\mathrm{d}k\,. \tag{3.32}$$

3.4 Unsteady forces: The case of bridge girders

Below, literature models for self-excited forces are reviewed, discussed and placed into the introduced common framework for wind load models.

3.4.1 Self-excited forces in frequency domain through aeroelastic derivatives

The most widely used unsteady load model for self-excited forces was introduced in Scanlan and Tomko, 1971, and further extended in order to

account also for along-wind displacements and force. The force components induced by a harmonic motion are

$$
\begin{aligned}
F_x^{AD} &= qB\left(KP_1^*\frac{\dot{x}}{U}+KP_2^*\frac{B\dot{\alpha}_y}{U}+K^2P_3^*\alpha_y+K^2P_4^*\frac{x}{B}-KP_5^*\frac{\dot{z}}{U}-K^2P_6^*\frac{z}{B}\right),\\
F_z^{AD} &= qB\left(KH_1^*\frac{\dot{z}}{U}-KH_2^*\frac{B\dot{\alpha}_y}{U}-K^2H_3^*\alpha_y+K^2H_4^*\frac{z}{B}-KH_5^*\frac{\dot{x}}{U}-K^2H_6^*\frac{x}{B}\right),\\
M_y^{AD} &= qB^2\left(-KA_1^*\frac{\dot{z}}{U}+KA_2^*\frac{B\dot{\alpha}_y}{U}+K^2A_3^*\alpha_y-K^2A_4^*\frac{z}{B}+KA_5^*\frac{\dot{x}}{U}+K^2A_6^*\frac{x}{B}\right),
\end{aligned}
\tag{3.33}
$$

where $\overline{P}_h$, $\overline{H}_h$, and $\overline{A}_h$ ($h=1,\ldots,6$) are non-dimensional coefficients ('aeroelastic derivatives[3]' or 'flutter[4] derivatives'), which depend on the reduced frequency and, in general, on the angle of attack (hence the overbar indicating that they are evaluated in the mean steady configuration). The superscript 'd', is for 'derivatives'. In the most common convention for aeroelastic derivatives, often referred to as Scanlan's convention, lift force and vertical displacement are assumed as positive downwards. Therefore the signs in Eq (3.33) have been adjusted accordingly in order to match the convention adopted here (Figure 3.2).

Aeroelastic derivatives are measured experimentally in the wind tunnel as functions of the reduced frequency and, in general, of the mean angle around which the load is linearized.

Here, unsteady forces are rewritten as

$$
\begin{aligned}
\overline{F}_x^{ad} &= q_0B\left[\overline{D}_{F_x\dot{x}}\frac{\dot{x}}{U}+\overline{E}_{F_x\dot{x}}\frac{B}{U}\frac{\ddot{x}}{U}+\overline{D}_{F_x\dot{z}}\frac{\dot{z}}{U}+\overline{E}_{F_x\dot{z}}\frac{B}{U}\frac{\ddot{z}}{U}+\overline{D}_{F_x\alpha_y}\alpha_y+\overline{E}_{F_x\alpha_y}\frac{B}{U}\dot{\alpha}_y\right],\\
\overline{F}_z^{ad} &= q_0B\left[\overline{D}_{F_z\dot{x}}\frac{\dot{x}}{U}+\overline{E}_{F_z\dot{x}}\frac{B}{U}\frac{\ddot{x}}{U}+\overline{D}_{F_z\dot{z}}\frac{\dot{z}}{U}+\overline{E}_{F_z\dot{z}}\frac{B}{U}\frac{\ddot{z}}{U}+\overline{D}_{F_z\alpha_y}\alpha_y+\overline{E}_{F_z\alpha_y}\frac{B}{U}\dot{\alpha}_y\right],\\
\overline{M}_y^{ad} &= q_0B^2\left[\overline{D}_{M_y\dot{x}}\frac{\dot{x}}{U}+\overline{E}_{M_y\dot{x}}\frac{B}{U}\frac{\ddot{x}}{U}+\overline{D}_{M_y\dot{z}}\frac{\dot{z}}{U}+\overline{E}_{M_y\dot{z}}\frac{B}{U}\frac{\ddot{z}}{U}+\overline{D}_{M_y\alpha_y}\alpha_y+\overline{E}_{M_y\alpha_y}\frac{B}{U}\dot{\alpha}_y\right],
\end{aligned}
\tag{3.34}
$$

[3] The term 'derivative' can be ascribed to the fact that, historically, unsteady coefficients substituted those of the linearized quasi-steady load model, which in turn are just the *derivatives* of the steady coefficients with respect to the angle of attack, at least in the case of thin airfoil where the drag force is zero.

[4] This name is due to the main historical use of the unsteady coefficients, i.e. the prediction of flutter threshold. Nevertheless, this seems now quite reductive. The importance of unsteady self-excited effects in the buffeting response is widely demonstrated; self-excited forces are responsible in fact for a coupling effect between structural modes, which is fundamental for the accurate prediction of the bridge response.

i.e., by using the compact notation introduced in Section 3.2.4, as

$$\boxed{\overline{R}^{ad} = q_0 B^{\gamma_R} \sum_{r=\dot{x}/U,\dot{z}/U,\alpha_y} \left(\overline{D}_{Rr} r + \overline{E}_{Rr} \frac{B}{U} \dot{r} \right); \qquad R = F_x, F_z, M_y}. \tag{3.35}$$

All the expressions can be written in a compact form. Translational and rotational degrees of freedom and the conjugated forces can be treated with a unique notation, avoiding developing separate calculations for each case, which results in annoying cumbersome expressions, which are quite common in the literature.

The equivalence between the two conventions is easily obtained by considering a harmonic motion and comparing Eqs (3.33) and (3.34):

$$\boxed{\begin{array}{ll}
\overline{D}_{F_x\dot{x}} = K\overline{P}_1^*, & \overline{E}_{F_x\dot{x}} = -\overline{P}_4^*, \\
\overline{D}_{F_x\dot{z}} = -K\overline{P}_5^*, & \overline{E}_{F_x\dot{z}} = \overline{P}_6^*, \\
\overline{D}_{F_x\alpha_y} = K^2\overline{P}_3^*, & \overline{E}_{F_x\alpha_y} = K\overline{P}_2^*, \\
\overline{D}_{F_z\dot{x}} = -K\overline{H}_5^*, & \overline{E}_{F_z\dot{x}} = \overline{H}_6^*, \\
\overline{D}_{F_z\dot{z}} = K\overline{H}_1^*, & \overline{E}_{F_z\dot{z}} = -\overline{H}_4^*, \\
\overline{D}_{F_z\alpha_y} = -K^2\overline{H}_3^*, & \overline{E}_{F_z\alpha_y} = -K\overline{H}_2^*, \\
\overline{D}_{M_y\dot{x}} = K\overline{A}_5^*, & \overline{E}_{M_y\dot{x}} = -\overline{A}_6^*, \\
\overline{D}_{M_y\dot{z}} = -K\overline{A}_1^*, & \overline{E}_{M_y\dot{z}} = \overline{A}_4^*, \\
\overline{D}_{M_y\alpha_y} = K^2\overline{A}_3^*, & \overline{E}_{M_y\alpha_y} = K\overline{A}_2^*.
\end{array}} \tag{3.36}$$

The choice of $\dot{x}/U$, $\dot{z}/U$, and α_y as significant degrees of freedom highlights the different role of displacements and rotation. A rotation produces changes of angle of attack in the same way as translational velocities do. When a harmonic motion is considered, the quadrature terms are those containing the angular velocity $\dot{\alpha}_y$ and translational accelerations $\ddot{x}/U$ and $\ddot{z}/U$.

Some advantages of this representation will be clarified here; further details are given in Salvatori and Borri, 2007, and Salvatori, 2007. Another representation, similar to some extent to the one introduced here, is discussed in Zasso, 1996.

We observe that Eqs (3.13) and (3.35) are formally identical. This simplifies the interpretation of the quasi-steady load model as the limit case of the unsteady load model at low reduced frequencies. In particular, we have that $d_{Rr} = \lim_{K\to 0} D_{Rr}$, which is commonly accepted and is demonstrated by experimental results (e.g. Chowdhury and Sarkar, 2004). Moreover, by

assuming $e_{Rr} = \lim_{K_\omega \to 0} E_{Rr}$, we define a possible criterion for estimating the quasi-steady coefficients e_{Rr} in a physically-consistent way.

The quadrature coefficients for the translational degrees of freedom $\overline{E}_{Rr}$ ($r = \dot{x}/U, \dot{z}/U$) multiply translational accelerations; therefore, they can be interpreted as an equivalent inertia that may represent the mass of the air moving together with the cross-section. On the contrary, in the classical notation of Eq (3.33), the coefficients multiplying translations and are seen as a kind of equivalent stiffness that does not any physical meaning.

The coefficients $\overline{D}_{Rr}$ and $\overline{E}_{Rr}$ do not depend on the normalization and allows a comparison of forces between different cross-sections. Contrary to the classical representation in terms of $\overline{P}_h$, $\overline{H}_h$, and $\overline{A}_h$ ($h = 1,\ldots,6$), a variation in a coefficients $\overline{D}_{Rr}$ or $\overline{E}_{Rr}$ is directly proportional to the variation of the relevant forces, independently of the reduced frequency. This fact will be advantageous while identifying indicial functions from measured aeroelastic derivatives (see Section 3.5.2).

For sake of the completeness, we also report two other common notations for aeroelastic self-excited forces. The signs are adjusted to match the convention on forces of Figure 3.3.

Küssner's convention, e.g. Virgoleux, 1992, is mainly used in France. Vertical force and moment read

$$\begin{aligned} F_z &= qB\left(-2\pi k_1^a \frac{z}{B} - 2\pi k_2^a \frac{\dot{z}}{\omega U} - \pi k_1^b \alpha_y - \pi k_2^b \frac{\dot{\alpha}_y}{\omega}\right), \\ M_y &= qB^2\left(-\pi m_1^a \frac{z}{B} - \pi m_2^a \frac{\dot{z}}{\omega U} - \frac{\pi}{2} m_1^b \alpha_y - \frac{\pi}{2} m_2^b \frac{\dot{\alpha}_y}{\omega}\right). \end{aligned} \tag{3.37}$$

The coefficients k_1^a, k_2^a, k_1^b, k_2^b, m_1^a, m_2^a, m_1^b, and m_2^b can be easily related to Scanlan's derivatives. This notation offers no specific advantages, and it is in fact often converted to Scanlan's one.

The *convention used at the Politecnico di Milano*, described in details in Zasso, 1996, expresses the forces as

$$\begin{aligned} F_z &= qB\left(-h_1^* \frac{\dot{z}}{U} + h_4^* \frac{\pi}{2U_\omega^{*2}} \frac{z}{B} - h_2^* \frac{B\dot{\alpha}_y}{U} + h_3^* \alpha_y\right), \\ M_y &= qB^2\left(-a_1^* \frac{\dot{z}}{U} + a_4^* \frac{\pi}{2U_\omega^{*2}} \frac{z}{B} - a_2^* \frac{B\dot{\alpha}_y}{U} + a_3^* \alpha_y\right). \end{aligned} \tag{3.38}$$

The main objective of this notation is to provide unsteady coefficients h_i^*, a_i^* ($i = 1,2,3,4$) converging to steady values, and to allow an easy graphical comparison between different cross-sections.

The self-excited load model via aeroelastic derivatives is well suited for frequency domain analyses but results quite unpractical for time-domain

simulations, since the aeroelastic derivatives depend on the frequency of the response. It is possible to use sophisticate frequency-domain analyses methods or, as an alternative, equivalent time-domain methods can be developed.

3.4.2 Self-excited forces in time domain through indicial functions

The classical unsteady load model for self excited forces in the time domain reads (Caracoglia and Jones, 2003c)

$$\begin{aligned}
\overline{F}_x^{ai} &= q_0 B \overline{C}'_D \left[\int_{-\infty}^{t} \overline{\Phi}_{F_x\dot{x}}(t-\tau) \frac{\ddot{x}(\tau)}{U} d\tau - \int_{-\infty}^{t} \overline{\Phi}_{F_x\dot{z}}(t-\tau) \frac{\ddot{z}(\tau)}{U} d\tau + \right. \\
&\qquad \left. + \int_{-\infty}^{t} \overline{\Phi}_{F_x\alpha}(t-\tau)\, \dot{\alpha}(\tau)\, d\tau \right], \\
\overline{F}_z^{ai} &= q_0 B \overline{C}'_L \left[-\int_{-\infty}^{t} \overline{\Phi}_{F_z\dot{x}}(t-\tau) \frac{\ddot{x}(\tau)}{U} d\tau + \int_{-\infty}^{t} \overline{\Phi}_{F_z\dot{z}}(t-\tau) \frac{\ddot{z}(\tau)}{U} d\tau + \right. \\
&\qquad \left. - L \int_{-\infty}^{t} \overline{\Phi}_{F_z\alpha}(t-\tau)\, \dot{\alpha}(\tau)\, d\tau \right], \qquad (3.39) \\
\overline{M}_y^{ai} &= q_0 B^2 \overline{C}'_M \left[\int_{-\infty}^{t} \overline{\Phi}_{M_y\dot{x}}(t-\tau) \frac{\ddot{x}(\tau)}{U} d\tau - \int_{-\infty}^{t} \overline{\Phi}_{M_y\dot{z}}(t-\tau) \frac{\ddot{z}(\tau)}{U} d\tau \right. \\
&\qquad \left. + \int_{-\infty}^{t} \overline{\Phi}_{M_y\alpha}(t-\tau)\, \dot{\alpha}(\tau)\, d\tau \right].
\end{aligned}$$

This model will be further discussed in Section 3.5.

3.4.3 Buffeting forces in frequency domain through admittance functions

The unsteadiness of the buffeting effects is usually accounted for by means of frequency-dependent transfer functions (aerodynamic admittances). The resulting buffeting forces are

$$\begin{aligned}
\overline{F}_x^{bq} &= q_0 B\left[2\overline{C}_D \overline{\chi}_{F_x u}\frac{u}{U} + \left(\overline{C}'_D - \overline{C}_L\right)\overline{\chi}_{F_x w}\frac{w}{U}\right],\\
\overline{F}_z^{bq} &= q_0 B\left[2\overline{C}_L \overline{\chi}_{F_z u}\frac{u}{U} + \left(\overline{C}'_L + \overline{C}_D\right)\overline{\chi}_{F_z w}\frac{w}{U}\right],\\
\overline{M}_y^{bq} &= q_0 B^2\left[2\overline{C}_M \overline{\chi}_{M_y u}\frac{u}{U} + \overline{C}'_M \overline{\chi}_{M_y w}\frac{w}{U}\right],
\end{aligned} \tag{3.40}$$

where χ_{Ru} and χ_{Rw} ($R = F_x, F_z, M_y$) are (frequency-dependent) admittance functions for the along-wind and vertical turbulence components respectively, and the overbar denotes that admittance functions are measured at the mean steady angle of attack. The resulting frequency-domain load model is intrinsically restricted to linear structures.

3.4.4 Buffeting forces in time domain

Admittance functions can be transformed into indicial functions by means of a procedure analogous to the one used to transform aeroelastic derivatives (Salvatori, 2007).

3.5 Development of an improved indicial function load model

In the following Section 3.5.1, the indicial function model for unsteady loading in the time domain is further developed so that some issues of literature models are solved and the convergence to the quasi-steady limit is ensured. Moreover, in Section 3.5.2, a procedure for the identification of the model coefficients is proposed and implemented, so that accuracy problem of previous procedures are overcome and the variance of experimental data is taken into account.

3.5.1 The load model

An alternative for self-excited loads in the pure time-domain is offered by the formulation via indicial functions, based on the extension to bluff cross-sections of the formulation theoretically developed for the airfoil. This technique has been introduced in wind engineering by Scanlan et al., 1974. A deep discussion is available in Scanlan, 1993. Its further extensions are described by Caracoglia and Jones, 2003c. The basic idea is to imagine the history of motion as a series of infinitesimal step-wise increments. Indicial functions describe the non-stationary evolution in time of loads due to translational velocities and rotations.

Let us consider the unsteady force $R = F_x, F_z, M_y$ at time t due to a unit step-wise change of $r = \dot{x}/U, \dot{z}/U, \alpha_y$ that occurs at time $\tau < t$. We write the step-change in terms of Heaviside function $H(.)$,

$$\tilde{r}(t) = H(t-\tau); \tag{3.41}$$

then we assume that the relevant unsteady force can be written as

$$\overline{R}_{\tilde{r}}^{ai}(t) = q_0 B^{\gamma_R} \overline{d}_{Rr} \overline{\Phi}_{Rr}(t-\tau), \tag{3.42}$$

where the indicial functions $\overline{\Phi}_{Rr}$ describe the evolution in time of the normalized unsteady force. The superscript 'i' is for 'indicial'. As highlighted by the overdash on the variables, indicial functions can be evaluated at different mean angles of attack and identified from the aeroelastic derivatives measured at the same angles. Because the step-change of $r = \dot{x}/U, \dot{z}/U, \alpha_y$ results in a constant change of angle of attack, after a transient stage due to the sudden change, the flow reaches a new steady state around the new position of the cross-section. Therefore the unsteady force must converge to the equivalent steady one in Eq (3.13). Formally we have that

$$\lim_{t\to\infty} \tilde{r}(t) = 1, \qquad \lim_{t\to\infty} \overline{R}_{\tilde{r}}^{ai}(t) = q_0 B^{\gamma_R} \overline{d}_{Rr}. \tag{3.43}$$

By comparing Eq (3.42) and (3.43), we have that the indicial functions converges to unit for time that goes to infinity,

$$\lim_{t\to+\infty} \overline{\Phi}_{Rr}(t) = 1. \tag{3.44}$$

We also observe that $\overline{\Phi}_{Rr}(t)$ is not properly defined for $t < 0$; we assume $\overline{\Phi}_{Rr}(t) = 0$.

Under the assumption of linearity, this model can be extended to any history of motion by considering the convolution of the indicial function with the motion itself,

$$\overline{R}_r^{ai}(t) = q_0 B^{\gamma_R} \overline{d}_{Rr} \int_{-\infty}^{r} \overline{\Phi}_{Rr}(t-\tau) dr(\tau) = q_0 B^{\gamma_R} \overline{d}_{Rr} \int_{-\infty}^{t} \overline{\Phi}_{Rr}(t-\tau) \dot{r}(\tau)\, d\tau. \tag{3.45}$$

It is more practical to consider a motion starting at time $t = 0$. Therefore, the lower integration limit is modified and an initial condition must be added[5]:

$$\overline{R}_r^{ai}(t) = q_0 B^{\gamma_R} \overline{d}_{Rr} \left[\overline{\Phi}_{Rr}(t)\, r(0) + \int_0^t \overline{\Phi}_{Rr}(t-\tau) \dot{r}(\tau)\, d\tau \right]. \tag{3.46}$$

The dependence on the initial condition of the motion can be removed by integrating by parts Eq (3.46),

$$\overline{R}_r^{ai}(t) = q_0 B^{\gamma_R} \overline{d}_{Rr} \left[\overline{\Phi}_{Rr}(0)\, r(t) + \int_0^t \dot{\overline{\Phi}}_{Rr}(t-\tau) r(\tau)\, d\tau \right]. \tag{3.47}$$

This expression has the further advantage of allowing the development of a simpler optimization in the computational implementation (see Section 3.6).

It is worth to notice that the right-hand expression in Eq (3.47) can be obtained directly by considering the convolution integral of the response function $I_{Rr}(t)$ to a unit impulse (Chen et al., 2000b; Fung, 1968),

$$\overline{I}_{Rr}(t) = B^{\gamma_R} \overline{d}_{Rr} \left[\delta(t)\, \overline{\Phi}_{Rr}(0) + \dot{\overline{\Phi}}_{Rr}(t) \right], \tag{3.48}$$

and by reminding that Dirac delta function $\delta(.)$ acts as the 'identity' with respect to convolution.

The final expression of self-excited forces accounting for all cross-sectional degrees of freedom reads

$$\boxed{\overline{R}^{ai}(t) = q_0 B^{\gamma_R} \sum_{r=\dot{x}/U, \dot{z}/U, \alpha_y} \overline{d}_{Rr} \int_{-\infty}^{t} \overline{\Phi}_{Rr}(t-\tau) \dot{r}(\tau)\, d\tau; \qquad R = F_x, F_z, M_y;} \tag{3.49}$$

or, by considering the motion starting at $t = 0$,

[5] Formally, one can write $r(t) = r(0) + \int_0^t \dot{r}(\tau) d\tau = H(t)\, r(0) + \int_0^t H(t-\tau)\, \dot{r}(\tau) d\tau$ and then consider the assumption of linearity and the fact that the response associated to the stepwise displacement $H(t)$ is $q_0 B^{\gamma_R} \overline{d}_{Rr} \overline{\Phi}_{Rr}(t)$.

$$\boxed{\overline{R}^{ai}(t) = q_0 B^{\gamma_R} \sum_{r=\dot{x}/U,\dot{z}/U,\alpha_y} \overline{d}_{Rr} \left[\overline{\Phi}_{Rr}(0)\, r(t) + \int_0^t \dot{\overline{\Phi}}_{Rr}(t-\tau) r(\tau)\, d\tau \right]; \quad R = F_x, F_z, M_y.} \tag{3.50}$$

A part from the synthetic notation, the expression proposed here introduces some improvements with respect to the usual formulation (e.g. Caracoglia and Jones, 2003b; Costa, 2004). In fact, the load model used there was borrowed from the theory of the thin airfoil, where no drag force is present; the coefficients indicated here as $\overline{d}_{R_r}$ (Eq (3.15)) were erroneously set as $\overline{d}_{F_x\dot{x}} = \overline{d}_{F_x\dot{z}} = \overline{d}_{F_x\alpha_y} = \overline{C}'_D$, $\overline{d}_{F_z\dot{x}} = \overline{d}_{F_z\dot{z}} = \overline{d}_{F_z\alpha_y} = \overline{C}'_L$, and $\overline{d}_{M_y\dot{x}} = \overline{d}_{M_y\dot{z}} = \overline{d}_{M_y\alpha_y} = \overline{C}'_M$, so that the steady limit behaviour was not captured. The significance of that convergence was already pointed out by Scanlan, 1993. In other works where the equivalence between frequency- and time-domain was considered (e.g. Lin and Yang, 1983), no reference to asymptotic behaviour was made.

On the other hand, the expressions introduced here are consistent with the quasi-steady limit, and guarantee the convergence to the actual forces for all the force components excited by all the motion components.

The explicit form of Eq (3.49) is

$$
\begin{aligned}
\overline{F}_x^{ai} &= q_0 B \left[\begin{array}{l} -2\overline{C}_D \int_{-\infty}^{t} \overline{\Phi}_{F_x\dot{x}}(t-\tau) \dfrac{\ddot{x}(\tau)}{U} d\tau + \\ -\left(\overline{C}'_D - \overline{C}_L\right) \int_{-\infty}^{t} \overline{\Phi}_{F_x\dot{z}}(t-\tau) \dfrac{\ddot{z}(\tau)}{U} d\tau + \\ +\overline{C}'_D \int_{-\infty}^{t} \overline{\Phi}_{F_x\alpha}(t-\tau)\, \dot{\alpha}(\tau)\, d\tau \end{array} \right], \\
\overline{F}_z^{ai} &= q_0 B \left[\begin{array}{l} -2\overline{C}_L \int_{-\infty}^{t} \overline{\Phi}_{F_z\dot{x}}(t-\tau) \dfrac{\ddot{x}(\tau)}{U} d\tau + \\ -\left(\overline{C}'_L + \overline{C}_D\right) \int_{-\infty}^{t} \overline{\Phi}_{F_z\dot{z}}(t-\tau) \dfrac{\ddot{z}(\tau)}{U} d\tau + \\ +\overline{C}'_L \int_{-\infty}^{t} \overline{\Phi}_{F_z\alpha}(t-\tau)\, \dot{\alpha}(\tau)\, d\tau \end{array} \right], \\
\overline{M}_y^{ai} &= q_0 B^2 \left[\begin{array}{l} -2\overline{C}_M \int_{-\infty}^{t} \overline{\Phi}_{M_y\dot{x}}(t-\tau) \dfrac{\ddot{x}(\tau)}{U} d\tau + \\ -\overline{C}'_M \int_{-\infty}^{t} \overline{\Phi}_{M_y\dot{z}}(t-\tau) \dfrac{\ddot{z}(\tau)}{U} d\tau + \\ +\overline{C}'_M \int_{-\infty}^{t} \overline{\Phi}_{M_y\alpha}(t-\tau)\, \dot{\alpha}(\tau)\, d\tau \end{array} \right],
\end{aligned}
\tag{3.51}
$$

which correct the limit behaviour of Eq (3.39).

3.5.2 Identification of indicial functions from measured aeroelastic derivatives

Experimental procedures to identify indicial functions have been achieved only recently by Caracoglia and Jones, 2003a, and are not yet well established as those to obtain aeroelastic derivatives. Moreover, imposing the theoretical sudden rotation to the cross-section into the wind tunnel poses evident physical problems. The same problems also occurs in the attempts to obtain indicial functions through computational fluid dynamics simulations (e.g. Eusani, 2005; Larsen, 2003).

Alternatively, it is possible to obtain an approximation of indicial functions from (measured or simulated) aeroelastic derivatives.

The usual approximation of indicial functions is a sum of exponential filters (e.g. Höffer, 1997) in the form

$$\boxed{\overline{\Phi}_{Rr}(s) = 1 - \sum_{n=1}^{N_{Rr}} \overline{a}_n^{Rr} \exp\left(-\overline{b}_n^{Rr} s\right)}, \tag{3.52}$$

where $s = 2Ut/B$ is the non-dimensional time[6], $\overline{a}_n^{Rr}$ and $\overline{b}_n^{Rr}$ are non-dimensional coefficients, and N_{Rr} is the number of terms chosen to approximate the indicial function Φ_{Rr}. Since indicial functions must converge to unit when time goes to infinity, the constrain $\overline{b}_n^{Rr} > 0$ is enforced.

By imposing a harmonic motion for one degree of freedom at a time in the expression of self-excited forces via aeroelastic derivatives and via indicial functions, Eqs (3.35) and (3.49) respectively, it is possible to express both models in the frequency domain. If also the exponential filters of Eq (3.52) are substituted into Eq (3.35), the convolution integrals can be calculated analytically. Thus, the two load models can be compared, and relationships between indicial function coefficients $\overline{a}_n^{Rr}$ and $\overline{b}_n^{Rr}$, and aeroelastic derivatives are obtained,

$$\boxed{\begin{aligned} \frac{\overline{D}_{Rr}}{\overline{d}_{Rr}} &= 1 - \pi^2 \sum_{n=1}^{N_{Rr}} \frac{\overline{a}_n^{Rr}}{\left(U_* \overline{b}_n^{Rr}\right)^2 + \pi^2}, \\ \frac{\overline{E}_{Rr}}{\overline{d}_{Rr}} &= -\frac{U_*^2}{2} \sum_{n=1}^{N_{Rr}} \frac{\overline{a}_n^{Rr} \overline{b}_n^{Rr}}{\left(U_* \overline{b}_n^{Rr}\right)^2 + \pi^2}. \end{aligned}} \tag{3.53}$$

It is worth to notice that the quasi-steady behaviour is obtained if $\overline{a}_n^{Rr} = 0$, in this case the wind forces do not depend anymore on the motion-history, i.e. the unsteady memory-effect is lost. Moreover, the higher the values of $\overline{a}_n^{Rr}$ the more pronounced the unsteady effects are. On the other hand the parameters $\overline{b}_n^{Rr}$ determine the reduced frequencies where the unsteady effects are more relevant. As a consequence, the relevant indicial functions have indeed a longer or a shorter decay. Rearranging Eqs (3.53) one has

$$\begin{aligned} \frac{\overline{D}_{Rr} - \overline{d}_{Rr}}{\overline{d}_{Rr}} &= -\sum_{n=1}^{N_{Rr}} \overline{a}_n^{Rr} \frac{\pi^2}{\left(U_* \overline{b}_n^{Rr}\right)^2 + \pi^2}, \\ \frac{\overline{E}_{Rr}}{\overline{d}_{Rr}} &= -\sum_{n=1}^{N_{Rr}} \overline{a}_n^{Rr} \frac{\overline{b}_n^{Rr} U_*^2/2}{\left(U_* \overline{b}_n^{Rr}\right)^2 + \pi^2}. \end{aligned} \tag{3.54}$$

[6] The time is normalized with respect to the time required for the flow to travel the cross-section semi-chord.

The first equation describes the relative unsteady correction to the in-phase unsteady coefficients with respect to the steady limit, whereas the second represents the unsteady quadrature correction. They are expressed as a linear combination with coefficients $\overline{a}_n^{Rr}$ of the functions

$$f_D^n\left(U_*\right)=\frac{\pi^2}{\left(U_*\overline{b}_n^{Rr}\right)^2+\pi^2},\quad f_E^n\left(U_*\right)=\frac{\overline{b}_n^{Rr}\,U_*^2/2}{\left(U_*\overline{b}_n^{Rr}\right)^2+\pi^2}, \tag{3.55}$$

respectively, which are represented in Figure 3.10. We have that

$$\lim_{U_*\to\infty} f_D^n\left(U_*\right)=0,\quad \lim_{U_*\to\infty} f_E^n\left(U_*\right)=\frac{1}{2\overline{b}_n^{Rr}}. \tag{3.56}$$

The unsteady in-phase correction tends to zero, i.e. the behaviour tends to the quasi-steady one; the quadrature correction tends to a constant value.

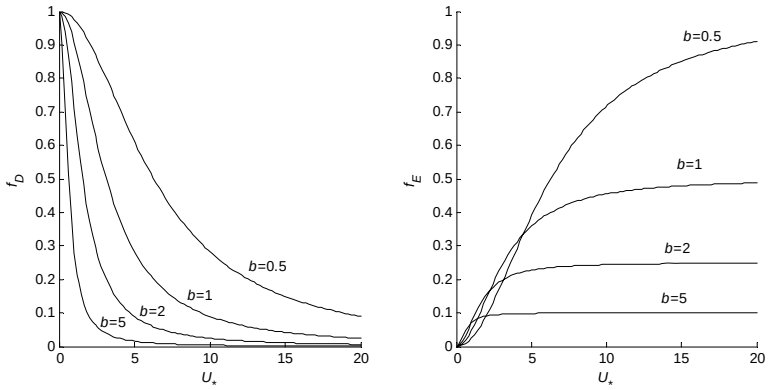

Figure 3.10 Representation of unsteady corrections

Subsequently, indicial functions coefficients can be identified by means of a nonlinear least-square optimization on aeroelastic derivatives $\overline{D}_{Rr}^m$ and $\overline{E}_{Rr}^m$ measured at discrete values of the reduced wind velocity U_*^m, $m=1,\ldots,M$. The error function ε to be minimized is

$$\varepsilon_{Rr}\left(\overline{\mathbf{p}}_{Rr}\right)=\sum_{m=1}^{M}\left[\left(D_{Rr}\left(\overline{\mathbf{p}}_{Rr},U_*^m\right)-\overline{D}_{Rr}^m\right)^2+\left(E_{Rr}\left(\overline{\mathbf{p}}_{Rr},U_*^m\right)-\overline{E}_{Rr}^m\right)^2\right], \tag{3.57}$$

where the vector

$$\overline{\mathbf{p}}_{Rr}=\left[\overline{a}_1^{Rr},\ldots,\overline{a}_{N_{Rr}}^{Rr},\overline{b}_1^{Rr},\ldots,\overline{b}_{N_{Rr}}^{Rr}\right]^T \tag{3.58}$$

collects the parameters to be determined through the optimization procedure. If the aerodynamic coefficients for a certain cross-section are not known, it is possible to treat $\overline{d}_{Rr}$ as an additional parameter to be identified. In that case, the parameter vector becomes

$$\overline{\mathbf{p}}_{Rr} = \left[\overline{d}_{Rr}, \overline{a}_1^{Rr}, \ldots, \overline{a}_{N_{Rr}}^{Rr}, \overline{b}_1^{Rr}, \ldots, \overline{b}_{N_{Rr}}^{Rr}\right]^T . \tag{3.59}$$

In this case one must consider that the coefficients $\overline{d}_{Rr}$ are not independent ones from the others as they depend on steady coefficients and their derivatives, see Eqs (3.15). Therefore, the optimization must be performed considering more than one couple of unsteady coefficients $\overline{D}_{Rr}$ and $\overline{E}_{Rr}$ at a time.

An approach similar to the one developed here is the approximation of aeroelastic derivatives through rational functions (e.g. Chen et al., 2001; Chen et al., 2000a; Karpel, 1982). Some discussion on the rational function approximation compared to quasi-steady modelling is available in Lazzari, 2005.

In other formulations (e.g. Borri et al., 2002; Borri and Höffer, 2000), some additional coefficients are introduced. These do not have direct physical interpretation and might introduce an excessive redundancy that complicates the identification procedure.

It is worth to point out that the representation of unsteady coefficients in terms of $\overline{D}_{Rr}$ and $\overline{E}_{Rr}$ is more suitable for the identification procedure than the classical representation in terms of $\overline{P}_h$, $\overline{H}_h$, and $\overline{A}_h$, $h = 1,\ldots,6$, where the values at low reduced velocities are scaled down, see Eq (3.36). Therefore the values at high reduced velocities would be weighted too much in the total error, resulting in a poor approximation at low reduced velocities, where unsteadiness is more important.

In Caracoglia and Jones, 2003b, a procedure for obtaining indicial functions from experimental data has been applied to a set of indicial functions for lift and moment. They report that for bluff deck sections with 'aeroelastically irregular' behaviour, the identification of indicial function coefficients can be challenging, and a low correspondence between the experimental behaviour in the frequency-domain and its prediction through the indicial function is obtained. On the other hand, they observe that the indicial function approach can be potentially successfully applied to streamlined or moderately bluff deck sections. This however does not seem to be a significant restriction. Nowadays, a general tendency of the designers towards box girders with excellent aerodynamic performance is in fact registered.

It is concluded that the approach based on indicial functions identified from aeroelastic derivatives can be considered as equivalently suitable with respect to frequency-domain formulations. Time-domain methods might be used for bridge analyses where the frequency-domain approach is more

complicated (e.g. coupled buffeting analysis, analyses including localized damping devices), or where it is not applicable (e.g. analyses including structural nonlinearities, nonlinear damping devices).

Finally, in evaluating the accuracy of the approximation reached during the identification, one must not forget that unsteady coefficients are not deterministic values, but they are affected by experimental errors. Thus, the quality of the approximation should be compared with the dispersion of the measures. When statistical information on measured unsteady coefficients is available, the error function to be minimized can be improved. It seems in fact more consistent with the experimental nature of unsteady coefficients, to use

$$\boxed{\varepsilon_{Rr}\left(\overline{\mathbf{p}}_{Rr}\right)=\sum_{m=1}^{M}\left[\frac{\left(D_{Rr}\left(\overline{\mathbf{p}}_{Rr},U_{*}^{m}\right)-\overline{D}_{Rr}^{m}\right)^{2}}{\sigma_{\overline{D}_{Rr}^{m}}^{2}}+\frac{\left(E_{Rr}\left(\overline{\mathbf{p}}_{Rr},U_{*}^{m}\right)-\overline{E}_{Rr}^{m}\right)^{2}}{\sigma_{\overline{E}_{Rr}^{m}}^{2}}\right]}, \quad (3.60)$$

where $R=F_{x},F_{z},M_{y}$, $r=\dot{x}/U,\dot{z}/U,\alpha_{y}$, $\sigma_{\overline{D}_{Rr}^{m}}^{2}$ and $\sigma_{\overline{E}_{Rr}^{m}}^{2}$ are the variance of m-th measured point for the unsteady coefficients, and $\overline{D}_{Rr}^{m}$ and $\overline{E}_{Rr}^{m}$ are the relevant mean values. In this way the accuracy of the experimental data is taken into account in the identification of the indicial functions.

3.6 Numerical issues in the identification and use of indicial functions

Below, some numerical issues in the identification of indicial functions and in the implementation of the load model in numerical codes are discussed.

3.6.1 Nonlinear optimization

Techniques of nonlinear optimization applied to the present problem are discussed in Salvatori and Zahlten, 2005.

As the objective function to be optimized (Eqs (3.57) or (3.60)) is nonlinear in the parameters $\overline{b}_{n}^{Rr}$ (see also Eqs (3.53)), an iterative approach is required. The procedure starts with an initial guess $\mathbf{p}_{0}$. At each step, a correction $\Delta\mathbf{p}$ is evaluated, and the calculations are iterated until convergence is obtained.

Some minimization techniques require the calculation of the gradient $\mathbf{g}=\partial\varepsilon/\partial\mathbf{p}$ and of the Hessian matrix $\mathbf{G}=\partial^{2}\varepsilon/\partial\mathbf{p}^{2}$ of the error function with respect to the vector of the parameters. These quantities can be calculated numerically or analytically. The latter approach is considered here (the small effort is more than compensated by the increase in the algorithm efficiency). By deriving Eq (3.57), one obtains

$$
\begin{aligned}
g_i(\mathbf{p}) &= \frac{\partial \varepsilon}{\partial p_i} = 2\sum_m \left[(D - D^m) \frac{\partial D}{\partial p_i} + (E - E^m) \frac{\partial E}{\partial p_i} \right], \\
G_{ij}(\mathbf{p}) &= \frac{\partial^2 \varepsilon}{\partial p_i \partial p_j} = \\
&= 2\sum_m \left[\frac{\partial D}{\partial p_i} \frac{\partial D}{\partial p_j} + (D - D^m) \frac{\partial^2 D}{\partial p_i \partial p_j} + \frac{\partial E}{\partial p_i} \frac{\partial E}{\partial p_j} + (E - E^m) \frac{\partial^2 E}{\partial p_i \partial p_j} \right].
\end{aligned}
\tag{3.61}
$$

where the scripts Rr and the overbar are omitted for the sake of brevity.

The expressions in Eqs (3.61) require the analytical calculation of the first and second derivatives of Eqs (3.53); the results of the analytical calculations are

$$
\begin{aligned}
&\frac{\partial D}{\partial d} = 1 - \pi^2 \sum_{n=1}^{N} \frac{a_n}{U_*^2 b_n^2 + \pi^2}, \quad \frac{\partial E}{\partial d} = -\frac{U_*^2}{2} \sum_{n=1}^{N} \frac{a_n b_n}{U_*^2 b_n^2 + \pi^2}, \\
&\frac{\partial D}{\partial a_h} = -\pi^2 d \frac{1}{U_*^2 b_h^2 + \pi^2}, \qquad \frac{\partial E}{\partial a_h} = -d \frac{U_*^2}{2} \frac{b_h}{U_*^2 b_h^2 + \pi^2}, \\
&\frac{\partial D}{\partial b_h} = 2\pi^2 U_*^2 d \frac{a_h b_h}{\left(U_*^2 b_h^2 + \pi^2\right)^2}, \quad \frac{\partial E}{\partial b_h} = \frac{U_*^2}{2} da_h \frac{U_*^2 b_h^2 - \pi^2}{\left(U_*^2 b_h^2 + \pi^2\right)^2},
\end{aligned}
\tag{3.62}
$$

$$
\frac{\partial^2 D}{\partial d^2} = 0, \qquad \frac{\partial^2 E}{\partial d^2} = 0,
\tag{3.63}
$$

$$
\begin{aligned}
&\frac{\partial^2 D}{\partial d \partial a_h} = -\pi^2 \frac{1}{U_*^2 b_h^2 + \pi^2}, \\
&\frac{\partial^2 D}{\partial d \partial b_h} = 2\pi^2 U_*^2 \frac{a_h b_h}{\left(U_*^2 b_h^2 + \pi^2\right)^2}, \\
&\frac{\partial^2 D}{\partial a_h \partial a_l} = 0, \\
&\frac{\partial^2 D}{\partial a_h \partial b_l} = \delta_{hl} 2\pi^2 U_*^2 d \frac{b_h}{\left(U_*^2 b_h^2 + \pi^2\right)^2}, \\
&\frac{\partial^2 D}{\partial b_h \partial b_l} = \delta_{hl} 2\pi^2 U_*^2 da_h \frac{\pi^2 - 3U_*^2 b_h^2}{\left(U_*^2 b_h^2 + \pi^2\right)^3},
\end{aligned}
\tag{3.64}
$$

$$
\begin{aligned}
\frac{\partial^2 E}{\partial d \partial a_h} &= -\frac{U_*^2}{2}\frac{b_h}{U_*^2 b_h^2 + \pi^2}, \\
\frac{\partial^2 E}{\partial d \partial b_h} &= \frac{U_*^2}{2} a_n \frac{U_*^2 b_h^2 - \pi^2}{\left(U_*^2 b_h^2 + \pi^2\right)^2}, \\
\frac{\partial^2 E}{\partial a_h \partial a_l} &= 0, \\
\frac{\partial^2 E}{\partial a_h \partial b_l} &= \delta_{hl}\frac{U_*^2}{2} d \frac{U_*^2 b_h^2 - \pi^2}{\left(U_*^2 b_h^2 + \pi^2\right)^2}, \\
\frac{\partial^2 E}{\partial b_h \partial b_l} &= \delta_{hl} U_*^4 d a_h b_h \frac{3\pi^2 - U_*^2 b_h^2}{\left(U_*^2 b_h^2 + \pi^2\right)^3},
\end{aligned}
\tag{3.65}
$$

where δ_{hl} is the Kronecker symbol ($\delta_{hl} = 0$, if $h \neq l$; $\delta_{hl} = 1$, if $h = l$).

Different minimization algorithms have been considered in order to develop a robust and accurate identification procedure. Most of the highlighted properties are general characteristics of the methods (e.g. Nash, 1979), and they are tested here on the specific problem.

Steepest-descent and damped steepest-descent methods. As the gradient points opposite to the 'fall line' of the surface $\varepsilon(\mathbf{p})$, a correction $\Delta\mathbf{p} = -\alpha\mathbf{g}$ is considered, with the purpose of going 'downhill'. One problem with this method lies in the choice of the constant α , which is usually arbitrary. The solution might zigzag down 'valleys' and overshoot the minimum. Moreover, the procedure becomes very slow close to an extreme value, since the gradient approaches the null vector. The results of the identification procedure are very poor, even when a 'damped' version is considered (before accepting a new value of $\mathbf{p}$, the new error is evaluated and, if it is higher than the previous one, α is halved and a new correction is evaluated).

Gauss-Newton and damped Gauss-Newton methods. The extremum condition of vanishing gradient results in a system of nonlinear equations that can be solved by a Newton-Raphson technique. This leads to the correction $\Delta\mathbf{p} = -\mathbf{G}^{-1}\mathbf{g}$. This method is very efficient and accurate close to an extremum. Nevertheless, a poor initial estimate of $\mathbf{p}_0$ might cause divergent iterations, as it was already pointed out for the present problem in Scanlan et al., 1974. Moreover, the Hessian matrix might become singular. Gauss-Newton method can be 'damped' too by scaling down the correction $\Delta\mathbf{p}$ if the error increases with respect to previous iterations. This helps in some cases but does not completely solve the problem of numerical instability far away from the minimum.

Levenberg-Marquardt method. It is an attempt to combine the advantages of the steepest-descent and Gauss-Newton methods. The correction is evaluated as $\Delta\mathbf{p} = -\left(\mathbf{G} + \beta\mathbf{I}\right)^{-1}\mathbf{g}$. The method starts close to Gauss-Newton's one with a 'small' value of the parameter β . If the error

increases, β is doubled, and the steepest-descent contribution is amplified. In this way, a 'downhill' path is ensured and the method acts like the steepest-descent one far from the global minimum, and like Gauss-Newton's one close to it. For the present problem, however, no substantial improvement in robustness is highlighted.

Direct-search methods. Direct methods do not require the calculation of the gradients. Here, the Nelder-Mead method is considered as described in Lagarias et al., 1998. A simplex (a set of $N_p + 1$ points in the parameter space, where N_p is the number of optimization parameters) is generated around the initial guess $\mathbf{p}_0$. The error function is sampled at the simplex vertexes. At a new iteration a point is generated, which substitutes the vertex of the old simplex in which the error-function took the higher value. In this way the simplex moves over the parameter space and eventually contracts around the minimum. For the present problem, Nelder-Mead algorithm evidences a weaker dependence on the initial guess with respect to the other methods, but still diverges in some cases. Moreover, it proves relatively inaccurate.

Trust-region methods. The idea is to approximate the error function with a simpler one (e.g. a second order Taylor expansion) in a neighbourhood (trust region) of the current guess. A local minimization sub-problem is then solved by means of the preconditioned conjugate gradient technique. The resulting point is checked in the original function: if it improves the solution it is accepted, otherwise the trust region is shrunk and the step is repeated. Sophisticated versions of this algorithm allow one to restrict the variation of some parameters within an interval. Here, the interior-reflective Newton algorithm described by Coleman and Li, 1996, and implemented in MatLab® R13 has been considered. Trust-region methods, even if they converge more slowly than Gauss-Newton's one close to the minimum, prove to be the most robust algorithms among those considered here. They exhibit a reduced sensitivity to the initial guess, especially if upper and lower boundaries for the parameters are specified.

It has been shown that most of the minimization algorithms may exhibit inaccuracy, instability, and a strong sensitivity to the initial guess. Although the solution can be found by means of a trial procedure on the initial estimate, this could be time-consuming and impracticable when the number of parameter is high. Here, a more practical and reliable procedure is defined as a combination of the bounded trust-region method with the standard Gauss-Newton method. The former algorithm provides a robust initial-guess-independent approximation of the solution, which is then refined by the latter algorithm that is more precise but would diverge with a poor initial guess.

Bounding the parameter domain proves very effective in preventing divergent iterations, and it improves the robustness of the overall procedure.

As a further development, *genetic algorithms* should be considered as suitable candidate for the optimization procedure. Due to their robustness when dealing with many parameters, they may be able to manage a large number of exponential terms, providing a better approximation of aeroelastic derivatives with irregular behaviour.

As to the number of exponential groups used in the approximation of indicial functions, we briefly discuss literature results, although they are obtained with different versions of the load model. For streamlined cross-sections, with uniform and 'well-defined' trends in all derivatives, the use of one (Costa, 2004) or two (as in Jones' approximation of Theodorsen's function) groups of exponential terms is sufficient to capture the general behaviour. The use of three or four groups is shown to be necessary (Caracoglia and Jones, 2003b) for other cross-sections, but they may eventually lead to statistically unmanageable systems, numerically high values of the coefficients, and potentially large confidence intervals.

Here, the number of exponential groups is chosen by means of statistical consideration, i.e. by implementing an automatic procedure that compares the results obtained with different values of N_{Rr}, by using random values for the initial guess, and then selects the most accurate result from statistics.

3.6.2 Domain of indicial function parameters for the optimization

The problem concerns both the identification of the indicial function and the evaluation of the convolution integrals.

The robustness of the identification procedure has been tested also by performing a fully automatic identification as a part of a Monte Carlo analysis for the evaluation of the reliability of indicial functions with respect to the scatter of experimental data (Borri, Costa and Salvatori, 2005).

Bounding the scope of the parameters b_h^{Rr} proves to be very effective in preventing the divergence of the identification procedure. The only physical constraint is $b_h^{Rr} > 0$, as it has been discussed in the previous Section. Nevertheless, narrower boundaries must be imposed for computational reasons.

Quickly decaying indicial functions require in fact very small time-steps in order for the convolution integrals to be accurately evaluated. For avoiding excessive computational costs, the time-step size must be chosen only with regard to the structure (e.g. following the 'thumb-rule' of using $1/20 \div 1/50$ of the smaller modal period to be simulated). Therefore, an upper limit $b_h^{Rr}(\max)$ must be provided (the higher is b_h^{Rr}, the quickest the indicial functions decay). The adopted empirical rule is to chose $b_h^{Rr}(\max)$ so that $\exp\left(-b_h^{Rr}(\max)\,\Delta t\, 2U/B\right)=0.9$.

On the other hand very small values of b_h^{Rr} would require very long time-histories in order to correctly account for unsteadiness. The adopted empirical rule for the lower limit is to chose $b_h^{Rr}(\min)$ so that $\exp\left(-b_h^{Rr}(\min)\,T_{ref}\,2U/B\right)=0.5$, where T_{ref} is a reference structural period.

All this could appear quite tricky, if one thinks to the physical meaning of indicial functions. Nevertheless, many clues (Salvatori and Zahlten, 2005 Borri, Costa and Salvatori, 2005) suggest that different sets of indicial functions could be identified, all leading to a correct modelling of the unsteady forces. It seems in fact that the model presents some kind of redundancy. This delicate aspect must of course be more deeply investigated.

The use of boundaries is suggested and discussed by Salvatori and Borri, 2005.

3.7 Numerical example of identification of indicial functions

We use the aeroelastic properties of a streamlined bridge cross-section with semicircular fairings and width-to-height ratio $B/D=14.3$ that has been tested in the wind tunnel by Chowdhury and Sarkar, 2004 (there, referred to as 'cross-section B1').

In the representation of the unsteady coefficients defined in Eqs (3.36), the quasi-steady limit can be more easily recognized (from Figure 3.11 to Figure 3.15). Also, this representation is more suitable for the identification of the indicial functions, since the error in the approximation of D_{Rr} and E_{Rr} is proportional to the one in the approximation of the self-excited forces, at all the reduced velocities.

As measured steady coefficients are not available for the adopted cross-section, it has been chosen to identify also $\overline{C}_D$, $\overline{C}'_L$, and $\overline{C}'_M$ from the aeroelastic derivatives.

The number of exponential groups in the approximation of each indicial function is kept as low as possible, also because of the small number of measured values available for the optimization. One group proves adequate for modelling all the unsteady contributions except for the vertical force excited by the rotation, for which at least two groups are needed.

The optimization is performed by using a trust-region algorithm and developing analytical expressions for the error gradients $\partial\varepsilon_{Rr}/\partial\mathbf{p}_{Rr}$ and $\partial^2\varepsilon_{Rr}/\partial\mathbf{p}_{Rr}^2$. The parameters resulting from the optimization are reported in Table 3.1 and the Figures show the approximations of the unsteady coefficients (a-b) and the relevant identified indicial functions (c).

From the identified coefficients d_{Rr} through Eqs (3.15) we obtain $\overline{C}_D=0.71$, $\overline{C}'_L=5.59$, and $\overline{C}'_M=1.23$. The value of the drag coefficient appears much too high for the considered streamlined cross-section.

Nevertheless the trend of P_1^* is appropriately captured in its quasi-steady limit (see Figure 3.11b and remind that $KP_1^* = D_{F_x\dot{x}} \to d_{F_x\dot{x}} = -2\overline{C}_D$ as $U_* \to \infty$). Moreover, this numerical example has purely heuristic purposes; the goal is to compare the calculations in frequency and time domain. Therefore we accept the experimental data as input and do not further discuss them here.

Both the frequency- and time-domain stability analyses are performed by incrementing the mean wind velocity step by step. At each step, the mean configuration is evaluated by means of a nonlinear static analysis under steady wind load. For this purpose, the aerodynamic coefficients C_D, C_L, and C_M are assumed to be linear functions of the angle of attack (Figure 5.5); this choice is obligatory, as the values of the coefficients and of their first derivative are known only at zero angle of attack. An example of deformed configuration under mean steady wind is shown. Since the experimental aeroelastic derivatives we use are measured only at zero angle of attack, the load is always linearized around this angle and only the changes in the structural stiffness due to mean steady deformations are accounted for. This does not affect the generality of the method; since different sets of indicial functions could be identified for each mean angle for which measured aeroelastic derivatives were available.

Since the considered cross-section is symmetric with respect to the X axis, at zero angle of attack the steady lift and moment must vanish and the drag must be stationary, i.e. $\overline{C}_L = \overline{C}_M = 0$ and $\overline{C}'_D = 0$. From Eqs (3.15) it follows that $d_{F_x\dot{z}} = d_{F_x\alpha_y} = d_{F_z\dot{x}} = d_{M_y\dot{x}} = 0$.

As regards the self-excited loads, the vertical force and pitching moment due to the horizontal velocity and the horizontal forces due to the vertical velocity and rotation are neglected due to the symmetry of the cross-section.

Table 3.1 Identified indicial function coefficients

Indicial function		Identified coefficients				
R	r	d	a_1	b_1	a_2	b_2
F_x	$\dot{x}/U$	-1.42	0.756	0.381	-	-
F_x	$\dot{z}/U$	0.00	-	-	-	-
F_x	θ	0.00	-	-	-	-
F_z	$\dot{x}/U$	0.00	-	-	-	-
F_z	$\dot{z}/U$	-6.30	0.415	0.283	-	-
F_z	θ	5.59	2.445	0.986	-5.531	2.000
M_y	$\dot{x}/U$	0.00	-	-	-	-
M_y	$\dot{z}/U$	-1.23	0.321	0.415	-	-
M_y	θ	1.23	2.069	2.000	-	-

Rectangular prisms have also been considered (Matsumoto, Kobayashi et al., 1995; Matsumoto et al., 1996) in Chapter 5.

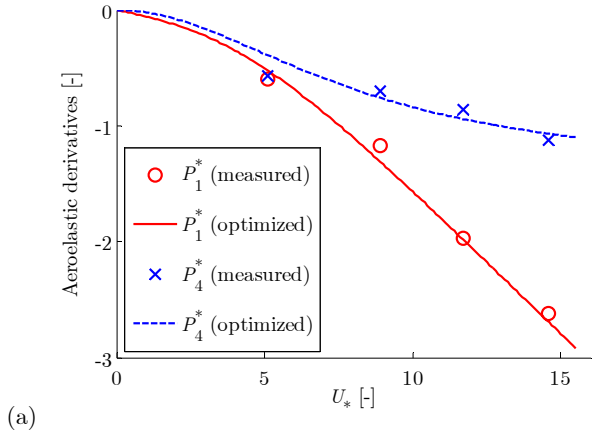

(a)

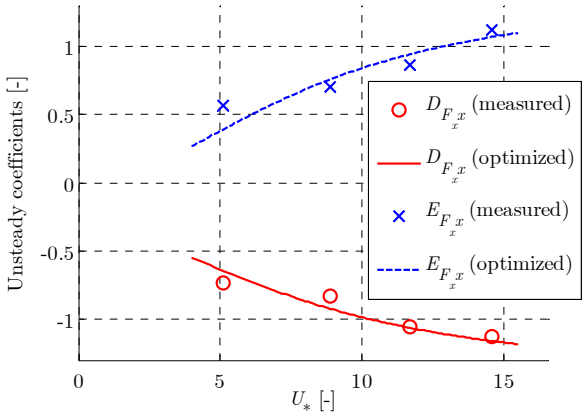

(b)

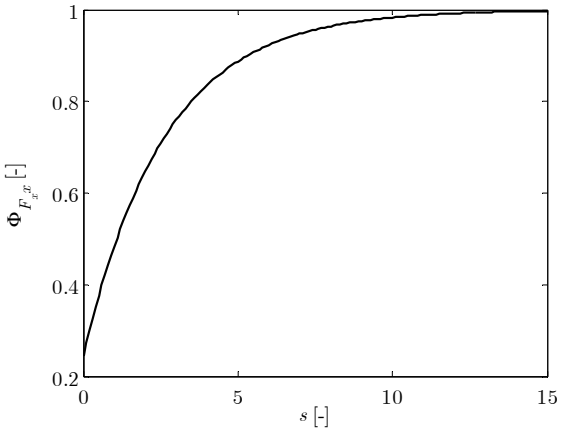

(c)

Figure 3.11 Deck 1, horizontal force due to horizontal velocity: unsteady coefficients in Scanlan's (a) and proposed (b) notation, and relevant indicial function (c)

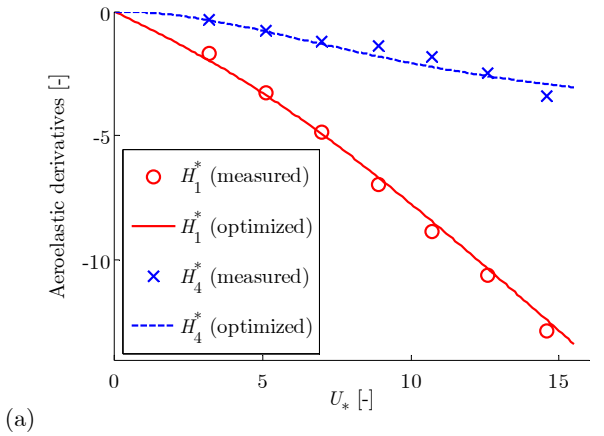

(a)

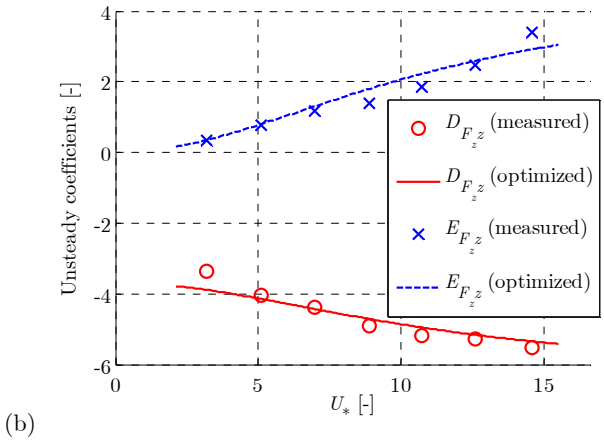

(b)

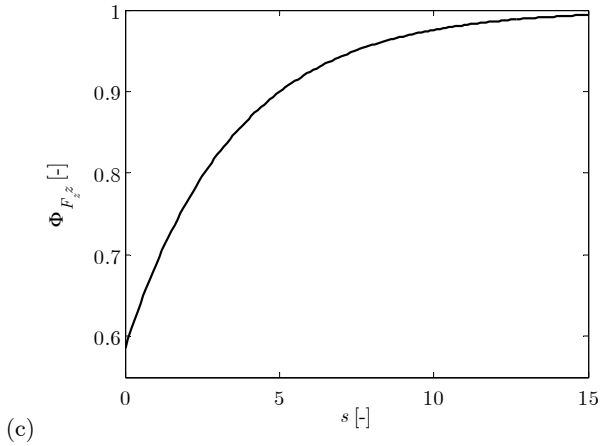

(c)

Figure 3.12 Deck 1, vertical force due to vertical velocity: unsteady coefficients in Scanlan's (a) and proposed (b) notation, and relevant indicial function (c)

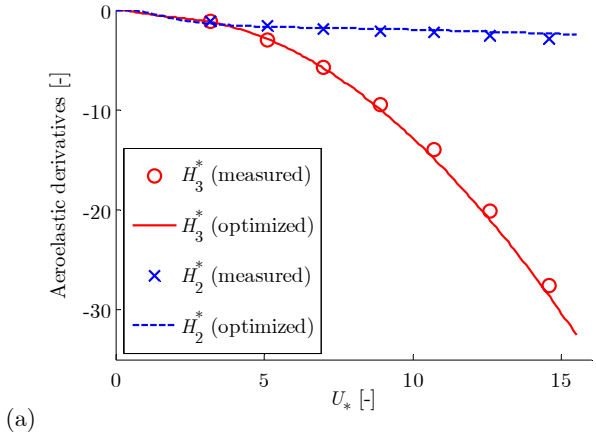

(a)

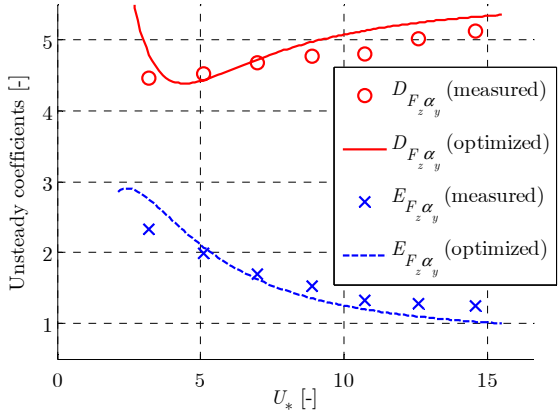

(b)

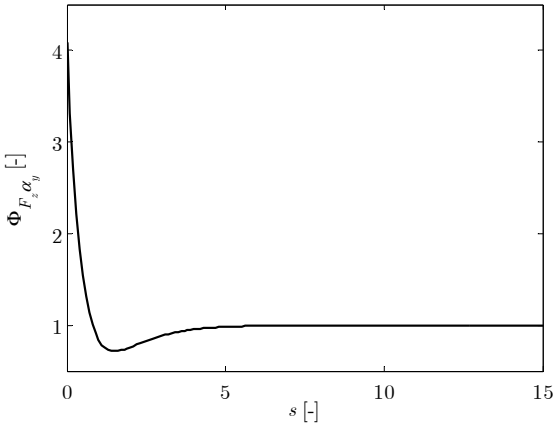

(c)

Figure 3.13 Deck 1, vertical force due to rotation: unsteady coefficients in Scanlan's (a) and proposed (b) notation, and relevant indicial function (c)

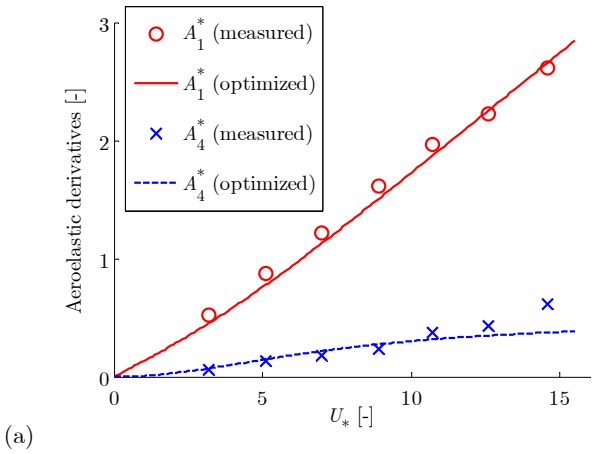

(a)

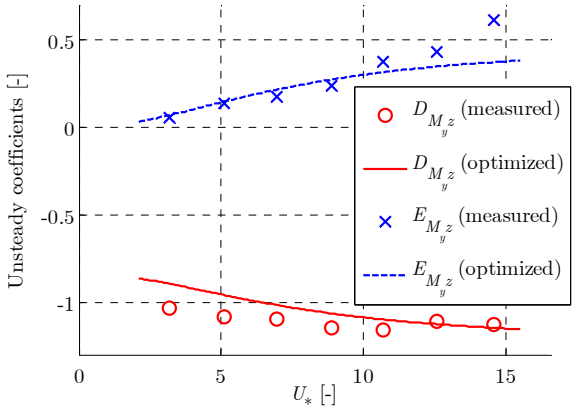

(b)

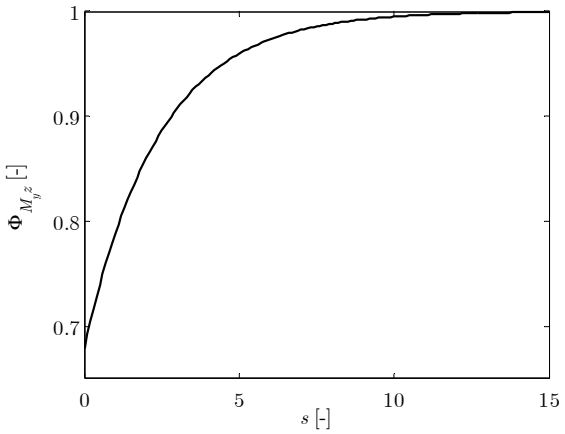

(c)

Figure 3.14 Deck 1, pitching moment due to vertical velocity: unsteady coefficients in Scanlan's (a) and proposed (b) notation, and relevant indicial function (c)

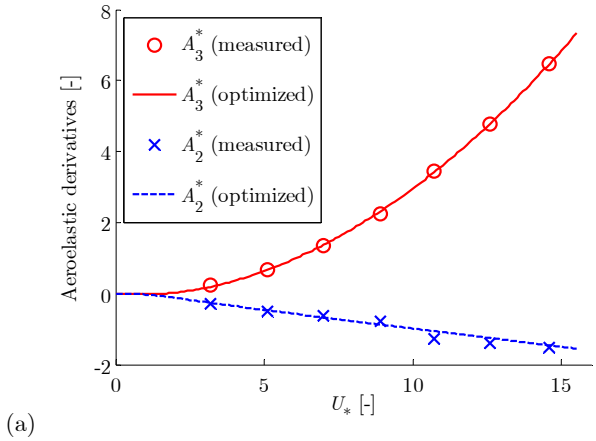

(a)

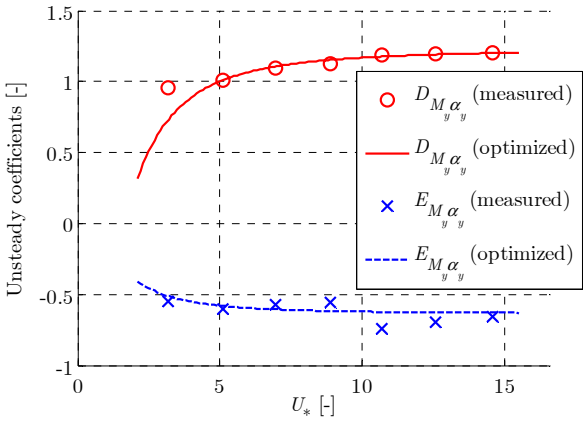

(b)

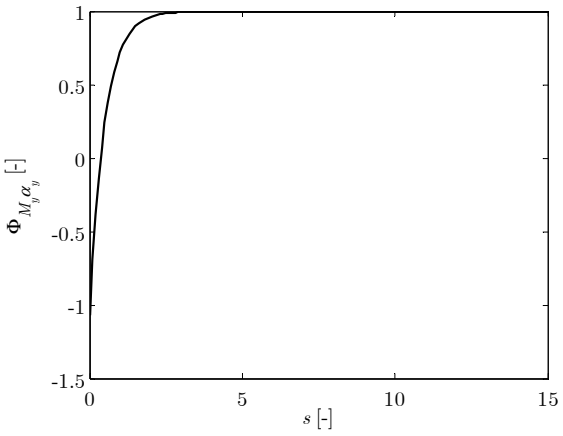

(c)

Figure 3.15 Deck 1, pitching moment due to rotation: unsteady coefficients in Scanlan's (a) and proposed (b) notation, and relevant indicial function (c)

Chapter 4

Numerical Procedures

In this Chapter a numerical framework for the numerical analysis of bridges under wind action is developed. It is based on a finite element discretization of the structure and on the semi-empirical load models presented in Chapter 3. A computer program and original numerical procedures are developed for evaluating aeroelastic stability and buffeting response in presence of self-excited forces, in both frequency and time domains. The computational framework includes the generation of the time-histories of the wind velocity field, nonlinear structural finite elements formulated according to the co-rotational approach, several types of analysis, and macros for the parametric generation of the structural models and for Monte Carlo simulations. In this way, arbitrary bridges (including also damping devices) can be easily simulated and the principal structural and aerodynamic features can be taken into account.

4.1 Computational framework

The wind load models described in Chapter 3 are used to analyze three-dimensional bridges. The main strategy is to discretize first the continuous problem by considering a discrete set of cross-sections, then to correlate with one another these cross-sections. More precisely, the velocity field of the oncoming wind is correlated between neighbouring discrete points which are connected by finite elements along the span of the bridge.

A computer program is developed ad hoc. It includes:

- The parametric generation of the topology of the finite element model;
- A finite element core with an original implementation of geometrical nonlinearities and the modelling of the tension-only behaviour of the cables;
- Quasi-steady and unsteady cross-sectional wind loading in the frequency and time domains;

- The generation of multi-correlated time-histories of the turbulent wind velocity through auto-regressive filters;
- The implementation of some original analysis procedures (in addition to literature ones);
- Post-processing and macros for Monte Carlo analyses.

4.2 Structural models

In the following sections, three approaches to the modelling of a suspension bridge are shown: (i) two-degree-of-freedom cross-sectional mechanical model, (ii) simplified mechanical models with two cross-sections; and (iii) full three-dimensional structural models.

4.2.1 Cross-sectional model

The simplest mechanical model for bridge analysis consists in a two-dimensional unit-span rigid cross-section restrained in the along-wind direction and elastically supported (Figure 4.1). The stiffness of the vertical and rotational springs is usually chosen in such a way as to obtain the correct frequencies for two selected modes (a vertical bending one and a torsional one).

This model reproduces the cross-sectional physical models that are tested into the wind tunnel in order to measure unsteady coefficients. It is able to predict flutter speed in bridges with 'good' behaviour, i.e. those where only two structural modes give significant contribution to the critical flutter mode.

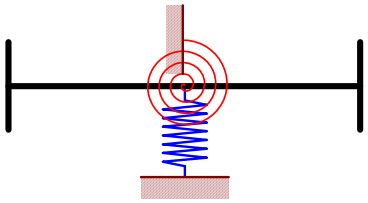

Figure 4.1 Cross-sectional mechanical model with two-degree-of-freedom

4.2.2 Simplified bridge model with two cross-section

In some analyses presented in Section 5.3, a simplified finite element model of a suspension bridge with two loaded cross-sections and with neglected flexibility of the towers will be considered. This model, depicted in Figure 4.2, represents a first extension of the cross-sectional model toward the three-dimensional behaviour and allows one to consider four structural modes, namely the symmetric and the skew-symmetric vertical and

torsional ones. Thanks to the reduced number of degrees of freedom, it is possible to simulate very long time histories of the buffeting response in a reasonable computational time. In this way, an analysis of the extreme values of the response is made possible.

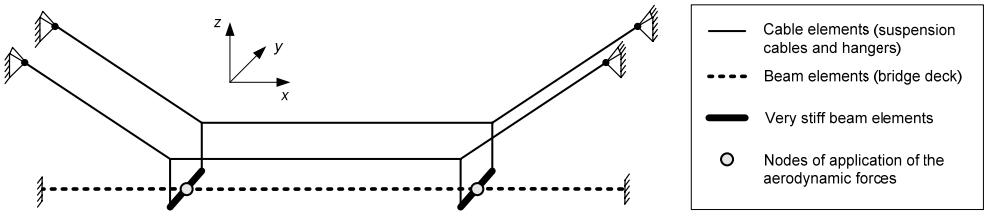

Figure 4.2 Simplified structural model of a suspension bridges with two cross-sections

4.2.3 Full bridge model

Finally, complete three-dimensional finite-element models of the bridge are considered. In the analyses presented in Chapter 5, 'fishbone-like' models will be used (Figure 4.3). The rigidity of the deck cross-section is obtained through a penalty approach, although multi-degree-of-freedom geometrical constrains would also be possible.

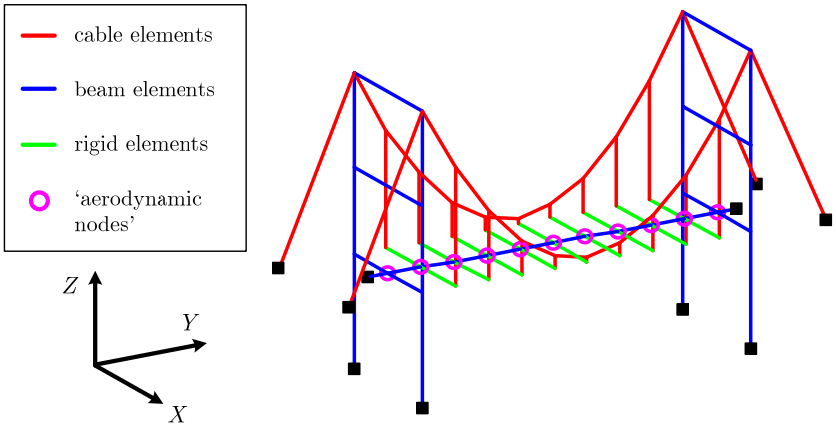

Figure 4.3 Schematic representation of the discrete structural model of a suspension bridge

4.3 Finite element discretization

The structure is modelled by means of finite elements (e.g. Bathe, 1996). The geometrical nonlinearities of beam and cable elements are implemented according to the co-rotational approach, and also the tension-only behaviour of cables is modelled.

4.3.1 Co-rotational approach to geometrical nonlinearities

Geometrical nonlinearities are included by means of the so-called co-rotational approach (e.g. Felippa, 2000).

The basic idea is to consider arbitrary rigid body motions and small deformations around the rigidly-displaced configuration $\mathcal{C}_r$ (Figure 4.4).

The main advantage of this formulation is that, once the nonlinear transformation of the finite element degrees of freedom from the original configuration to the configuration $\mathcal{C}_r$ is applied, standard small-strain finite elements, including those with material nonlinearities, can be used. In this way, literature models can be easily reused. The internal forces obtained in the configuration $\mathcal{C}_r$ can be back-transformed into the original finite-element coordinates by imposing that the rate of deformation energy is conserved in the co-rotational transformation.

For the sake of brevity, no details will be given in this dissertation, and only the elements that will be used in bridge analysis are listed in the next Sections.

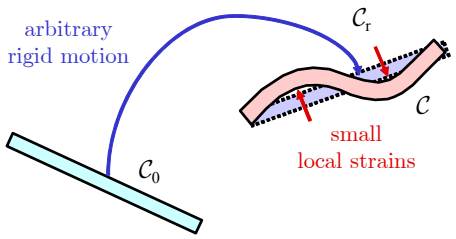

Figure 4.4 Co-rotational approach

4.3.2 Cable element

A two-node three-dimensional cable element is developed. In this case the only small-strain degree of freedom is the length variation d_1. The relevant internal force F_1 is the normal force in the cable.
In addition to the geometrical nonlinearities, a simple nonlinear constitutive law is introduced in order to simulate the tension-only behaviour of cables. The local force is given by

$$F_1^{(e)} = \begin{cases} 0, & \text{if } d_1^{(e)} \le 0, \\ \dfrac{E^{(e)} A^{(e)}}{\ell^{(e)}} d_1^{(e)}, & \text{if } d_1^{(e)} > 0, \end{cases} \tag{4.1}$$

where E is the (equivalent) Young modulus of the cable, A is the cable cross-section, and the notation (e) denotes the e-th elements, being $\ell^{(e)}$ its length.

4.3.3 Beam element

In order to model bridge deck and towers, a two-node three-dimensional beam element is also developed. The element has six small-strain degrees of freedom: the length variation, the relative torsion between the two nodes, and two rotations for each node in the directions orthogonal to the element axis in the current configuration.

Here, it is only worth mentioning that a second-order-tensor description of rotations (e.g. Crisfield, 1991) is required, since the classical approach is valid only in the case of small rotations (where the order of two consecutive rotations does not affect the final result).

Just to show the capabilities of the developed nonlinear approach, a simple example of a cantilever beam in bending is shown in Figure 4.5. For each load step only a few iterations (3 to 5) are required for evaluating the new configuration with a relative precision of 10^{-9}.

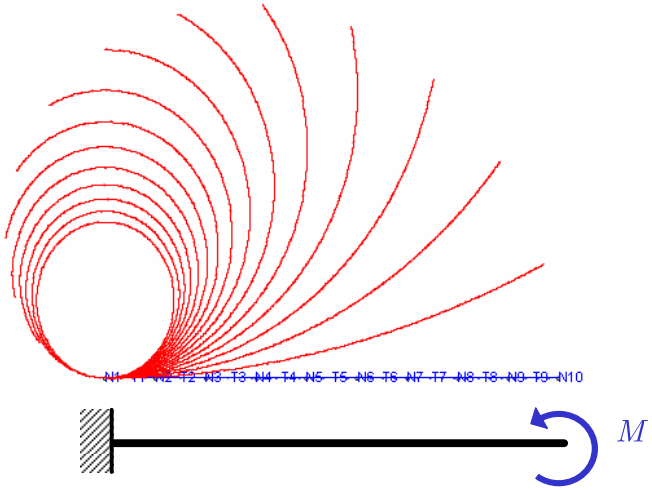

Figure 4.5 Cantilever beam discretized by 9 co-rotational elements: deformed configuration for increasing bending moment M

4.3.4 Further structural elements

Further structural elements, which will be used in Chapter 6 to model damping devices, are springs and viscous dashpots. A two-degree-of-freedom visco-elastic element is used, whose local internal forces are given by

$$\mathbf{F}_K^{(e)} = \begin{bmatrix} F_1 \\ F_2 \end{bmatrix} = k \begin{bmatrix} 1 & -1 \\ -1 & 1 \end{bmatrix} \begin{bmatrix} \dot{d}_1 \\ \dot{d}_2 \end{bmatrix} + c \begin{bmatrix} 1 & -1 \\ -1 & 1 \end{bmatrix} \begin{bmatrix} d_1 \\ d_2 \end{bmatrix}, \tag{4.2}$$

where k is the spring constant, c the linear viscous damping, d_1 and d_2 are the finite-element degrees of freedom, and F_1 and F_2 the internal forces power-conjugated with the rates of d_1 and d_2.

It is worth noticing that nonlinear elements can be readily implemented once their constitutive behaviour is assigned.

4.3.5 Aerodynamic loading

Wind actions are applied through special one-node 'elements' characterized by an orientation and an along-span influence length ℓ. The nodal wind forces are given by

$$\mathbf{P}_{wind}^{(e)} = \ell^{(e)} \begin{bmatrix} F_x^{(e)} \\ F_z^{(e)} \\ M_y^{(e)} \end{bmatrix}, \tag{4.3}$$

where F_x, F_z, and M_y are given by the load models described in Chapter 3, depending on the analysis.

4.4 Generation of wind field time histories

Discrete time-histories of the turbulent wind are considered at the nodes of the finite element model.

The auto-regressive filters described in Section 2.1.3 are used for the numerical generation of the multi-correlated processes, by using the power spectral densities in Eqs (2.13), (2.14), and (2.15). The cross-spectrum of the along-wind and vertical turbulence components is assumed as in Eq (2.20), and the exponentially decaying coherence functions described in Section 2.1.2 are used.

The order of the auto-regressive filter has been chosen as $P = 15$.

As an example, Figure 4.6 shows a generated time-history of the along wind turbulence component. In Figure 4.7, the power spectral density of the generated time-history is compared to the original target spectrum. A good agreement is observed.

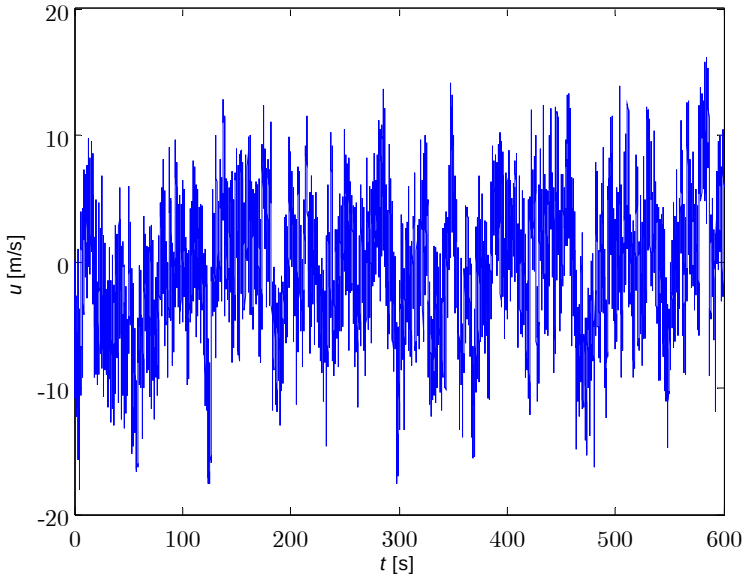

Figure 4.6 Example of generated time-history of turbulent wind velocity

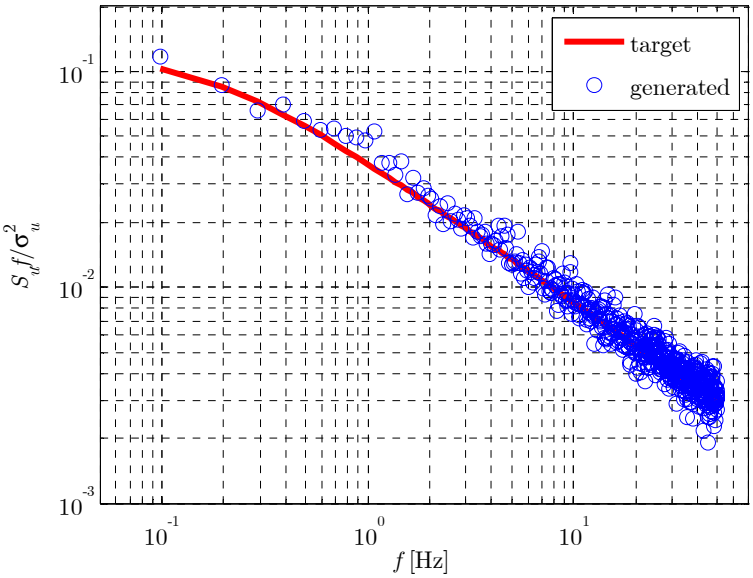

Figure 4.7 Example of target and generated turbulent spectrum

4.5 Nonlinear static analysis under steady wind

Let us first consider the case in which the wind loading is static, i.e. the mean quasi-steady forces are applied. The balance equation of the discrete model at a given mean wind velocity is given by

$$\mathbf{F}_K(\mathbf{d}) = \mathbf{P}_{dead} + \mathbf{P}_s(\mathbf{d}) \tag{4.4}$$

where $\mathbf{F}_K$ is the vector of the internal structural forces, $\mathbf{d}$ the vector of the nodal degrees of freedom of the finite element model, $\mathbf{P}_{dead}$ the load vector of dead loads, and $\mathbf{P}_s$ the vector of the aerodynamic steady loads obtained by assembling the load in Eq (3.1), i.e. $\mathbf{P}_s^{(e)}\left(\mathbf{d}^{(e)}\right) = \ell^{(e)}\left[F_x^s\left(\alpha_y^{(e)}\right), F_z^s\left(\alpha_y^{(e)}\right), M_y^s\left(\alpha_y^{(e)}\right)\right]^T$, where $\ell^{(e)}$ is the influence length assigned to the e-th one-node 'element' representing a finite length strip of bridge deck, and $\mathbf{d}^{(e)} = \left[x^{(e)}, z^{(e)}, \alpha_y^{(e)}\right]^T$ the relevant node displacements.

The static analysis includes structural and aerodynamic nonlinearities and is performed by means of an incremental-iterative procedure, where the mean wind velocity is incremented stepwise, and the equilibrium is found at each step by solving Eq (4.4) through a Newton-Raphson technique: the displacement vector $\overline{\mathbf{d}}$ in the steady configuration is then obtained.

4.6 Stability analysis: divergence

The stability analysis with respect to divergence can be performed during the static analysis under steady wind by checking at each incremental step of the mean wind velocity the eigenvalues of the total tangent stiffness matrix $\mathbf{K}_{\text{tot}} = \mathbf{K} + \mathbf{K}_{\text{a,s}}$, where $\mathbf{K} = \partial \mathbf{F}_K / \partial \mathbf{d}$ is the tangent stiffness matrix of the structure and $\mathbf{K}_{\text{a,s}} = \partial \mathbf{P}_{\text{s}} / \partial \mathbf{d}$ is the stiffness contribution due to the steady aerodynamic forces. As soon as the matrix $\mathbf{K}_{\text{tot}}$ is no more positive defined the critical wind velocity for divergence is reached.

4.7 Modal analysis around the deformed configuration

Modal analysis around the equilibrium configuration is performed by solving the standard eigenproblem

$$\left(\mathbf{M} - \overline{\omega}_m^2 \overline{\mathbf{K}}\right) \overline{\mathbf{\Phi}}_m = \mathbf{0} \tag{4.5}$$

where $\mathbf{M}$ is the mass matrix, $\overline{\omega}_m$ and $\overline{\mathbf{\Phi}}_m$ are the circular frequency and the shape of the m-th eigenmode respectively, and the overdash denotes

that a quantity is evaluated at the steady configuration $\mathbf{d} = \overline{\mathbf{d}}$ [1]. From now on, mode shapes are considered as mass-normalized.

4.8 Time-domain simulations

Let us now consider the dynamic settings. The discretized equation of motion reads

$$\mathbf{M}\ddot{\mathbf{d}} + \mathbf{C}\dot{\mathbf{d}} + \mathbf{F}_K(\mathbf{d}) = \mathbf{P}_{dead} + \mathbf{P}_{wind}, \tag{4.6}$$

where $\mathbf{d}$ is the vector of nodal degrees of freedom, $\mathbf{M}$ the mass matrix (we use a lumped-mass approach, otherwise also inertia forces would be nonlinear in the co-rotational formulation), $\mathbf{C}$ the linear damping matrix, $\mathbf{F}_K$ the vector of the internal structural forces, and $\mathbf{P}_{dead}$ and $\mathbf{P}_{wind}$ are the dead and wind loads respectively.

For the dynamic analyses we consider a model linearized around the mean steady configuration $\overline{\mathbf{d}}$, which is evaluated through nonlinear static calculations for each given value of the mean wind velocity U by solving the algebraic system $\mathbf{F}_K\left(\overline{\mathbf{d}}\right) = \mathbf{P}_{dead} + \mathbf{P}_s\left(\overline{\mathbf{d}}, U\right)$, where the vector $\mathbf{P}_s$ assembles the wind steady forces. The linearized equation of motion is

$$\mathbf{M}\ddot{\mathrm{d}} + \mathbf{C}\dot{\mathrm{d}} + \overline{\mathbf{K}}\mathrm{d} = \overline{\mathbf{P}}_a + \overline{\mathbf{P}}_b, \tag{4.7}$$

where $\delta = \mathbf{d} - \overline{\mathbf{d}}$ is the vector of the displacements around the mean steady configuration, $\overline{\mathbf{K}} = \left[\partial \mathbf{F}_K / \partial \mathbf{d}\right]_{\mathbf{d}=\overline{\mathbf{d}}}$ the tangent structural stiffness matrix, and $\overline{\mathbf{P}}_a$ and $\overline{\mathbf{P}}_b$ are the vectors assembling the self-excited aeroelastic forces and the buffeting forces respectively, all evaluated in the mean steady configuration.

In the case of the load model based on aeroelastic derivatives, the vector of the aeroelastic load is

$$\mathbf{P}_a^{AD} = -\mathbf{K}_a^{AD}(U,\omega)\,\mathrm{d} - \mathbf{C}_a^{AD}(U,\omega)\,\dot{\mathrm{d}}, \tag{4.8}$$

where the matrixes $\mathbf{K}_a^{AD}$ and $\mathbf{C}_a^{AD}$ assemble the contributions of each modelled cross section, i.e.

[1] In general, also inertia forces have nonlinear expressions in a co-rotational approach to finite elements. In this case, however, the masses have been lumped into the nodes in order to consider linear inertia forces. Therefore, $\mathbf{M}$ does not depend on the configuration and the overdash is not required in the notation.

$$\mathbf{k}_a^{AD} = -qB\ell\,\frac{1}{B}\begin{bmatrix} -K^2E_{F_x\dot{x}} & -K^2E_{F_x\dot{z}} & D_{F_x\alpha_y}B \\ -K^2E_{F_z\dot{x}} & -K^2E_{F_z\dot{z}} & D_{F_z\alpha_y}B \\ -K^2E_{M_y\dot{x}}B & -K^2E_{M_y\dot{z}}B & D_{M_y\alpha_y}B^2 \end{bmatrix},$$
$$\mathbf{c}_a^{AD} = -qB\ell\,\frac{1}{U}\begin{bmatrix} D_{F_x\dot{x}} & D_{F_x\dot{z}} & E_{F_x\alpha_y}B \\ D_{F_z\dot{x}} & D_{F_z\dot{z}} & E_{F_z\alpha_y}B \\ D_{M_y\dot{x}}B & D_{M_y\dot{z}}B & E_{M_y\alpha_y}B^2 \end{bmatrix}, \tag{4.9}$$

respectively.

Below we also consider the quasi-steady case.

If the structural behaviour is linearized around $\overline{\mathbf{d}}$ and the load nonlinearities are kept, equation (4.6) becomes

$$\mathbf{M}\ddot{\mathbf{d}} + \mathbf{C}\dot{\mathbf{d}} + \overline{\mathbf{K}}\left(\mathbf{d}-\overline{\mathbf{d}}\right) + \overline{\mathbf{F}}_K = \mathbf{P}_{dead} + \mathbf{P}_{q,nl}\left(\mathbf{d},\dot{\mathbf{d}},t\right) \tag{4.10}$$

If also the load is linearized, one has

$$\mathbf{M}\ddot{\mathbf{d}} + \mathbf{C}\dot{\mathbf{d}} + \overline{\mathbf{K}}\left(\mathbf{d}-\overline{\mathbf{d}}\right) + \overline{\mathbf{F}}_K = \mathbf{P}_{dead} + \overline{\mathbf{P}}_{q,l}\left(\mathbf{d}-\overline{\mathbf{d}},\dot{\mathbf{d}},t\right), \tag{4.11}$$

where

$$\overline{\mathbf{P}}_{q,l}\left(\delta,\dot{\delta},t\right) = \overline{\mathbf{P}}_s + \overline{\mathbf{P}}_b\left(t\right) - \overline{\mathbf{K}}_a\delta - \overline{\mathbf{C}}_a\dot{\delta} \tag{4.12}$$

is the vector of linearized quasi-steady forces obtained by assembling equations (8), $\delta = \mathbf{d}-\overline{\mathbf{d}}$ is the vector of the (small) displacements around the steady configuration, $\overline{\mathbf{P}}_b$ results from the assembly of equations (3.11) with $\overline{\mathbf{P}}_b^{(e)} = \ell^{(e)}\left[\overline{F}_x^{bq(e)}, \overline{F}_z^{bq(e)}, \overline{M}_y^{bq(e)}\right]^T$, $\overline{\mathbf{K}}_a$ and $\overline{\mathbf{C}}_a$ are the matrixes collecting the opposites of the coefficients multiplying displacements and velocities respectively in equations (3.13), i.e.

$$\mathbf{k}_a^{QS} = -qB\ell\,\frac{1}{B}\begin{bmatrix} -K^2e_{F_x\dot{x}} & -K^2e_{F_x\dot{z}} & d_{F_x\alpha_y}B \\ -K^2e_{F_z\dot{x}} & -K^2e_{F_z\dot{z}} & d_{F_z\alpha_y}B \\ -K^2e_{M_y\dot{x}}B & -K^2e_{M_y\dot{z}}B & d_{M_y\alpha_y}B^2 \end{bmatrix},$$
$$\mathbf{c}_a^{QS} = -qB\ell\,\frac{1}{U}\begin{bmatrix} d_{F_x\dot{x}} & d_{F_x\dot{z}} & e_{F_x\alpha_y}B \\ d_{F_z\dot{x}} & d_{F_z\dot{z}} & e_{F_z\alpha_y}B \\ d_{M_y\dot{x}}B & d_{M_y\dot{z}}B & e_{M_y\alpha_y}B^2 \end{bmatrix}, \tag{4.13}$$

Finally, one obtains

$$\mathbf{M}\ddot{\delta} + \left(\mathbf{C} + \bar{\mathbf{C}}_a\right)\dot{\delta} + \left(\bar{\mathbf{K}} + \bar{\mathbf{K}}_a\right)\delta = \bar{\mathbf{P}}_b(t). \tag{4.14}$$

The solution in the time domain is obtained here by means of conditionally stable Newmark method or by Runge-Kutta methods by reducing the system to a first-order one as shown in Section 3.4. If structural or load nonlinearities are considered, standard Newton-Raphson iterations are performed at each time-step.

In the time domain the unsteady linearized problem reads

$$\bar{\mathbf{M}}\ddot{\mathrm{d}} + \bar{\mathbf{C}}\dot{\mathrm{d}} + \bar{\mathbf{K}}\mathrm{d} = \mathbf{P}_a^{IF} + \mathbf{P}_b^{IF} = -\mathbf{K}_a^{IF}\mathrm{d} - \mathbf{C}_a^{IF}\dot{\mathrm{d}} + \mathbf{P}_{a,conv}^{IF} + \mathbf{P}_{b,conv}^{IF}, \tag{4.15}$$

where the vector $\mathbf{P}_a^{IF}$ is obtained from the indicial function load model in Eqs (3.50). The matrixes $\mathbf{K}_a^{IF}$ and $\mathbf{C}_a^{IF}$ and the vector $\mathbf{P}_{conv}^{IF}$ assemble the contributions from each modelled cross-section, i.e.

$$\begin{aligned}
\mathbf{k}_a^{IF} &= -qB\ell \begin{bmatrix} 0 & 0 & d_{F_x\alpha_y}\Phi_{F_x\alpha_y}(0) \\ 0 & 0 & d_{F_z\alpha_y}\Phi_{F_z\alpha_y}(0) \\ 0 & 0 & d_{M_y\alpha_y}\Phi_{M_y\alpha_y}(0)\,B \end{bmatrix}, \\
\mathbf{c}_a^{IF} &= -qB\ell/U \begin{bmatrix} d_{F_x\dot{x}}\Phi_{F_x\dot{x}}(0) & d_{F_x\dot{z}}\Phi_{F_x\dot{z}}(0) & 0 \\ d_{F_z\dot{x}}\Phi_{F_z\dot{x}}(0) & d_{F_z\dot{z}}\Phi_{F_z\dot{z}}(0) & 0 \\ d_{M_y\dot{x}}\Phi_{M_y\dot{x}}(0)\,B & d_{M_y\dot{z}}\Phi_{M_y\dot{z}}(0)\,B & 0 \end{bmatrix}, \\
\mathbf{p}_{conv}^{IF} &= qB\ell \sum_{r=\dot{x}/U,\dot{z}/U,\alpha_y} \int_0^t \begin{bmatrix} d_{F_xr}\dot{\Phi}_{F_xr}(t-\tau)\,r(\tau) \\ d_{F_zr}\dot{\Phi}_{F_zr}(t-\tau)\,r(\tau) \\ d_{M_yr}\dot{\Phi}_{M_yr}(t-\tau)\,r(\tau)\,B \end{bmatrix} d\tau,
\end{aligned} \tag{4.16}$$

respectively.

The time integration of Eq (4.15) is performed by means of Newmark's scheme with the trapezoidal rule, whereas the convolution integrals are evaluated through the left rectangular rule. The trapezoidal rule is unconditionally stable for linear problems but it may induce spurious oscillations in the solution Bathe and Baig, 2005; Kuhl and Crisfield, 1999. However, this usually occurs when a transient component changes 'quickly' with respect to the time-step size, which is not the case of the present analysis. When typical bridge characteristics are used, the choice of the time-step size is dictated by the evaluation of the convolution integrals, so that no particular problem arises in the integration of the equations of

motion. The computational efficiency can be improved by using a smaller time-step for the evaluation of the convolution integrals and a larger one for the integration of the equations of motion; in this case an interpolation scheme must be provided from the coarser to the finer time-discretization. Other computational aspects are discussed in Borri, Salvatori et al., 2005.

The formulation described by Eq (4.16) has some similarities with the one obtained through the rational function approach; a discussion on this method is available in Lazzari, 2005, where a comparison with the quasi-steady approach is presented in the case of a two-degree-of-freedom system.

Below, an applicative example of a full bridge is offered. For expository reasons, the results in frequency- and time-domain will be presented in reverse order with respect to the one of the theoretical descriptions in this Section.

4.8.1 Computational efficiency of the indicial-function approach

Time-domain aeroelastic simulations of bridges through indicial functions might be expensive in terms of computational resources, since:

- The time-step used in the simulations must be kept small to avoid numerical damping and to accurately evaluate the convolution integrals of Eq (3.50);
- Iterations must be performed at each time-step, in order to take into account the structural nonlinearity, if necessary;
- Several simulations at different mean wind velocity must be carried out, both for determining aeroelastic stability threshold and for evaluating buffeting response;
- Simulations must be long enough in order to accurately observe the critical condition, or to perform Monte Carlo simulations for buffeting effects;
- At each time-step the convolution integrals become longer and longer; the time to compute the loads increases therefore as the square of time-steps.

For systematic studies as well as in the preliminary design phase of a bridge, strategies to save computing time would be very useful. One approach, discussed in Borri, Salvatori et al., 2005, and Salvatori and Spinelli, 2006b, is to reduce the complexity of the FE structural model and therefore the number of cross-sections where the convolution integrals must be evaluated.

Here, computational strategies dealing with finite aeroelastic memory are discussed. In Eq (3.50), time-derivatives of indicial functions $\dot{\bar{\Phi}}_{Rr}$ appear. These vanish for time that goes to infinity. In particular, for a T_{mem} 'sufficiently large', the following implications hold:

$$t > T_{\text{mem}} \quad \Rightarrow \quad \frac{\left|\dot{\bar{\Phi}}_{Rr}(t)\right|}{\max_{\tau \geq 0}\left|\dot{\bar{\Phi}}_{Rr}(\tau)\right|} \ll 1$$
$$\Rightarrow \quad \int_0^t \dot{\bar{\Phi}}_{Rr}(t-\tau) r(\tau) d\tau \simeq \int_{t-T_{\text{mem}}}^t \dot{\bar{\Phi}}_{Rr}(t-\tau) r(\tau) d\tau \tag{4.17}$$

Thus, Eq (3.50) can be rewritten as

$$\boxed{\bar{R}^{ai}(t) = q_0 B^{\gamma_R} \sum_{r=\dot{x}/U,\dot{z}/U,\alpha_y} \bar{d}_{Rr} \left[\bar{\Phi}_{Rr}(0)\, r(t) + \int_{t-T_{mem}}^t \dot{\bar{\Phi}}_{Rr}(t-\tau) r(\tau)\, d\tau\right]; \quad R = F_x, F_z, M_y} \tag{4.18}$$

A finite memory approach with an incremental formulation was proposed in Borri et al., 2002, but no investigation of the computing time involved was performed and the choice of the length of the memory was made in a safe but arbitrary way. Here the question of the memory length is systematically investigated, weighting computational performance and accuracy. Thanks to the expressions of the load adopted here (Eq (3.50)), an optimized non-incremental model with fading aeroelastic-memory is developed and implemented, and a criterion to evaluate the optimal size of the memory is proposed. An abrupt reduction in the computing time is observed when passing to the finite memory model. Buffeting Monte Carlo simulations greatly profit of the computational efficiency of the proposed procedure.

In order to find a general criterion for the choice of the memory length T_{mem} suitable for a given set of indicial functions, the scalar index

$$\psi\left(T_{\text{mem}}\right) = \max_{\substack{R=F_x,F_z,M_y \\ r=\dot{x}/U,\dot{z}/U,\alpha_y}} \left(\frac{\left|\dot{\bar{\Phi}}_{Rr}\left(T_{\text{mem}}\right)\right|}{\max_{\tau \geq 0}\left|\dot{\bar{\Phi}}_{Rr}(\tau)\right|} \right) \tag{4.19}$$

is proposed, which accounts for the relative size of the neglected tail of the indicial function that converges 'more slowly'.

4.8.2 Numerical solution of the integral-differential problem

Time-step size influences both the time-integration of the equations of motion and the evaluation of the convolution integrals of the self-excited loads. Different time-integration algorithms of different convergence order, as well as different algorithms for the evaluation of the convolution integrals are compared and a criterion for the optimal choice of the time-

step, providing computational performances and satisfying accuracy, is proposed.

The integration in the time-domain is obtained through Newmark's scheme. Constant average-acceleration is chosen in order to guarantee unconditional numerical stability. This is particularly important when self-excited forces are considered. They are in fact responsible for instability phenomena that must be clearly distinguishable from spurious numerical artefacts. If nonlinearities are accounted for, the solution at each time-step is obtained by means of the Newton-Raphson approach. For the linear case, Runge-Kutta integration methods have also been considered; although they provide higher order convergence, the additional computational effort is worthless, as the time-step must be kept small in any case in order to provide adequate precision for the integration of the convolution integrals of the load (see Section 3).

The convolution integrals are computed by means of the left rectangular rule:

$$\int_0^t \dot{\Phi}_{Rr}(t-\tau)\, r(\tau)\, d\tau \simeq \Delta t \sum_{h=0}^{n-1} \dot{\Phi}_{Rr}\big((n-h)\Delta t\big)\, r\big(h\Delta t\big) \tag{4.20}$$

where n is the step number, and Δt = time-step size ($t = n\Delta t$). With this kind of numerical integration the result of the integral is independent on the current (unknown) state $r\big(n\Delta t\big)$. An alternative for increasing the accuracy of the integration over the steepest initial part of the indicial functions could be the choice of the trapezoidal integration rule or of Simpson's rule. The summation would include the current step.

4.9 Stability analysis: bifurcation in frequency domain

The aeroelastic stability of the system is studied, as usual, by considering the homogenous solution of the linearized system, i.e. equation (4.14).

Let $\bar{\mathbf{\Phi}} = \left[\bar{\mathbf{\Phi}}_{m_1}, \bar{\mathbf{\Phi}}_{m_2}, \ldots, \bar{\mathbf{\Phi}}_{m_N}\right]$ be the matrix whose columns are N selected mass-normalized modal shapes. Considering $\boldsymbol{\delta} \simeq \bar{\mathbf{\Phi}}\boldsymbol{\xi}$ (exactly equal if all structural modes are taken into account), the system is projected onto a reduced modal space, that is

$$\ddot{\boldsymbol{\xi}} + \bar{\mathbf{\Phi}}^T\left(\mathbf{C} + \bar{\mathbf{C}}_a\right)\bar{\mathbf{\Phi}}\dot{\boldsymbol{\xi}} + \bar{\mathbf{\Phi}}^T\left(\bar{\mathbf{K}} + \bar{\mathbf{K}}_a\right)\bar{\mathbf{\Phi}}\boldsymbol{\xi} = \bar{\mathbf{\Phi}}^T\bar{\mathbf{P}}_b(t), \tag{4.21}$$

and the homogeneous solution is in form

$$\boldsymbol{\xi}(t) = \hat{\boldsymbol{\xi}} e^{\lambda t}, \tag{4.22}$$

where $\hat{\boldsymbol{\xi}}$ is a constant vector. By introducing $\boldsymbol{\eta} = \dot{\boldsymbol{\xi}}$, the homogeneous system ($\overline{\mathbf{P}}_b = \mathbf{0}$) is represented in the state space and reduced to a first order system of differential equations, namely

$$\boldsymbol{\psi} = \overline{\mathbf{A}}\dot{\boldsymbol{\psi}} + \overline{\mathbf{b}}, \tag{4.23}$$

where $\boldsymbol{\psi} = \begin{bmatrix} \boldsymbol{\eta}^T & \boldsymbol{\xi}^T \end{bmatrix}^T$ and

$$\overline{\mathbf{A}} = \begin{bmatrix} -\overline{\boldsymbol{\Phi}}^T \left(\mathbf{C} + \overline{\mathbf{C}}_a\right) \overline{\boldsymbol{\Phi}} & -\overline{\boldsymbol{\Phi}}^T \left(\overline{\mathbf{K}} + \overline{\mathbf{K}}_a\right) \overline{\boldsymbol{\Phi}} \\ \mathbf{I} & \mathbf{0} \end{bmatrix}, \quad \overline{\mathbf{b}} = \begin{bmatrix} \overline{\boldsymbol{\Phi}}^T \overline{\mathbf{P}}_b(t) \\ \mathbf{0} \end{bmatrix}. \tag{4.24}$$

The solution of Eq is in the form $\boldsymbol{\xi}(t) = \hat{\boldsymbol{\xi}} \exp(\lambda t)$, where $\hat{\boldsymbol{\xi}}$ is a constant vector. Hence, we obtain the nonlinear complex eigenproblem

$$\left(\mathbf{A}(U, \omega) - \lambda_n \mathbf{I}\right) \hat{\boldsymbol{\psi}}_n = \mathbf{0} \tag{4.25}$$

where $\hat{\boldsymbol{\psi}}_n = \begin{bmatrix} \hat{\boldsymbol{\eta}}_n^T & \hat{\boldsymbol{\xi}}_n^T \end{bmatrix}^T = \begin{bmatrix} \lambda \hat{\boldsymbol{\xi}}_n^T & \hat{\boldsymbol{\xi}}_n^T \end{bmatrix}^T$. Consequently, the stability of the system is evaluated through the spectral analysis of $\overline{\mathbf{A}}$. Each couple of conjugated eigenvalues can be written as $\lambda_n = -\nu_n \omega_n \pm i\omega_n \sqrt{1 - \nu_n^2}$, where $\omega_n = \|\lambda_n\|$ is the circular frequency, $\nu_n = -\operatorname{Re}(\lambda_n) / \omega_n$ the damping ratio (including both structural and aerodynamic damping), and i the imaginary unit. Since the matrix $\overline{\mathbf{A}}$ depends on the frequency, the problem is nonlinear and each eigenvalue must be computed iteratively. Here we focus on the stability analysis, therefore, we are only interested in the lowest-damping mode, which is potentially responsible for instability. More in general, it is possible to repeat the nonlinear calculation for each mode; in this way the structural modes that were coupled by aeroelastic effects can again be uncoupled. This allows frequency-domain buffeting analyses.

The flowchart of the stability analysis is schematized in Figure 4.8. We start with zero mean wind velocity and an assumption on the frequency of the critical mode. Then U is increased step by step. At each step a nonlinear static analysis is performed in order to obtain the mean steady configuration; the angles of attack along the bridge span and the structural modes are evaluated. The matrix $\overline{\mathbf{A}}$ is assembled and its spectral analysis performed. Then the lowest-damping eigenvalue is selected. The relevant frequency is in general different from the trial one, therefore the calculation is repeated by updating the frequency at each iteration until convergence. The real part of the converged eigenvalue decides the stability of the system; if a positive damping is obtained, U is incremented and the old frequency is used as initial assumption for the next iterative loop. The analysis ends as soon as non-positive damping is obtained.

Each component of the critical eigenvector $\hat{\boldsymbol{\xi}}_{cr}$ can be interpreted as the contribution (in absolute value and phase angle) of the relevant structural

mode to the critical one. Finally, $\bar{\boldsymbol{\Phi}}\hat{\boldsymbol{\xi}}_{cr}$ is the complex critical mode shape in the coordinates of the finite element model.

Take note that the stability analysis could be performed directly in the state space of the finite-element degrees of freedom rather than by introducing a modal subspace. However there would be some computational disadvantages, and the comparison with the classical bi-modal approach (e.g. Dyrbye and Hansen, 1996) would not be possible.

In Jain et al., 1996a, a multi-modal flutter analysis is presented as an extension of the classical bi-modal analysis. The critical undamped harmonic solution is imposed into the discretized equations of motion. In order to allow non-trivial solutions, the matrix describing the system must be singular. The condition of vanishing (complex) determinant is found numerically by simultaneously varying the mean wind velocity and the frequency. One disadvantage of this procedure is that the determinant has no direct physical interpretation. On the other hand, by performing the eigenvalue analysis, as done here, one can follow the evolution of the frequency and damping of each mode at increasing wind velocity; in this way the parallelism with wind tunnel experimental tests, where the flow velocity is always controlled, is more evident.

This framework for multimodal analysis in the $2N$-dimensional state space can be extended to unsteady calculations (e.g. Jain et al., 1998) by introducing frequency dependent aeroelastic derivatives into the expressions of $\bar{\mathbf{C}}_a$ and $\bar{\mathbf{K}}_a$. This way, for each incremental velocity-step, additional iterations on the frequency must be performed. Nevertheless, the framework presented here is not followed for usual unsteady analyses, as aeroelastic derivatives with sufficiently fine dependence on the angle of attack are seldom available.

A similar nonlinear eigenvalue problem in the state-space is obtained in Chen et al., 2001 and Chen et al., 2000a, where a rational function approximation of aeroelastic derivatives is used for the frequency domain multi-modal analysis in order to obtain a frequency independent description.

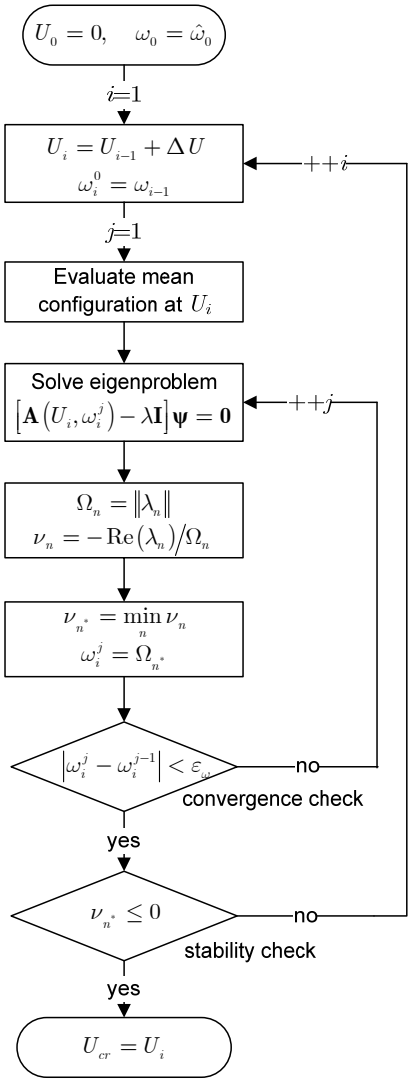

Figure 4.8 Flowchart of the stability analysis in the frequency-domain

A comparison of different frequency domain approaches considering two, more than two, or all the structural modes is followed in Ge and Tanaka, 2000, where it is pointed out that for long span bridges more than two modes can be involved into the flutter instability.

A multi-mode complex analysis including coupled buffeting response is also developed by Minh et al., 2000. An evaluation of the importance of the coupling aeroelastic effects on buffeting simulations is available in Chen et al., 2004.

The proposed method is completely general and covers all instability phenomena driven by unsteady self-excited forces. From the mathematical point of view, in fact, galloping, torsional flutter and coupled flutter are Hopf bifurcations and can be studied by means of the same procedure. A

posteriori, it is possible to 'label' the instability phenomenon by observing the modal contributions to the critical mode. If the vertical or the torsional modes prevail, one will have galloping or torsional flutter respectively, whereas if both vertical and torsional contributions are important, the phenomenon will be called coupled flutter.

Chapter 5

Computational Results

In this Chapter some computational results obtained through the implementation of the developed computational framework are presented. First of all, the proposed load model based on indicial functions is validated by means of a full-bridge analysis in which time-domain simulation results are compared with multi-modal frequency-domain ones. Then, the reliability of the indicial function approach is discussed. Furthermore, by means of a simplified structural model, it is shown how secondary critical modes can be simulated and visualized. Finally, some results that may be helpful in the prediction of structural vulnerability are presented: the effects on flutter and buffeting response of the along-span wind coherence, of the mean steady deformations, and of load and structural nonlinearities are evaluated.

5.1 Validation of the indicial function approach for full-bridge analyses

As a sample structure an ideal suspension bridge, similar to Jaingyin Bridge (Figure 5.1a), with 1400m main span and streamlined deck-aerodynamics is chosen. The main geometrical and mechanical characteristics of the structure are depicted in Figure 5.2 and reported in Table 5.1 (the stiffness properties of the towers are omitted for the sake of brevity); a steel deck is assumed. The main span of the bridge is discretized with 20 elements; the relevant finite element model has 714 degrees of freedom. Rayleigh damping is considered and a damping ratio of 0.5% is assigned to the first vertical and torsional modes. We use the aeroelastic properties of the streamlined bridge cross-section with semicircular fairings and width-to-height ratio $B/D = 14.3$ that has been tested in the wind tunnel by Chowdhury and Sarkar, 2004 (where it is referred to as 'cross-section B1').

A two-degree-of-freedom system is available in Zahlten et al., 2004. Three-dimensional results are obtained in Borri and Salvatori, 2006, and further developed in Salvatori and Borri, 2007.

(a) (b)

Figure 5.1 Jaingyin Bridge (a); Bosporus Bridge I (b)

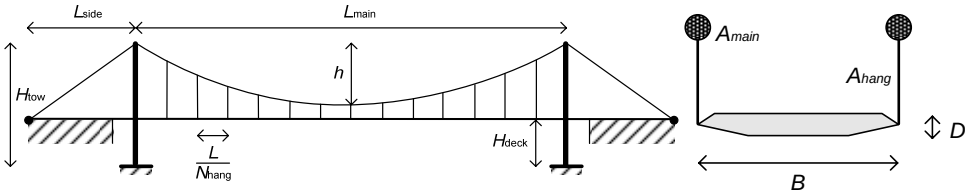

Figure 5.2 Geometry of the bridge

Table 5.1 Main geometrical and mechanical characteristics of the bridges

Description	Symb.	Unit	Jaingyin	Bosporus
main span length	L_{main}	[m]	1400	1074
side span length	L_{side}	[m]	320	231
tower height	H_{tow}	[m]	190	154.5
deck height above ground level	H_{deck}	[m]	60	60
main cable sag	h	[m]	128	91.5
number of hangers in the main span	N_{hang}	[-]	70	50
deck width	B	[m]	35	28
deck height	D	[m]	2.45	3.00
main cable cross-section area	A_{main}	[m^2]	0.5500	0.2045
hanger cross-section area	A_{hang}	[m^2]	0.0090	0.0060
deck mass per unit-span	m_{deck}	[ton/m]	14.0	10.3
deck rotational mass per unit-span	Θ_{deck}	[ton m^2/m]	1400	743
deck cross-section area	A_{deck}	[m^2]	1.40	1.10
deck moment of inertia about X	$J_{\text{y,deck}}$	[m^4]	2.50	1.70
deck moment of inertia about Z	$J_{\text{z,deck}}$	[m^4]	145	111
deck torsional constant	$J_{\text{t,deck}}$	[m^4]	11.00	6.05

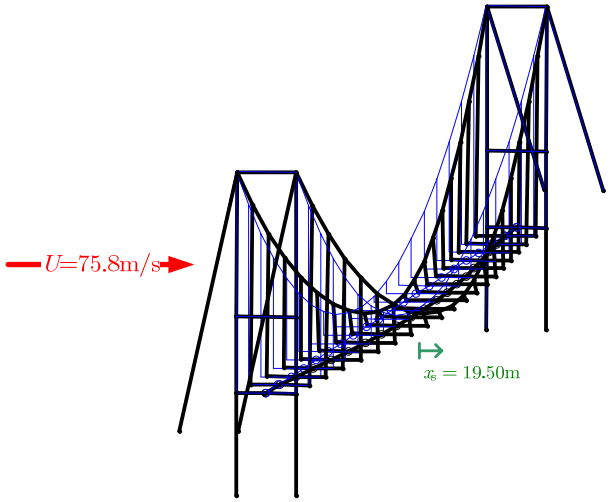

Figure 5.3 Reference configuration (thin blue lines) and mean configuration under critical wind (thick black lines); displacement magnification factor 1.0.

The frequency-domain approach based on aeroelastic derivatives and nonlinear complex eigenvalue analysis is compared with its equivalent time-domain counterpart based on indicial functions and direct integration of the equations of motion. The aeroelastic stability analysis is chosen as benchmark. A numerical example is offered where the equivalency of the two approaches is proved for a full-bridge model. Advantages and disadvantages of the two techniques are discussed.

The most sophisticated methods in the frequency domain are the so-called multi-modal approaches (e.g. Jain et al., 1998), where some selected modes of the structure can contribute to the bridge response and to the flutter critical mode.

An alternative approach is based on indicial functions (e.g. Borri and Höffer, 2000) or analogous time-domain counterparts of the aeroelastic derivatives (e.g. Chen et al., 2000b). Indicial functions can be identified through experimental tests or by means of a numerical procedure that uses experimental aeroelastic derivatives as input parameters.

When the indicial functions are extracted from aeroelastic derivatives, the multi-modal approach and the time-domain simulations are theoretically equivalent. Nevertheless, the numerical identification of indicial functions introduces a degree of approximation. Moreover, time-domain methods in bridge aeroelasticity are sometimes considered with some scepticism, since they require a more complicated numerical manipulation of the experimental data if compared with the well-established frequency-domain methods.

Here, the equivalence of frequency- and time-domain methods is verified through a full-bridge study case.

First, cross-sectional load models for self-excited forces are briefly reviewed and placed into one general framework. A new compact notation which also clarifies some physical aspects is introduced.

Three load models are considered: (i) the quasi-steady model, (ii) the frequency-domain unsteady model based on aeroelastic derivatives, and (iii) a time-domain unsteady model based on indicial functions. The first model is exactly valid only for constant angles of attack, the second one holds for harmonic motions, whereas the third one is completely general. Within the proposed common framework it is easier to compare the load models in those regimes where two or all of them hold true simultaneously. In particular:

- Loads obtained through aeroelastic derivatives (ii) should converge to quasi-steady loads (i) as the oscillation frequency goes to zero, i.e. the angle of attack changes very slowly with respect to the mean flow velocity;
- Indicial loads (iii) must tend asymptotically, as time goes to infinity, to quasi-steady loads (i) when a step-wise change of angle of attack is imposed; in this way a consistent normalization of the indicial functions is achieved;
- Indicial loads (iii) must be equivalent to the loads obtained through aeroelastic derivatives (ii) when a harmonic motion is considered; in this way a method for the identification of the unsteady contribution in the indicial function load model is obtained.

Based on these considerations, a method for the identification of the indicial functions from measured aeroelastic derivatives (and aerodynamic coefficients, if available) is presented. It is based on the approximation of indicial functions as sums of exponential filters and on nonlinear optimization techniques. Further details on the load model, the identification procedure, and the notation are given in Salvatori, 2007.

The stability analysis is then chosen as benchmark for the comparison of the load models.

In the frequency domain a multi-modal stability analysis based on nonlinear eigenproblem solution is developed as a generalization of the procedure presented in Salvatori and Spinelli, 2006a, for quasi-steady loads. In the time domain the analysis consists in the direct integration of the equations of motion and in the evaluation at each time-step of the unsteady load as a function of the history of motion.

A numerical example is offered, where an ideal suspension bridge is considered. The stability analysis is performed by using both frequency- and time-domain methods and the results are compared.

Pros and cons of the presented techniques are discussed, and some perspectives are given.

The main new achievements in the present work are:

- The formulation of an indicial function load model consistent with the quasi-steady limit;
- The identification of indicial functions from aeroelastic derivatives in such a way as to preserve a good approximation of the self-excited loads also at low reduced velocities;
- The development of a unified framework for frequency- and time-domain calculations of full-bridge aeroelasticity;
- The numerical validation of the equivalency of the two approaches for a three-dimensional full bridge model.

5.1.1 Stability analysis in the time domain

At each incremental step, the equations of motion are linearized around the mean steady configuration and the indicial-function load model is considered. A perturbation from the steady configuration is imposed as initial condition. Direct time-integration of equations of motion is performed by using a time-step of 0.001 s. Then the history of motion is analyzed. At sub-critical mean wind velocities the oscillations are damped down (Figure 5.4a), whereas at super-critical mean wind velocities diverging oscillations appear (Figure 5.4c). The borderline condition of stationary oscillations represents the critical stability threshold (Figure 5.4b) and is obtained for a mean wind velocity of 75.7 m/s. The relevant critical frequency of 0.241 Hz is computed through the Fourier analysis of the motion history.

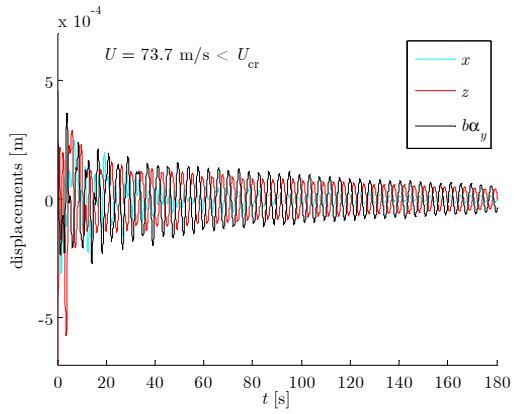

(a)

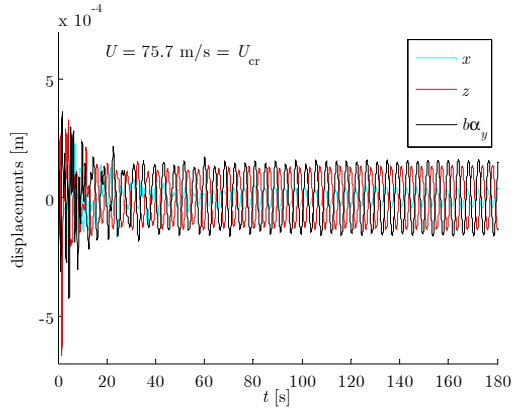

(b)

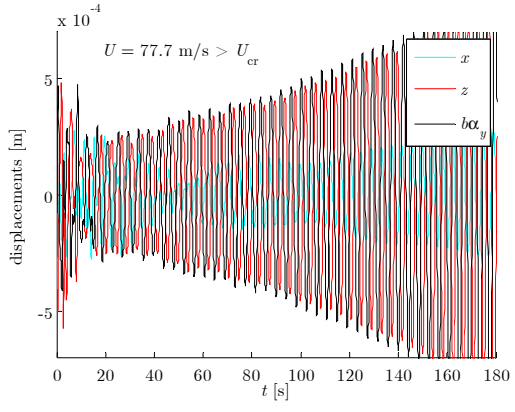

(c)

Figure 5.4 Time-histories of motion at mid-span: pre-critical (a), critical (b), and post-critical (c) regime

5.1.2 Stability analysis in the frequency domain

The stability analysis in the frequency domain is performed according to the procedure described in Section 4.9. Since the present goal is the comparison with the time-domain simulations of the full structure, a high-dimensional modal subspace is adopted by considering the first fifty natural modes of the bridge.

As a first analysis, we evaluate the aeroelastic stiffness and damping by using the approximation of unsteady coefficients given by Eqs (3.53). In this case the analysis is theoretically equivalent to the time-domain one based on identified indicial functions, as confirmed by the numerical results which agree within the computational accuracy. A mode with non-positive damping is firstly obtained at a mean wind velocity of 75.8m/s with a frequency of 0.236 Hz. The natural modes of the structure and their contributions to the critical mode are reported in Table 5.2 and a graphical representation is given in Figure 5.6. The critical mode is a symmetric coupled vertical-torsional flutter (Figure 5.7). Also a small lateral contribution is present; this might not be expected for a streamlined cross-section (consider also that the contribution of $D_{F_x\dot{x}} = KP_1^*$ always provides a positive aerodynamic damping). The lateral contribution is due to mixed structural modes (mainly the vertical-lateral mode #9), which appear as the structure is linearized around the steady configuration under mean wind. The mean configuration, in turn, is affected by the high steady drag which is responsible for large lateral displacements and consequent significant modifications in the tangent structural stiffness. The absolute value of the critical mode shape can also be easily obtained from the time-domain simulations by extracting the maxima from the displacement history. These, appropriately rescaled, are reported in Figure 5.7a, where a very good agreement with the frequency-domain results can be observed.

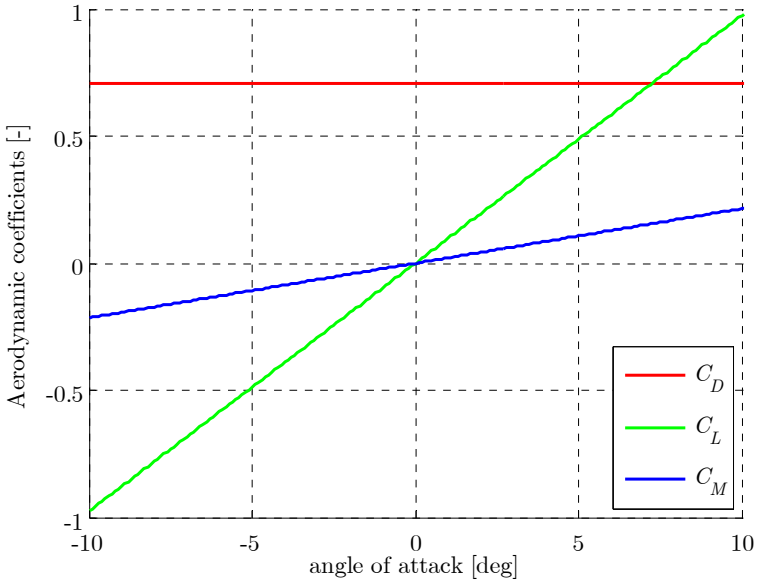

Figure 5.5 Aerodynamic coefficients

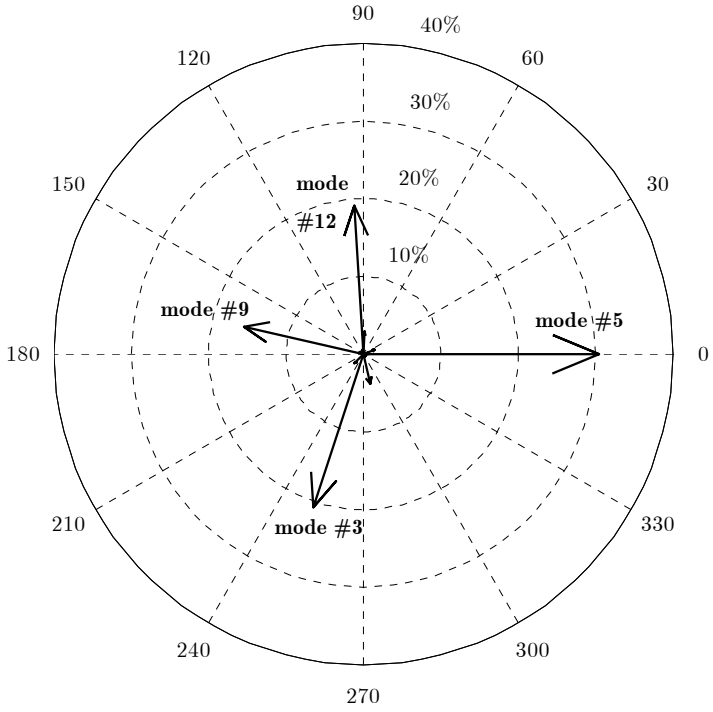

Figure 5.6 Relative contributions in absolute value [%] and phase angle [deg] of the structural modes to the critical mode

Table 5.2 Natural modes of the structure around the mean steady configuration and their contributions to the critical mode

Structural modes at $U = U_{cr} = 75.8$ m/s			Contribution to critical mode	
mode #	f [Hz]	Modal shape(*)	abs [%]	phase [deg]
1	0.081	L1+V1	3.0	-24
2	0.110	V2	0.0	146
3	0.139	V1	20.7	-21
4	0.183	L2	0.0	-172
5	0.191	V3	30.5	0
6	0.200	cables	0.6	140
7	0.204	cables	0.0	7
8	0.213	V4	0.0	-3
9	0.222	L1+V1	15.8	-175
10	0.259	L2+cables	0.0	-165
11	0.276	V5	3.9	-77
12	0.279	T1	19.1	127
13	0.334	V6	0.0	140
14	0.343	T2	0.0	148
15	0.349	L3	1.8	-27
16	0.352	L3+V5+cable	1.6	-56
17	0.357	cables	0.0	-34
18	0.368	cables	0.0	143
19	0.405	V7	0.1	92
20	0.421	L3+V7+cable	0.4	143
21	0.467	V7+cables	0.0	139
22	0.478	T2	0.2	-31
23	0.481	V8	0.0	-24
24	0.487	L3+cables	0.3	-29
25	0.530	cables	0.0	-34
26	0.539	T3	0.5	-67
27	0.553	L3+V9+cable	0.6	-25
28	0.559	V9	0.0	18
29	0.563	cables	0.0	151
30	0.643	cables	0.2	128

(*) Prevalent modal shape (L = lateral, V = vertical, T = torsional) and number of half-waves.

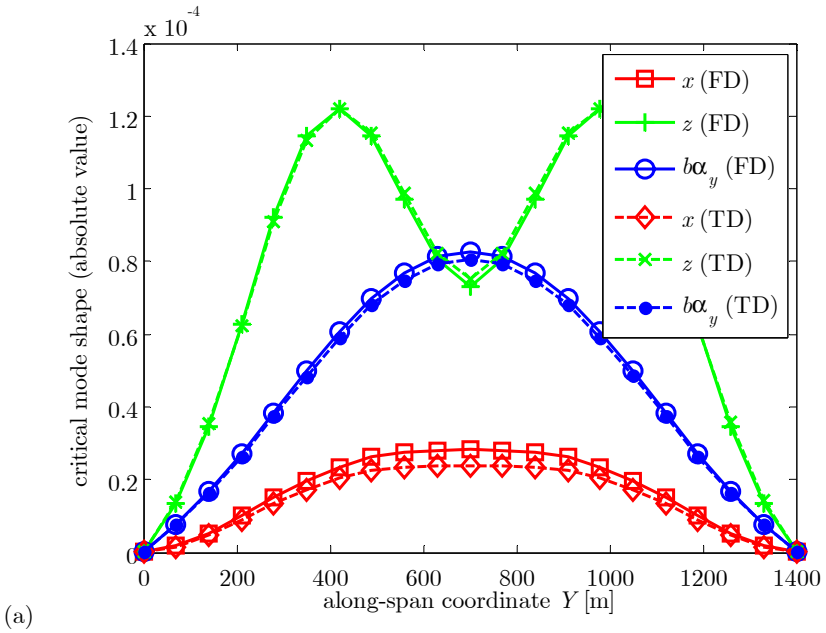

(a)

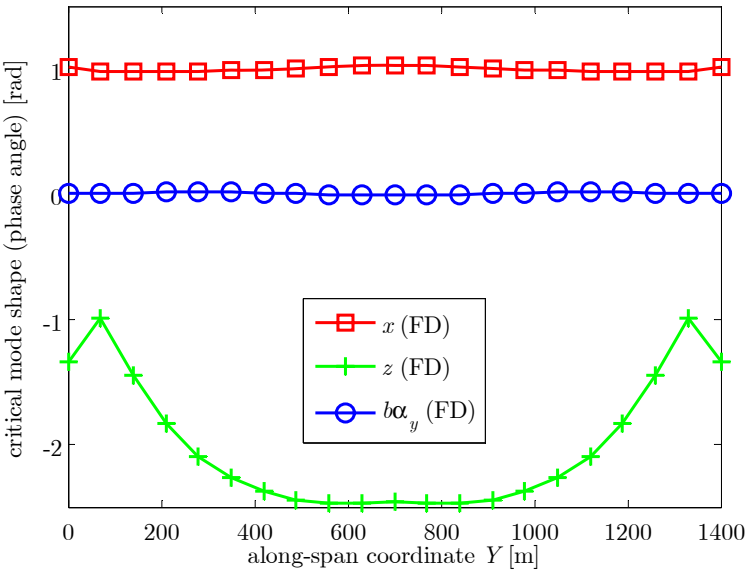

(b)

Figure 5.7 Critical mode shape: absolute value (a) and phase angle (b).

As a further analysis, the frequency-domain calculations are repeated by using linear and spline approximations of the unsteady coefficients. The results are summarized in Figure 5.8. Also the quasi-steady model described in Section 3.2.3 is considered for the comparison. Since quasi-steady coefficients are not frequency-dependent, the calculations can be performed

equivalently in the frequency- and time-domain; in particular the eigenproblem is solved without need for iterations.

The difference between distinct kinds of interpolation of the unsteady coefficients can be quite significant in case of coarse or scattered data. With reference to the cross-section considered here, Figure 5.8 shows the unsteady coefficient $E_{M_y\alpha_y} = KA_2^*$ which may play an important role in the aeroelastic stability. It is possible to observe that, at some reduced velocities, the difference between the two kinds of interpolation has the same magnitude of the difference between interpolations and approximation (even in this case where only one exponential group is used). In the final results, no remarkable differences are observed, since the critical condition is reached at a reduced velocity $U_*^{cr} \simeq 9$, where the interpolations and the approximation of all the significant unsteady coefficients are very close together.

One should not forget that aeroelastic derivatives are not deterministic data but are affected by experimental errors. Therefore the use of the approximation resulting from the identification of the indicial functions might be regarded as a suitable option also for the frequency-domain analysis.

Finally, it is observed that the quasi-steady load model, which is sometimes used where time-domain simulations are necessary (e.g. nonlinear structures), is not able to accurately predict the critical velocity. This remarks the importance of the developed unsteady load model in the time domain.

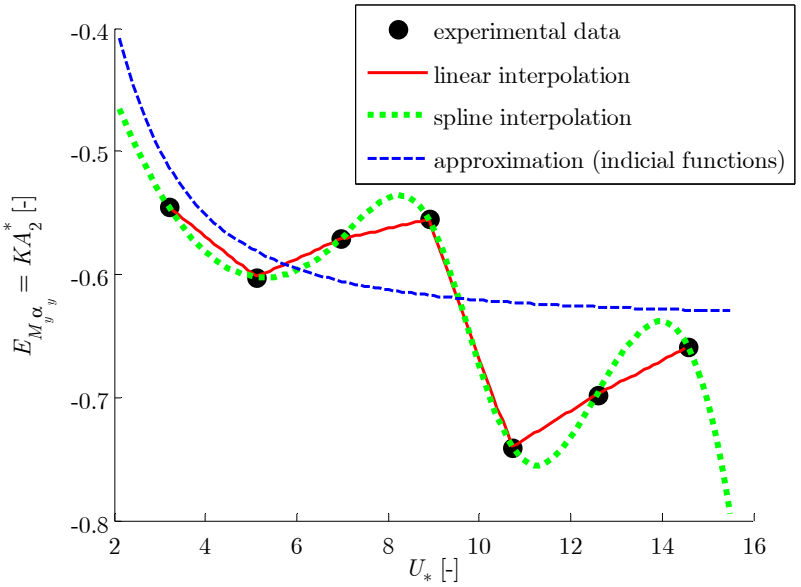

Figure 5.8 Interpolations and approximation of a sample derivative

Table 5.3 Critical conditions for aeroelastic stability bridge A (1400 m + bridge 1)

Analysis type	U_{cr} [m/s]	f_{cr} [Hz]
TD - indicial functions	75.7	0.241
FD - approximation of unsteady coefficients	75.8	0.236
FD - linear interpolation of unsteady	75.9	0.238
FD - spline interpolation of unsteady	75.3	0.239
Quasi-steady approach	66.0	0.245

5.1.3 Remarks

The indicial function load model for unsteady self-excited forces in the time-domain has been further developed by including the consistency with the quasi-steady limit. The indicial functions are identified from measured aeroelastic derivatives in a suitable representation of the data, in such a way that the accuracy of the predicted unsteady forces is preserved also at low reduced velocities.

In order to allow the comparison with frequency-domain results, a multi-modal analysis procedure based on the solution of a nonlinear complex eigenproblem in the state-space has been developed too.

A numerical example has been provided, in which a full three-dimensional model of a sample suspension bridge is considered. The flutter stability analysis has been taken as benchmark for the comparison of the time- and frequency-domain approaches. The analyzed case shows that full-bridge simulations based on identified indicial functions and multi-modal analysis based on aeroelastic derivatives are mathematically and numerically equivalent. In particular, the results are exactly the same (within numerical errors) when the approximation of the aeroelastic derivatives induced by the identification of the indicial functions is used also in the frequency domain. Moreover, when dealing with frequency-domain results, comparable differences may appear between distinct interpolations and between a specific interpolation and the indicial function approximation. On the other hand, the quasi-steady approach provides only qualitative results.

From the computational point of view, the stability analysis in the time domain is much more expensive, also because the time-step size must be kept small in order to accurately evaluate the convolution integrals. On the other hand, accounting for the modal coupling in the buffeting simulations is straightforward in the time-domain, whereas in the frequency domain the analysis is more complicated and requires the evaluation of several nonlinear eigenmodes and the integration over a wide range of frequencies.

We conclude that time-domain methods shall be used for bridge analysis where the frequency-domain approach is more complicated (presence of

localized damping devices, coupled buffeting analysis, etc.) or not applicable (analysis including structural nonlinearities Salvatori and Spinelli, 2006b, nonlinear damping, etc.). Most likely, where the two approaches are equivalent, as in the case of the stability analysis, frequency-domain methods shall be preferred since they rely directly on experimental data and are computationally less expensive. Nevertheless, also in these cases time-domain methods may be used as numerical proof, as the results are obtained through entirely different computations. In general, the two kinds of analysis shall be considered as complementary tools.

5.2 Reliability of the indicial function approach

In this Section a numerical procedure is set up to evaluate the reliability of indicial functions. In principle, analyses in frequency and time domain are equivalent. De facto, each step to identify critical flutter condition is affected by some error that can compromise the reliability of the global procedure. Below, frequency- and time-domain evaluations of critical flutter condition are compared in the case of non-deterministic values of the flutter derivatives and of the indicial functions identified from them; a rough but indicative probabilistic model is used (e.g. Borri, Costa and Salvatori, 2005).

A Monte-Carlo procedure is set up. Sets of aeroelastic derivatives are generated assuming a Gaussian distribution of the measurements. For each set of aeroelastic derivatives, an eigenvalue analysis is performed to identify the critical condition. Critical velocities and frequencies are stored for the statistical analysis.

For each set of generated aeroelastic derivatives, the relevant indicial functions are identified. Critical flutter velocity is then evaluated by means of time domain simulations by adjusting the wind velocity until the critical condition is reached.

The steps above are assembled in a unified automatic procedure in order to obtain statistics in terms of critical frequency and velocity (calculated both directly from the aeroelastic derivatives and from the relevant identified indicial functions). For indicial functions, the distributions of the estimated coefficients are also extracted.

As study case, a streamlined rectangular section with dimensional ratio $B/D = 12.5$ is considered; the relevant aeroelastic derivatives are shown in Figure 5.9. For the evaluation of the critical condition, the mechanical system, whose properties are collected in Table 5.4, is selected.

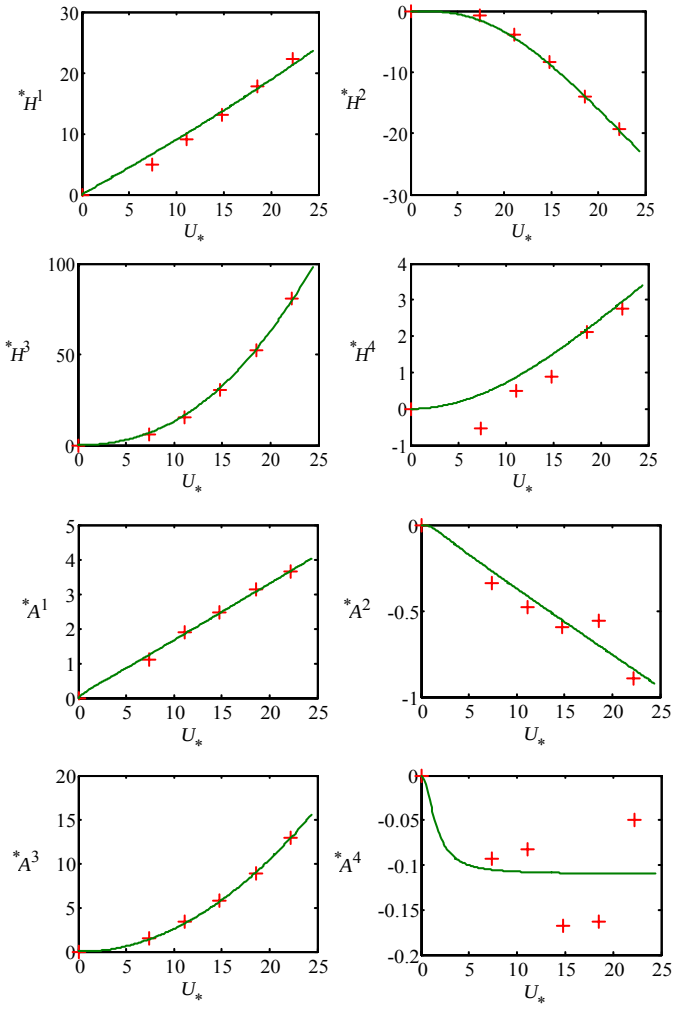

Figure 5.9 Measured aeroelastic derivatives (+) and approximation obtained through the indicial function identification (-)

Table 5.4 Geometrical and mechanical properties of the analysed cross-section

length	$L =$	0.920 m
width	$B =$	0.375 m
height	$D =$	0.03 m
vertical-mode frequency	$f_z =$	5.87 Hz
mass	$m =$	3.810 kg/m
vertical-mode damping ratio	$\nu_z =$	0.0018
torsional-mode frequency	$f_\alpha =$	8.30 Hz
rotational inertia	$I =$	0.037 kg m^2/m
torsional-mode damping ratio	$\nu_\alpha =$	0.0028

Critical velocity U_{cr}^{0} and critical frequency f_{cr}^{0} corresponding to non-scattered measured data are calculated as reference values. The disagreement between the frequency- and the time-domain results are due to the use of the literature indicial function load model as in Section 3.3.2 instead of the one developed in Section 3.5 that, as it has been shown in Section 5.1, eliminate this discrepancy.

For the Monte-Carlo procedure, the standard deviation of the aeroelastic derivatives is taken as 20% of the mean value. In order to obtain some first rough indications, 700 sets of scattered aeroelastic derivatives are generated. In the identification procedure, all the indicial functions are approximated with one exponential group.

The distributions of critical flutter velocities and frequencies are compared for frequency- and time-domain analyses (Figure 5.10), and relevant statistics are quantified in Table 5.5 and Table 5.6.

Table 5.5 Critical velocities obtained from aeroelastic derivatives (AD) and indicial functions (IF)

	U_{cr}^{0} [m/s]	$\mu\,(U_{cr})$ [m/s]	$\sigma\,(U_{cr})$ [m/s]	$y\,(U_{cr})$ [-]	$k\,(U_{cr})$ [-]
AD	18.22	18.35	2.17	-0.96	5.02
IF	15.73	15.06	1.34	0.32	3.59

Table 5.6 Critical frequencies obtained from aeroelastic derivatives (AD) and indicial functions (IF)

	f_{cr}^{0} [Hz]	$\mu\,(f_{cr})$ [Hz]	$\sigma\,(f_{cr})$ [Hz]	$y\,(f_{cr})$ [-]	$k\,(f_{cr})$ [-]
AD	7.02	7.00	0.37	0.71	5.63
IF	7.51	7.56	0.11	-0.33	2.91

This statistical analysis shows that results obtained with time domain simulations are less sensitive to the scatter of data, if compared with those obtained by means of eigenvalue analyses due to the averaging effect of the identification procedure. It is underlined that this is a purely numerical effect.

Statistics on aerodynamic (Figure 5.11) and indicial function coefficients (Figure 5.12) are also obtained. The identified coefficients have broad distributions that result in very different indicial functions, as evidenced in Figure 5.11. On the other hand, the results in the simulations produce narrow banded distributions of critical velocities and critical frequencies.

The bipolar distribution observed in some of the coefficients underlines a certain redundancy in the self-excited model. Analyses on different cross-sections and in the sub-critical wind velocity range should be further addressed.

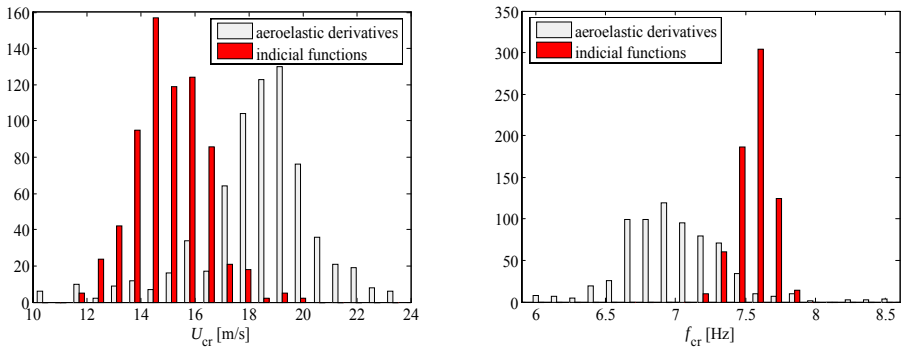

(a) (b)

Figure 5.10 Distributions of critical flutter velocity (a) and frequency (b) calculated via aeroelastic derivatives and indicial functions (vertical axis reports the number of samples)

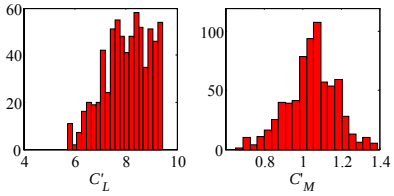

Figure 5.11 Distribution of aerodynamic coefficients of indicial functions (vertical axis reports the number of samples)

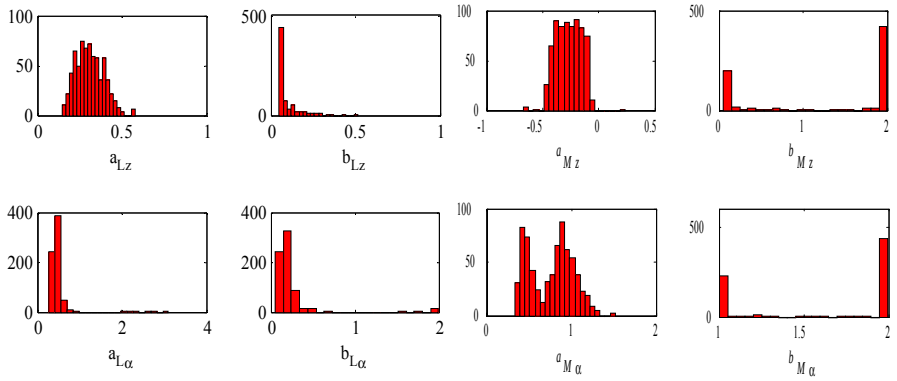

Figure 5.12 Distributions of indicial function coefficients (vertical axis reports the number of samples)

Three main results are observed: (i) the critical wind velocity and the critical frequency based on the non-scattered data almost coincide with the mean values of the distribution obtained, (ii) the variances obtained with indicial functions are much lower than those obtained through aeroelastic derivatives, and (iii) the distribution of critical condition obtained through

indicial functions are narrow-banded, in spite of the broad boundaries of the indicial functions that produced them.

The indicial functions take into account all the reduced frequencies simultaneously; therefore, some scatter is compensated. Since the results based on aeroelastic derivatives are directly based on experimental tests, their reliability can be tentatively assumed in order to express in probabilistic terms the risk of aeroelastic phenomena (Mannini, 2006). On the other hand, indicial functions are a numerical device for using measured aeroelastic derivatives in the time domain. The apparent increase in the reliability of results obtained through indicial functions is only a numerical effect. For this reason, where probabilistic analyses are required, indicial functions shall be used with care.

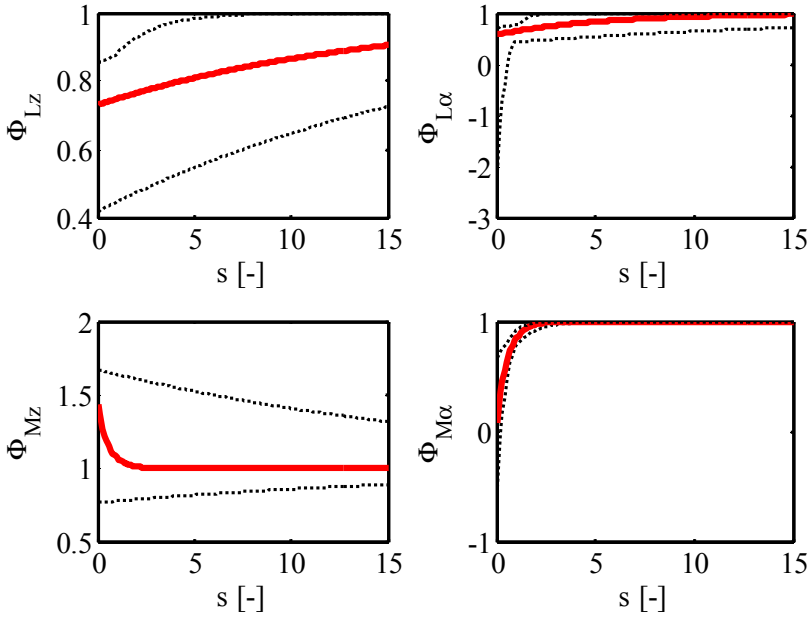

Figure 5.13 Indicial functions for non-scattered data (full lines) and boundaries of the envelopes for scattered data (dashed lines)

5.3 Effects of structural nonlinearity and of along-span turbulence coherence

The response of suspension bridges to wind excitation is studied by means of numerical simulations with a specifically developed finite element program implementing full structural nonlinearities. A pure time-domain load model, linearized around the average configuration, is considered. The self-excited effects are included through the indicial function formulation,

whereas the buffeting is considered according to the quasi-steady model. The response under turbulent wind, both fully and partially correlated, is evaluated through a Monte Carlo approach. A simplified structural model is considered, where only two cross-sections are modelled. This allows a high reduction of the number of degrees of freedom (DoFs) but maintains many characteristics of the true bridge, precluded to the classical 2-DoF sectional-model (e.g. considering more than two modes, including structural nonlinearities, introducing along-span wind coherence). The case studies of a long-span suspension bridge and a light suspension footbridge are analyzed. It is observed that structural nonlinearities deemphasize the presence of a critical flutter wind velocity, as they limit the oscillation amplitudes. On the other hand, fully correlated flow may produce an important underestimation of the structural response.

Due to the theoretical complexity arising for bluff cross-sections with irregular geometry, the predominant design tool in wind engineering is the boundary layer tunnel, where intensive experimental campaigns with scaled-down models are performed. Long bridges present however scaling problems, as they require a very small scale to fit into wind tunnels. For instance, the testing of an Akashi-Kaikyo Bridge 1:100 model has been carried out in an over 40 m wide wind tunnel. As well known, it is impossible for intrinsic scaling problems to reproduce the real flow in the wind tunnel. In particular, the along-span correlation of turbulence can be very tricky to simulate.

For these reasons, the most common approach consists in testing cross-sectional models. These models are commonly used for the aerodynamic characterization of the selected deck through aerodynamic coefficients and aeroelastic derivatives. The extension of cross-sectional results to the entire structure, however, is not straightforward. Frequency-domain multi-modal approach Jain et al., 1996a offers interesting possibilities but does not allow structural nonlinearities to be taken into account. On the other hand, mixed frequency-time domain simulations usually evaluate aeroelastic derivatives at a single frequency that is often obtained through a trial procedure and is valid only at the critical flutter condition (e.g. Zahlten, 2004). A different approach in the mixed domain is proposed in Diana et al., 2005, which divide the spectrum in several 'bands' and, after solving the equations of motion in the time domain for each band, apply the superposition effects. This method is confined however to linear structures too.

The suspension cables have a strong geometrical stiffness only for uniform loads and offer different stiffness characteristics for symmetric and non-symmetric load patterns. Moreover, structural nonlinearities are important for cable-structures as suspension bridges, and the hangers themselves could exhibit nonlinear behaviour, as they are unable to sustain compressions (e.g. Augusti et al., 2002).

In order to take into account the effects of structural nonlinearities, full time-domain simulations must be performed (e.g. Chen and Kareem, 2001; Ding and Lee, 1999), that could be done through indicial function model (e.g. Borri et al., 2002).

Time-domain simulations also offer other advantages. The overall structural behaviour is automatically taken into account, avoiding modal decomposition. Furthermore, the combination of self-excited and buffeting forces is straightforward and the along-span wind coherence can be easily considered (e.g. Iannuzzi and Spinelli, 1986).

The present work will investigate the effects of structural nonlinearities and along-span coherence through time-domain simulations. The questions are, on one hand, how structural nonlinearities affect the response in the vicinity of the flutter velocity, and, on the other hand, whether the along-span coherence influences in a positive or a negative manner the behaviour of suspension bridges.

As the adopted indicial function load model introduces an explicit dependence of the load on the displacement history, it is not possible to use standard structural analysis programs. An 'ad hoc' developed finite element (FE) implementation is then provided.

5.3.1 Mechanical models

The simplest mechanical model for the study of bridge deck aerodynamics is a *cross-sectional model*. This classical academic model consists in a simple 2D rigid cross-section, whose translational and rotational DoFs are supported by (usually linear) springs. The model has three DoFs (which often reduce to two as horizontal displacement is neglected). Once assigned the translational and rotational masses to the cross-sectional model, the stiffness of the springs is chosen so that the frequencies of three selected modes (one vertical, one lateral and one torsional) of the complete structure are reproduced. The cross-sectional model is well suited for testing load models and for comparison with wind tunnel experimental tests. Nevertheless, the results obtained through this model are of uncertain extensibility to the complete structure. Moreover, it is not possible to include realistic structural nonlinearities.

An alternative, adopted in the present work, consists in developing *finite element models* of the structure and to consider the wind action as applied on several cross-sections (either as nodal load or as distributed load on specific one-dimensional elements).

A bridge model can include many tens of loaded cross-sections and can have few thousands DoFs. In some cases, the computing time may become quite an issue, in fact:

- Non-stationary forces require the calculation of the convolution integrals of the indicial function model (for each cross-section);
- The time-step size must be sufficiently 'small', to avoid numerical damping and to accurately evaluate the convolution integrals;
- At each time-step the solution is found iteratively, if structural nonlinearities are considered;
- Simulations are carried out at different mean wind velocities;
- Time-histories must be sufficiently long to provide reliable statistics, if a Monte Carlo approach for turbulence effect evaluation is followed (like in this work).

For preliminary studies, *simplified models* with a low number of cross-sections should be considered in order to reduce the computational costs.

The simplest non-trivial model considering two cross-sections is shown in Figure 4.2, where the additional assumption of negligible compliance of the pylons is made. Neglecting the drag effect allows a further reduction of the number of DoFs.

The two-sectional FE model represents a computationally-light extension of the classical cross-sectional model, and introduces some important features of the full bridge. It considers in fact four relevant modes (vertical symmetric and skew-symmetric, torsional symmetric and skew-symmetric), it includes the geometrical nonlinearities of suspension cables and the mono-lateral behaviour of hangers, and it allows a first evaluation of the effect of the along-span wind turbulence coherence. Emphasizing symmetric and skew-symmetric effects, the two-sectional model gives a clear view of the tendency of structural behaviour depending on different load and structural properties. Finally, although more detailed models are necessary to accurately analyze a true structure, simplified models can be a useful tool during the preliminary design phase.

5.3.2 Numerical model

A comprehensive program for the analysis of bridges under wind excitation has been developed. In fact, commercial programs cannot consider history-dependent loads. Moreover, a single tool including model generation, multi-correlated wind field generation, FE solver and post-processing analyses, allows a simpler integration of the various part and an easier autoimmunization of the simulations.

At first, a pre-processing routine generates the FE model, given a few geometrical and mechanical characteristics as dimensions, section properties, etc. In addition, the number of modelled cross-section is an input for the pre-processor. This allows, after the analysis of a simplified model, the generation of more refined discretization just by modifying one

input parameter. As to loading, indicial self excited forces and quasi-steady buffeting are superposed (e.g. Salvatori and Spinelli, 2004; Salvatori and Spinelli, 2006b; Scanlan, 1984).

5.3.3 Numerical example

In order to show the effectiveness of the proposed approach, the results of numerical simulations on two-cross-section FE models are presented for two different structures.

A long-span suspension bridge is considered, with the dimensions and the mechanical characteristics of the Bosporus Bridge (Turkey). The geometrical and mechanical properties are reported together with the results of the modal analysis in Table 5.1.

Table 5.7 modal periods T and shapes (right).

Mode	T [s]	Mode shape
1	9.26	Vertical Skew-symmetric
2	5.14	Vertical Symmetric
3	2.39	Torsional Symmetric
4	1.62	Torsional Skew-symmetric

For the aerodynamic characteristics the rectangular cross-section with width/height ratio $B/D = 12.5$ is used. This streamlined cross-section is known to flutter in a coupled vertical-torsional mode, as also experimentally verified in Righi, 2003.

5.3.4 Linear structure in laminar flow

As a first step, simulations are performed with linear structure under laminar flow.

Without wind fluctuations, a perturbation from the static equilibrium (i.e. an initial condition on displacements or velocities) must be provided in order to activate the self-excited forces. Here, initial displacements are imposed considering a random-coefficient linear superposition of the four significant mode shapes (assuming a 1cm maximum nodal displacement).

The structural response is characterized by aerodynamically damped oscillation at 'low' mean wind velocity (Figure 5.14a) and by diverging oscillation at 'high' mean wind velocity (Figure 5.14c). The borderline condition of stable amplitude oscillation (Figure 5.14b) is obtained at an intermediate wind velocity U_{cr} that characterizes the critical flutter condition. A coupled symmetrical flutter is obtained at a critical wind velocity $U_{\mathrm{cr,sym}} = 61$ m/s, with a flutter frequency $f_{\mathrm{cr,sym}} = 0.35$ Hz (the symmetrical vertical and torsional modes contributing to flutter instability have frequencies $f_{\mathrm{vert,sym}} = 0.19$ Hz and $f_{\mathrm{tors,sym}} = 0.42$ Hz respectively). Such

results are in good agreement with the bi-modal analytical solution $U_{\mathrm{cr,sym}} = 62$ m/s and $f_{\mathrm{cr,sym}} = 0.33$ Hz, that is obtained considering an idealized 2-DoF structural model reproducing the symmetric vertical mode and the symmetric torsional mode (Dyrbye and Hansen, 1996).

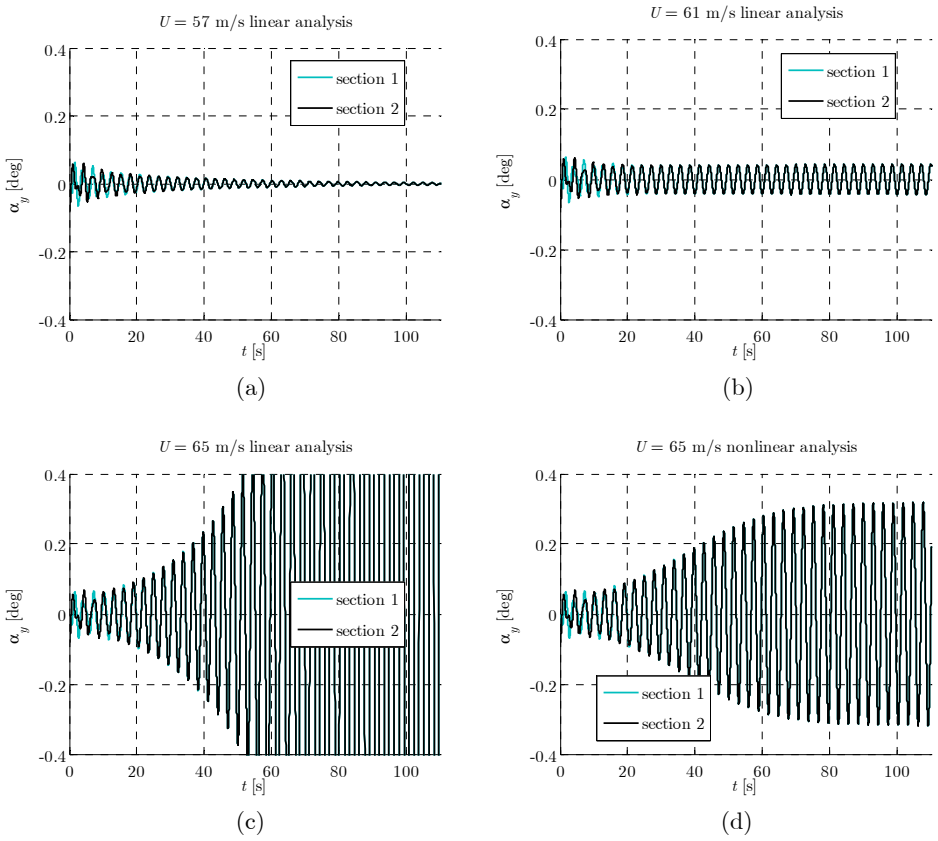

Figure 5.14 Time-histories of motion: (a) sub-critical velocity and linear structure, (b) critical velocity and linear structure, (c) super-critical velocity and linear structure, (d) super-critical velocity and nonlinear structure

5.3.5 Secondary unstable flutter modes

Theoretically, each couple of vertical and torsional modes that have 'similar' shapes can couple into a flutter mode that has the same shape and is characterized by a critical frequency (usually intermediate between those of the two structural modes) and a critical wind velocity. Of course, only the flutter mode with the lowest wind velocity is stable and has therefore a practical relevance. Nevertheless, it is interesting to verify the theoretical predictions through time-domain simulations. In the example, it is in fact possible to observe the secondary flutter mode, by imposing purely skew-symmetric initial conditions to the motion and $U > U_{\mathrm{cr,sym}}$. In this way, the

symmetric flutter is not activated as long as the numerical error does not introduce a spurious symmetric component into the motion, which then jumps to the stable symmetric flutter, as shown in Figure 5.16.

The unstable coupled skew-symmetric flutter is obtained for a wind velocity $U_{\mathrm{cr,ant}} = 92$m/s, with a flutter frequency $f_{\mathrm{cr,ant}} = 0.30$ Hz (the skew-symmetric vertical and torsional modes have frequency $f_{\mathrm{vert,ant}} = 0.11$ Hz and $f_{\mathrm{tors,ant}} = 0.62$ Hz respectively, the analytical solution gives $U_{\mathrm{cr,ant}} = 99$ m/s and $f_{\mathrm{cr,ant}} = 0.45$ Hz).

5.3.6 Nonlinear structure in laminar flow

If the structural nonlinearities are taken into account, the structural response changes at super-critical velocities. In laminar flow, after a diverging phase, the oscillations stabilize at constant amplitude (Figure 5.14d), whose value depends only on the wind mean velocity. This effect is well known in the aeronautic field, where several authors investigated the post-critical behaviour of a 2-DoF airfoil supported by nonlinear springs with polynomial (usually cubic or quadratic) restoring forces (e.g. Poirel and Price, 1997; Shahrzad and Mahzoon, 2002). In this work, the 'actual' structural nonlinearities of the bridge are taken into account, and the limit cycle oscillation amplitudes at different wind velocities are plotted in Figure 5.17 (qualitatively similar plots can be found in the last mentioned reference).

It can be observed that the effects of structural nonlinearities in limiting the oscillation amplitude is more pronounced for the torsional motion than for the vertical one. This could also be explained by considering the quality of the structural nonlinearities. The torsional motion exhibits as a matter of fact a bilateral hardening behaviour. For the vertical motion, on the other hand, the structure hardens when moving downwards and softens when moving upwards, as the main cable tension increases or decreases respectively.

5.3.7 Effects of fully and partially correlated wind fluctuations and of structural nonlinearities

In the cases of turbulent wind (partially or fully correlated), a Monte Carlo approach is adopted. Four cases are considered combining fully and partially correlated wind fields with linear and nonlinear analyses.

Simulations are performed varying the mean wind velocity from 5 m/s to 100 m/s (step 5 m/s plus some extra values in the vicinity of the critical velocity). For each value of the mean wind velocity, five fully correlated and five partially correlated wind time-histories are generated (simulating 600 s each). The structural response is then calculated through both linear

and nonlinear analyses. An example of wind and relevant response time-histories is reported in Figure 5.15.

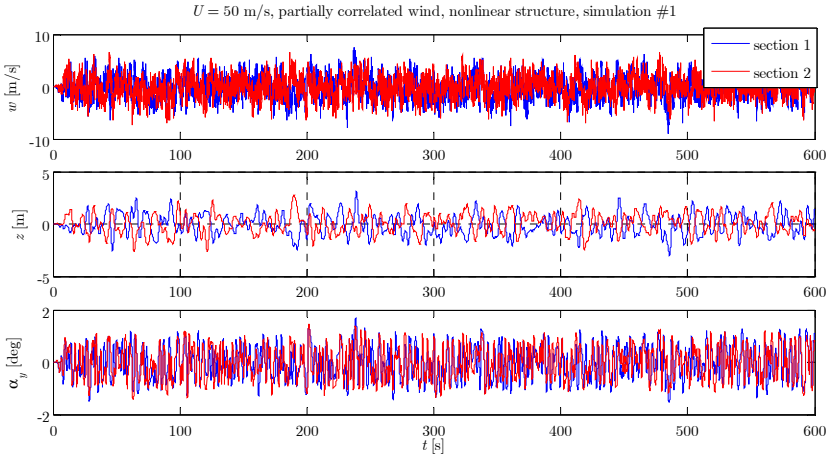

Figure 5.15 Example of time-history: wind fluctuations (top); vertical response (middle); torsional response (bottom)

The response time-histories are divided into time-intervals in such a way as the motion can be considered uncorrelated. This is achieved by choosing the duration of each interval equal to the time lag of the autocorrelation functions to be less than 20%. Finally, the peak value in each interval is used for a statistical analysis.

An example of motion peak distribution is plotted in Figure 5.18. The median value is used as a significant measure of the central tendency, and will be referred to as 'oscillation amplitude' in the following.

The oscillation amplitudes at different mean wind velocities are plotted in Figure 5.19 for the four combinations of partially and fully correlated turbulence with linear and nonlinear structures.

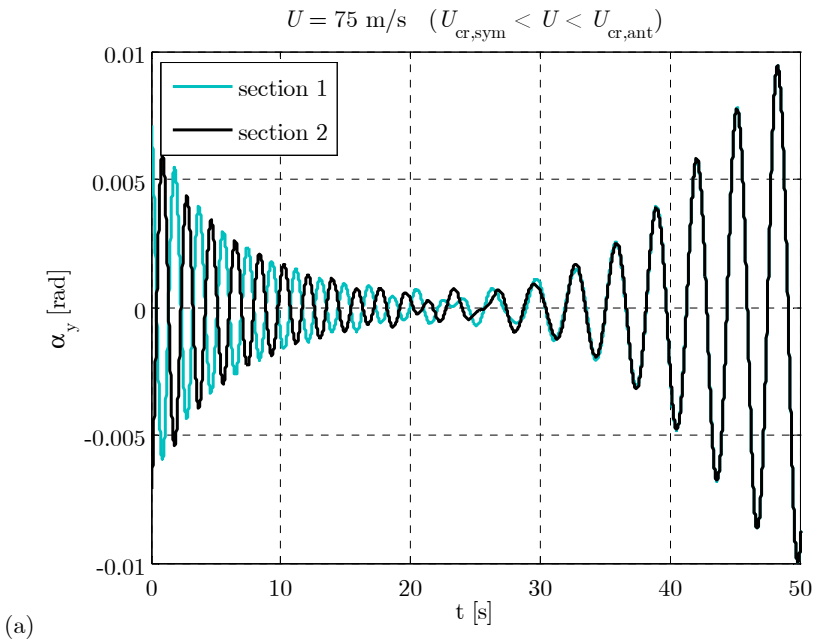

(a)

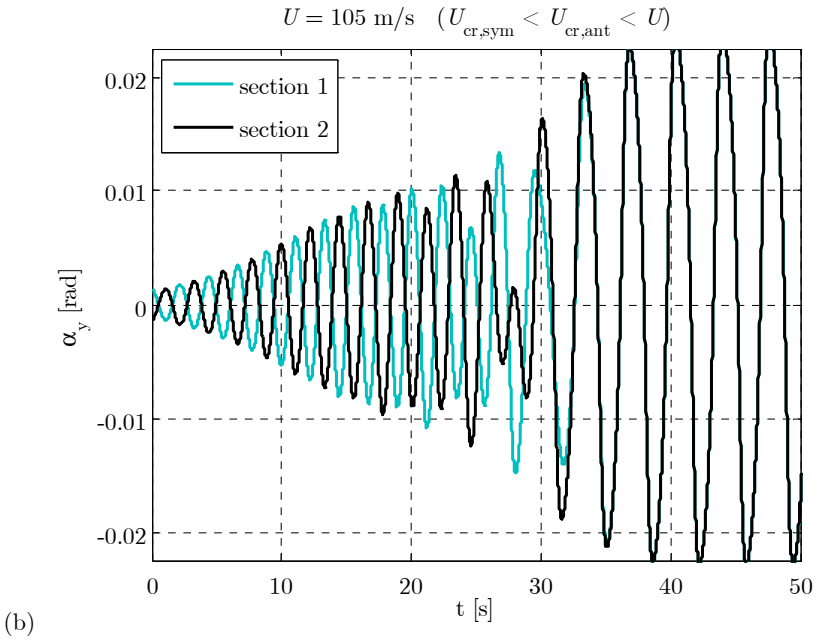

(b)

Figure 5.16 Time-histories of motion for second unstable flutter mode (skew-symmetric): (a) inter-critical velocity $U_{cr,sym} = 61$ m/s $< U = 75$ m/s $< U_{cr,ant} = 92$ m/s, the skew-symmetric motion is damped; (b) super-critical velocity $U_{cr,sym} = 61$ m/s $< U_{cr,ant} = 92$ m/s $< U = 105$ m/s, the skew-symmetric motion diverges. In all cases, after a few cycles, the motion jumps to the diverging symmetric flutter

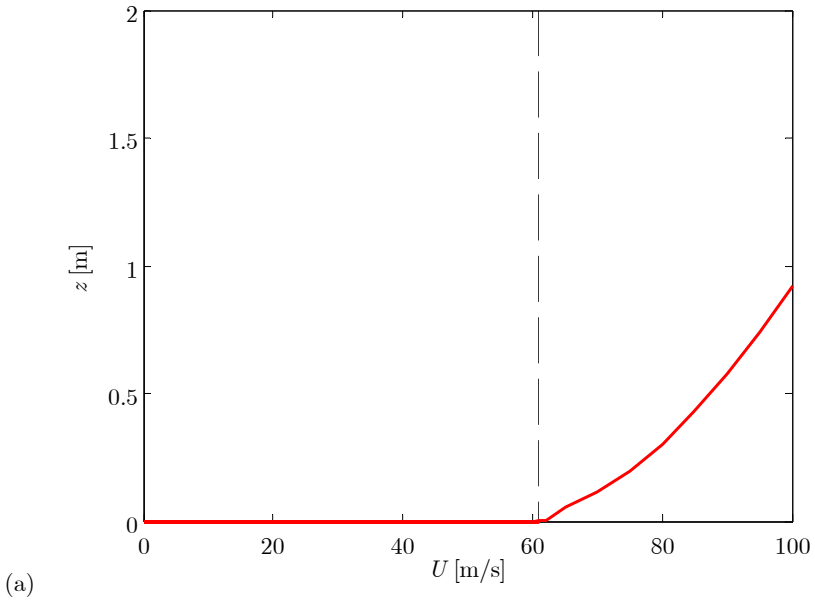

(a)

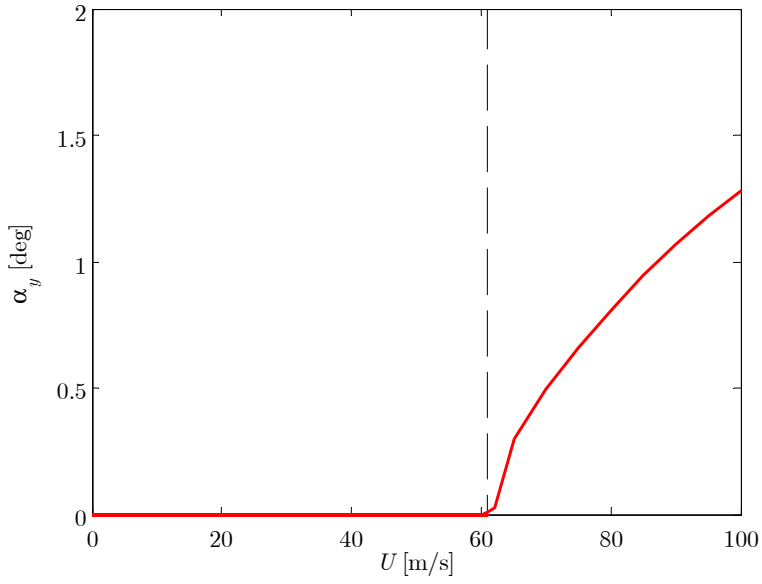

(b)

Figure 5.17 Amplitudes in the limit cycle oscillation at different mean wind velocities: vertical (a) and torsional (b) DoFs

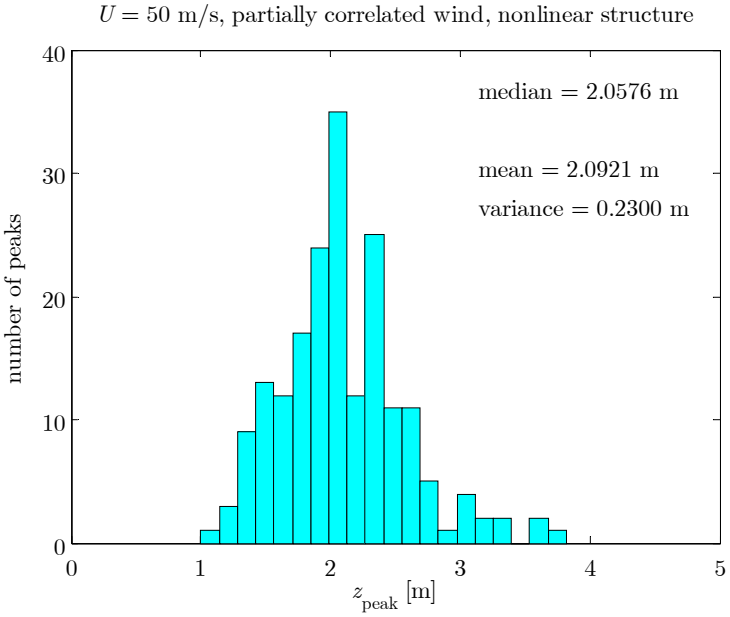

(a)

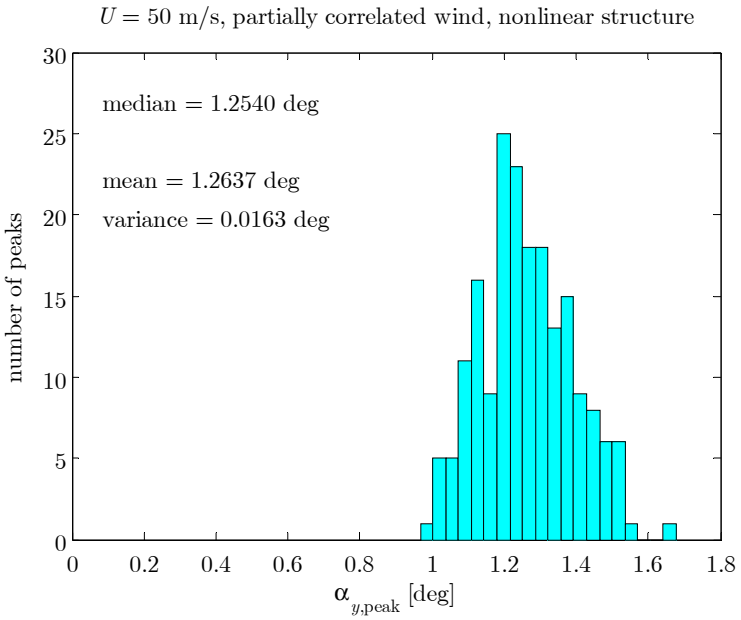

(b)

Figure 5.18 Example histograms of the distribution of peaks for vertical (a) and torsional (b) DoFs

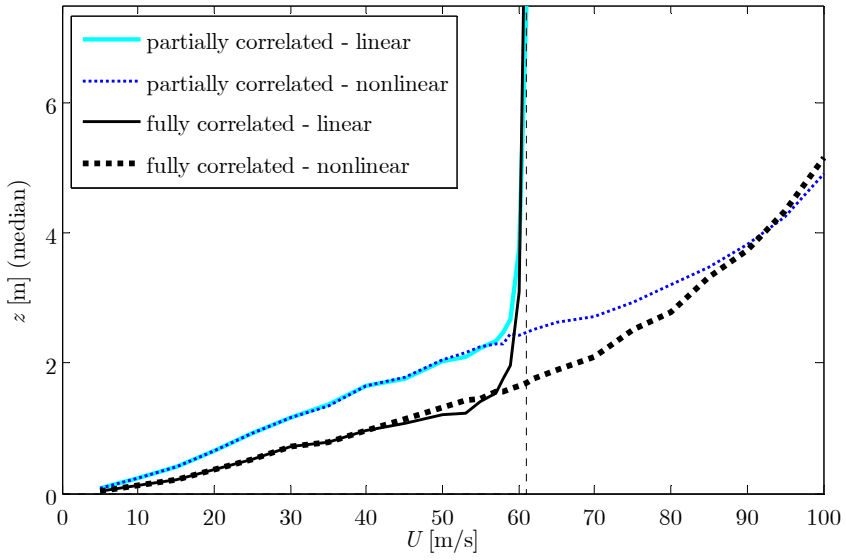

(a)

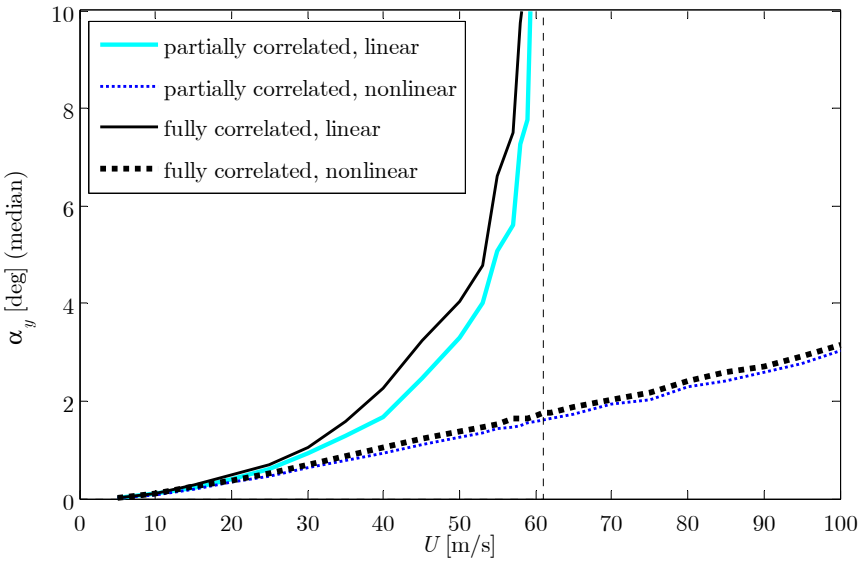

(b)

Figure 5.19 Vertical (a) and torsional (b) responses versus mean wind velocity. The dotted vertical line at $U = 61$ m/s corresponds to the critical mean wind velocity at flutter evaluated through the simulations in laminar flow.

Focusing on the linear structure behaviour, it is observed that the motion amplitude grows as the mean wind velocity increases, and, both for fully correlated and for partially correlated winds, it diverges in correspondence of the critical wind velocity calculated in laminar flow.

For the nonlinear structure, on the other hand, no divergence is observed and the motion amplitude keeps increasing but is limited also at super-critical wind velocities. As already remarked, a more effective limitation is observed for the torsional motion than for the vertical one.

By comparing the oscillation amplitudes for fully and partially correlated winds (for both linear and nonlinear structures), it is evinced that the vertical oscillation amplitude is much greater for partially correlated wind, whereas the torsional amplitude is slightly larger for fully correlated wind.

This behaviour can be explained by observing that: (i) the lower frequency modes are the most excited by the turbulence, as the wind turbulence has higher power at the lowest frequencies; (ii) fully correlated wind introduces energy into the system only for the symmetric modes (the work of a symmetric load on an skew-symmetric displacement is zero), whereas partially correlated wind excites also skew-symmetric modes; (iii) as the lower-frequency vertical mode of the structure is skew-symmetric, it follows that the vertical motion will have larger amplitude in case of partially correlated wind. On the other hand, the lower-frequency torsional mode is symmetric and therefore will be more excited by fully correlated wind.

Finally, it is worth to report that no hanger going slack has been detected.

5.3.8 Remarks

A comprehensive tool for the time-domain analysis of suspension bridges has been developed. It includes the parametric generation of the structural model, a fully nonlinear FE solver, where history-dependent wind loads have been implemented, and a post-processor for result analysis. The use of simplified models reduces the computational effort, allowing Monte Carlo simulations. Many fundamental aspects of the true bridge are still considered (more than two modes, mass and geometrical nonlinearities of suspension cables, mono-lateral behaviour of hangers, along-span wind turbulence coherence).

According to the implemented structural and load models, the numerical simulations show that:

- If the bridge is considered as a linear structure, the critical value of the mean wind velocity is not affected by the presence of turbulence or by its level of correlation.

- If structural nonlinearities are considered, the oscillation amplitude is usually reduced in the sub-critical velocity range. Moreover, the critical wind velocity is no more a meaningful limit, as the oscillations are limited also in the super-critical velocity range.
- To consider fully correlated turbulence can result in an important underestimation of the structural response, especially if the structure is dominated by skew-symmetric modes, as may happen for suspension bridges. Therefore, along-span coherence should be considered in the bridge design.

It seems that the hanger slack is not a crucial problem for practical applications.

Although the results are obtained on a simplified model with two cross-sections, they suggest a qualitative trend. More refined discretization (which will allow considering more modes, as well as a more accurate evaluation of along-span coherence effects) will be considered in the future.

5.4 Nonlinearities and linearizations

In the analyses presented below (Salvatori and Spinelli, 2006a), the structural nonlinearities are considered only in the static calculations used to determine the mean steady position around which the motion develops. Frequency-domain stability analysis intrinsically requires a linearized model. This is adopted also in the time-domain in order to allow the comparison with frequency-domain results.

Unlike steady coefficients, aeroelastic derivatives and admittance functions require a relatively complicated experimental procedure for their identification. For this reason, they are usually measured for a single mean angle of attack (typically the null value). Only recently, for the cross-sections of important bridges, aeroelastic derivatives have been identified also for a few different values of the mean angle of attack. Therefore, it is not possible in practical calculations (or it is possible only in a very rough way) to take into account the correct configuration around which the unsteady load model is linearized.

A framework for the numerical analysis of bridges under wind excitation is outlined. It is based on a structural finite element scheme and cross-sectional wind load models. Two aspects are investigated: (i) how considering the mean steady configuration in the aerodynamic stability calculation; and (ii) the effects of load nonlinearities on structural response. A quasi-steady load model is adopted, which is able to deal with the considered problems by using experimental data easily available in the practice. By means of numerical examples, it is pointed out (i) that both the modifications in structural tangential stiffness and in the aerodynamic

coefficients due to the mean steady deformation may affect the aeroelastic stability threshold and (ii) that load linearization may produce an underestimation of the structural response.

Bridges are strongly sensitive to the wind action which may increase the vulnerability of crucial links as the length of the main spans becomes larger and larger and the architectonic design follows complex shapes due to aesthetic needs.

In order to evaluate wind loads, wind tunnel tests are commonly carried out. Since scaled-down models of complete bridges are expensive and present intrinsic scaling problems, in general the aerodynamic characterization of cross-sectional models is used. Nevertheless, it is not straightforward to extend cross-sectional results to the whole bridge, and to capture accurately the overall behaviour of complex structures.

Some approaches based on cross-sectional load models are discussed below. The main focus is on load models based on steady coefficients. As will be clarified in what follows, these models are actually suitable for the present investigations and they make use of experimental data easily available for practical calculations.

Two main aspects are investigated:

- The influence of the steady deformations due to the mean component of the wind action on the critical wind velocity for aerodynamic stability.
- The effects of load nonlinearities on the structural response.

An essential problem in analyzing bridges is the evaluation of the flutter threshold, i.e. the critical mean wind velocity that induces dynamic instability due to fluid-structure interaction. The most common approach for practical calculations relies on a linear representation of the wind loads based on unsteady coefficients. Two or more structural modes are combined, and the consequent stability problem is solved in the frequency domain. The standard bi-modal procedure is described in Dyrbye and Hansen, 1996; more recently, multimodal procedures have been introduced, as described in Jain et al., 1998. Commonly, the deformations induced by the mean wind action are neglected for both the structure and the aerodynamics. The structural modes are evaluated in the reference configuration (static equilibrium under dead loads) by means of standard computer codes, and the aeroelastic derivatives are obtained from experimental tests by considering oscillations around the zero angle of attack. Really, the wind-induced motion develops around a deformed configuration which can be evaluated by means of a nonlinear static analysis. The linearization of the problem should then be performed around that configuration, as pointed out by Scanlan and Jones, 1990. Structural modes should be evaluated by using tangent stiffness and the variation of the angle of attack along the span of the bridge should be considered. On

the other hand, aeroelastic derivatives are usually measured only for the zero angle of attack, or, in some extraordinary cases, for a very small number of values of the same angle. Alternatively, it is possible to use a quasi-steady approach to aeroelasticity. This way, unsteady effects in the fluid-structure interaction are neglected but it is sufficient to use steady coefficients. These are obtained from simple experimental tests and are commonly available for a wider range of angles and in a refined manner. For this reason, the quasi-steady approach is chosen here to obtain an estimate of the error that arises by neglecting steady deformations for the structure and/or the aerodynamics. The results of stability analysis obtained by linearization around the reference configuration and around the steady deformed configuration are compared.

A second problem is the evaluation of the structural response to wind gusts. Again, the quasi-steady load model allows us to easily include load nonlinearities as well as the coupling between buffeting and self-excited actions. It is therefore a suitable tool for evaluating the effects of load nonlinearities on the structural behaviour in a consistent way. The structural response obtained by means of the nonlinear quasi-steady load model will be compared with that obtained through a linearization of the same model. The use of the quasi-steady approach represents a simplification to the problem that allows the use of more easily available experimental data. Although the unsteady effects are neglected, qualitatively correct results can be expected for streamlined bridge decks at low reduced frequencies.

5.4.1 Numerical examples

As a sample structure, the Bosporus suspension bridge (Turkey, main span 1074 m) is considered. Rayleigh damping coefficients are chosen in such a way as to assign a damping ratio of 0.5% to the first two vertical modes.

With respect to the aerodynamic properties, two different cross-sections are considered: a streamlined one (section 'A') and a bluffer one (section 'B').

Cross-section 'A' is the one of Severn suspension bridge (whose aerodynamics is very similar to the one of the actual Bosporus Bridge). The relevant coefficients are plotted in Figure 5.20, as measured in Falco et al., 1978, where $\beta = -0.3$ is suggested for this cross-section; it is also pointed out that the considered cross-section is only slightly affected by the value of the reduced velocity, i.e. the quasi-steady approximation should be acceptable.

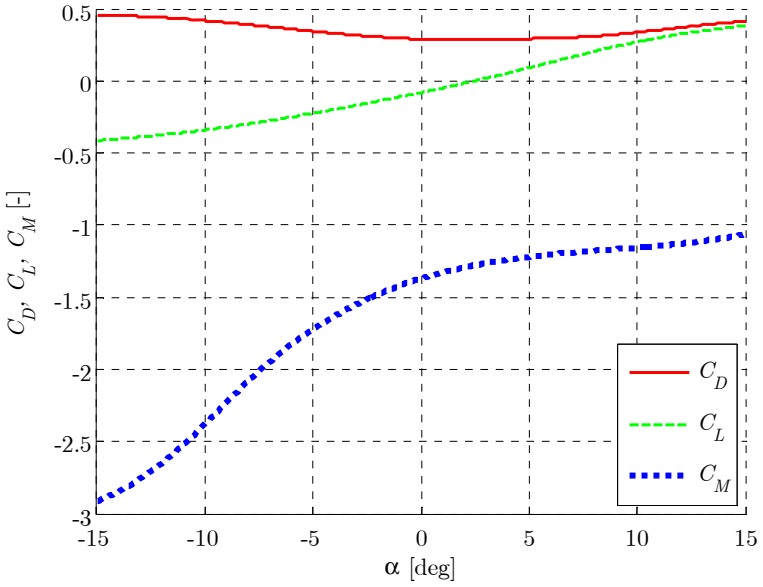

Figure 5.20 Cross-section 'A': aerodynamic coefficients

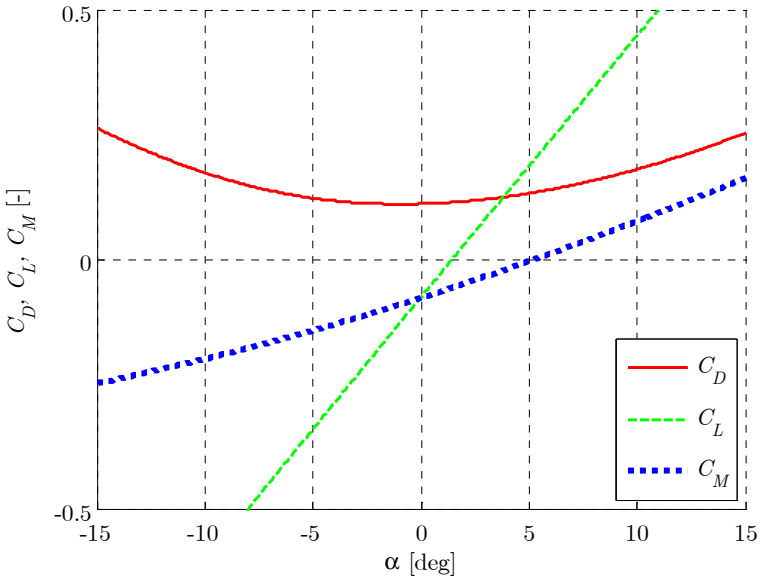

Figure 5.21 Cross-section 'B': aerodynamic coefficients

Cross-section 'B' is the one of the Tacoma replacement bridge. The relevant aerodynamic coefficients are plotted in Figure 5.21, as reported in Simiu and Scanlan, 1996. As no further experimental indication is available, the usual assumption $\beta = 0$ is accepted. The use of this kind of cross-section for such a bridge is of course merely hypothetic and no variation in

deck stiffness or inertia has been considered in order to focus on the aerodynamic differences. Moreover, unsteady effects are of basic importance for bluff cross-sections. Therefore, the results obtained with the quasi-steady approach have mainly heuristic purposes in this case.

All the analyses presented below are obtained by discretizing the main span into 10 elements (11 aerodynamic cross-sections). Preliminary tests with more refined discretizations proved to bring no significant accuracy improvement, whereas the computational cost increases rapidly with the number of cross-sections.

5.4.2 Effects of mean angle of attack on stability

Let us focus on the critical wind speed for aerodynamic stability by making use of the analysis presented. In order to evaluate the matrix $\overline{\mathbf{A}}$, a nonlinear static analysis should be performed for each increasing value of the mean wind velocity and the tangent structural and aerodynamic stiffness and the aerodynamic damping should be evaluated for the relevant mean steady value of the displacements.

As a matter of fact, the effects of displacements on structural stiffness are often neglected. Moreover, aerodynamic stiffness and damping are usually evaluated through aeroelastic derivatives measured only at zero mean-angle of attack. This way, although the unsteadiness is taken into account, the possible influence of the deformed configuration is completely neglected. Aware of this fact, the designers of bridge cross-sections have recently started to obtain aeroelastic derivatives at a few different mean angles of attack.

Here, the approach based on quasi-steady load model is adopted. Even though unsteadiness is neglected, the effects of the angle of attack are accounted for in a consistent way (Salvatori and Spinelli, 2005; Salvatori and Spinelli, 2006a).

The critical conditions for aerodynamic instability are sought by using tangent structural stiffness and aerodynamic coefficients in the reference configuration $\mathcal{C}_0$ or in the configuration $\mathcal{C}_U$ deformed under mean wind.

For each aerodynamic cross-section, the critical wind velocity is determined in four cases by combining structural properties in $\mathcal{C}_0$ or $\mathcal{C}_U$ with aerodynamic properties in $\mathcal{C}_0$ or $\mathcal{C}_U$. The system is projected into the space of the first 20 natural modes (enough to include the skew-symmetric torsional mode). The results in terms of critical condition are reported in Table 5.8.

It can be noticed that both the modification in structural tangent stiffness and the changes in the angle about which we linearize the aerodynamic coefficients affect the critical velocity. For cross-section 'B', the differences are quite large, and the result considering reference configuration both for structure and for aerodynamics are not safety

preserving. Moreover, in case of aerodynamics evaluated in $\mathcal{C}_0$ and structure evaluated in $\mathcal{C}_U$, the dynamic instability is not even obtained as shown in Figure 5.22, where no negative damping is reached.

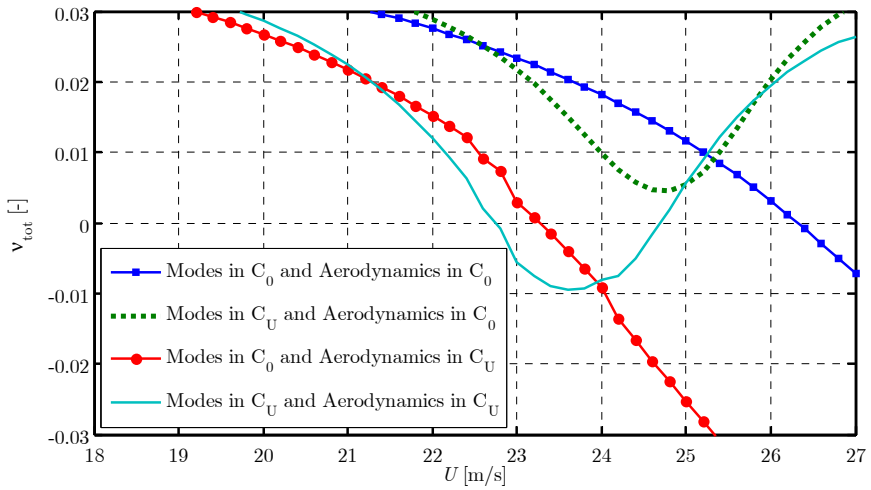

Figure 5.22 Cross-section 'B': total damping (structural + aerodynamic) versus mean wind velocity

Deformed configurations at critical wind velocities are visualized in Figure 5.23 and Figure 5.24, whereas the results of modal analysis in the reference and deformed configurations at critical wind velocity are reported in Table 5.9. For cross-section 'A', the small values of the pitching moment induces small (negative) rotations and the negative lift produces higher tension in the main cables, resulting in higher natural frequencies (hardening behaviour). For cross-section 'B', the high negative pitching moment induces large negative rotations; this results in the partial unloading of the downwind cable which reduces its geometrical stiffness and therefore its natural frequencies.

For the two cases of structure and aerodynamics evaluated in the same (reference or deformed) configuration, the instability modes are visualized in Figure 5.31 and Figure 5.32. As expected, the streamlined cross-section 'A' is subjected to couple vertical-torsional flutter instability, whereas the bluff cross-section 'B' is prone to torsional flutter instability. The contributions of the natural modes to the instability modes are reported in Table 5.10 and Table 5.11 and visualized in Figure 5.25 and Figure 5.26. Take note that in case of coupled flutter (cross-section 'A') the torsional contribution is mainly given by the first torsional mode, whereas the vertical contribution is given by the first two symmetric modes. It can be also observed that the mean static deformation influences slightly the critical shapes and the relative contributions of structural modes instability

mode, but the critical wind velocity is significantly affected by the choice of the centre of the linearization, especially in the case of cross-section 'B'.

Table 5.8 Critical flutter conditions

Cross-section 'A'	U_{cr} [m/s]	f_{cr} [Hz]
Modes and aerodynamics in $\mathcal{C}_0$	67.5	0.322
Modes in $\mathcal{C}_U$, aerodynamics in $\mathcal{C}_0$	67.9	0.323
Modes in $\mathcal{C}_0$, aerodynamics in $\mathcal{C}_U$	67.2	0.325
Modes and aerodynamics in $\mathcal{C}_U$	68.7	0.325
Cross-section 'B'		
Modes and aerodynamics in $\mathcal{C}_0$	26.4	0.330
Modes in $\mathcal{C}_U$, aerodynamics in $\mathcal{C}_0$	-	-
Modes in $\mathcal{C}_0$, aerodynamics in $\mathcal{C}_U$	23.3	0.334
Modes and aerodynamics in $\mathcal{C}_U$	22.8	0.336

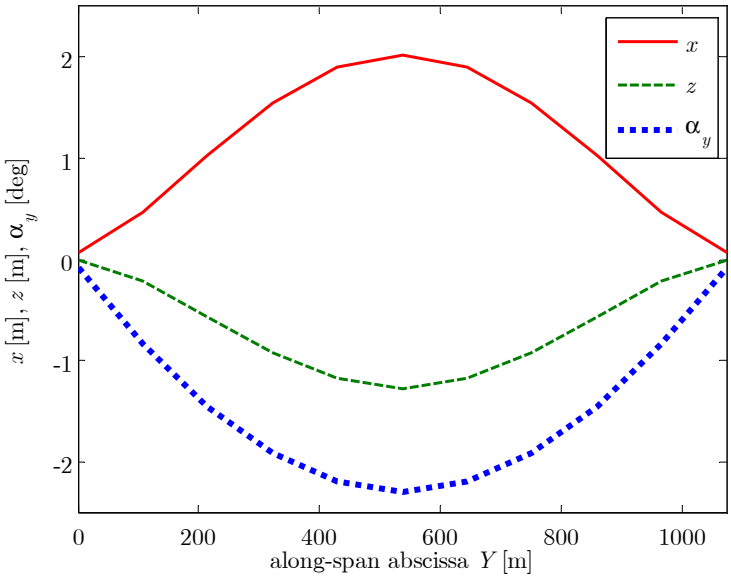

Figure 5.23 Cross-section 'A': steady displacements at critical velocity ($U_{\text{cr}} = 68.7$ m/s)

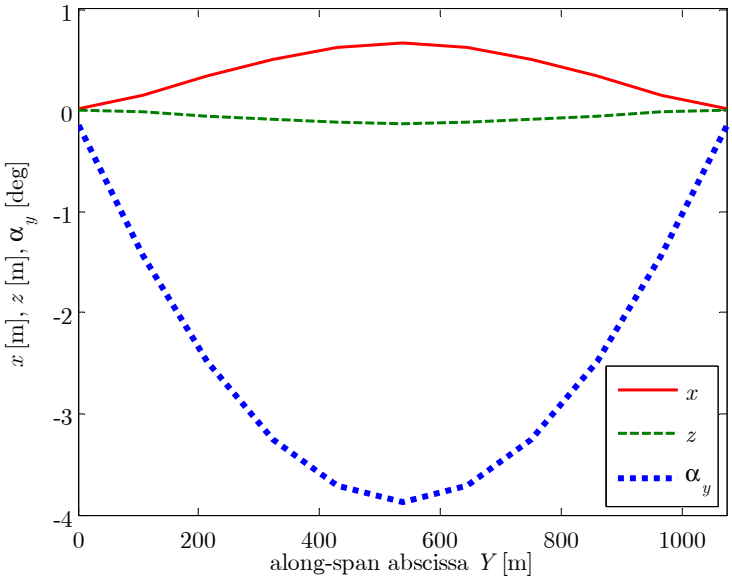

Figure 5.24 Cross-section 'B': steady displacements at critical velocity ($U_{\text{cr}} = 22.8$ m/s)

Table 5.9 Structural modes in the reference configuration and in the steady configuration under critical mean wind velocity

	No wind		Section 'A' at U_{cr} = 68.7 m/s		Section 'B' at U_{cr} = 22.8 m/s	
mode #	f [Hz]	mode shape(*)	f [Hz]	mode shape(*)	f [Hz]	mode shape(*)
1	0.105	L1	0.10	L1	0.105	L1
2	0.131	V2	0.13	V2	0.132	V2
3	0.156	V1	0.16	V1	0.156	V1
4	0.211	V3	0.21	V3	0.211	V3
5	0.262	L2	0.26	L2	0.261	L2
6	0.266	V4	0.27	V4	0.267	V4
7	0.297	cables	0.31	cables	0.289	cables
8	0.313	cables	0.32	cables	0.310	cables
9	0.321	cables	0.34	cables	0.330	cables
10	0.344	cables	0.35	V5	0.347	V5
11	0.347	V5	0.36	cables	0.351	cables
12	0.369	T1	0.37	T1	0.369	T1
13	0.430	V6	0.44	V6	0.431	V6
14	0.468	cables	0.48	cables	0.458	cables
15	0.496	cables	0.52	cables	0.503	cables
16	0.516	V7	0.52	V7	0.517	V7
17	0.553	cables	0.56	T2	0.537	cables
18	0.559	T2	0.57	cables	0.559	T2
19	0.572	cables	0.60	cables	0.588	V8
20	0.583	cables	0.60	V8	0.592	cables

(*) L = lateral, V = vertical, T = torsional, # = number of half-waves in the mode shape

Table 5.10 Cross-section 'A': contributions of natural modes to instability mode

	Structure and aerodynamics in $\mathcal{C}_0$ (U_{cr} = 67.5 m/s)		Structure and aerodynamics in $\mathcal{C}_U$ (U_{cr} = 68.7 m/s)	
mode #	contribution [%]	phase [deg]	contribution [%]	phase [deg]
1	0.5	7	0.1	-56
2	0.0	-179	0.0	2
3	**24.5 (V1)**	**-178**	**24.5 (V1)**	**2**
4	**17.3 (V3)**	**6**	**15.9 (V3)**	**-174**
5	0.0	169	0.0	180
6	0.0	9	0.0	154
7	0.0	66	0.8	23
8	0.0	-151	0.0	150
9	0.9	-42	**6.7 (mixed)**	**-8**
10	0.0	131	**4.7 (V5)**	**-49**
11	**6.9 (V5)**	**-51**	0.0	-11
12	**49.5 (T1)**	**0**	**46.7 (T1)**	**0**
13	0.0	178	0.0	167
14	0.1	17	0.0	-64
15	0.0	-11	0.3	-177
16	0.3	166	0.3	-13
17	0.0	-104	0.0	13
18	0.0	19	0.0	30
19	0.0	163	0.0	177
20	0.1	85	0.0	180

Table 5.11 Cross-section 'B': contributions of natural modes to instability mode

	Structure and aerodynamics in $\mathcal{C}_0$ (U_{cr} = 26.4 m/s)		Structure and aerodynamics in $\mathcal{C}_U$ (U_{cr} = 22.8 m/s)	
mode #	contribution [%]	phase [deg]	contribution [%]	phase [deg]
1	0.5	-1	0.8	-173
2	0.0	-32	0.0	-177
3	3.2	2	1.7	-178
4	2.3	-1	1.1	1
5	0.0	-93	0.0	-149
6	0.0	0	0.0	-179
7	0.0	-19	0.7	9
8	0.0	-123	0.0	-177
9	**9.3 (mixed)**	**179**	**17.6 (mixed)**	**29**
10	0.0	92	1.0	-2
11	1.8	-178	0.0	-89
12	**82.6 (T1)**	0	**76.6 (T1)**	**0**
13	0.0	89	0.0	1
14	0.2	-2	0.4	-176
15	0.0	-172	0.1	3
16	0.1	5	0.0	180
17	0.0	79	0.0	173
18	0.0	-121	0.0	-110
19	0.0	-144	0.1	7
20	0.6	-91	0.0	9

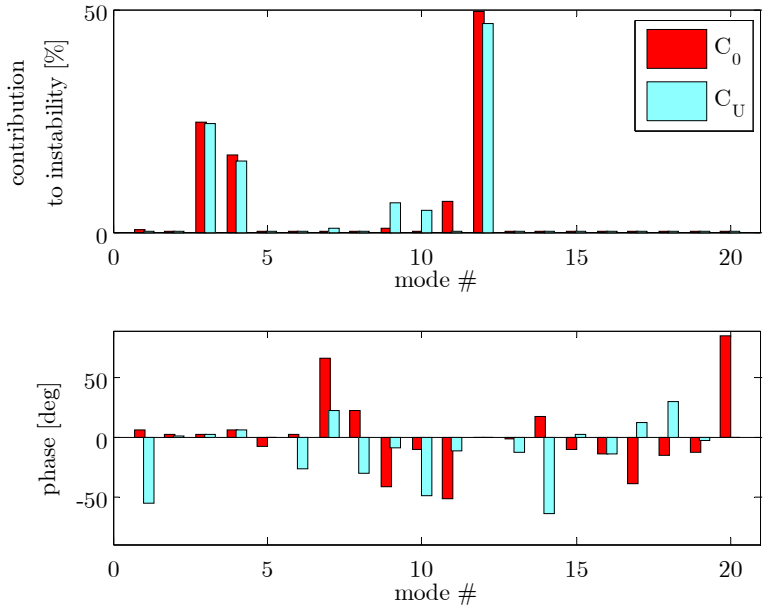

Figure 5.25 Cross-section 'A': contributions of structural modes to instability mode

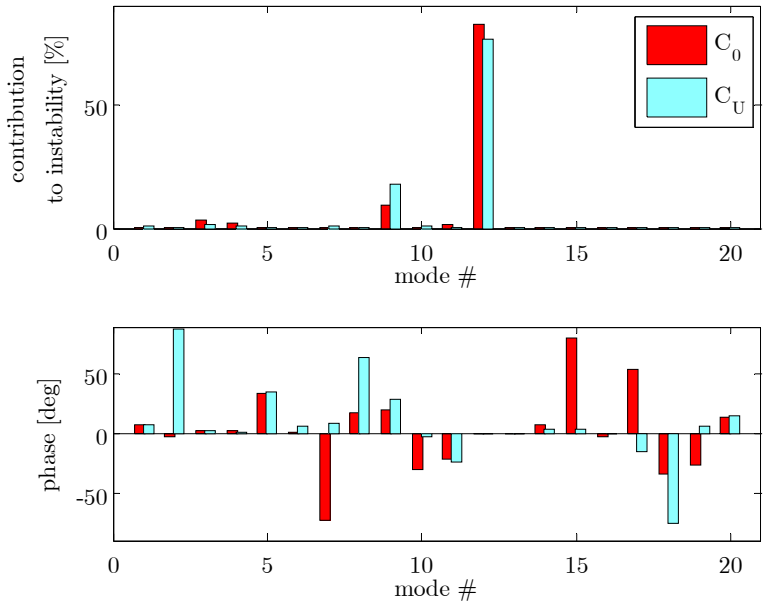

Figure 5.26 Cross-section 'B': contributions of structural modes to instability mode

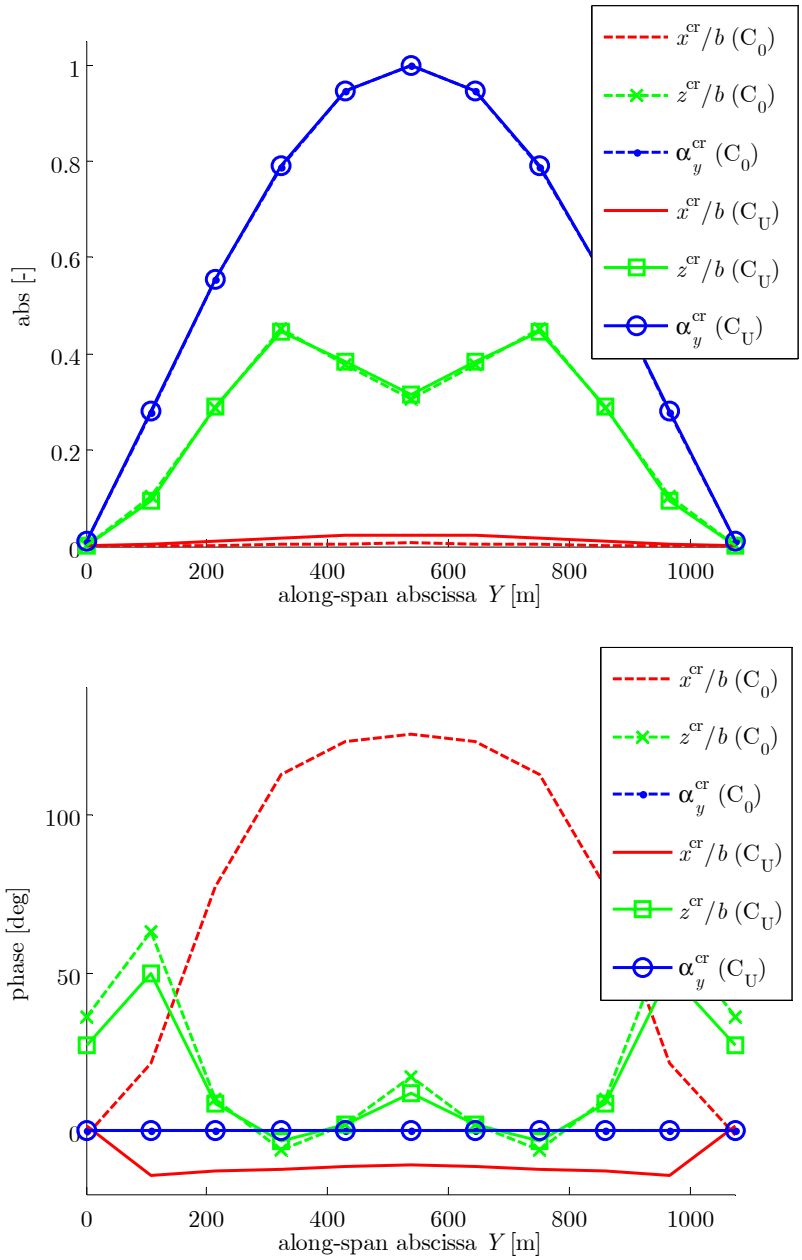

Figure 5.27 Cross-section 'A': instability mode shape (absolute value) and phase angle

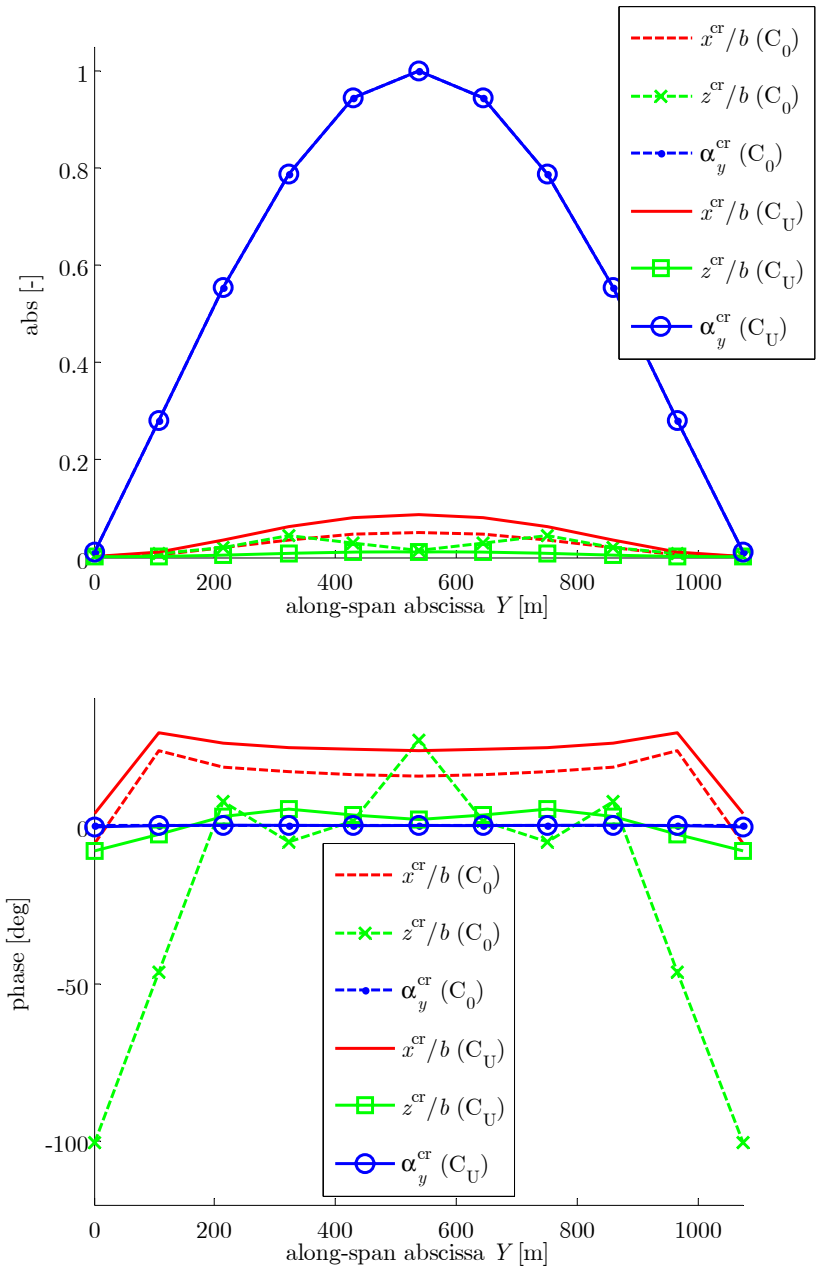

Figure 5.28 Cross-section 'B': instability mode shape (absolute value) and phase angle

5.4.3 Effects of load nonlinearities

In order to evaluate the effects of load nonlinearities, a Monte Carlo approach based on time-domain simulations is adopted. The structural response is evaluated both with the nonlinear quasi-steady load model and with the linearized quasi-steady load model, while the structure is assumed to behave always linearly. For the linearization of structure and loads (in case of linearized loads), the mean steady configuration is considered.

Analyses are performed for several values of the mean wind velocity, ranging from zero to the critical one. For each velocity step, 1800s of wind field time-history (with time-step 0.05s) are generated, and time integrations are performed by using the nonlinear and the linearized versions of the quasi-steady load model.

The results in terms of root mean square (RMS) and maximum (MAX) of the response at mid-span are depicted in Figure 5.29 for the cross-section 'A' and in Figure 5.30 for the cross-section 'B'.

Figure 5.31 and Figure 5.32 show the RMS of along-span response at sample mean wind velocities for cross-section 'A' and 'B' respectively. It can be noticed that the along-span maximum in the vertical response is not at mid-span. The wind turbulence provides in fact more energy at the lower frequencies. As the vertical mode with lower frequency is skew-symmetric (mode 2), it gives no contribution at mid-span and maximum contributions at quarter- and three-quarter-span.

It can be seen that the linearized model produces an underestimation of the response, in case of both cross-sections, and even in the serviceability velocity range. A similar conclusion has also been obtained by Chen and Kareem Chen and Kareem, 2001, by using an unsteady load model which includes nonlinear effects of the low-frequency turbulence.

As to the critical flutter threshold, no influence of load nonlinearities is observed. This result is confirmed by other works such as Borri and Costa, 2004, where a cubic development of quasi-steady self-excited load is applied to a 2-DoF spring-supported cross-section. In the present work, the investigation is extended to the case of fully nonlinear load and complete three-dimensional modelling of the bridge.

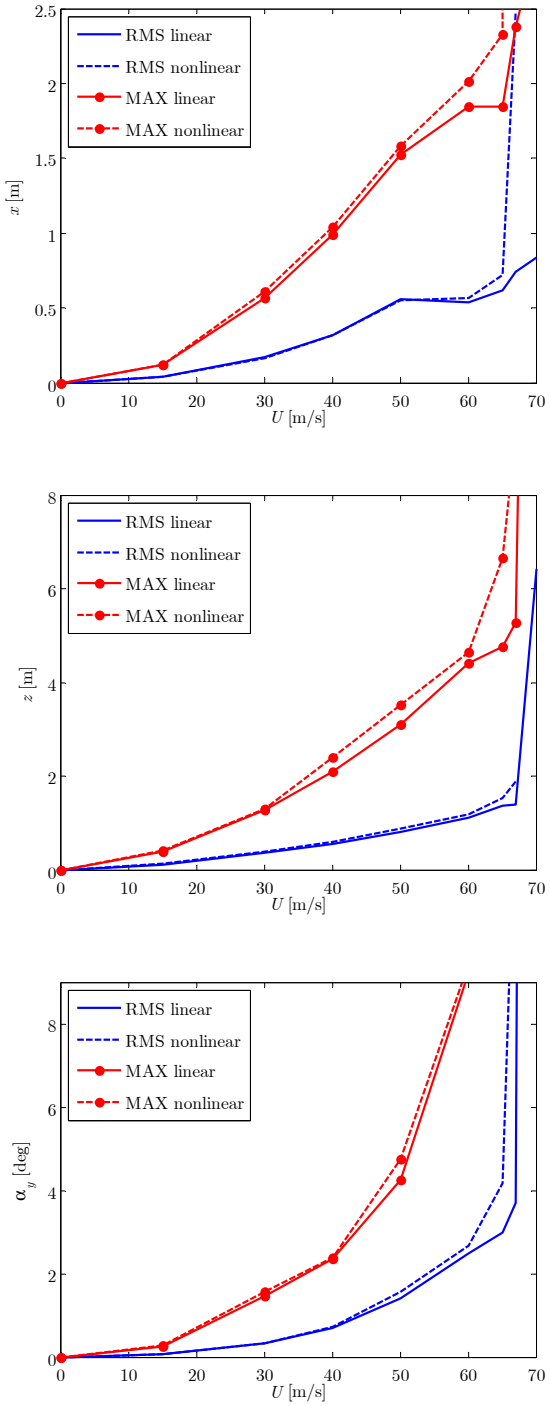

Figure 5.29 Cross-section 'A': comparison of linear and nonlinear response at mid-span

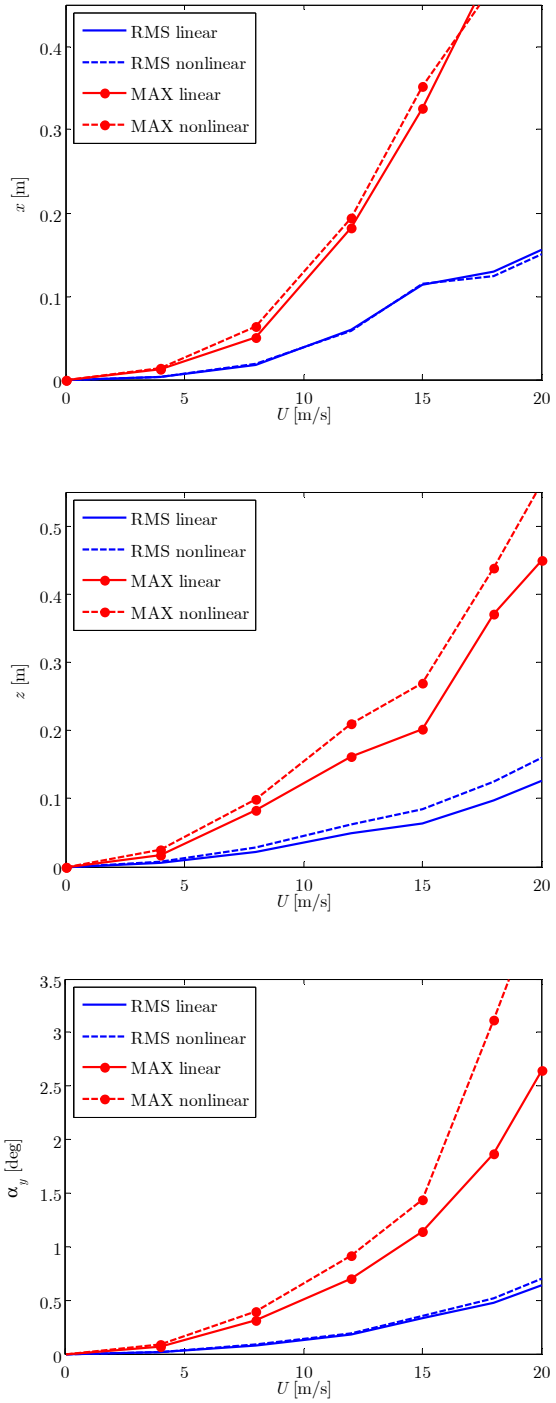

Figure 5.30 Cross-section 'B': comparison of linear and nonlinear response at mid-span

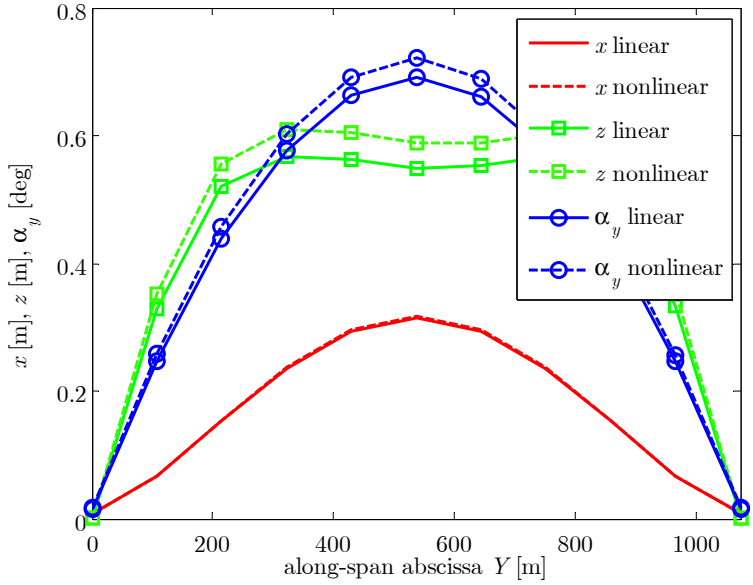

Figure 5.31 Cross-section 'A': RMS of structural response at $U = 40$ m/s

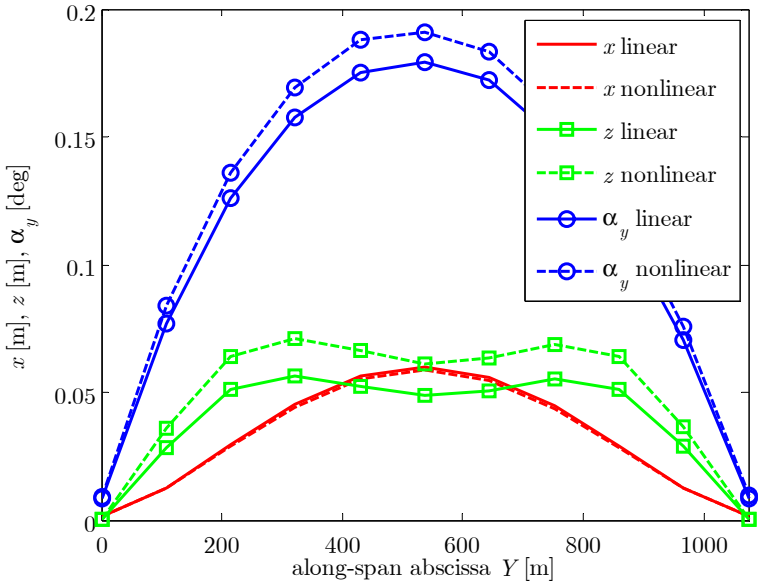

Figure 5.32 Cross-section 'B': RMS of structural response at $U = 12$ m/s

5.4.4 Remarks

The proposed approach allows us to easily consider the dependence of wind load on the angle of attack and load nonlinearities, and requires experimental coefficients that can be obtained by simple tests.

Two main aspects have been investigated:

- the error introduced in the estimation of the critical stability threshold by neglecting the influence of the steady deformed configuration on the modal analysis or on the aerodynamic properties (mean angle of attack),
- the effects of load nonlinearities on the structural response.

As to the first item, the examples indicate that the steady deformations could not always be neglected and significant, possibly not safety preserving, errors can be introduced by the linearization around the reference configuration. Moreover, it seems that both the variations of structural stiffness and of aerodynamics are influent. Therefore, the results of the steady analysis (nonlinear static) should be taken into account for the calculation of the modal shapes and frequencies, as well as for the introduction of the appropriate angles of attack in the aerodynamic coefficients. Where aeroelastic derivatives measured at the proper angles of attack are available, the framework developed here for the calculation of the stability threshold could be easily extended to consider load unsteadiness by introducing iterations on the critical frequency. The use of unsteady coefficients would be of course mandatory in order to obtain accurate results, especially for bluff cross-section (as cross-section 'B' in the examples which may be affected by the simplifications in the quasi-steady load model); further analyses seem necessary in that direction.

As to the second item, it appears that the linearization of the loads is qualitatively acceptable but may produce an underestimation of the structural response, and be therefore not safety preserving. As the design is usually carried out by performing only linearized analyses, this effect should be at least included as safety factor. On this topic, more refined investigations are advised, supported by experimental campaigns and numerical fluid dynamic simulations.

Further structures and aerodynamics should be investigated in order to generalize this results that are based on selected examples.

The modelling of bridge aerodynamics is a challenging topic and many aspects are not yet resolved. The designers should carefully consider the type of analysis to perform and be aware of the possible underestimation of the response due to some kind of simplifications. Although the unsteadiness

of the fluid-structure interaction is lost, the quasi-steady load model is able to provide qualitative indications.

The proposed method is simple to apply, as it does not require complicate wind tunnel tests, and allows useful estimates.

On one hand, it is possible to perform the stability analysis choosing different linearizations of the structure and of the aerodynamics. If the results obtained by linearization around the reference configuration would be deeply different from those obtained around the steady configuration, one may decide to measure aeroelastic derivatives also by taking into account the proper angles of attack, and to perform the relevant unsteady calculations for the stability threshold.

On the other hand, it is possible to compare the structural response to gust excitation by using nonlinear or linearized load models. This aspect provides an estimate of the error produced by the linearization of the load. A comparable relative error may be expected in presence of unsteadiness and, if relevant, it may be included as a factor to the results obtained by using unsteady linearized models. Possible large differences between linear and nonlinear quasi-steady results may motivate experimental campaigns and stimulate further development and validation of nonlinear unsteady load models.

5.5 Summary of results

The results obtained in this Chapter can be summarized as follows:

- It has been shown that full-bridge simulations based on identified indicial functions and multi-modal analysis based on aeroelastic derivatives are mathematically and numerically equivalent. In particular, they give exactly the same results (within numerical errors) when the approximation of the aeroelastic derivatives induced by the identification of the indicial functions is used also in the frequency domain. Moreover, when dealing with frequency-domain results, comparable differences may appear between distinct interpolations and between a specific interpolation and the indicial function approximation. On the other hand, the quasi-steady approach provides only qualitative results.

- When a probabilistic approach to unsteady coefficients is adopted, identified indicial functions tend to compensate the scatter in the measured aeroelastic derivatives, as all the reduced frequencies are simultaneously considered. Since this effect might be considered as purely numerical, it should not be mistaken for an increase in reliability. Nevertheless, if safety coefficients obtained from the direct application of aeroelastic derivatives are considered, the indicial function approach can be confidently used.
- Time-domain methods shall be used for bridge analysis where the frequency-domain approach is more complicated (presence of localized damping devices, coupled buffeting analysis, etc.) or not applicable (analysis including structural nonlinearities, nonlinear damping, etc.). Most likely, where frequency- and time-domain approaches are equivalent, as in the case of the stability analysis, frequency-domain methods shall be preferred since they rely directly on experimental data and are computationally less expensive. Nevertheless, also in these cases time-domain methods may be used as a numerical proof, as the results are obtained through entirely different computations. In general, the two kinds of analysis shall be considered as complementary tools.
- The critical velocity for aeroelastic instability may be significantly affected by the mean steady deformations of the structure, which modify both the structural stiffness and the aerodynamic response (by changing the angle of attack).
- The role of nonlinear terms in wind loading is estimated through a quasi-steady approach by comparing nonlinear loading to linearized one. In general the linearization produces an underestimation of the buffeting response.
- Structural nonlinearities affect buffeting response too. Also in the post-critical regime the oscillation amplitude is limited by structural nonlinearities, and oscillations with a limit cycle are observed, if laminar oncoming flow is considered.
- The effects of along-span wind coherence have been investigated too. Of course, the coherence is crucial in estimating a realistic buffeting response. Moreover, the use of perfectly correlated wind may not be always safety-preserving. In fact, if the buffeting response is dominated by skew-symmetric structural modes, as it is the case with most suspension bridges at moderate wind speeds, a perfectly correlated turbulence would not contribute to the excitation of these modes.

Chapter 6

Mitigation Strategies

In this Chapter some design strategies for the mitigation of wind risk are presented and compared by means of a risk-based analysis. The risk of bridge collapse due to aeroelastic instability and the one of bridge closure to traffic due to excessive buffeting vibrations are considered. After a short review of the possible approaches for reducing wind-induced vulnerability, some examples are offered in the special case of a suspension bridge. In particular the possible advantages of introducing secondary cables with opposed curvature, crossed hangers, or tuned mass control devices are evaluated. The examples offered are of heuristic nature and show the potentiality of the risk management framework in helping the decision making process, as well as the versatility of the developed computational environment in simulating the behaviour of different structures. The effectiveness of tuned mass control systems in mitigating aeroelastic instability and buffeting risks is highlighted.

6.1 Bridge performances

Long-span bridges represent a great challenge in structural engineering. Their sensitivity to wind action has been already discussed in Sections 1.3 and 2.2. Here the general performances are briefly recalled before focusing on two specific wind-related issues, namely the risk of failure due to aeroelastic instability and the risk of closure to traffic due to excessive buffeting vibrations.

In fact, the total wind risk for a bridge is given by the sum of several contributions that can be roughly summarized as follows:

- Risk of collapse due to aeroelastic instability. This aspect is discussed in Section 6.1.1.

- Risk of total or partial strength failure due to mean wind action, buffeting action, and (more rarely) vortex induced vibrations. The consequences of this risk are the collapse of the bridge or the costs of its reparation (including those of temporary closure to traffic).
- Risk of fatigue damage due to buffeting, vortex-induced vibrations, and wind-rain vibrations. The consequences are the costs of the substitution of the damaged elements and closure to traffic during the reparations.
- Risk of temporary loss of serviceability. Under strong winds regular traffic may be prevented by the discomfort due to buffeting or vortex-induced vibrations, or by the direct wind loading on vehicles. Also, if the bridge carries a railway, excessive mean deformations may produce a loss of serviceability by preventing trains form using the bridge. The risk of serviceability loss due to buffeting are treated in Section 6.1.2.

In a general case it would be useful to define three limit states, which may be associated to mean wind velocities: (1) a *warning* limit, at which the management of the bridge should activate the alert state, (2) an *activation* limit, at which the bridge should be actually closed to traffic, and (3) a *failure* limit, at which the bridge is in danger of collapse. The activation limit and the failure limit will be discussed in Sections 6.1.2 and 6.1.1, respectively. As to the warning limit, it could be defined by taking into account the probability that a mean wind velocity could evolve to the activation limit velocity.

6.1.1 Aeroelastic instability

Aeroelastic instabilities represent an ultimate limit state for a bridge. If the critical velocity for a static instability is exceeded, the bridge will collapse or be severely damaged before reaching a post-critical stable configuration. If a critical velocity for a dynamic aeroelastic instability is exceeded, the large oscillations (although limited by nonlinear aerodynamic or structural effects, as it has been shown in Sections 5.3 and 5.4) will rapidly lead the bridge to partial or total collapse.

The calculation of the probability of failure due to aeroelastic instabilities requires the knowledge of the probability distributions of the mechanic and aerodynamic parameters and of the mean wind velocity in the bridge location. All these probability function should be suitably combined (see Section 1.1) and the result is a yearly probability of failure.

Static instability is seldom a concern for standard bridges. Where torsional divergence is a problem, it would be possible to solve the problem by improving the torsional stiffness of the bridge or by modifying the cross-

section aerodynamics in such a way that a smaller slope of the moment coefficient is achieved.

According to Simiu and Scanlan, 1996, aeroelastic stability can be improved with respect to flutter by:

- Changing the geometry of the cross section. Streamlined closed-box girders are more stable than solid girders with 'H-types' sections (like original Tacoma Bridge's ones) or truss girders with unslotted roadways.
- Increasing the torsional frequency and the torsion-to-bending frequency ratio. This can be achieved by using closed box girder, deep truss-girders closed by roadway and wind bracing to constitute a latticed tube, or by different structural schemes as discussed in Sections 6.3.1 and 6.3.2.
- Increasing the bridge damping (see Section 6.3.3).
- Increasing deck inertia. This solution, however, has obvious disadvantages in the static setting.

6.1.2 Loss of serviceability due to buffeting action

Long span bridges constitute crucial links; therefore, their closure due to excessive discomfort for the users or due to blockage by an accident must be avoided as far as possible.

The loss of serviceability might be caused by the direct action of the wind on vehicles (see Section 1.4) or by excessive vibrations due to vortex shedding or buffeting.

Here the case of user discomfort due to buffeting vibrations is discussed.

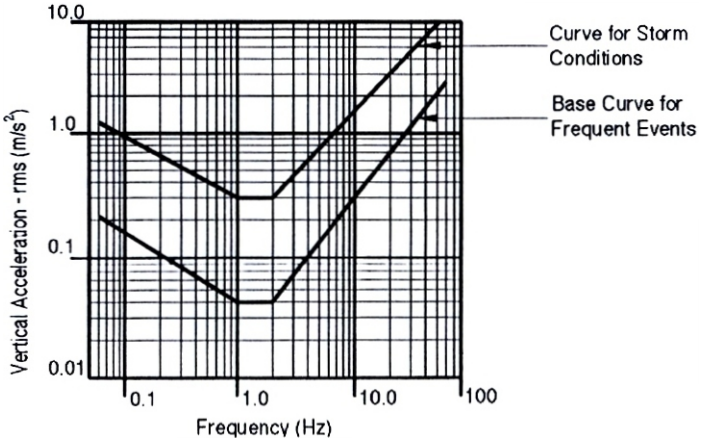

Figure 6.1 Maximum acceptable accelerations for vertical motion (Irwin, 1978)

The psychological effect of bridge oscillations is a crucial aspect. The human response to vibration depends on several factors, including the acceleration, the frequency of vibration, the duration of the event, and the

direction of the motion relative to the human body. In case of suspended-span bridges the motion due to buffeting and vortex shedding is predominantly vertical (although in suspension bridges a lateral motion is also possible). Irwin, 1978, suggested base curves of acceptability of vertical vibrations due to frequent and rare events as functions of the frequency of oscillation (Figure 6.1).

More often, the comfort criterion is expressed in terms of acceleration only, either considering the peak value or the standard deviation.

According to the British Standards, the peak acceleration during a wind storm must be lower than 0.04 g , where g is the acceleration of gravity, as long as the mean wind speed is below 20 m/s.

In Canada (e.g. Peter, 1999) the serviceability criterion prescribes peak accelerations be smaller than 0.05 g or 0.10 g depending on whether the wind speed is below or above 13 m/s.

Gu et al., 2002, proposed a criterion based on the design wind speed U_d of the bridge with the maximum acceptable peak acceleration given by

$$a_{peak} = 0.1g \exp\left(0.9163 \frac{U - U_d}{U_d - 20}\right), \tag{6.1}$$

where U and U_d are expressed in m/s. It is clear that Eq (6.1) is not well defined. Moreover, for the present purposes the criteria in which the limit acceleration depends on the wind velocities do not seem to be acceptable.

In the case of vortex induced vibrations, lower limit accelerations are considered due to the higher probability of occurrence; British instructions (United Kingdom Department of Transport, 2001) recommend that accelerations may be considered acceptable up to approximately 0.0025 m/s^2 for vehicles and 0.04 m/s^2 for pedestrians, whereas the American Society of Civil Engineers suggests a limit of 0.005 g (American Society of Civil Engineers, 1981).

6.2 Strategies for wind-risk mitigation in suspension bridges

As a matter of fact, the current solution for very-long-span bridges is the *suspension* scheme, as demonstrated by some recent achievements such as Humber Bridge (UK, 1981, centre span of 1410 m), Jiangyin Bridge (China, 1998, 1385 m), Storebælt Bridge (Denmark, 1998, 1624 m), Akashi-Kaikyo Bridge (Japan, 1998, 1991 m), and by the proposed designs for Messina Strait Crossing (Italy, 3300 m).

In the practice, the sensitivity of these structures to wind action has been faced so far mainly by acting on the *bridge deck* design, either by

increasing the stiffness through a very rigid truss-girder (as preferred in US and Japan), or by improving the aerodynamic performances through closed box or multi-box girders (as mostly adopted in Europe and, more recently, in China). In Figure 6.2, two paradigmatic examples of these two design philosophies are shown: the heavy latticed girder of the Akashi-Kaikyo Bridge (Figure 6.2a) and the very streamlined deck of the Jaingyin Bridge (Figure 6.2b). The relevant cross-sections are reported in Figure 6.3a and Figure 6.3b respectively.

Solid plate stiffening girders with deck slab have extremely poor aerodynamic and aeroelastic properties and are sensitive to vortex-shedding excitation. They also have very small torsional stiffness that results in a proneness to flutter instability. For these reasons, they are used nowadays only for short span bridges.

(a) (b)

Figure 6.2 Latticed truss girder of the Akashi-Kaikyo Bridge, 1991 m main span (a); streamlined box girder of the Jaingyin Bridge, 1385 m main span (b)

Open truss deck girders generally do not develop significant lift forces and are not sensitive to vortex shedding excitation, since they shred the flow to such an extent that coherent vortexes are not likely to be produced. However, these girders receive very high drag forces.

As to aeroelastic stability, this is usually achieved by providing a high torsional-to-vertical frequency ratio. Horizontal bracing are adopted in order to produce an effective closed torsion cell. The aeroelastic properties of truss girders can be improved by incorporating longitudinal slots in the deck which permit ventilation between the upper and lower surfaces.

The demand for lateral stiffness against high drag and for torsional stiffness against aeroelastic instability results in heavy bridge decks and, as a consequence, in expensive designs. Nevertheless, since this solution is based on a well-established knowledge, it is considered quite reliable. Significantly, the designer of the longest-span bridge to date, the Akashi-Kaikyo Bridge, after a very long and thorough experimental campaign in the wind tunnel, where many tens of different aerodynamic solutions where tested, decided for an heavy and expensive latticed girder in order to ensure a sufficient reliability.

An alternative approach consists in trying to reduce the stiffness and strength demand by improving the aerodynamic performances of the deck. The idea is to minimize the forces on the structure instead of contrasting them.

The choice of streamlined box girders with good aeroelastic characteristics allows reducing the demand for torsional stiffness. Decks with lower thickness are therefore possible, and the drag force is consequently reduced. In this way, the aforementioned vicious circle can be somehow reversed.

Extreme examples of this design philosophy are the multi-box girders such as the one proposed for the Messina Bridge (Figure 6.3c). The resulting cross-sections have very appealing aerodynamic and aeroelastic properties that, in principle, reduce the demand for structural resources. As a matter of fact, a multi-box girder has a much lower torsional stiffness than a single box girder with the same cross-sectional dimensions.

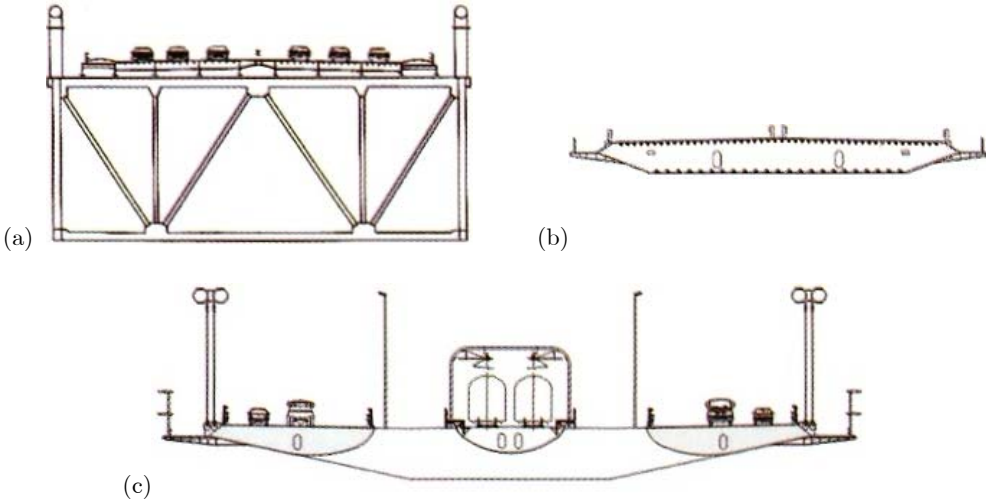

Figure 6.3 Truss girder of the Akashi-Kaikyo bridge (a); single box girder of the Jaingyin Bridge (b); multi box girder of the Messina Bridge design

Our knowledge of fluid structure interaction problems in case of bluff bodies is incomplete and is therefore supported by intensive (and expensive) wind tunnel campaigns performed on cross-sectional models, in order to characterize the aerodynamic behaviour of the selected deck. For intrinsic scaling problems, however, it is not possible to reproduce in the wind tunnel all the characteristic of a full-scale real flow. Therefore, an extreme aerodynamic optimization based on such cross-sectional tests might not cover all the risks concerning the global behaviour and it has no chance to capture three-dimensional phenomena in the flow.

For these reasons, it may seem unreliable to base the design of strategic structures only on the aerodynamic aspect, for which the theoretical knowledge is weaker.

A strong optimization of the deck in the aerodynamic sense needs to be supported by additional structural resources which the transparent deck is unable to provide.

Useful structural devices are restraining the suspended deck torsionally at the towers and providing a rigid connection between the main cable and the deck at mid-span so that the stiffness of the structural system for skew-symmetric loading is improved (Gimsing, 1983).

The structural scheme may be enhanced by using different hanger arrangements (e.g. hangers crossed in the transversal plane or zigzagging in the longitudinal direction between the main cables and the bridge deck) or the introduction of secondary cables as originally proposed by Musmeci, 1971. These solutions are further explored in Sections 6.3.1 and 6.3.2.

Matsumoto et al., 2006, suggest reducing the coupling effect of structural modes by modifying the mode shapes.

In any case, in order to improve the design and increase its reliability it is possible to include damping systems. Passive dampers in different schemes, tuned mass control (TMC) systems, or even active damping devices are possible. On one hand, damping proves helpful against buffeting and vortex induced vibrations. On the other hand, localized damping devices may increase the critical wind velocity for flutter instability. Some possible solutions are discussed in Section 6.3.3.

Finally, it is possible to consider devices that dynamically modify the aerodynamic and aeroelastic properties of the cross-section. These may be active or passive controlled winglets (Figure 6.4) that modify the flow around the cross-section according to its movement (e.g. Cobo del Arco and Aparicio, 1999; Fujino, 2002; Wilde et al., 1999).

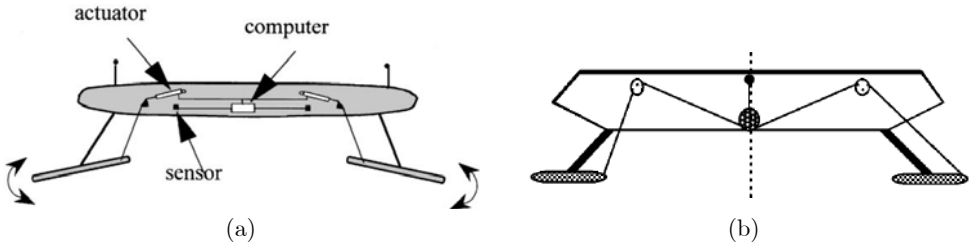

Figure 6.4 Active (a) and passive (b) aerodynamic control (Fujino, 2002; Wilde et al., 1999)

6.3 Numerical examples of wind-risk mitigation

Some examples of risk mitigation on a specific suspension bridge are offered in the next Sections.

As a sample structure a suspension bridge with the mechanical characteristics of Bosporus Bridge (see Figure 5.1, Table 5.1, Figure 5.2)

and the aerodynamics of the rectangular cross-section with width-to-height ratio $B/D = 12.5$ (see Chapter 3) is considered.

A location with a reference wind speed of 25 m/s and a terrain roughness length $Z_0 = 0.0035\,\text{m}$ is chosen.

Three approaches to wind-risk reduction are considered: (i) the introduction of hanger crossed in a vertical plane orthogonal to the axis of the bridge span, (ii) the use of secondary cables with opposed curvature with respect to the main cables, and (iii) the installation of tuned mass control devices.

The structural damping is assumed as 0.5% of the critical modal damping in all the analyses. In addition to this, the contribution of the viscous elements, where present, is considered as described in Section 4.3.4.

The standard suspension scheme is taken as reference for the evaluating the effectiveness of the mitigating approaches against mean steady deformations, aeroelastic instability, and buffeting vibrations.

The mean steady deformations are evaluated according to the procedure described in Section 4.5. This preliminary static analysis is performed for providing the correct linearization of structure and aerodynamics before checking the aeroelastic stability. The results in terms of mean steady displacements at mid-span for an arbitrary mean wind velocity of 50 m/s are reported for each solution considered in order to give an estimate of the structural stiffness.

The aeroelastic stability analysis is performed according to the procedures developed in Section 4.9. In all the considered cases, the critical condition is given by the onset of coupled flutter. For the reference structure a critical mean wind velocity of 60.9 m/s is obtained.

The critical mean wind velocity is evaluated and rendered in probabilistic terms by using the mean wind velocity profile in Eq (2.2) and the extreme value distribution in Eq (2.3).

As to the buffeting analysis, the bridge response is simulated at several mean wind velocities by following a Monte Carlo approach in the time-domain. The self-excited aeroelastic coupling effects are included through the proposed extended indicial function model, whereas buffeting loading is evaluated through a quasi-steady approach. The turbulent wind field is generated through auto-regressive filters, starting from literature spectra and coherence functions, according to the procedure described in Section 4.4.

Since the wind process is assumed as ergodic, the typical response can be obtained through a single simulation, provided that sufficiently long time histories are simulated. For each example, the average response in terms of displacements in the mid-span cross-section is plotted versus the mean wind velocity.

The adopted time-domain approach is particularly important in the analyses that follow. In fact, structural nonlinearities are particularly important for the considered cable structures (e.g. Salvatori and Spinelli,

2006b), and the mono-lateral response of hangers, which is not an issue for standard suspension bridges, must be carefully considered when crossed-hangers or complex cable configurations are adopted. Finally, time-domain methods are particularly useful in the simulation of the damping devices, even in the linear case, since the frequency-domain analysis is usually restricted to modal damping only.

The serviceability conditions of the bridge are evaluated according to the curve for storm conditions proposed by Irwin, 1978 (see Section 6.1.2). The analysis procedure is described below.

The time histories of the vertical displacements at the leading and trailing edge of the cross section for a given mean wind velocity are given by

$$\begin{aligned} z_{+}(Y,t) &= z(Y,t) + b\alpha_{y}(Y,t), \\ z_{-}(Y,t) &= z(Y,t) - b\alpha_{y}(Y,t), \end{aligned} \tag{6.2}$$

where Y is the along-span abscissa. The maxima along the bridge span of the root mean square acceleration at the leading and trailing edge are

$$\begin{aligned} a_{+}^{\mathrm{rms}} &= \max_{Y}\Big(\operatorname*{rms}_{t}\big(\ddot{z}_{+}(Y,t)\big)\Big), \\ a_{-}^{\mathrm{rms}} &= \max_{Y}\Big(\operatorname*{rms}_{t}\big(\ddot{z}_{-}(Y,t)\big)\Big). \end{aligned} \tag{6.3}$$

The larger of these is selected as characteristic response of the structure:

$$a_{\mathrm{rms}} = \max\big(a_{+}^{\mathrm{rms}}, a_{-}^{\mathrm{rms}}\big). \tag{6.4}$$

In this way a curve that relate a_{rms} to the mean wind velocity is obtained for each example.

The obtained response in terms of a_{rms} must be compared to the acceptable values of the RMS acceleration as in Figure 6.1.

The frequency of excitation is evaluated from the power spectral density function of the bridge response. Since several peaks, corresponding to the structural modes 'corrected' by the aeroelastic effects, are present, some further assumptions have been made. By looking at the diagrams in Figure 6.1, it is clear that in the frequency range of the first structural modes of the bridge (below 1 Hz) the lower frequencies are potentially more disturbing. It has then been decided to consider the maximum acceptable acceleration corresponding to the lowest-frequency mode among those that contribute to buffeting response in the vertical direction. In the cases analyzed the skew-symmetric vertical one with frequencies around 0.13 Hz is selected. This mode also gives the most important contribution to

buffeting response at low wind velocities (whereas at higher wind velocities the symmetric contributions increase more and more until a symmetric coupled flutter instability is initiated). The relevant tolerable RMS acceleration is about 0.6 m/s^2. This value is then used to obtain the critical velocity for loss of serviceability U_{cr}^{serv} from the curves that relate the response in terms of a_{rms} to the mean wind velocity.

From the values of the critical velocity for loss of serviceability and the extreme value distribution of the mean wind velocity, it is possible to obtain the average number of days per year n in which the bridge has to stay closed to traffic:

$$n = 365 \cdot \mathcal{P}_U \left(U_{cr}^{serv} \right), \tag{6.5}$$

where $\mathcal{P}_U$ denotes the yearly probability of exceedance of the mean wind velocity and is assumed as in Eq (2.2).

The hypotheses used for the analyses in next sections are summarized below:

i) Fully nonlinear structural behaviour;
ii) Wind loading on bridge deck only;
iii) Vortex excitation neglected;
iv) Unsteady indicial self-excited loading;
v) Quasi-steady buffeting loading;
vi) Ultimate limit state for aeroelastic instability (static and dynamic);
vii) Serviceability limit state for excessive vertical acceleration;
viii) Deterministic structure and aerodynamics (*Vulnerability*);
ix) Type I extreme value distribution for the mean wind velocity (*Hazard* $*$ *Exposure*);
x) Deterministic values of the losses (*Consequences*).

The simplifying hypotheses (ii) and (v) could be easily removed once the aerodynamic characteristics of towers and cables and the admittance functions for the bridge deck are provided. The relevant load models are already implemented in the developed computational program.

In order to obtain a fully probabilistic model the probability distributions of structural and aerodynamic properties should also be considered in order to evaluate the *Vulnerability*. In Section 5.2 it has been shown that a probabilistic approach to aerodynamic behaviour is in general possible. Nevertheless, it is the Author's opinion that this can only provide a rough estimate of the true probability distribution of the aerodynamic properties, since it is very difficult to predict how the uncertainties of wind tunnel measurements propagate to the full scale, where, just for instance, the Reynolds number are some order of magnitude higher (unless high-

pressure or low-temperature wind tunnels are used, which is unlikely to happen for civil structures).

The risk term *Hazard* ∗ *Exposure* is given by the probability of having (in the bridge location and for a given time span) a wind storm with a given mean wind velocity in the direction orthogonal to the bridge span.

Some remarks on the *Consequences* of the risk are given in Section 6.4.

6.3.1 Example 1: Crossed-hangers

In order to increase the torsional stiffness of the bridge deck, it is possible to cross some hangers in such a way that they connect each cable with the opposite side of the deck. This is usually not possible at mid-span, where the crossed hangers would interfere with the vehicular traffic and would be in any case inefficient due to their high inclination with respect to the vertical direction.

In the present example, the hangers are crossed only in the first and last fifth of the main span, so that a suitable clearance is ensured for the vehicles (Figure 6.5).

The results of the static, buffeting, and stability analyses are reported in Table 6.1.

A general increase (around 15%) in the torsional stiffness is highlighted by the reduction of both the mean steady rotations and the period of the main torsional mode. Although the torsion-to-bending frequency increases, no significant enhancement in the critical velocity for flutter instability is observed. This can be explained by the strong multi-modal nature of the critical mode, which receives crucial contributions by more than two structural modes, so that the classical flutter solution based on bi-modal analysis becomes meaningless (see also Salvatori and Spinelli, 2006c). It seems however that an higher efficiency against flutter instability is possible for other bridges and with different arrangements of the crossed hangers (Bartoli et al., 2006).

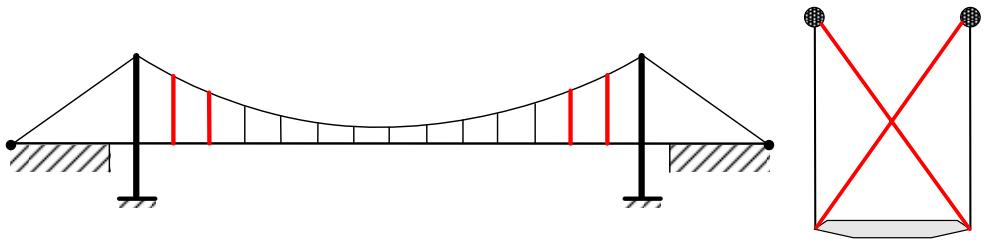

(a) (b)

Figure 6.5 Suspension scheme with crossed hangers (a); cross-section (b)

Table 6.1 Results for the mitigation through crossed hangers

	Reference bridge	X-hangers

Mean steady displacements	x	[m]	1.07	1.06
(mid-span, $U = 50$ m/s)	z	[m]	-0.47	-0.43
	θ_y	[deg]	-1.05	-0.89
Period of symmetric modes	lat.	[s]	9.50	9.50
	vert.	[s]	6.42	6.42
	tors.	[s]	2.71	2.29(*)
Vertical-to-torsional frequency ratio		[-]	2.37	2.80(*)
Critical velocity for stability		[m/s]	60.9	61.2
Critical velocity for serviceability		[m/s]	27.9	33.0

(*) mixed modes: the frequency ratio is not well-defined in these cases

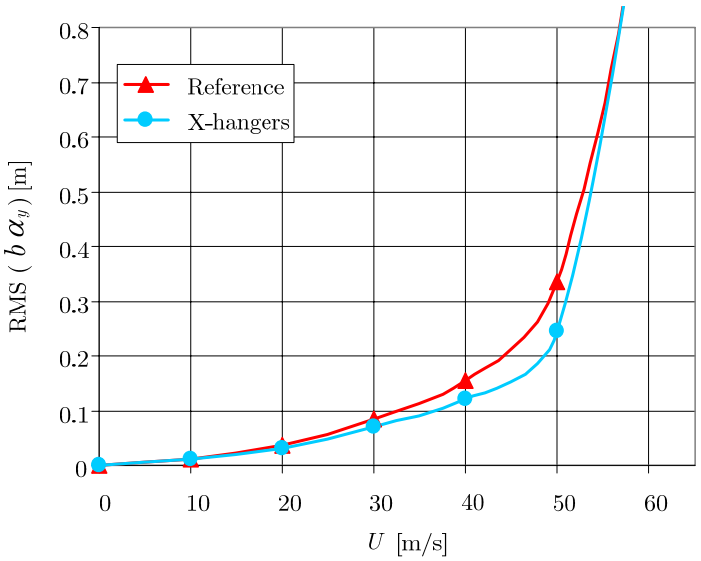

Figure 6.6 Buffeting response at mid-span for the torsional degree of freedom (crossed hangers)

As to buffeting vibrations, a non negligible reduction of the response amplitude is observed. As an example, in Figure 6.6 the buffeting response of the torsional degree of freedom at mid-span is compared to the relevant one for the classical suspension scheme. According to the adopted criteria of serviceability, the mean wind velocity for closure to traffic increases by 18% with respect to the one in the classical suspension solution with vertical hangers. The achieved mitigation of buffeting response will be further discussed in Section 6.4.

6.3.2 Example 2: Cables with opposite curvature

The idea of a cooperating structural system composed by a deck supported by a multi-cable system has been first suggested for long span bridges by Musmeci, 1971, who proposed an interesting structural model of suspension bridge integrated by stabilizing cables with opposed curvature for the

design of Messina Strait Crossing (Figure 6.7). The secondary cables should provide additional stiffness and resistance. The lateral stiffness can be further increased by laying the secondary cables on non-vertical planes. The idea is that a structural redundancy may result in additional safety, which could compensate some not-yet-experienced effects on super long spans. Some first investigations on this innovative suspension scheme have been carried out by Borri et al., 1993, who evidenced remarkable benefits under the action of steady wind. Astiz, 1998, pointed out the potentialities of this solution. In Borri, Costa, Majowiecki and Salvatori, 2005, a more detailed study on the efficiency of an analogous scheme is presented by means of a simplified model under dynamic wind loading. Then, in Salvatori and Spinelli, 2006c, the model is further extended to cover the full three-dimensional behaviour, including the drag effects, the structural nonlinearities, as well as self-excited and buffeting loading.

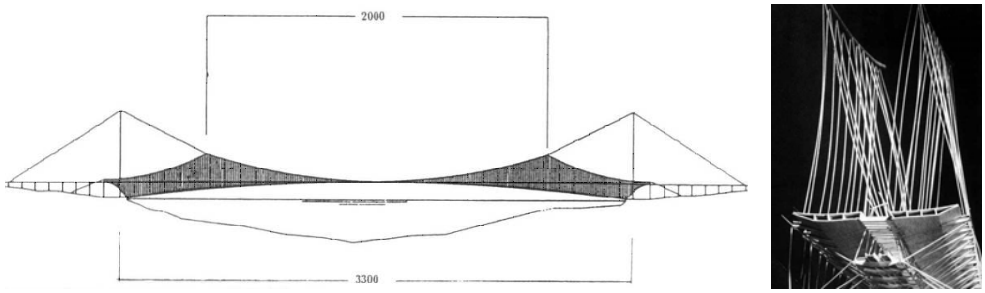

(a) (b)

Figure 6.7 Musmeci's suspension scheme (a) and detail of the bridge deck (b) (Musmeci, 1971)

Below, three versions of the suspension schemes with secondary cables are analyzed: (i) one with the secondary cables lying on vertical planes (Figure 6.8), (ii) one with the secondary cables lying on planes inclined by 45 degrees with respect to the vertical (Figure 6.9), and (iii) one with the secondary cables lying on slightly inclined planes and including crossed hangers below the bridge deck (Figure 6.10).

The relevant analysis results are summarized in Table 6.2.

Let us first analyze the case of secondary cables lying on a vertical plane. The main advantage of this scheme is the reduction of the mean steady deformations due to an overall increase in stiffness. At mid-span the mean steady displacements are reduced by 20%, 34%, and 13% in the lateral and vertical directions and in pitching rotation respectively.

The effects on flutter are even self-defeating, as it can be easily explained by using simple mechanical model.

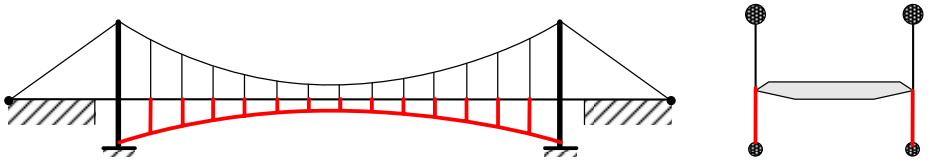

(a) (b)

Figure 6.8 Suspension scheme with secondary cables lying on vertical planes (a); cross-section (b)

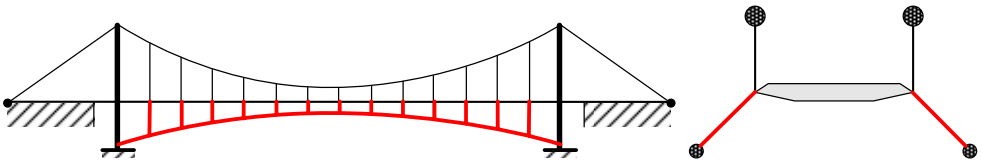

(a) (b)

Figure 6.9 Suspension scheme with secondary cables lying on 45-deg planes (a); cross-section (b)

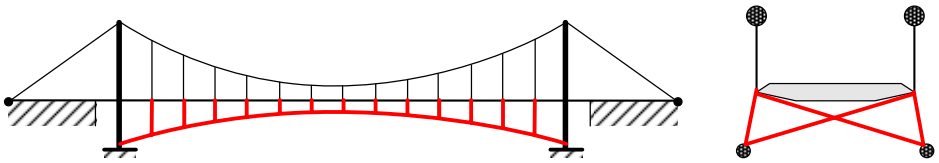

(a) (b)

Figure 6.10 Suspension scheme with secondary cables and crossed hangers below the deck (a); cross-section (b)

Let us first consider the suspension cables of a bridge without the deck (Figure 6.11a). In this case it is obvious that the vertical and torsional frequencies are exactly equal. Now we add the bridge deck (Figure 6.11b): since its mass is not concentrated at the deck sides the torsional frequency is decreased by deck inertia less than the bending frequency; moreover, also the deck stiffness plays a role in separating the frequencies. In fact, the vertical bending stiffness, which is inversely proportional to the cube of span length, is negligible with respect to the torsional one, which is inversely proportional to the span length. Therefore, the vertical-torsional frequency separation is mainly given by the relative contribution of the bridge deck to the total stiffness and inertia of the bridge. When the secondary cables are introduced (Figure 6.11c), the relative contribution of the bridge deck is reduced in favour of that of the cable system. In our example the frequency ratio reduces from 2.37 to 1.95 with a negative effect on the critical velocity for instability. In fact only a slight reduction is observed, because the effect of the reduced frequency separation is partially balanced by the overall increase of the frequencies. The negative effects described can be partially alleviated by the use of Kevlar and carbon fibre

cables because of their lighter weight (Borri, Costa, Majowiecki, Salvatori et al., 2005).

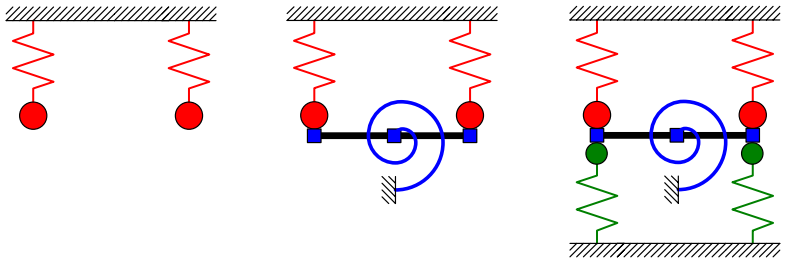

Figure 6.11 Schematic representation of the main cables (a), of the classical suspension scheme (b), and of the suspension scheme with secondary cables (c)

Buffeting vibrations are only slightly mitigated, and the critical velocity for serviceability increases by about 5% (see also Figure 6.12).

In order for the secondary cables not to go slack during buffeting excitation, a pre-stress equivalent to 40% of the deck dead weight must be considered. It is then clear that this solution is not economical for long span bridges since the increased stresses will result in much larger cable cross-sections and consequent augmented construction costs. On the other hand, this solution is quite appealing for footbridges (where the negative lift cancelling the deck dead weight can be cured by the presence of the secondary cables).

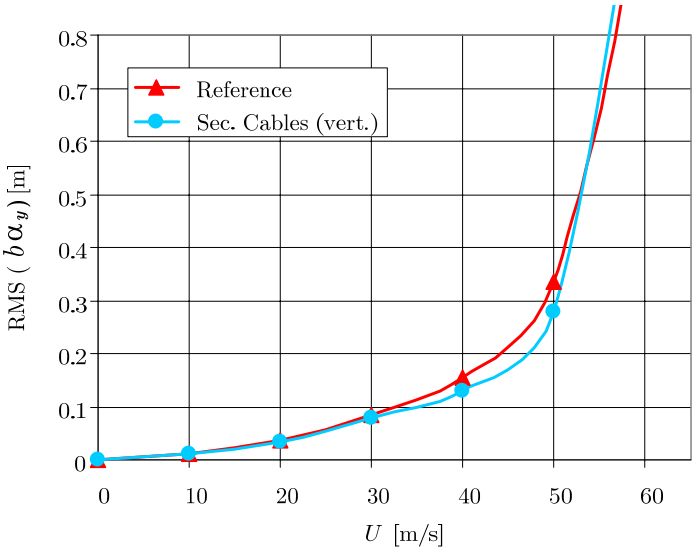

Figure 6.12 Buffeting response at mid-span for the torsional degree of freedom (secondary cables, vertical)

When the secondary cables are disposed on 45-deg-inclined planes, the lateral stiffness is further increased, so that lateral displacements are 36% smaller of those for the standard suspension scheme. No additional advantages are highlighted for stability and buffeting (see also Figure 6.13). In this case the pre-stress had to be increased up to a 47% of those induced by dead weight.

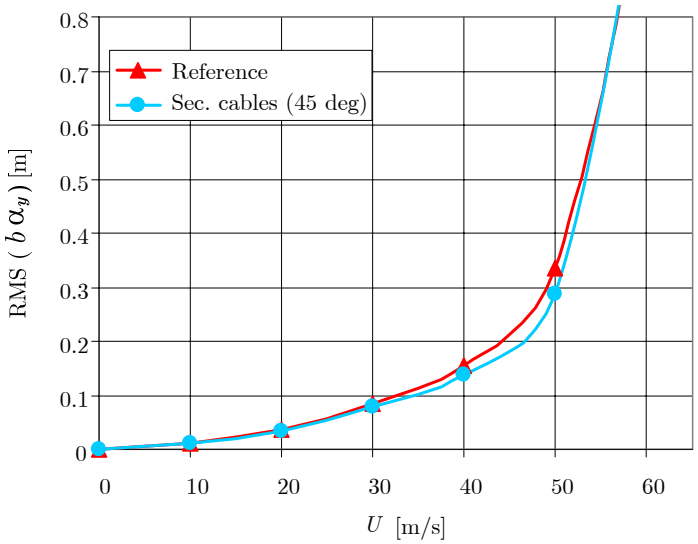

Figure 6.13 Buffeting response at mid-span for the torsional degree of freedom (secondary cables at 45 deg)

Table 6.2 Results of mitigation through secondary cables in various arrangements

			Reference bridge	Secondary cables		
				vert.	45 deg	X-hang.
Mean steady displacements (mid-span, $U = 50$ m/s)	x	[m]	1.07	0.86	0.68	0.75
	z	[m]	-0.47	-0.31	-0.50	-0.29
	θ_y	[deg]	-1.05	-0.91	-1.14	-0.73
Period of symmetric modes	lat.	[s]	9.50	8.87	7.49	8.28
	vert.	[s]	6.42	5.38	5.66	5.34
	tors.	[s]	2.71	2.76	2.97	2.60(*)
Vertical-to-torsional frequency ratio		[-]	2.37	1.95	1.91	2.05(*)
Critical velocity for stability		[m/s]	60.9	60.8	61.1	66.3
Critical velocity for serviceability		[m/s]	27.9	29.3	29.4	32.0

(*) mixed modes: the frequency ratio is not well-defined in these cases

An interesting characteristic of the suspension scheme with secondary cables is that crossed hangers can be placed below the bridge deck. Contrary to the case in which the hangers are crossed above the deck, in this case the crossed hangers can be placed along the whole bridge span without interfering with traffic. This results in an important increase in stiffness, particularly for the pitching degree of freedom, for which the

steady rotation are reduced by more than 30%. Again, in presence of crossed hangers the structural modes are no more purely vertical or torsional, but many mixed modes appear. The flutter instability can be reliably predicted only through a multi-modal analysis (or through direct time domain simulations). In our example, the critical velocity for flutter instability increases of 9%, although the frequency ratio reduces from 2.37 to 1.95. The presence of secondary cables with crossed hangers reduces the buffeting response. According to the adopted criteria of serviceability, the mean wind velocity for closure to traffic increases by 15% with respect to the one in the classical suspension scheme (see also Figure 6.14). The achieved mitigation of buffeting response will be further discussed in Section 6.4.

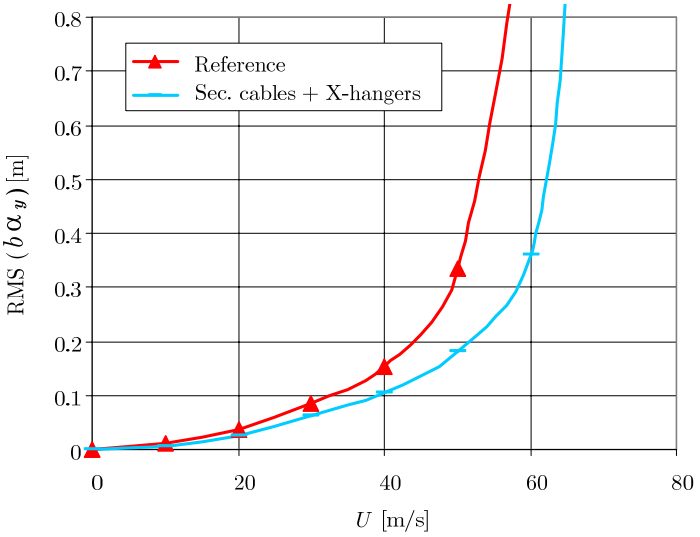

Figure 6.14 Buffeting response at mid-span for the torsional degree of freedom (secondary cables + crossed hangers below the bridge deck)

6.3.3 Example 3: Tuned Mass Control Systems

The effectiveness of damping in controlling several kind of vibrations, including buffeting and vortex induced ones, is well known by bridge designers.

On the other hand, structural damping is traditionally not considered as an effective measure against aeroelastic instability. Nevertheless, localized damping devices might increase also the critical wind flutter velocity, contrary to modal damping which only slightly affects the flutter threshold.

Some long-span suspension bridges such as the Severn Bridge (UK) adopt inclined hangers zigzagging between the main cables and the bridge deck in order to take advantage of the hysteresis of the helical ropes (Gimsing, 1983). Distributed dampers installed in a suspension bridge deck

are used for seismic retrofitting in Murphy and Collins, 2004. In Li et al., 2005, multiple TMC devices are designed to control the vibrations induced by high-speed trains in suspension bridges. Dampers have been also used to solve problems of pedestrian-bridge dynamic interaction in footbridges such as the Millennium Bridge in London.

TMC systems (TMCSs) have been considered to withstand aeolian risk too, including buffeting vibrations (e.g. Kwok and Samali, 1995; Ricciardelli et al., 2003) and flutter instability.

In Pourzeynali and Datta, 2005, the efficacy of TMCSs in increasing the critical flutter velocity is pointed out, especially if semi-active devices are used. Semi-active lever-type TMCSs, where the frequency can be tuned by varying the lever arm length, are proposed also by Gu et al., 2002. Optimization of multiple TMCSs against flutter instability is studied by Kwon and Park, 2004, who also account for the uncertainties in wind tunnel coefficients. Active control through piezoelectric actuators is also possible (e.g. Songa et al., 2006). In Gu et al., 1998, numerical and experimental analyses are carried out; mass and frequency ratios, the viscous damping of the devices and the modal damping of the structure are treated parametrically; an increase up to 40% of the critical mean wind velocity is obtained, corresponding to a mass ratio of 5.6%. Passive TMCSs provided of disk brakes have been installed, for instance in the Bronx Whitestone Bridge (e.g. Barelli et al., 2006). In Figure 6.15 an example of TMCS designed against torsional flutter in a footbridge is shown (see also Zahlten and Eusani, 2006).

(a) (b)

Figure 6.15 Kehl-Strasbourg footbridge on the Rhine (a) and the installed tuned mass control systems (b)

Chen and Kareem Chen and Kareem, 2003, propose a method for optimizing TMCS parameters against flutter and observe that the effectiveness of this countermeasure strongly depends on the aeroelastic properties of the cross-section. They distinguish between 'soft' and 'hard' type flutter. In the former case, the negative aerodynamic damping increases slowly with the reduced velocity in such a way that the control

due to TMC devices is quite effective and a significant increase in the critical flutter velocity is obtained. In the latter case, the aerodynamic damping increases rapidly with the reduced velocity and only a slight increase in the critical flutter velocity can be obtained. The question of the oscillation amplitude of control masses and the actual possibility of housing them inside a steel-box deck is raised. Other authors (e.g. Chen and Cai, 2003) suggest that special movable devices allowing large displacements of the masses can be temporarily installed to maintain the serviceability of critical links during hurricanes.

Passive devices do not require any power source and are therefore more suitable in case of catastrophic events.

Here it is chosen to equip the bridge with linear TMCSs (e.g. Beards, 1995; Beranek and Vér, 1992; Petersen, 2001) distributed along the central fifth of the main span and positioned as schematized in Figure 6.16.

Each mass-dashpot-spring device is chosen with the same properties. Two cases with different values of the total control mass are considered, namely 50 and 100 tons per deck side. These correspond to 0.6% and 1.2% of the total mass of the bridge deck respectively, so that the static design of the structure is not significantly affected by the presence of the control devices. The stiffness of the springs is initially chosen in such a way as to obtain a frequency of each device equal to the critical flutter frequency of the original bridge and then varied until an optimum response is obtained (e.g. Eusani, 2005). The damping of the devices is assumed as 4% of the critical damping of each oscillator and is not varied in this preliminary analysis.

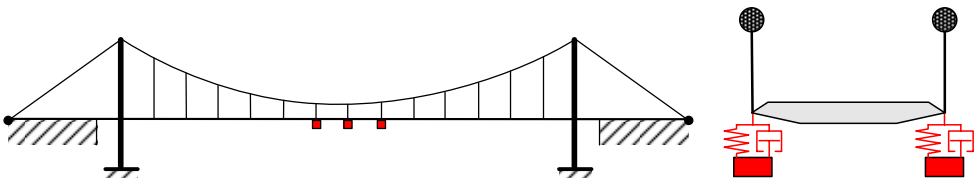

Figure 6.16 Suspension bridge with attached tuned mass control devices (a); cross-section (b)

The relevant analysis results are summarized in Table 6.3.

As expected, neither the static response under mean wind nor the modal frequencies are significantly modified by the presence of the control devices. A remarkable increase in the critical flutter velocity is observed (+8% and +23% with 50- and 100-ton-TMC respectively). Also the buffeting response is significantly reduced (see Figure 6.17), so that the critical velocity for loss of serviceability increases of 10% and 26% in the two analyzed configurations. It is worth noticing that the benefits increase more than proportionally with the total control mass and that they are achieved without modifying the overall design of the bridge (the mass of the devices

is negligible with respect to the one of the bridge deck and of the main cables). The achieved mitigation of buffeting response will be further discussed in Section 6.4.

The introduction of tuned mass devices appears as the most effective solution in reducing both instability and buffeting risks. Even without performing a detailed optimization, it has been shown that significant advantages can be obtained by adding a relatively small amount of mass.

Table 6.3 Results of mitigation through tuned mass control systems

			Reference bridge	TMC	
				50 ton	100 ton
Mean steady displacements (mid-span, $U = 50$ m/s)	x	[m]	1.07	1.06	1.06
	z	[m]	-0.47	-0.46	-0.46
	θ_y	[deg]	-1.05	-1.04	-1.04
Period of symmetric modes	lat.	[s]	9.50	9.57	9.63
	vert.	[s]	6.42	6.48	6.54
	tors.	[s]	2.71	3.33$^{(*)}$	3.42$^{(*)}$
Vertical-to-torsional frequency ratio		[-]	2.37	1.92$^{(*)}$	1.91$^{(*)}$
Critical velocity for stability		[m/s]	60.9	65.7	74.7
Critical velocity for serviceability		[m/s]	27.9	30.8	35.2

(*) mixed modes: the frequency ratio is not well-defined in these cases

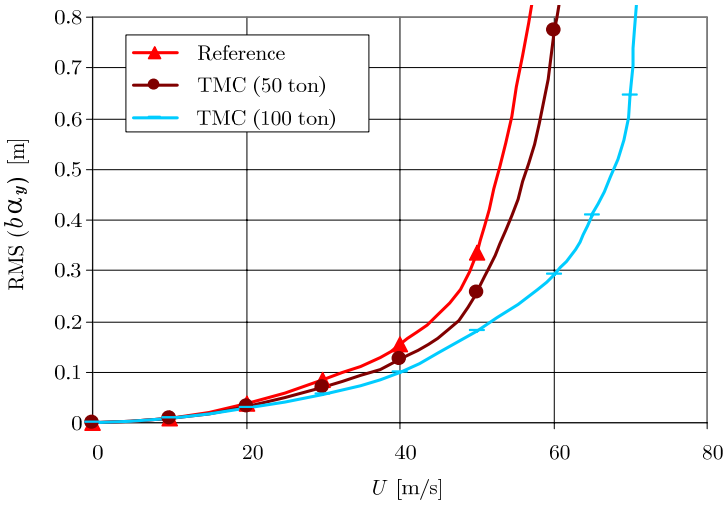

Figure 6.17 Buffeting response at mid-span for the torsional degree of freedom (tuned mass control systems)

6.4 Summary of results

The results obtained in the previous Sections are summarized in Table 6.4 and visualized in Figure 6.18 in terms of critical wind velocity for aeroelastic instability and loss of serviceability.

Table 6.4 Summary of results

Bridge	Crit. velocity (stability) [m/s]	Probability of failure [1/year]	Critical vel. (serviceability) [m/s]	Closure to traffic [days/year]
Reference	60.9	8.1×10^{-14}	27.9	32.4
X-hangers	61.2 (+0.5%)	5.7×10^{-14}	33.0 (+18%)	1.8
Sec. cables (vert.)	60.8 (-0.2%)	9.1×10^{-14}	29.3 (+5%)	15.5
Sec. cables (45 deg)	61.1 (+0.3%)	6.5×10^{-14}	29.4 (+5%)	14.7
Sec. cables (X-hang.)	66.3 (+9%)	1.1×10^{-16}	32.0 (+15%)	3.3
TMC (50 ton)	65.7 (+8%)	2.2×10^{-16}	30.8 (+10%))	6.7
TMC (100 ton)	74.7 (+23%)	1.0×10^{-18}	35.2 (+26%))	0.4

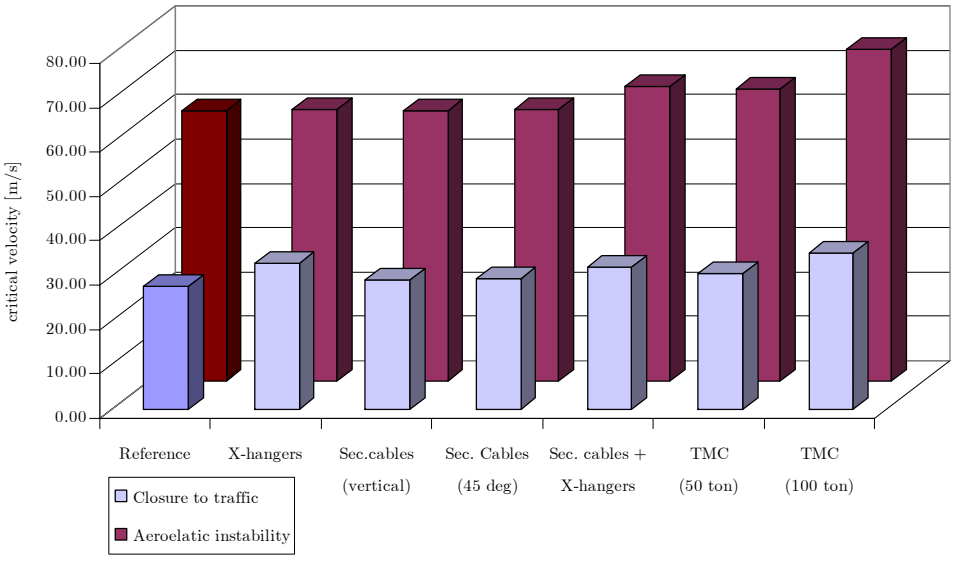

Figure 6.18 Critical wind velocities for serviceability and ultimate limit states

These results can be readily rendered in probabilistic terms by using the extreme value distribution of the mean wind velocity and the wind velocity profile as described in Section 6.3.

In this way the yearly probability of bridge failure due to aeroelastic instability can be obtained. The relevant results are reported in Figure 6.19. It is clear that instability is definitely not an issue for the analyzed bridge, since the relevant probabilities of failure are negligible in all cases. However, the interesting benefits of a three-dimensional cable-structure solution and of the introduction of tuned mass control devices are noticeable.

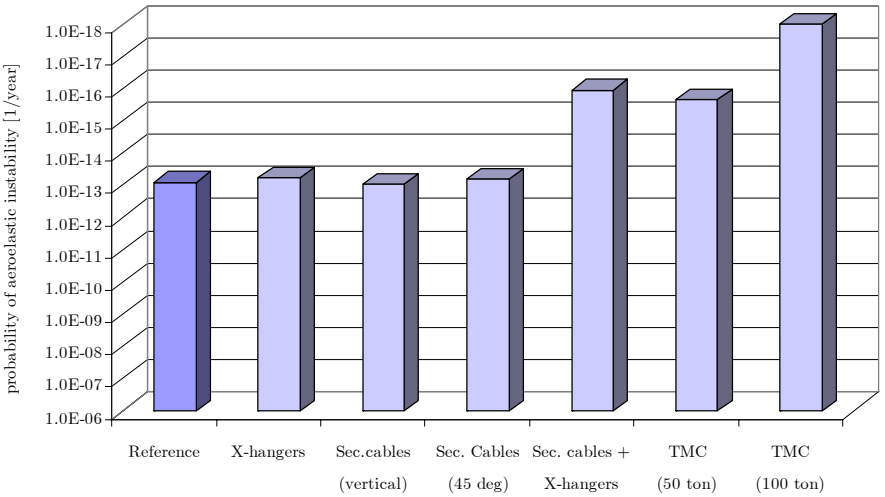

Figure 6.19 Yearly probability of failure due to aeroelastic instability

In a similar way, the critical velocity for bridge serviceability can be translated into economical terms by evaluating the average number of days per year in which the bridge must be closed to traffic due to excessive vibrations. The relevant results are reported in Figure 6.20.

In the case of buffeting response, the classical suspension solution appears as unacceptable, since the bridge would stay closed about one month per year in average. All the considered alternative solutions actually help to improve serviceability. Where crossed hangers are introduced, either from the main cables or from the secondary cables, the benefits are more pronounced, since the torsional contribution to buffeting is dramatically reduced by the improved torsional stiffness. The most effective solutions are however those where tuned mass control devices are used. In particular, in the case in which devices with a total mass of 100 tons are used, the average closure to traffic drops to 0.4 days/year.

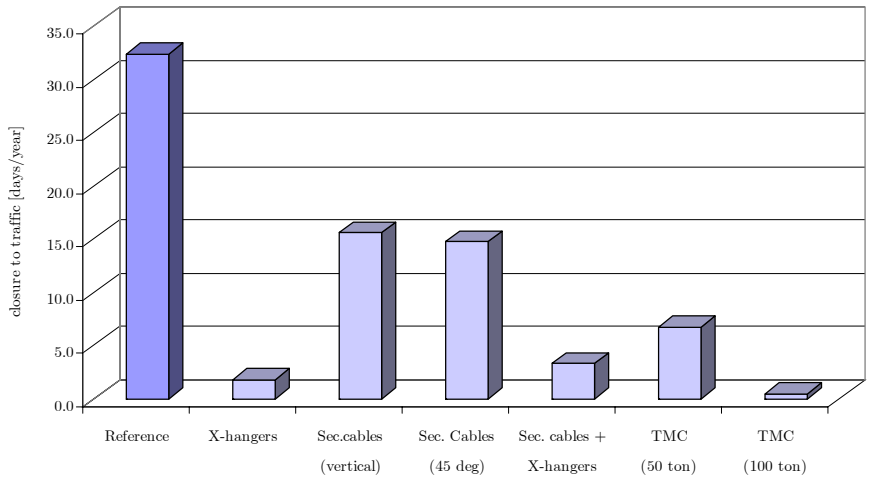

Figure 6.20 Loss of survivability due to buffeting vibrations

The results obtained can then be easily translated into economical terms and used to choose among different solutions by comparing their costs with their benefits.

The general costs of bridge closure or failure include social losses that are very difficult to assess, but in the case in which the risk analysis is performed by the company that builds and manages a bridge (a realistic scenario), the losses due to the bridge closure can be estimated for instance from the non-perceived toll incomes, in such a way that the money spent to build a mitigation device can be compared to the extra income the device allows during the lifetime of the bridge.

It can be concluded that improvements in the structural scheme and the use of control devices may provide reliable benefits in bridges with optimized aerodynamics (and therefore poor structural resources of the deck).

More detailed analyses should include the evaluation of stresses in the solutions based on cables arrangements in order to evaluate the actual feasibility of these suspension schemes and allow their structural design.

As to the solutions based on tuned mass control devices, they appear very promising, if one considers that only a rough optimization of the control parameters has been performed. Therefore, optimization (e.g. Lee et al., 2006; Zuo and Nayfeh, 2004) is one of the natural development of the preliminary encouraging results. The issue of the travel length of the masses and of the possibility of placing the devices within the bridge deck height shall also be evaluated. Oscillation amplitude can be possibly limited by the introduction of passive or semi-active mechanical devices. The proposed analysis method in the time domain is especially suitable for this purpose, since the direct simulation of the nonlinear devices is readily possible. Also,

the fatigue life of the viscous elements of the control devices shall be estimated in order to include its cost in the risk analysis.

In a more complete risk approach, the probabilistic approach should be extended to structure and aerodynamics and the risks due to vortex shedding and direct loading on vehicles should be included.

Finally, one may expect that different solution may be optimal in different ranges of span length. Therefore, parametric analyses are eventually planned, where a bridge with typical characteristics might be (automatically) designed with different lengths, and the effectiveness of the different mitigation strategies might be compared.

The main results described in this Chapter can be summarized as follows:

- The versatility and usefulness of the developed computational environment have been shown;
- Some particular strategies for mitigating the risk of aeroelastic instability and buffeting discomfort have been analyzed;
- The effectiveness of tuned mass control devices in the simultaneous mitigation of flutter and buffeting risks, at least in the considered study case, has been demonstrated by numerical results;
- Some of potentialities of the risk management framework in helping the decision making process have presented.

Chapter 7

Concluding Remarks

The present work has addressed the vulnerability of flexible bridges under wind action within the general framework of the risk management. Particular attention has been paid to the risk of aeroelastic instabilities and of buffeting oscillations in presence of self-excited phenomena.

In order to assess the bridge response during a wind storm, a computational framework based on semi-empirical cross-sectional models for the wind loading and on the finite element discretization of the structure has been developed.

A time-domain model for unsteady wind loading has been derived as a development of load models based on indicial functions. Some inaccuracy issues of the existing load models have been overcome, and the consistency with the quasi-steady limit has been ensured. A numerical procedure for the identification of the load model coefficients from wind tunnel experimental data has been proposed and implemented, with regard also for the reliability of the original measured quantities. The proposed time-domain method for full-bridge simulations has been then validated against multi-modal frequency-domain analyses (the two approaches must be equivalent, if a linear structural behaviour is assumed in the time-domain analyses too). The time-domain approach is particularly important, because it allows the simulation of structural nonlinearities and damping devices which are crucial aspects in the analysis of flexible bridges and in the relevant wind-risk mitigation.

By using the developed computational environment, several results on the evaluation of bridge response, and therefore of the vulnerability, have been obtained. In particular, the effects on aeroelastic stability and buffeting response of the along-span wind coherence, of the mean steady deformations, and of load and structural nonlinearities have been evaluated.

Finally, mitigation strategies against aeroelastic instability and buffeting oscillations have been discussed. A risk-based comparison of some of the mitigating solutions has been performed in the special case of a suspension bridge. Structural improvements such as crossed hangers and secondary cables with opposed curvature have been considered, as well as the

possibility of installing tuned mass control devices. The results have been rendered in terms of probability of collapse and expected number of days of closure to traffic per year. In this way, a cost-benefit analysis of different solutions for risk mitigation is easily achievable. The solutions based on damping devices have provided promising results in buffeting- and flutter-risk mitigation.

Further developments are possible in several directions.

As to load models, the systematic identification of different aerodynamic cross-sections is in progress, together with an improvement of the buffeting model, including some considerations on nonlinear unsteady loading. This analysis shall also include the validation of the method by the numerical comparison of unsteady buffeting response in the time and frequency domains for a full bridge, in a similar way to the one presented in this work for the stability analysis.

The method for risk assessment and comparison of mitigation strategies, which has been developed here, is only partially based on probabilistic methods, since the structural and the aerodynamic properties have been assumed as deterministic. As a matter of fact, a fully probabilistic model would be possible only in the case of a particular structure, and would require detailed specific information. Therefore, only a sensitivity analysis seems possible. The framework that has been developed would be useful for further analyses, where tentative probability distributions for the structural and aerodynamic characteristics could be assumed and the way they combine together in affecting the final results could be parametrically investigated. In that case the target would be the definition of safety coefficients, which appears as the only approach suitable for practical applications.

Finally, the developed computational environment, thanks to its generality, makes it possible to envision new analyses for assessing the effectiveness of further structural solutions against wind risk. For example, the feasibility and efficiency of nonlinear damping devices or of structural solutions characterized by geometrical or physical nonlinearities could be easily evaluated by direct simulations.

References

Alexander D (2004). Lectures in: Methods and models for risk evaluation (socio-economic aspects). *Proceedings of Doctoral Course on Risk Management on the Built Environment*, 3 April - 7 March, Firenze.

American Society of Civil Engineers (1981). Recommended design loads for bridges. *Journal of the Structural Division ASCE*, 107(ST7):1161-1213.

Astiz MA (1998). Flutter stability of very long suspension bridges. *Journal of Bridge Engineering*, 3(3):132-139.

Augusti G (2006). Lecture: What do we mean by "risk"? *Proceedings of Summer School*, 8-13 May, Firenze.

Augusti G, Borri C, Niemann H-J (2001). Is Aeolian risk as significant as other environmental risks? *Reliability Engineering and System Safety*, 74(227-237.

Augusti G, Diaferio M, Sepe V (2002). Unilateral behavior of the suspending hangers in the wind induced response of large span bridges. *Proceedings of VII IN-VENTO*, Milano, Italy.

Barelli M, White J, Billington DP (2006). History and Aesthetics of the Bronx-Whitestone Bridge. *Journal of Bridge Engineering*, 11(2):230-240.

Bartoli G, D'Asdia P, Febo S, Mannini C, Pastò S, Procino L (2006). Analisi di sensibilità aeroelastica nella progettazione di ponti sospesi di grande luce. Parte II: aspetti progettuali. *Proceedings of IX IN-VENTO*, 18-21 June, Pescara, Italy.

Bathe K-J (1996). *Finite Element Procedures*. Prentice Hall, Upper Saddle River, NJ.

Bathe K-J, Baig MMI (2005). On a composite implicit time integration procedure for nonlinear dynamics. *Computers and Structures*, 83(2513–2524.

Beards CF (1995). *Engineering Vibration Analysis with Application to Control Systems*. Arnold, London.

Beranek LL, Vér IL (1992). *Noise and Vibration Control Engineering: Principles and Applications*.

Berz G, Rauch E (1997). Winterstürme über Deutschland, ein Schadensrückblick über die letzten 30 Jahre. *Windtechnologische Gesellschaft Deutschland-Österreich-Schweiz*, 5(5-7.

Billah KY, Scanlan RH (1991). Resonance, Tacoma Narrows bridge failure, and undergraduate physics textbooks. *American Journal of Physics*, 59(2):118-124.

Bisplinghoff RL, Ashley H, Halfman RL (1955). *Aeroelasticity*. Addison-Wsley, Reading (MA).

Borri C (1988). *Generation procedures of stationary random processes simulating wind time series*.

Borri C, Costa C (2004). Quasi-steady analysis of a two-dimensional bridge deck element. *Computers and Structures*, 82(993-1006.

Borri C, Costa C, Majowiecki M, Salvatori L (2005). Large Suspension Bridges to Withstand Wind Loading. *Proceedings of ACWE*, Batorn Rouge, LA.

Borri C, Costa C, Majowiecki M, Salvatori L, Spinelli P (2005). Re-thinking the classical scheme of very long suspension bridges under wind loading. *Proceedings of IV EuroDyn Conference*, 4-7 September 2005, Paris.

Borri C, Costa C, Salvatori L (2005). Reliability of indicial functions in bridge deck aeroelasticity. *Proceedings of 9th ICOSSAR*, Rome.

Borri C, Costa C, Zahlten W (2002). Non-stationary flow forces for numerical simulation of aeroelastic instability of bridge decks. *Computers and Structures*, 80(1071-1079.

Borri C, Höffer R (2000). Aeroelastic Wind Forces on Flexible Bridge Girders *Meccanica*, 35(1):1-15.

Borri C, Majowiecki M, Spinelli P (1993). The aerodynamic advantages of a double-effect large span suspension bridge under wind loading. *Journal of Wind Engineering and Industrial Aerodynamics*, 48(317-328.

Borri C, Marradi L (1986). A numerical simulation procedure for dynamic interactio0n wind-structure, with application to guyed masts. *Costruzioni Metalliche*, 3(3-19.

Borri C, Pastò S (2006). *Lezioni di ingegneria del vento*. Firenze University Press, Firenze.

Borri C, Salvatori L (2006). Numerical Modelling of Full-Bridge Aeroelasticity: Frequency- and Time- Domain Methods. *Proceedings of IX IN-VENTO*, 18-21 June, Pescara.

Borri C, Salvatori L, Zahlten W (2005). Finite-element time-domain simulations of bridge aeroelasticity: implementation and profiling. *Computational Fluid and Solid Mechanics*, 1(103-107.

Caracoglia L, Jones NP (2003a). A methodology for the experimental extraction of indicial functions for streamlined and bluff deck sections. *Journal of Wind Engineering and Industrial Aerodynamics*, 91(609-636.

Caracoglia L, Jones NP (2003b). Time domain vs. frequency domain characterization of aeroelastic forces for bridge deck sections. *Journal of Wind Engineering and Industrial Aerodynamics*, 91(371–402.

Caracoglia L, Jones NP (2003c). The Use of Indicial Functions in Bridge Response Assessment. *Proceedings of 11th International Conference on Wind Engineering (11-ICWE)*, June 2-5, 2003, Lubbock, TX.

Chen SR, Cai CS (2003). Multi-objective Wind Hazard Mitigation for Long-span Bridges in Hurricane-prone Area. *Proceedings of 16th ASCE Engineering Mechanics Conference*, July 16-18, Seattle.

Chen SR, Cai CS, Chang CC, Gu M (2004). Modal coupling assessment and approximated prediction of coupled multimode wind vibration of long-span bridges. *Journal of Wind Engineering and Industrial Aerodynamics*, 92(393-412.

Chen X, Kareem A (2001). Nonlinear response analysis of long-span bridges under turbulent winds. *Journal of Wind Engineering and Industrial Aerodynamics*, 89(1335-1350.

Chen X, Kareem A (2003). Efficacy of Tuned Mass Dampers for Bridge Flutter Control. *Journal of Structural Engineering ASCE*, 129(10):1291-1300.

Chen X, Kareem A, Matsumoto M (2001). Multimode coupled flutter and buffeting analysis of long span bridges. *Journal of Wind Engineering and Industrial Aerodynamics*, 89(649–664.

Chen X, Matsumoto M, Kareem A (2000a). Aerodynamic Coupling Effects on Flutter and Buffeting of Bridges. *Journal of Engineering Mechanics ASCE*, 126(1):17-26.

Chen X, Matsumoto M, Kareem A (2000b). Time domain flutter and buffeting response analysis of bridges. *Journal of Engineering Mechanics ASCE*, 126(1):17-26.

Chowdhury AG, Sarkar PP (2004). Identification of eighteen flutter derivatives of an airfoil and a bridge deck. *Wind and Structures*, 7(3):187-202.

Cobo del Arco D, Aparicio AC (1999). Improving suspension bridge wind stability with aerodynamic appendages. *Journal of Structural Engineering ASCE*, 125(12):1367-1375.

Coleman TF, Li Y (1996). An Interior, Trust Region Ap-proach for Nonlinear Minimization Subject to Bounds. *SIAM Journal of Optimization*, 6(418-445.

Costa C (2004). Time-domain models in bridge deck aeroelasticity. *Ph.D. thesis*, Università degli Studi di Firenze, Florence.

Crisfield MA (1991). *Non-linear Finite Element Analysis of Solids and Structures*. John Wiley & Sons, New York.

Davenport AG (1967). Gust loading factors. *Journal of the Structural Division ASCE*, 93(11-34.

den Hartog JP (1932). Transmission line vibration due to sleet. *AIEE Transactions*, 51(1074-1076.

Diana G, Bruni S, Cigada A, Collina A (1993). Turbulence effect on flutter velocity in long span suspended bridges. *Journal of Wind Engineering and Industrial Aerodynamics*, 48(329-342.

Diana G, Bruni S, Rocchi D, Resta F, Belloli M (2005). An experimental device to investigate aerodynamics non linearities in bridge response to turbulent wind. *Proceedings of EuroDyn*, Paris.

Diana G, Resta F, Belloli M, Rocchi D (2006). On the vortex shedding forcing on suspension bridge deck. *Journal of Wind Engineering and Industrial Aerodynamics*, 94(341-363.

Ding Q, Lee PKK (1999). Computer simulation of buffeting actions of suspension bridges under turbulent wind. *Computer and Structures*, 76(787-797.

Dorfman MS (1997). *Introduction to Risk Management and Insurance*. Prentice Hall,

Dyrbye C, Hansen SO (1996). *Wind Loads on Structures*. John Wiley & Sons, New York.

Eurocode 1 (1997). *UNI ENV 1991*.

Eusani R (2005). Zur numerischen Zeitbereichssmulation der aeroelastischen Instabilität bei Seilbrüchen. *PhD thesis*, Berghische Universität Wuppertal, Wuppertal.

Facchini L (1996). The Numerical Simulation of Gaussian Cross-Correlated Wind Velocity Fluctuations by Means of a Hybrid Model. *Journal of Wind Engineering and Industrial Aerodynamics*, 64(187-202.

Falco M, Gasparetto M, Scaramelli F (1978). *Ricerca sul comportamento aeroelastico dei ponti sospesi a grande luce*.

Felippa CA (2000). *A Systematic Approach to the Element-Independent Corotational Dynamics of Finite Elements*.

Flamand O (1995). Rain-wind induced vibration of cables. *Journal of Wind Engineering and Industrial Aerodynamics*, 57(353-362.

Fujino Y (2002). Vibration, control and monitoring of long-span bridges—recent research, developments and practice in Japan. *Journal of Constructional Steel Research*, 58(71-97.

Fung YC (1968). *An Introduction to the Theory of Aeroelasticity*. Dover, New York.

Garrick IE (1938). On some reciprocal relations in the theory of nonstationary flows. *NACA TR 629*,

Ge YJ, Tanaka H (2000). Aerodynamic flutter analysis of cable-supported bridges by multi-mode and full-mode approaches. *Journal of Wind Engineering and Industrial Aerodynamics*, 86(123-153.

Geurts C, Vrouwenvelder T, van Staalduinen P, Reusink J (1998). Numerical modelling of rain-wind-induced vibration: Erasmus Bridge, Rotterdam. *Structural Engineering International*, 8(2):129-135.

Gimsing NJ (1983). *Cable supported bridges: concept and design*. John Wiley & Sons, Chichester.

Glauert H (1919). Rotation of an airfoil about a fixed axis. *Aeronautical Research Commitee*, R and M 595(

Gu M, Chang CC, Wu W, Xiang HF (1998). Increase of critical flutter wind speed of long-span bridges using tuned mass dampers. *Journal of Wind Engineering and Industrial Aerodynamics*, 73(111-123.

Gu M, Chen SR, Chang CC (2002). Control of wind-induced vibrations of long-span bridges by semi-active lever-type TMD. *Journal of Wind Engineering and Industrial Aerodynamics*, 90(111-126.

Hamburger RE, Court AB, Soulages JR (1995). Vision 2000: A Framework for Performance Based Engineering of Buildings. *Proceedings of SEAOC Annual Convention*, Indian Wells, California.

Hikami Y, Shiraishi N (1988). Rain-wind induced vibrations of cables stayed bridges. *Journal of Wind Engineering and Industrial Aerodynamics*, 29(1-3):409-418.

Höffer R (1997). Stationäre und instationäre Modelle zur Zeitbereichssimulation von Windkräften an linienförmigen Bauwerken. *Ph.D. thesis*, TU-Bochum, Bochum.

Iannuzzi A, Spinelli P (1986). Wind effects on bridge girders: aerodynamic behaviour and numerical simulation. *Costruzioni Metalliche*, 1-2(2-28.

Irwin AW (1978). Human response to dynamic motion of structures. *The structural engineer*, 56A(237-244.

Istruzioni CNR (2006). *Azioni del vento sulle costruzioni*.

Jain A, Jones NP, Scanlan RH (1996a). Coupled aeroelastic and aerodynamic response analysis of long-span bridges. *Journal of Wind Engineering and Industrial Aerodynamics*, 60(69-80.

Jain A, Jones NP, Scanlan RH (1996b). Coupled Flutter and Buffeting Analysis of Long-Span Bridges. *Journal of Structural Engineering ASCE*, 122(7):716-725.

Jain A, Jones NP, Scanlan RH (1998). Effect of modal damping on bridge aeroelasticity. *Journal of Wind Engineering and Industrial Aerodynamics*, 77-78(421-430.

Jones WP (1945). Aerodynamic forces on wings in nonuniform motion. *British Aeronautical Research Committee Reports and Memoranda 2117*,

Kaimal JC (1972). Spectral Characteristics of Surface-Layer Turbulence. *Journal of the Royal Meteorology Society*, 98(563-589.

Karpel M (1982). Design for active flutter suppression and. gust alleviation using state-space aeroelastic modeling. *Journal of Aircraft*, 19(3):221-227.

Kasperski M (1998). Climate change and design wind load concepts. *Wind and Structures*, 1(2):145-160.

Katsuchi H, Jones NP, Scanlan RH (1999). Multimode Coupled Flutter and Buffeting Analysis of the Akashi-Kaikyo Bridge. *Journal of Structural Engineering ASCE*, 125(1):60-70.

Kern G, Matiz A (1998). Self-Excited Wind-Induced Vibrations and Limit Cycles in Bundled Conductors. *Meccanica*, 33(243-253.

Kristensen L, Jensen NO (1979). Lateral Coherence in Isotropic Turbulence and in the Natural Wind. *Boundary Layer Meteorology*, 17(353-373.

Kuhl D, Crisfield MA (1999). Energy-Conserving and Decaying Algorithms in Non-Linear Structural Dynamics. *International Journal for Numerical Methods in Engineering*, 45(569-599.

Küssner HG (1936). Zusammenfassender Bericht über den instationären Auftrieb von Flügeln. *Luftfahrtforschung*, 13(410-424.

Kwok KCS, Samali B (1995). Performance of tuned mass dampers under wind loading. *Engineering Structures*, 17(9):655-667.

Kwon S-D, Park K-S (2004). Suppression of bridge flutter using tuned mass dampers based on robust performance design. *Journal of Wind Engineering and Industrial Aerodynamics*, 92(919-934.

Lagarias JC, Reeds JA, Wright MH, Wright PE (1998). Convergence Properties of the Nelder-Mead Simplex Method in Low Dimensions. *SIAM Journal of Optimization*, 9(112-147.

Larsen A (2003). Aerodynamic derivatives from simulated indicial functions. *Proceedings of IC-WE-2003*, Lubbock, Texas.

Larsen A, Esdahl S, Andersen JE, Vejrum T (2000). Storebælt suspension bridge - vortex shedding excitation and mitigation by guide vanes. *Journal of Wind Engineering and Industrial Aerodynamics*, 88(283-296.

Lazzari M (2005). Time domain modelling of aeroelastic bridge decks: a comparative study and an application. *International Journal of Numerical Methods in Engineering*, 62(1064-1104.

Lee C-L, Chen Y-T, Chung L-L, Wang Y-P (2006). Optimal design theories and applications of tuned mass dampers. *Engineering Structures*, 28(43-53.

Li J, Su M, Fan L (2005). Vibration Control of Railway Bridges under High-Speed Trains Using Multiple Tuned Mass Dampers. *Journal of Bridge Engineering*, 10(3):312-320.

Lin YK, Yang JN (1983). Multimode Bridge Response to Wind Excitations. *Journal of Engineering Mechanics ASCE*, 109(2):586-603.

Lumley LT, Panofsky HA (1964). *The Structure of Atmospheric Turbulence*. John Wiley & Sons, New York.

Macdonald JHG (2002). Separation of the contributions of aerodynamic and structural damping in vibrations of inclined cables. *Journal of Wind Engineering and Industrial Aerodynamics*, 90(19-39.

Mannini C (2006). Flutter vulnerability assessment of flexible bridges. *PhD thesis*, International Doctoral Course on Risk Management, Firenze and Braunschweig.

Matsumoto M (2005). Flutter instability of structures. *Proceedings of The Fourth Eurpoean & African Conference on Wind Engineering (EACWE4)*, 11-15 July 2005, Prague.

Matsumoto M, Daito Y, Yoshizumi F, Ichikawa Y, Yabutani T (1997). Torsional flutter of bluff bodies. *Journal of Wind Engineering and Industrial Aerodynamics*, 69-71(871-882.

Matsumoto M, Kobayashi Y, Niihara Y, Shirato H, Hamasaki H (1995). Flutter mechanism and its stabilization of bluff bodies. *Proceedings of IX ICWE*, New Delhi.

Matsumoto M, Kobayashi Y, Shirato H (1996). The influence of aerodynamic derivatives on flutter. *Journal of Wind Engineering and Industrial Aerodynamics*, 60(227-239.

Matsumoto M, Mizuno K, Okubo K, Ito Y, Matsumiya H (2006). Flutter instability and recent
development in stabilization of structures. *Surface Science*, doi: 10.1016/j.susc.2007.01.032(

Matsumoto M, Saitoh T, Kitazawa M, Shirato H, Nishizaki T (1995). Response characteristics of rain-wind induced vibration of stay-cables of cable-stayed bridges. *Journal of Wind Engineering and Industrial Aerodynamics*, 57(323-333.

Matsumoto M, Shiraishi N, Shirato H, Shigetaka K, Niihara Y (1993). Aerodynamic derivatives of coupled/hybrid flutter of fundamental structural sections. *Journal of Wind Engineering and Industrial Aerodynamics*, 49(1-3):575-584.

Matsumoto M, Yoshizumi F, T. Yabutani, Abe K, Nakajima N (1999). Flutter stabilization and heaving-branch flutter. *Journal of Wind Engineering and Industrial Aerodynamics*, 83(289-299.

Minh NN, Yamada H, Miyata T, Katsuchi H (2000). Aeroelastic complex mode analysis for coupled gust response of the Akashi Kaikyo bridge model. *Journal of Wind Engineering and Industrial Aerodynamics*, 88(307-324.

Modi VJ, Welt F, Seto ML (1995). Control of wind-induced instabilities through application of nutation dampers: a brief overview. *Engineering Structures*, 17(9):626-638.

Murphy TP, Collins KR (2004). Retrofitting Suspension Bridges Using Distributed Dampers. *Journal of Structural Engineering ASCE*, 130(10):1466-1474.

Musmeci S (1971). La campata di 3000 m di Musmeci. *L'industria delle costruzioni*, 22(10-27.

Nakamura Y (1978). An analysis of binary flutter of bridge deck sections. *Journal of Sound and Vibrations*, 57(4):471-482.

Nakamura Y (1996). Flutter of coupled bending-torsion systems with a frequency ratio colse to one. *Journal of Fluid and Structures*, 10(47-56.

Nash JC (1979). *Compact numerical methods for computers - Linear algebra and function minimization*. Adam Hilger, Bristol.

Nasu S, Tatsumi M (1995). Effect of the Southern Hyogo Earthquake on the Akashi-Kaikyo Bridge. *Proceedings of 4th International Workshop on Accelerator Alignment*, 14-17 November, Tsukuba, Japan.

Neves LC, Frangopol DM (2005). Condition, safety and cost profiles for deteriorating structures with emphasis on bridges. *Reliability Engineering and System Safety*, 89(2):185-198.

Panofsky HA, al. e (1974). Two-Point Velocity Statistics over Lake Ontario. *Boundary Layer Meteorology*, 7(309-321.

Panofsky HA, Singer IA (1965). Vertical Structure of Turbulence. *Journal of Royal Meteorolgical Society*, 91(339-344.

Pastò S (2005). Fatigue-induced risk assessment of slender structures with circular cross-section at lock-in. *PhD thesis*, Doctoral Course on Risk Management, Firenze and Braunschweig.

Paulotto C, Ciampoli M, Augusti G (2004). Some proposals for a first step towards a Performance Based Wind Engineering. *Proceedings of 1st International Forum in Engineering Decision Making*, 5-9 December, Stoos, Switzerland.

Peil U (2006). Lecture in: Stochastic Dynamics in Risk Management Procedures. *Proceedings of Summer School*, 8-13 May, Firenze.

Peil U, Behrens M (2007). Aerodynamic admittance models for buffeting excitation of high and slender structures. *Journal of Wind Engineering and Industrial Aerodynamics*, 95(73-90.

Peil U, Dreyer O (2007). Rain-wind induced vibrations of cables in laminar and turbulent flow. *Wind and Structures*, 10(1):83-97.

Peil U, Nahrath N (2003). Modeling of rain-wind induced vibrations. *Wind and Structures*, 6(1):41-52.

Peil U, Ndle H, Wangb ZH (1996). Dynamic behaviour of guys under turbulent wind load. *Journal of Wind Engineering and Industrial Aerodynamics*, 65(43-54.

Peter AI (1999). *Technical notes of the Rowan Williams Davies & Irvin Inc.* Ontario, Canada.

Petersen C (2001). *Schwingungsdämpfer im Ingenieurbau.* Maurer Söhne, München.

Plate E (2000). Flood risk and flood management. *Proceedings of European Conference on Advances in Flood Research*, Potsdam.

Poirel DC, Price SJ (1997). Post-Instability Behavior of a Structurally Nonlinear Airfoil in Longitudinal Turbulence. *Journal of Aircraft*, 34(5):619-626.

Pourzeynali S, Datta TK (2005). Semiactive Fuzzy Logic control of Suspension Bridge Flutter. *Journal of Structural Engineering ASCE*, 131(6):900-912.

Ricciardelli F (1996). Prediction of the response of suspension and cable-stayed bridge towers to wind loading. *Journal of Wind Engineering and Industrial Aerodynamics*, 64(145-159.

Ricciardelli F (2003). On the wind loading mechanism of long-span bridge deck box sections. *Journal of Wind Engineering and Industrial Aerodynamics*, 91(2003.

Ricciardelli F, de Grenet ET, Hangan H (2002). Pressure distribution, aerodynamic forces and dynamic response of box bridge sections. *Journal of Wind Engineering and Industrial Aerodynamics*, 90(1135-1150.

Ricciardelli F, Pizzimenti AD, Mattei M (2003). Passive and active mass damper control of the response of tall buildings to wind gustiness. *Engineering Structures*, 25(1199-1209.

Righi M (2003). Aeroelastic stability of long span suspended bridges: flutter mechanism on rectangular cylinders in smooth and turbulent flow. *PhD thesis*, Università degli Studi di Firenze, Firenze.

Ryall MJ, Parke GAR, Harding JE (2000). *Manual of Bridge Engineering*.

Salvatori L (2007). Wind-Bridge Interaction: Load Models and Identification. *Submitted*,

Salvatori L, Borri C (2005). Toward a reliable usage of indicial functions in the practice of bridge design: numerical issues and implementation details. *Proceedings of AIMETA*, Firenze.

Salvatori L, Borri C (2007). Frequency- and Time-Domain Methods for the Numerical Modeling of Full Bridge Aeroelasticity. *Computers and Structures*, doi:10.1016/j.compstruc.2007.01.023(

Salvatori L, Spinelli P (2004). Influence of structural non-linearities on the response of suspended bridges under wind excitation: numerical simulations on simplified structures. *Proceedings of VIII IN-VENTO Conference*, Reggio Calabria.

Salvatori L, Spinelli P (2005). Three-dimensional simulations of suspension bridges under wind load: Influence of mean steady configuration and effects of load nonlinearities. *Proceedings of EACWE-4*, Prague.

Salvatori L, Spinelli P (2006a). A discrete 3D model for bridge aerodynamics and aeroelasticity: Nonlinearities and linearizations. *Meccanica*, 42(31-46.

Salvatori L, Spinelli P (2006b). Effects of structural nonlinearity and along-span wind coherence on suspension bridge aerodynamics: some numerical simulation results. *Journal of Wind Engineering and Industrial Aerodynamics*, 94(5):415-430.

Salvatori L, Spinelli P (2006c). Mitigation Strategies of Wind Risk in Suspension Bridges: Some First Numerical Results. *Proceedings of IX IN-VENTO*, 18-21 June, Pescara.

Salvatori L, Zahlten W (2005). On the Identification of Indicial Functions from measured Aeroelastic Derivatives. *Proceedings of VI EuroDyn*, Paris.

Saul WE, Jayachandran P, Peyrot AH (1976). Response to stochastic wind of *N*-degree Tall Buildings. *Journal of the Structural Division ASCE*, 102(ST5):1059-1075.

Scanlan RH (1984). Role of Indicial Functions in Buffeting Analysis of Bridges. *Journal of Structural Engineering ASCE*, 110(7):1433-1446.

Scanlan RH (1993). Problematics in formulation of wind-force models for bridge decks. *Journal of Engineering Mechanics ASCE*, 119(7):1353–1375.

Scanlan RH, Béliveau J-G, Budlong K (1974). Indicial aerodynamics functions for bridge decks. *Journal of Engineering Mechanics*, 100(657-672.

Scanlan RH, Jones NP (1990). A minimum design methodology for evaluating bridge flutter and buffeting response. *Journal of Wind Engineering and Industrial Aerodynamics*, 36(2):1341-1353.

Scanlan RH, Sabzevari A (1969). Experimental Aerodynamic Coefficients in the Analytical Study of Suspension Bridge Flutter. *Journal Mechanical Engineering Science*, 11(3):234-242.

Scanlan RH, Tomko A (1971). Airfoil and Bridge Deck Flutter Derivatives. *Journal of Engineering Mechanics*, 97(1717-1737.

Schewe G (1983). On the force Fluctuations acting on a circular cylinder in crossflow from subcritical up to transcritical Reynolds numbers. *Journal of Fluid Mechanics*, 133(265-285.

Sears WR (1941). Some aspects of non-stationary airfoil theory and its practical application. *Journal of Aeronautical Science*, 8(104-108.

Shahrzad P, Mahzoon M (2002). Limit cycle flutter of airfoils in steady and unsteady flows. *Journal of Sound and Vibrations*, 256(2):213-225.

Shinozuka M, Jan CM (1972). Digital simulation of random processes and its applications. *Journal of Sound and Vibrations*, 25(111-128.

Simiu E, Scanlan RH (1996). *Wind effects on Structures*. New York.

Simpson A (1971). On the flutter of a smooth circular cylinder in a wake. *The Aeronautical Quarterly*, XXII(25-41.

Solari G, Piccardo G (2001). Probabilistic 3-D turbulence modeling for gust buffeting of structures. *Probabilistic Engineering Mechanics*, 16(1):73-86.

Songa G, Sethib V, Lic H-N (2006). Vibration control of civil structures using piezoceramic smart materials: A review. *Engineering Structures*, 28(1513-1524.

Starr C, Rudman R, Whipple C (1976). Philosophical Basis for Risk Analysis. *Annual Review of Energy*, 1(629-662.

Stoyanoff S (2001). A unified approach for 3D stability and time domain response analysis with application of quasi-steady theory. *Journal of Wind Engineering and Industrial Aerodynamics*, 89(1591-1606.

Theodorsen F (1935). General Theory of Aerodynamic Instability and the Mecchanism of Flutter. *NACA TR 496*,

United Kingdom Department of Transport (2001). *Design manual for roads and bridges: BD 49/01 design rules for aerodynamic effects on bridges*.

van der Hoven I (1957). Power spectrum of horizontal wind speed in the frequency range 0.0007 to 900 cycles per hour. *Journal of Meteorology*, 14(160-164.

Vassie P (2000). *Bridge Management*.

Verwiebe C, Ruscheweyh H (1998). Recent research results concerning the exciting mechanisms of rain-wind-induced vibrations. *Journal of Wind Engineering and Industrial Aerodynamics*, 74-76(1005-1013.

Vickery BJ (1970). On the Reliability of Gust Loading Factors. *Proceedings of Technical Meeting Concerning Wind Loads on Buildings and Structures*, Washington.

Virgoleux M (1992). *Wind design and analysis for the Normandy Bridge*.

von Kármán T (1948). Progress in the statistical theory of turbulence. *Journal of Maritime Research*, 7(

Wagner H (1925). Über die Entstehung des dynamischen Auftriebes von Tragflügeln. *Zeitschrift fur Angewandte Mathematik und Mechanik*, 5(17-35.

Wilde K, Fujino Y, Kawakami T (1999). Analytical and experimental study on passive aerodynamic control of flutter of a bridge deck. *Journal of Wind Engineering and Industrial Aerodynamics*, 80(105-119.

Wilde K, Witkowski W (2003). Simple model of rain-wind-induced vibrations of stayed cables. *Journal of Wind Engineering and Industrial Aerodynamics*, 91(873-891.

Yamagata M, Yasuda M, Nitta A, Yamamoto S (1996). Effects on the Akashi Kaikyo Bridge. *Soils and foundations*, 1(179-187.

Zahlten W (2004). Simulation of the aeroelastic response of bridge structures including instability. *Proceedings of Impact of Wind and Storm on City Life and Built Environment*, Rhode-Saint-Genèse.

Zahlten W, Eusani R (2006). Numerical simulation of the aeroelastic response of bridge structures including instabilities. *Journal of Wind Engineering and Industrial Aerodynamics*, 94(11):909-922.

Zahlten W, Salvatori L, Borri C (2004). On the identification of indicial functions from measured aeroelastic derivatives. *Proceedings of VIII INVENTO*, 21-23 June, Reggio Calabria, Italy.

Zasso A (1996). Flutter derivatives: Advantages of a new representation convention. *Journal of Wind Engineering and Industrial Aerodynamics*, 60(35-47.

Zuo L, Nayfeh SA (2004). Minimax optimization of multi-degree-of-freedom tuned-mass dampers. *Journal of Sound and Vibrations*, 272 (893-908.